THE ROLE OF THE AXIAL MELT LENS IN CRUSTAL ACCRETION AT FAST-SPREADING MID-OCEAN RIDGES

Matthew Phillip Loocke

Submitted in partial fulfilment of the requirements for the degree of PhD.

August 2016

Declaration

This work has not been submitted in substance for any other degree or award at this or any other university or place of learning, nor is being submitted concurrently in candidature for any degree or other award.

Signed …… (candidate)

Date ……

Statement 1

This thesis is being submitted in partial fulfilment of the requirements for the degree of PhD.

Signed …… (candidate)

Date ……

Statement 2

This thesis is the result of my own independent work/investigation, except where otherwise stated, and the thesis has not been edited by a third party beyond what is permitted by Cardiff University's policy on the Use of Third Party Editors by Research Degree Students. Other sources are acknowledged by explicit references. The views expressed are my own.

Signed …… (candidate)

Date ……

Statement 3

I hereby give consent for my thesis, if accepted, to be available online in the University's Open Access repository and for inter-library loan, and for the title and summary to be made available to outside organisations.

Signed …… (candidate)

Date ……

Statement 4

I hereby give consent of my thesis, if accepted, to be available online in the University's Open Access repository and for inter-library loans after expiry of a bar on access previously approved by the Academic Standards & Quality Committee.

Signed …… (candidate)

Date ……

Table of Contents

List of Figures

List of Tables

ABSTRACT

Fast-spreading mid-ocean ridges (MOR) are underlain by a thin, quasi-steady-state melt or crystal mush body at the base of the sheeted dykes, referred to as the axial melt lens (AML). Although the AML is thought to play a key role in the development of MOR basalts (MORB), debate persists regarding the composition of the AML and the role it plays in the accretion of the lower crust. I address this question by studying a suite of varitextured gabbronorites from the Hess Deep rift valley in the equatorial Pacific Ocean which are interpreted to have formed in the AML of the East Pacific Rise. This unique sample set provides an unparalleled opportunity to conduct the first comprehensive investigation of the AML at a fast-spreading MOR. To facilitate this study, I here develop a method for the quantitative assessment of compositional distribution (QACD) in whole-thin-section element maps. QACD facilitates rapid data collection and processing to generate mineral modes, element and molar-ratio maps, and quantifying full-sample compositional distributions. My application of QACD to the Hess Deep AML suite reveals that mineral phases within the AML here are too evolved to be in equilibrium with MORB. I test the broader applicability of this conclusion by conducting detailed mapping and sampling of an analogous AML horizon in the Oman Ophiolite (Wadi Saq, Ibra Valley). This section is characterised by an evolved sheeted dyke complex rooting into a quartz diorite-hosted AML, supporting the supposition that the AML accommodates the fractionation of highly-evolved melts.

I propose a model wherein the AML is predominantly fed by small volumes of evolved interstitial melts expelled from the underlying crystal mush. In the months preceding decadal eruption events, short-lived, focused injections of primitive melts into the AML mix with the extant highly-fractionated melt and trigger eruptions. This model reconciles the apparent mismatch between the volcanic and plutonic records and inferences made on geophysical and petrological grounds. I suggest that the AML is an active player in the development of MORB, permitting the fractionation and storage of evolved melts expelled from the underlying crystal mush and recording the mixing of that material with primitive melt, hence fulfilling more of a passive role with respect to lower crustal accretion than previously proposed.

ACKNOWLEDGEMENTS

There have been so many people whose contributions and support over the last three years have helped me in some way. I will do my best to thank you all in person, but please forgive me if you've been left off of the list. I guarantee it's not intentional, the break-neck speeds at which I have had to write this thesis have left me a bit brain-fried and generally lacking mental faculties (we all know I've always been lacking in such things).

First, I'd like to thank the BGS team of *Kathryn Goodenough*, *Dave Schofield*, and *Mike Styles* of the British Geological Survey for their contributions to and support of my Oman field season.

The PhD students- I can't possibly list all of you, but every one of you has provided some sort of support in my time here, mostly the occasional cup of tea and, more frequently, pint of beer.

The faculty and staff- Tony Oldroyd, Duncan Muir, Katie Dobbie, Andrew Kerr, Julian Pearce, Hazel Prichard, Wolfgang Maier, Ake Fagereng, and Alan Channing. Tony, Duncan, and Katie, you are all legends and deserve medals for your support and everything that you do.

Hannah Hughes- Though you have moved on to greater things, you continue to keep me involved in collaborations on some pretty amazing projects. Thank you for your endless entertainment and continued collaboration!

Iain McDonald- You deserve at least a medal, maybe even a lifetime supply of your choice liquor for the amount of support and inspiration you have provided. Thank you for your fruitful discussions and continued support.

Alodie Bubeck- Thank you for being a partner in crime and a welcome source of much needed decompression with copious amounts of gin & tonic.

Henry Coombs- You know what you did.

Bethan Phillips- You have been an immense source of support and inspiration and someone who I know I can count on through thick and thin. I feel fortunate to have known you and to refer to you as my best friend. Thank you to the moon and back.

Chris MacLeod- Without having met you during the 2010 OCC conference in Cyprus, I would not have thought to ask about PhD projects at the 2012 AGU Fall Meeting, and I would not have come to Cardiff. You have been, to say the least, a great source of entertainment and guidance in my time here. Thank you for everything!

Johan Lissenberg- I'd like to say that you know what you did, and you probably do (you're just that good), but you have had a profound effect on me as a scientist. You have provided immense amounts of support and created a positive environment for me to let my scientific imagination run wild. You also haven't coddled me; you pull no punches and have no problem reigning me in when I find myself on tangential flights of fancy. You have taught me to critically think about what I'm doing in such a way as to keep me from carrying out needless tasks. Thank you for everything that you have done, especially the time-killing conversations about 80/90s music and 'King of the Hill'.

To all- There are often times when I feel like I don't deserve the support or opportunities that I have been given, but you always try to convince me otherwise. You have no idea how much that means to me. Thank you all!

Finally, I'd like to thank my parents and family. You have never stopped supporting me, regardless of how 'bright' my ideas have been. I know you don't get to pick your family, but I'm glad I ended up with this particular group of high-functioning, dysfunctional, lovable misfits. I love you guys.

CHAPTER 1
Introduction

1.1 Background

Mid-ocean ridge (MOR) volcanism is responsible for the production of igneous crust over approximately 2/3 of the Earth's surface, driving hydrothermal systems which exchange chemical elements and heat between the ocean-crust system. The tectonic and volcanic characteristics of MORs have been found to systematically vary with magma supply and spreading rate (e.g., MacDonald et al., 1992; Perfit and Chadwick, 1998; Small, 1998; Rubin and Sinton, 2007), with fast-spreading ridges (80-180 mm/yr) typically characterised by small (50-1,000 m tall) volcanoes which form a semi-continuous ridge with lava fields extending several kilometres off its sides (Rubin et al., 2012) and slow-spreading ridges (20-55 mm/yr) characterised by a ~5-15 km wide rift valley where volcanism can be sparse, forming elongate volcanic ridges (Searle et al., 2010).

Current models for the architecture of oceanic crust at fast-spreading MORs are the result of decades of geophysical experiments (e.g., Morton and Sleep, 1985; Detrick et al., 1987; Harding et al., 1989; Kent et al., 1990) and in situ petrological and structural studies of ophiolites (e.g., Oman: Hopson et al., 1981; Pallister and Hopson, 1981; Nicolas et al., 1988a, 2000; Umino et al., 2003). The classic Penrose Ophiolite model, as defined by the Penrose Ophiolite Conference in 1972, consists of a sequence from top to bottom of volcanic pillows, sheeted dykes, high level intrusives (e.g. trondhjemites and gabbros), layered cumulates (e.g. olivine gabbros, pyroxenites, and peridotites), and mantle peridotites (Greenbaum, 1972). Since the formation of the Penrose model, geophysical studies at mid-ocean ridges have provided further constraints on the architecture of the oceanic crust, reflected in the addition of seismically defined layers in the Penrose model.

Based on decades of observations at MORs which have revealed a large variability in crustal architecture over the range of global spreading rates (<10-160 mm/yr) we now recognise that the mechanisms of accretion of the oceanic crust vary fundamentally with spreading rate (Dick et al., 2006). For example, seafloor spreading at slow-spreading ridges exhibits both spatial and temporal heterogeneity as a result of reduced magma supply, significant tectonic stretching

and the incorporation of mantle materials into the lithosphere at the ridge axis. As it stands, the simplified Penrose model for oceanic crustal stratigraphy is likely to be applicable only to intermediate- to fast-spreading ridges (Dick et al., 2006).

1.1.1 Fast-spreading mid-ocean ridges

Beneath fast-spreading MORs, upwelling mantle undergoes decompression melting over a several hundred km wide region (Forsyth et al., 1998, Key et al., 2013; Han et al., 2014), generating basaltic or picritic melt (O'Hara, 1968). These melts are focused towards the ridge axis during upwelling (e.g., Aharonov et al., 1995; Katz et al., 2004, 2006; Han et al., 2014), where they are delivered to shallow levels to form oceanic crust.

Early geophysical investigations at fast-spreading ridges, such as the East Pacific Rise (EPR), identified a thin lens-like body of melt at the base of the sheeted dykes referred to as the axial melt lens (AML) (Detrick et al., 1987; Sinton and Detrick, 1992). The AML overlies a larger region of 'hot-rock' (i.e., a seismic low-velocity zone or LVZ) consisting largely of a crystal mush with small (10-20%, ~18% average; Crawford and Webb, 2002) proportions of melt (Crawford et al., 1999; Crawford and Webb, 2002; Dunn et al., 2000) (Figure 1.1). This larger LVZ has a width of ~1-2 km beneath the ridge axis and deepens and broadens beneath the ridge flanks to ~10-12 km at the base of the crust (Sinton and Detrick, 1992). As a whole, this crustal scale LVZ is commonly referred to as the axial magma chamber. The properties of this crystal mush region and the magmatic processes occurring within it are poorly constrained.

Geophysical experiments have constrained the size of the AML to be ~500-1000 m wide and ~30- 100 m thick (Detrick et al., 1987; Kent et al., 1993; Collier and Singh, 1997; Singh et al., 1998; Xu et al., 2014). These partially molten bodies have been imaged beneath a large portion of the EPR (Detrick et al., 1987; Kent et al., 1993; Tolstoy et al., 1996), suggesting that they are relatively steady-state features at fast-spreading ridges. The physical properties of the AML have been the subject of various geophysical studies over the past ~30 yr (e.g., Detrick et al., 1987, 1993; Harding et al., 1989; Kent et al., 1990, 1993a, b; Vera et al., 1990; Caress et al., 1992; Hussenoeder et al., 1996; Collier and Singh, 1997,1998; Singh et al., 1998, 1999). Many of these AML studies have focused on the portion of the East Pacific Rise (EPR) that lies between 9-10°N along the ridge, where the AML

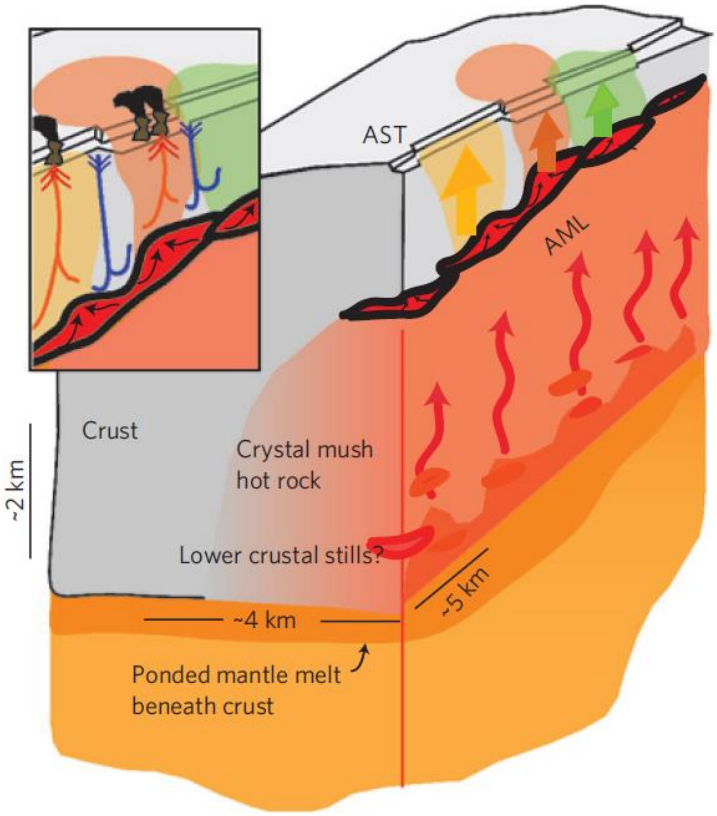

Figure 1.1: A schematic representation of a fast-spreading MOR magmatic system (c.f., Carbotte et al., 2013), with a segmented AML (red) sitting atop a crystal mush zone with potential lower crustal sills (light red).

has been imaged at ~1-2 km below the seafloor (Kent et al., 1993a; Marjanovic et al., 2015). Although qualitative and quantitative estimates of the proportion of melt within the AML (Singh et al., 1998; Canales et al., 2006; Xu et al., 2014) have been inferred from shear wave properties of the feature, the actual amount of melt present within the AML at various focus sites still remains poorly constrained (Marjanovic et al., 2015), with the best estimates at anywhere from <40% melt (Marjanovic et al., 2015) to between 40-60% melt (Singh et al., 1998) present within the AML mush. Several recent investigations have reported geophysical observations of variations in melt content and distribution over scales of a few hundred metres (i.e., smaller distances than the length of fine-scale AML segments = ~5-15 km) within the AML (Carbotte et al., 2013; Marjanovic et al., 2015). It is unclear whether the melt present within the AML is distributed in thin metre-scale sills (Barth et al., 1994) or in millimetre- to centimetre-scale pockets within a rigid crystal mush network (Marsh, 1989).

1.1.2 The architecture of the AML and the gabbroic lower crust

Most of our current understanding regarding the petrological, structural, and geochemical nature of the AML has been inferred from geophysical studies at MORs (Marjanovic et al., 2015) and detailed petrological investigations of bespoke fossilised melt lenses in ophiolites (MacLeod and Yaouancq, 2000; Coogan et al., 2002a). The gabbroic lower crust, as described from ophiolites like Oman, is composed of, from bottom to top, intercalated gabbros and dunites of the Moho transition zone, layered gabbros, and foliated gabbros which are commonly capped by a structurally and petrologically complex group of gabbros immediately beneath the sheeted dykes within a horizon which is commonly referred to as the dyke-gabbro transition (DGT). The structurally highest gabbros have been variously referred to as the 'high-level', 'isotropic', 'massive', 'upper', 'recrystallised' or 'varitextured' gabbros by previous authors (e.g., Gass, 1980; Pallister and Hopson, 1981; Lippard et al., 1986; MacLeod and Rothery, 1992; MacLeod and Yaouancq, 2000; Coogan et al., 2002a). Though many investigations include the foliated gabbros when referring to high-level gabbros, we have chosen to use the term as defined by MacLeod and Yaouancq (2000) which includes only the varitextured, isotropic gabbroic rocks which lie between the base of the sheeted dykes and the top of the foliated gabbros. The high-level gabbros as defined by MacLeod and Yaouancq (2000) are generally characterised as fine- to medium-grained, isotropic, ophitic gabbro, pegmatitic gabbro, oxide gabbro, diorite, and, in some cases, oceanic plagiogranites (see section 2.2.1 and section 6.4.2 for more information) (Rothery, 1983; Nicolas and Boudier, 1991; MacLeod and Yaouancq, 2000; Coogan et al., 2002a; Nicolas et al., 2008; France et al., 2009).

The first characterisation of the high-level gabbros as a fossilised AML was from the Wadi Abyad section of the Oman ophiolite (MacLeod and Yaouancq, 2000). The high-level gabbros within ~150 m of the base of the sheeted dykes at Wadi Abyad exhibit very strong geochemical, structural and textural variability (i.e., varitextured gabbros), containing abundant oxides associated with subordinate lenses of pegmatitic Fe-rich gabbros (i.e., ferrogabbros). MacLeod and Yaouancq (2000) interpreted the rocks as preserving the lateral edges of an AML approximately basaltic (Mg# of 65) in composition, which was derived from melt expelled from the underlying crystal mush. Investigations of the DGT and the AML published prior to (e.g., Rothery, 1983; Nicolas and Boudier, 1991; MacLeod and

Rothery, 1992; Gillis and Roberts, 1999) and since MacLeod and Yaouancq (2000) (e.g., Coogan et al., 2002a; Coogan et al., 2003; Gillis, 2008; Nicolas et al., 2008) have continued to debate aspects of the geochemical nature, evolution, and stability of the horizon and its relationship with the overlying sheeted dykes and underlying gabbroic crust (France et al., 2009). These investigations have resulted in a variety of models that characterise the AML and DGT as either a dynamic (Gillis and Roberts, 1999; Coogan et al., 2003; Wilson et al., 2006; Gillis, 2008) or relatively steady-state boundary layer (Rothery, 1983; Nicolas and Boudier, 1991; MacLeod and Yaouancq, 2000; Nicolas et al., 2008).

The internal crustal structure and MORB-like composition of the sheeted dyke complex and axial volcanic suite of the Oman ophiolite has been considered by many to be directly analogous to ocean lithosphere from MORs like the East Pacific Rise (EPR) (MacLeod et al., 2013). However, differences in magma composition between MORs and ophiolites limit their direct comparison and invite caution when considering analogous models for crustal accretion processes at fast-spreading MORs (see section 2.2) (MacLeod et al., 2013). Until recently, investigations of the AML horizon at MORs have suffered from a paucity of *in situ* samples: published mineral chemical data are only available for five shallow (<300 m below sheeted dykes) samples from Pito Deep (Perk et al., 2007) (Figure 1.2). Although gabbros drilled in IODP hole 1256D (Figure 1.2) have been suggested to represent AML gabbros (Koepke et al., 2011; France et al., 2009), drilling revealed that they are isolated intrusions into the sheeted dyke complex, suggesting that they may not directly relate to the main magmatic system in the lower crust.

1.1.3 The role of the axial melt lens

The AML is generally considered to be vital in the processes of crustal accretion, accommodating the fractionation of MOR basalts and feeding seafloor eruptions (Sinton and Detrick, 1992; Goss et al., 2010; Moore et al., 2014; Marjanovic et al., 2015), but its exact role is still heavily debated (Coogan et al., 2002a; Pan and Batiza, 2002, 2003). The AML is primarily thought to be the zone where melts aggregate before being injected during dyking and eruption events (Sinton and Detrick, 1992). Further, the base of the sheeted dykes is considered to be an important horizon in the interaction between hydrothermal convective

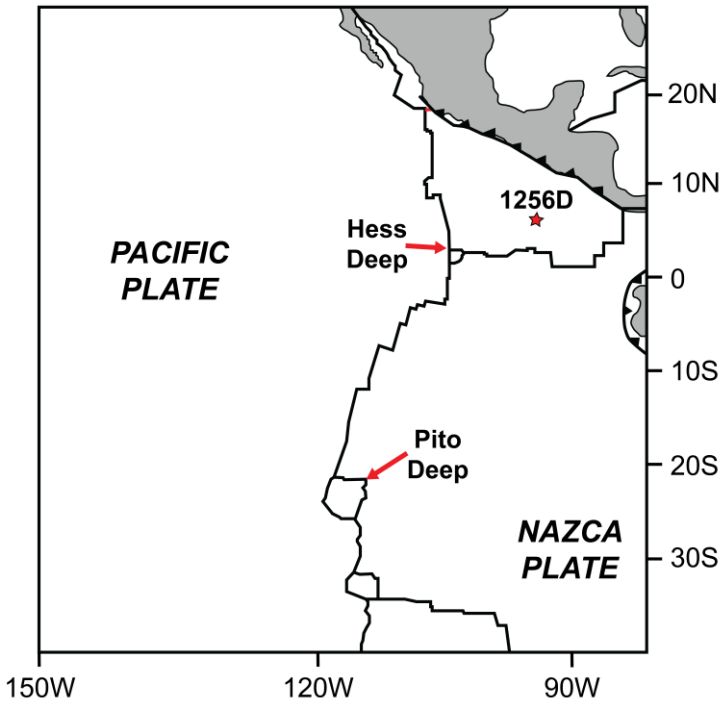

Figure 1.2: An illustration indicating the general locations of Hess Deep, Pito Deep and ODP/IODP hole 1256D in the Eastern Equatorial Pacific Ocean.

systems and the magmatic system at MORs (Gillis, 2008), serving as a major interface in the exchange of heat and chemical components between the oceanic crust and hydrothermal fluids (Liu and Lowell, 2009; Moore et al., 2014). Energy balance calculations of these axial hydrothermal systems require that the AML is replenished over decadal timescales in order to be maintained for any substantial length of time (Liu and Lowell, 2009), however, the particulars surrounding the compositions of replenished melt (i.e., MORB-like (Sinton and Detrick, 1992) vs more fractionated (Natland and Dick, 1996, 2009) vs more primitive (Singh et al., 1998)) and the exact timescales over which the replenishment occurs remain unclear (Moore et al., 2014).

There has also been much debate over the role of the AML in the accretion of the gabbroic lower crust. The majority of the models proposed for the magmatic accretion of the lower crust fall along an array between two dominant end-member models; the gabbro glacier model and the sheeted sill model (Figure 1.3). In the gabbro glacier model, primitive melts are delivered to the AML wherein crystals nucleate and accumulate along the floor of the AML and are then transported downwards and outwards by viscous, ductile flow to form the entire lower crust

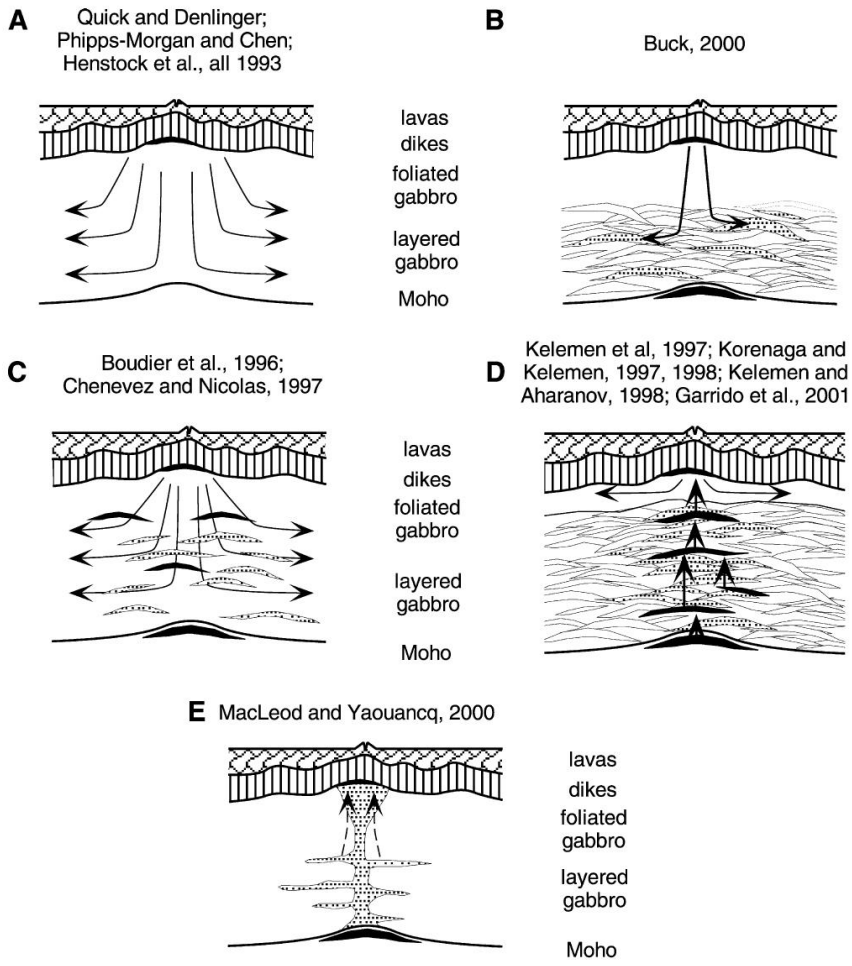

Figure 1.3: A comparison of the range of existing models for the accretion of the lower gabbroic crust at fast-spreading mid-ocean ridges (c.f., Coogan et al., 2002a). Arrows indicate directions of mass transport with dashed lines indicating directions of porous flow. (**a**) Crystals formed within the AMC subside downwards and outwards to form the lower crust in a so-called 'gabbro glacier'. (**b**) Crystals subside like in model A but this is focused to a narrow vertical conduit followed by spreading outwards in sill-like bodies. (**c**) Combines the 'gabbro glacier' in A with sill emplacement in the lower crust directly from the mantle. (**d**) The 'gabbro glacier' only forms the uppermost part of the crust and the entire lower crust (layered gabbros) is built from sills in a so-called 'sheeted sill' model. (**e**) The layered gabbros form in 'off-axis' sills and the foliated gabbros crystallise during porous melt migration up to the AMC.

(Sleep, 1975; Sinton and Detrick, 1992; Henstock et al., 1993; Morgan and Chen, 1993; Quick and Denlinger, 1993). In such a model, the majority of the latent heat of crystallisation is lost through the roof of the AML and the fabrics of the foliated and layered gabbros result from the down and outward flow of crystallised gabbroic material from the AML (Coogan et al., 2002a). In the sheeted sill model, the entire lower crustal gabbro section is accreted by crystallisation in sills within the lower crust with melts migrating through a network of sills before reaching the AML (Kelemen et al., 1997; Korenaga and Kelemen, 1997, 1998; Kelemen and Aharanov, 1998; Garrido et al., 2001; Lissenberg et al., 2004). MacLeod and

Yaouancq (2000) provided a recent variant on the sheeted sill model in which deeper, layered gabbros form in sills and the overlying foliated gabbros form by *in situ* crystallisation with the vertical fabrics developed by the upward flow of melt to the AML. Geological and petrological investigations of ophiolites have provided evidence that the lower oceanic crust is accreted from multiple levels of intruded melt sills between the AML and the Moho transition zone (Kelemen et al., 1997; Boudier et al., 1996; Kelemen and Aharanov, 1998; Korenaga and Kelemen, 1997; Bédard, 1993; Lissenberg et al. 2004). Such models are consistent with geophysical studies at fast-spreading ridges that suggest the presence of melt within the lower crust (10-20% melt; Crawford and Webb, 2002) (Singh et al., 2006; Crawford and Webb, 2002; Dunn et al., 2000; Garmany, 1989; Wilcock et al., 1992). Until recently, only seismic reflections from sills within the Moho-Transition Zone (MTZ) (Nedimovic et al., 2005) and AMLs (Detrick et al., 1987; Mutter et al., 1995; Singh et al, 1998) have been described, suggesting that melt is efficiently transported through the lower crust. Several investigations have seismically imaged a thin melt lens within the Moho-transition zone at the base of the lower crust (Garmany, 1989; Crawford et al., 1999; Canales et al., 2012). Canales et al. (2009) reported deep crustal seismic reflections collected off the southern Juan de Fuca ridge that they interpreted as originating from a molten sill within the presently accreting lower oceanic crust. More recently, Han et al. (2014) reported seismic imaging of several on- and off-axis magma bodies at multiple depths along the EPR between 9°39-40’N, suggesting that crustal accretion at fast-spreading MORs is not limited to the primary AML.

The critical difference between these models is the nature of the melt delivered to the AML and the origin of the foliated gabbros. The gabbro glacier models require that primitive melts which are added to the crust from the mantle pass through the AML, crystallise, and subside to form the lower crust; suggesting that there should be evidence for the delivery of primitive melts to the AML preserved within the horizon (Coogan et al., 2002b). Although complete closed system crystallisation as the AML moved off-axis would result in evolved compositions within the horizon, a significant volume of primitive material would be expected to be preserved there under a Gabbro Glacier regime. In contrast, the sheeted sill model requires for most melts to have undergone significant crystallisation within the lower crust prior to their delivery to the AML; suggesting

that there should be evidence for significantly more evolved melts being delivered to the AML (Coogan et al., 2002b). In this case, we would expect to find predominantly evolved compositions within the AML horizon with little to no evidence for primitive material. We would also expect to see a gradual evolution up-section through the foliated gabbros. Thus, the upper crustal gabbros of the AML should provide valuable information regarding (i) the composition of melts delivered to and (ii) the processes at work within the AML and (iii) the formation of the gabbroic lower crust as well as (iv) the formation and development of MORB.

The seemingly quasi-steady-state nature of the AML suggests that there are likely processes which define a steady state behaviour of the AML and those which act upon it during those times in which it deviates from steady state (Hooft et al., 1997; Carbotte et al., 1998); hence, it is likely that the answers to questions regarding the nature, composition, residence time and distribution of melt within the AML may be complex (Pan and Batiza, 2002; 2003). Such complexity is suggested by previous observations which show that the properties of the AML (e.g., depth, width, and crystal content) exhibit very poor correlation with axial depth and cross sectional area, which are indicators of magma supply (Kent et al., 1994; Hussenoeder et al., 1996; Hooft et al., 1997; Carbotte et al., 2000). Several alternative interpretations have been provided based on such observations suggesting that the AML is either: a recently injected melt body (Hussenoeder et al., 1996; Hooft et al., 1997; Carbotte et al., 2000) or a segregation melt expelled from the crystal mush beneath the AML horizon (Natland and Dick, 1996; Philpotts et al., 1996; Hussenoeder et al., 1996). Pan and Batiza (2003) conclude from a comparison of their detailed mineralogical and petrological studies of MORBs from the EPR with previous studies of ophiolites, MOR gabbros, continental lava flows and cooling lava lakes that the formation and compaction of crystal networks is the most important process occurring within the oceanic crust, leading to an AML characterised by highly evolved magmas expelled from the interstices of the compacting crystal mush and suggesting that AMLs play very little role in crustal accretion and the development of MORB. The model of Pan and Batiza (2003) was later contested by subsequent studies of whole rock geochemical data (Goss et al., 2010) for and phenocryst assemblages (Moore et al., 2014) of EPR lavas associated with the 1991-1992 and 2005-2006 eruptions of the EPR around 9°50’N which determined that the AML was fed by evolved melts from the crystal mush

during the period between the two eruptions with focused injections of large volumes of primitive melts into the AML preceding the 2005-2006 eruption.

1.2 Objectives

It follows from the discussion presented above that the role of the AML in both the development of MORB and the accretion of the lower crust is poorly constrained and heavily debated. This persisting uncertainty is mostly due to the paucity of *in situ* samples of this horizon. This dissertation represents the first thorough petrological characterisation of an AML from a fast-spreading MOR. Based on analyses of a unique sample set of an *in situ* fossilised AML recovered by ROV dive 78 of the JC21 site survey of the Hess Deep Rift Valley, Equatorial Eastern Pacific Ocean.

In order to facilitate a fully rigorous analysis of a large sample suite, a new method has been developed and optimised for the rapid collection and processing of full-thin section quantitative element maps. Serial thin sections of the JC21 AML suite were cut for petrographic analysis and quantitative element mapping. In conjunction with this investigation, detailed mapping and sampling of an upper crustal section in the north-eastern Ibra Valley of the southern Oman Ophiolite was carried out to provide an analogous suite of samples for comparison to the Hess Deep AML suite, and to provide constraints on the three-dimensional distribution of the rocks formed in the AML.

Combined with previous observations regarding the AML horizon at fast-spreading MORs, the application of our new element mapping technique to the Hess Deep AML suite has allowed for us to address first-order questions regarding the nature and role of the AML in oceanic crustal accretion, including:

- What are the compositions of melts delivered to the AML?
- What implications do these findings have for crustal accretion models?
- Is the AML an active or passive player in the development of MORB?
- Is the AML an active or passive player in the accretion of the lower gabbroic crust?

We aim to provide a holistic model which integrates our petrological data with existing constraints on the geophysical and structural nature of the AML.

1.3 Thesis organisation

This thesis is subdivided into 7 chapters. Following this introduction, Chapter 2 provides a review of our current understanding of the geological framework of the Hess Deep rift valley and the Oman ophiolite. A substantial component of this project was dedicated to the development and optimisation of an element mapping and processing technique for the quantitative assessment of compositional distribution (QACD) in igneous rocks, and a software package to facilitate the method. Chapter 3 provides the background and details surrounding the development and optimisation of the QACD method, as well as an overview of the QACD software. Chapter 4 presents the initial applications of the QACD method to various igneous rock samples to demonstrate the range and potential of the method in its application to geological materials. Chapter 5 presents the results of applying the QACD method to the AML samples recovered by expedition JC21 from Hess Deep. Chapter 6 presents the results of a detailed field investigation and whole rock geochemical study of an AML horizon in the vicinity of Wadi Saq in the north-eastern Ibra Valley, southern Oman Ophiolite. Finally, a brief summary of the project is presented in Chapter 7 which highlights the main conclusions of the overall study and addresses the primary questions posited in the previous section (Section 1.2). Additional sample information, analytical methods, geochemical data and quality control information are presented in the appendices at the end of the thesis. The electronic appendices include both electronic versions of the appendices included in the print copy of the thesis, as well as thin section photomicrographs for the Oman samples, element maps and histograms for the Hess Deep samples presented in Chapter 5, and the full python scripts and software manual for the QACD software developed by this study. Digital copies of this data can be requested from the author by emailing: matthew.loocke@uta.edu.

CHAPTER 2
Geological Framework

This dissertation focuses on the AML horizon from two locations: *in situ* samples representing the fossilised AML of the fast-spreading East Pacific Rise recovered from the Intrarift Ridge of the Hess Deep Rift, and those of an analogous AML horizon to the east of Wadi Saq, in the north-eastern Ibra Valley, southern Oman Ophiolite. Together, these two sample suites provide constraints on the compositional and textural variability of (i.e., Hess Deep samples) and the three-dimensional distribution of this variability (i.e., Wadi Saq samples) within the AML at fast-spreading MORs.

2.1 The Hess Deep rift valley

Hess Deep, in the Eastern Equatorial Pacific Ocean, is a ~5400 m deep rift valley that dissects ±1.3 Myr old crust formed at the EPR (Francheteau et al., 1990; Rioux et al., 2012a) (Figure 2.1) and exposes the most extensive section of *in situ* lower oceanic crust known from a fast-spreading MOR (Coogan et al., 2002b; Lissenberg et al., 2013). A large majority of our knowledge of lower crustal magmatic processes in fast-spreading oceanic crust is the result of focused submersible, dredge, and drilling studies of lower crustal rocks exposed on a topographic high within the rift valley called the Intrarift Ridge (e.g., Hekinian et al., 1993; Natland and Dick, 1996, 2009; Pedersen et al., 1996; Coogan et al., 2002b). A large proportion of the samples to date have been strongly concentrated around the upper portion of the Intrarift Ridge, where ODP leg 147 drilled ~150 m into gabbroic rocks (Gillis et al., 1993). Those rocks recovered by leg 147 are thought to represent a high stratigraphic level, several hundred metres below the sheeted dykes (site 894) and a portion of the moho transition zone (site 895) (Gillis et al., 1993). Drilling along the southern depths of the Intrarift ridge by IODP leg 345 recovered lower crustal, primitive, modally layered olivine gabbros and troctolites from two ~110-m-deep holes (U1415J and P) and one 35-m-deep hole (U1415I), providing a vital missing piece of the most complete composite section of fast-spreading EPR crust so far (Gillis et al., 2014). Overall, samples from the top of the gabbroic section, interpreted to be the level where the AML resides, are considered some of the most critically underrepresented horizons (Lissenberg et al., 2013).

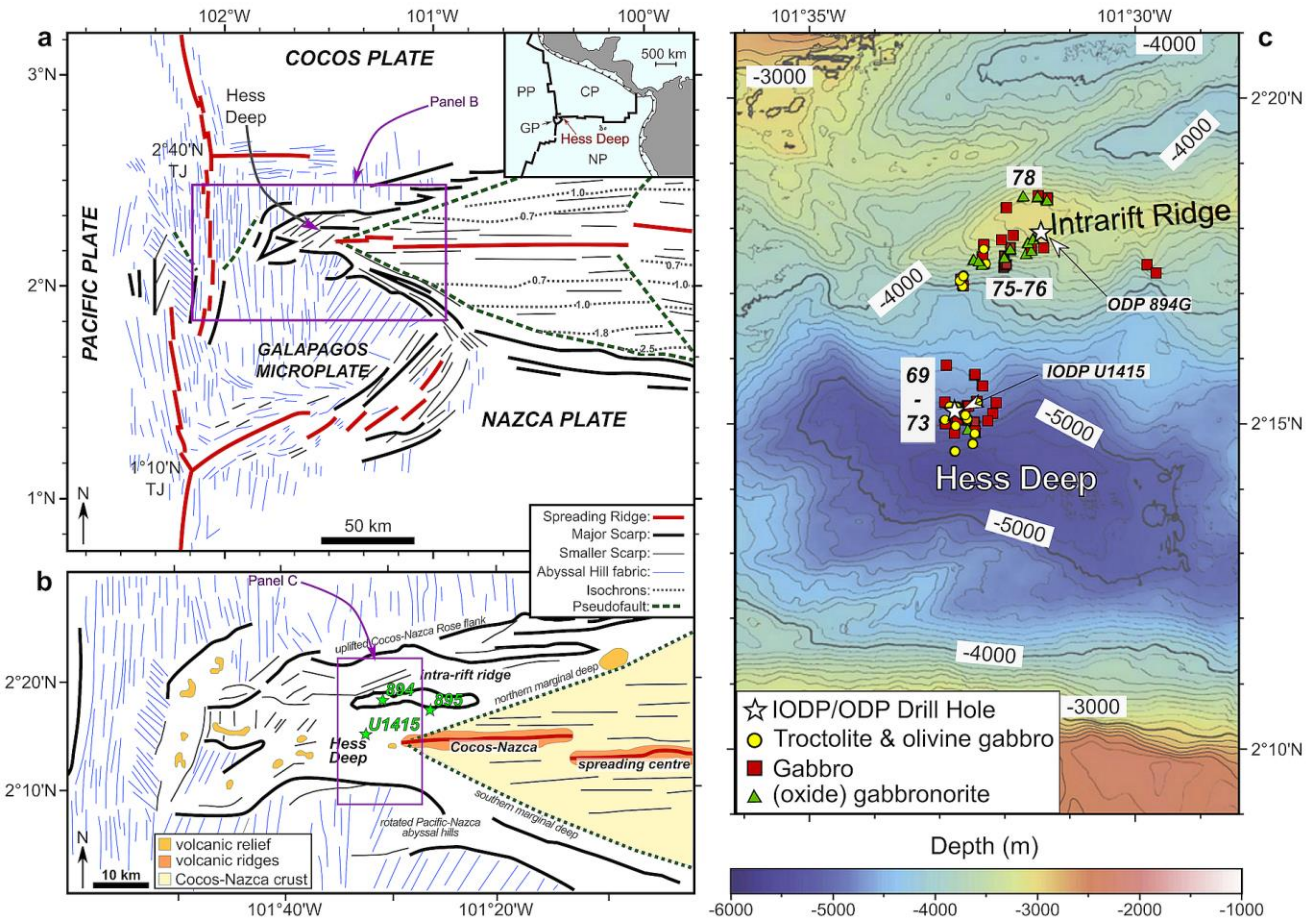

Figure 2.1: (**A**) Morphotectonic map of the region surrounding the Galapagos microplate (after Lonsdale, 1988; Rioux et al., 2012). Inset shows the location of Hess Deep (PP=Pacific plate; CP=Cocos plate; NP=Nazca plate; GP=Galapagos microplate). (**B**) Relief and structural interpretation of the Hess Deep rift basin (modified after Lonsdale, 1988) showing the location of IODP/ODP drilling within the rift basin (green stars). (**C**) Bathymetric map of Hess Deep showing the location of ODP/IODP sites 894G and U1415 (white stars) and gabbroic rocks sampled during cruise JC-21 (ROV dive numbers in bold italics) (c.f., Lissenberg et al., 2013).

The RSS James Cook cruise JC21 (January to February 2008) was carried out as a site survey for IODP Expedition 345. A suite of 93 gabbroic rocks ranging from primitive to evolved, consistent with previously recovered samples (Gillis et al., 1993; Hekinian et al., 1993), were collected by ROV *Isis*. The sample suite collected by the JC21 cruise represents the most extensive sampling of a more or less complete lower crustal section at a fast-spreading MOR, spanning from gabbros intercalated with mantle rocks at the base of the crust, through evolved oxide gabbronorites in the middle crust to highly-evolved, varitextured oxide gabbros and gabbronorites at the base of the sheeted dykes (Lissenberg et al., 2013). Predominantly (melt-impregnated) dunites alternating with olivine gabbros and troctolites, interpreted to represent the lowest portions of the gabbroic crust, were recovered from the lower south slope of the Intrarift ridge, while oxide

gabbronorites, like those found in ODP 894G (Gillis et al., 1993) were recovered from the top of the south slope of the Intrarift ridge.

ROV dive 78 sampled the structurally highest level, on the north slope of the Intrarift Ridge (Figure 2.1c). Twenty-three samples (8 dolerites, 14 gabbronorites, and 1 gabbro) were recovered from the traverse across the transition from the uppermost gabbros into the sheeted dykes, including variably but generally highly-evolved, oxide-bearing varitextured gabbros (ranging from rare olivine gabbro to oxide gabbronorite). These varitextured gabbronorites occur in close proximity to dolerite dykes, resemble the uppermost gabbros interpreted to represent fossilised AMLs at ophiolite complexes formed at fast-spreading rates (MacLeod and Yaouancq, 2000; Coogan et al., 2002a; Lissenberg et al., 2004), and occur at the level in the crust where geophysical surveys have detected the AML (Detrick et al., 1987; Sinton and Detrick, 1992; Carbotte et al., 2013; Marjanović et al., 2015); hence, the JC21 dive 78 samples have been interpreted to have formed in the AML of the EPR (Lissenberg et al., 2013).

Lissenberg et al. (2013) analysed a small subset of the dive 78 rocks along with a large portion of the other recovered gabbroic rocks from the JC21 cruise. Only 11 out of the 23 samples recovered by dive 78 were petrographically characterized by Lissenberg et al. (2013) with minimal geochemical analysis compared to samples recovered from deeper along the Intrarift Ridge. The extensive suite of lower crustal gabbroic rocks recovered by the JC21 cruise allowed for Lissenberg et al. (2013) to carry out a rigorous assessment of melt evolution over the scale of a MOR magma chamber using mineral major- and trace element analyses. For the past decades, igneous geochemists and petrologists working at MORs have used the composition of MORBs to derive information about the mantle beneath MORs (e.g., mantle composition and the processes of melting and melt migration) (see Rubin et al., 2009 for a review) by assuming that fractional crystallisation is solely responsible for the modification of melts within MOR magma chambers and correcting for this process (e.g., Grove et al., 1992). Lissenberg et al. (2013) demonstrate that the major- and trace element evolution within the lower crust at Hess Deep (as recorded by clinopyroxene) is controlled by reactive porous flow which leads to the fractionation of and enrichment in incompatible trace elements in the melt with compositions far outside of the range of MORBs. The signature of reactive porous flow spans the entirety of the lower crust at Hess Deep,

increasing in strength up section until it peaks within the dive 78 varitextured gabbros. Based on this observation, Lissenberg et al (2013) suggest that MORB migrating through the lower crust or stationary within the AML would likely interact with the reacted melt prior to eruption to produce trace element enriched MORB which departs from the predicted fractional crystallisation pathways for highly incompatible elements. Further, Lissenberg et al. (2013) conclude that the lower oceanic crust plays a more substantial and complex role in the modification and evolution of MORB compositions through the dominant process of reactive porous flow than previously thought.

2.2 The Oman Ophiolite

The Oman, or Semail, Ophiolite in the Sultanate of Oman is the largest (nearly 20,000 km^2) continuous sub-aerial exposure of oceanic crust resembling a Penrose ophiolite model on Earth (Anonymous, 1972; Nicolas et al., 2008) (Figure 2.2). The Oman crustal section is composed of, from bottom to top, mantle peridotites, intercalated gabbros and dunites of the Moho transition zone, layered gabbros, foliated gabbros which are commonly capped by a structurally and petrologically complex group of gabbros, sheeted dykes and extrusive lavas. The large area of crust and mantle rocks exposed in the Oman Ophiolite provides an opportunity to directly study lower crustal materials that are typically obscured by volcanic cover at modern ridges. Extensive studies over the years have capitalized on the great exposures in Oman to understand everything from the structure of the crust and mantle in the ophiolite (Ceuleneer et al., 1988; Lippard, 1986; Nicolas et al., 2000) to the processes of crustal accretion (Browning and Smewing, 1981; Kelemen et al., 1997; Nicolas et al., 1988; Pallister and Hopson, 1981) and the tectonic origins of the ophiolite (Boudier et al.,1988; Gray and Gregory, 2000; Hacker et al., 1996; Pearce et al., 1981; Searle and Malpas, 1980; Searle and Cox, 2002) in order to better constrain the current models for the accretion of the lower oceanic crust and the structure of the oceanic lithosphere (Rioux et al., 2012b).

Accretion of the Cretaceous-aged fragment of oceanic lithosphere exposed in Oman occurred about 96 myr ago along the margin of the Tethys Ocean (Tilton et al., 1981; Tippit et al., 1981). Based on structural and petrological observations, the main or initial phase of ophiolite development is thought to have occurred at a mid-ocean ridge (MOR). However, the specific tectonic setting in which this first

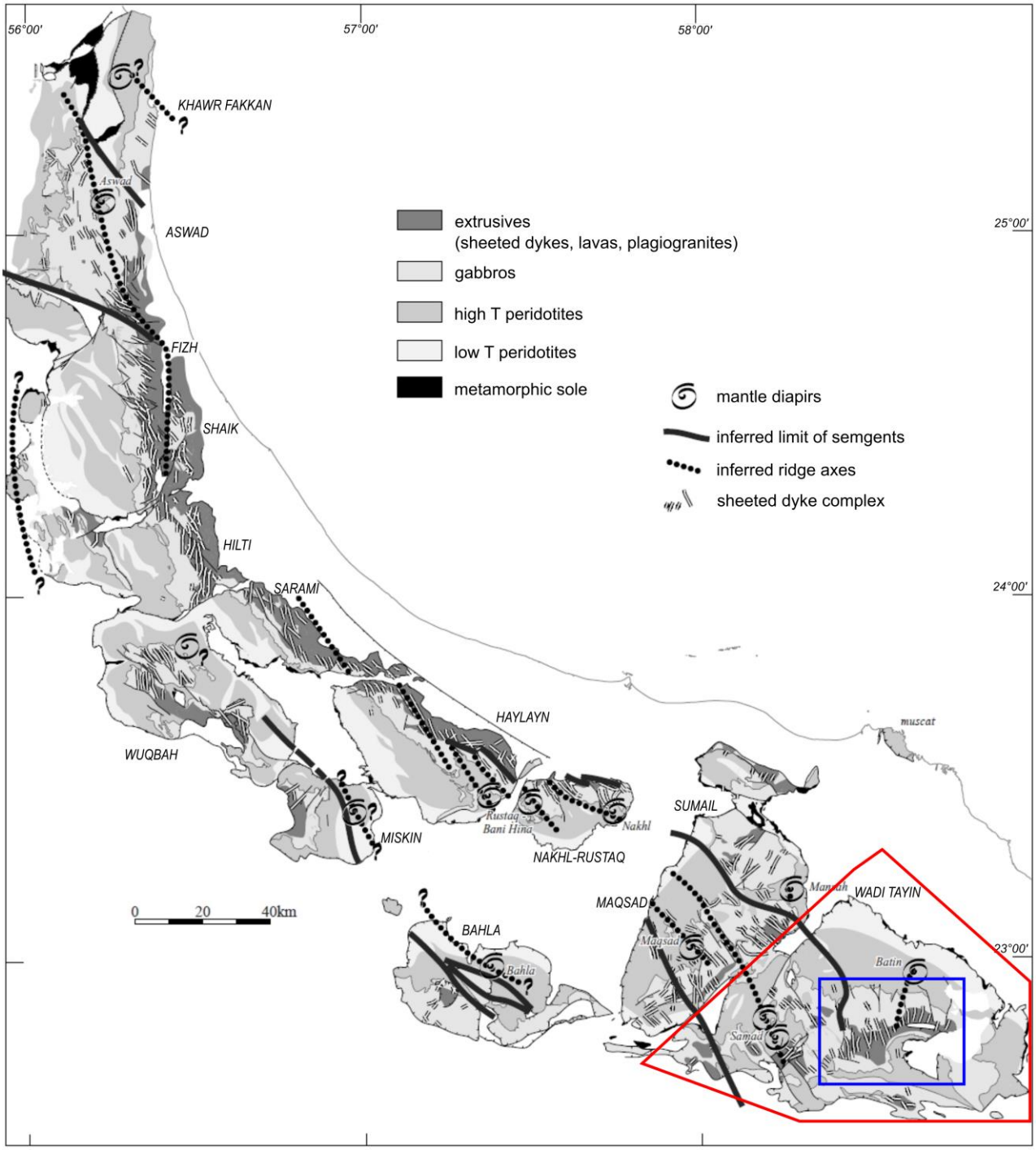

Figure 2.2: A simplified overview geological and structural map of the Oman-UAE ophiolite (c.f., Nicolas et al., 2000a) including the names and locations of diapiric areas and global segmentation derived from discussions in Nicolas et al (2000b). The Wadi Tayin massif is outlined by a red box and the approximate location of the Ibra Valley is indicated by the blue box.

phase of ophiolite construction occurred has been a point of great contention (Alabaster et al., 1982; Boudier and Nicolas, 2007; MacLeod et al., 2013; Pearce et al., 1981; Warren and Miller, 2007), with some studies arguing for its construction dominantly at a MOR (Ernewein et al., 1988; Nicolas, 1989; Boudier et al., 1997; Benoit et al., 1999; Boudier et al., 2000; Godard et al., 2006; Boudier and Nicolas,

2007; Koepke et al., 2009; Abily et al., 2011), while others argue for a supra-subduction zone (SSZ) related environment (Pearce et al., 1981, 1984; Alabaster et al., 1982). Workers favouring a MOR origin have suggested that the early detachment event (intra-oceanic thrusting) occurred soon after accretion at the ridge (95-98 Ma) (Boudier et al., 1988; Montigny et al., 1988). The process of obduction of the ophiolite onto the Arabian margin was complete by 70 Ma (Coleman, 1981; Glennie, 2005; Searle and Cox, 1999).

Detailed studies of the northern section of the ophiolite indicate that it formed during multiple, non-contemporaneous magmatic events accompanied by laterally variable and complex hydrothermal alteration (Lippard, 1986; Stakes and Taylor, 1992). The volcanic sections of the Northern region include several geochemically distinct lavas with arc-like signatures (i.e. 'V2' = Lasail, Alley; Ernewein et al., 1988) overlying lavas with normal MORB-like chemistry (i.e. 'V1' = Geotimes) (Pearce et al., 1981; Alabaster et al., 1982; Ernewein et al., 1988; Godard et al., 2006). The Lasail and Alley units, which are thought to be derived by hydrous melting of a depleted MORB mantle source (Alabaster et al., 1982; Godard et al., 2006), are characterised by depletions in incompatible elements with some of the Alley volcanics reaching boninitic compositions (Ishikawa et al., 2002). Several lines of evidence, including large-ion lithophile element enrichment relative to MORB, the presence of boninites, and elevated εSr values for Lasail-related quartz-diorite and tonalite intruding the base of the Geotimes volcanics, suggest a subduction influence for the later magmatic stages of the ophiolite (Pearce et al., 1981, 1984; Alabaster et al., 1982; Grimes et al., 2013; MacLeod et al., 2013; Tsuchiya et al., 2013).

In contrast, the southern portion of the ophiolite is generally considered less complex than the north, with a more analogous architecture and geochemistry for crust formed at fast-spreading mid-ocean ridges (Nicolas et al., 2008; Nicolas and Boudier, 2011). Geochemically, lavas in the southern part of the ophiolite, which are comprised of only the Geotimes lavas, have been interpreted as being directly comparable to N-MORB (Ernewein et al., 1988; Coogan et al., 2004; Godard et al., 2006). However, the Geotimes lavas extend to higher SiO_2 and lower MgO than MORB and are characterised by a notable enrichment in Th and a slight depletion in Nb (Pallister and Knight, 1981; Pearce et al., 1981; Alabaster et al., 1982; Braun, 2004; Bibby et al., 2011; MacLeod et al., 2012, 2013). The southern massifs, in

particular the Wadi Tayin massif, have therefore been used extensively as analogues for fast-spreading oceanic crust (e.g., Pallister and Hopson, 1981; Nicolas et al., 2000; Nicolas et al., 2008; Koepke et al., 2009; France et al., 2009; Nicolas et al., 2009; Boudier and Nicolas, 2011; Nicolas and Boudier, 2011). A recent geochemical compilation by MacLeod et al. (2013) indicates elevated water contents for Geotimes lavas along the length of the ophiolite including the southern massifs. This is incompatible with a MOR origin. The fractionation trends found within the Oman volcanic suite require water contents which are significantly higher than that found at modern MORs. MacLeod et al. (2013) find that the subduction signature developed rapidly with time in the Oman system and conclude that the ophiolite is likely an obducted forearc crustal section formed from a nascent forearc spreading system during subduction initiation. A similar model has been deduced for the Izu-Bonin-Mariana (IBM) system (e.g., Stern and Bloomer, 1992; Reagan et al., 2010) where MORB-like forearc basalts, remarkably similar to the Geotimes lavas, immediately follow subduction initiation (~52 Ma) and are succeeded by high-Mg andesites, boninites and arc tholeiites within a few million years (MacLeod et al., 2013). Although the Oman crustal sequence clearly formed by physical processes similar to those at modern fast-spreading MORs, its analogy is thus limited by our understanding of the effect of water on the physical and chemical behaviour of magma differentiation. Therefore, any model which seeks to address the processes of lithospheric accretion at fast-spreading MORs by comparison with ophiolites must carefully consider the role of water in such systems (MacLeod et al., 2013).

2.2.1 The Wadi Tayin Massif and the Ibra Valley

The Wadi Tayin Massif, the southern-most block of the Oman ophiolite, has a relatively simple volcanic and structural history, preserving a ~40 km long east-west transect perpendicular to the strike of the sheeted dykes and the inferred ridge axis (Figure 2.3) (Rioux et al., 2012b). Structural observations indicate that this region is the northern limb of an east-west syncline with an axis somewhere in the exposed pillow basalts in the centre of the Ibra valley (Hopson et al., 1981; Pallister and Hopson, 1981). The northern side of the valley sees multiple north-south drainages cutting the steeply south dipping limb and exposing a full lithospheric cross section. Faulting is limited to dominantly north- to northwest-striking normal faults that

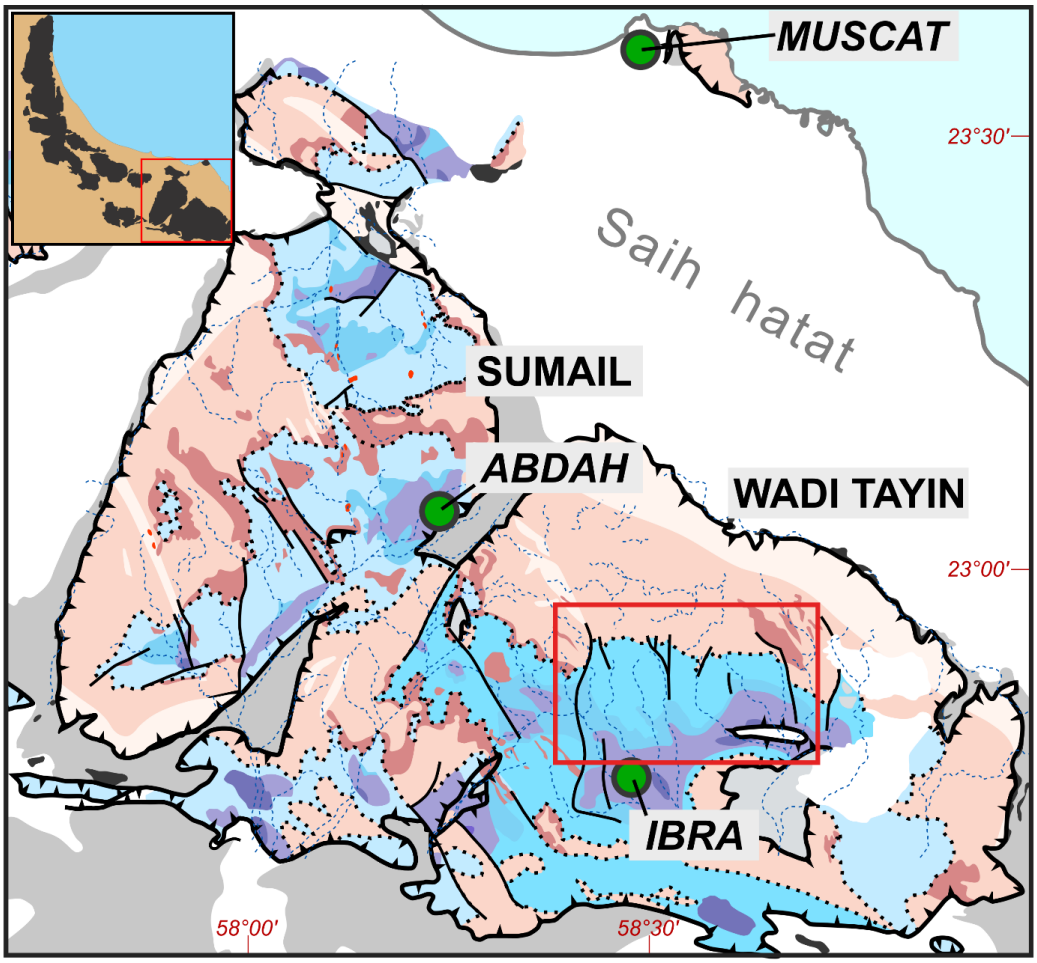

Figure 2.3: Close-up Geologic cartoon of the Sumail and Wadi Tayin massifs in the southern portion of the Oman ophiolite (modified after MacLeod et al., 2013). The red box indicates the area of the Wadi Tayin presented in Figure 6.2. The inset provides an overview of the Oman ophiolite with a red box indicating the approximate location of the Figure 6.2. Mantle lithologies are represented pink shades. Gabbroic lithologies are represented by blue shades. Volcanics are represented by purple shades.

generate little more than kilometre-scale offsets in the upper/lower gabbro contact and the crust-mantle transition (Rioux et al., 2012b).

The Ibra Valley, which sits at the core of the Ibra Valley syncline (Figure 2.4), lies to the south of the Jabal (or Jebel) Dimh, a ~1km high mountain range exposing the crust/mantle transition along its E-W trending crest line (Pallister, 1981; Pallister and Hopson, 1981). The crustal and mantle rocks of the Ibra Valley, as described by previous studies, are typical of lithosphere observed in other portions of the Oman ophiolite (Boudier and Coleman, 1981; Gregory and Taylor, 1981; Hopson et al., 1981; McCulloch et al., 1981; Pallister, 1981; Pallister and Hopson, 1981; Pallister and Knight, 1981; Kelemen et al.,1997; Nicolas et al., 2000; Garrido et al., 2001; Bosch, 2004; Van Tongeren et al., 2008; France et al., 2009; Nicolas et al., 2009; Hanghoj et al., 2010; Boudier and Nicolas, 2011) (Figure 2.3).

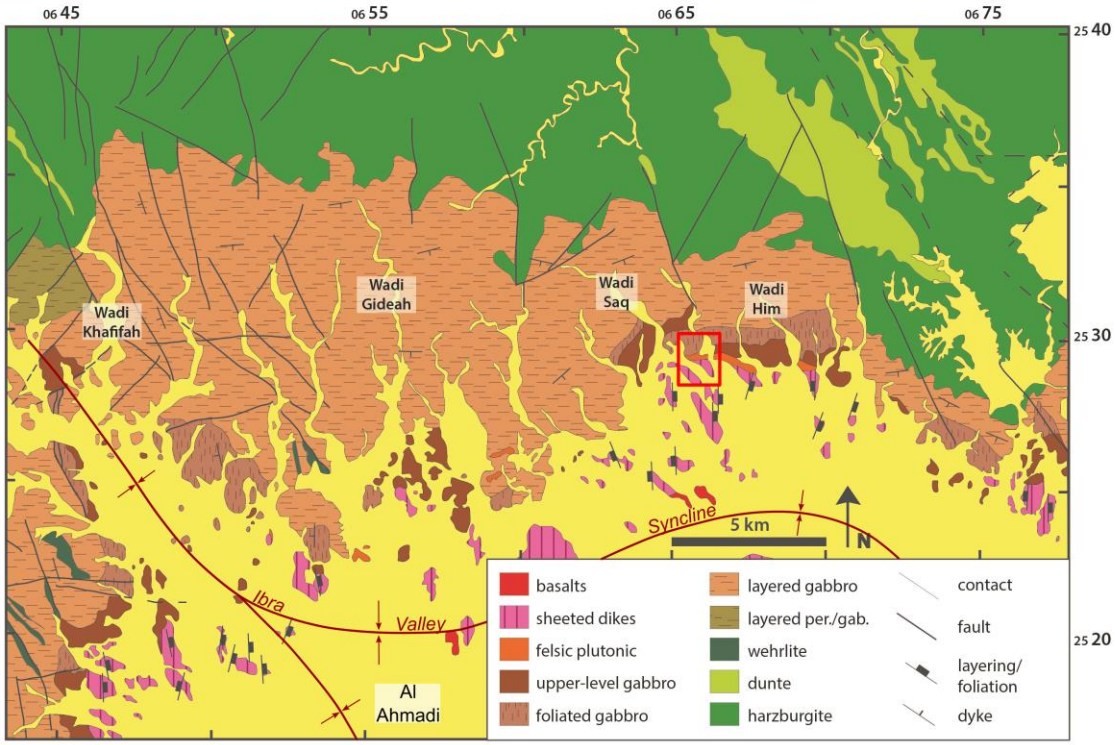

Figure 2.4: Geologic map of the northern Ibra Valley (UTM coordinate system) modified after Rioux et al. (2012). Representative layering, foliation and sheeted dyke orientations ae shown (tick in the down-dip direction). The red box on the map indicates the study area represented in Figure 6.1.

The general stratigraphy of the crust, from top to bottom, consists of basaltic pillows and lavas in the syncline core, sheeted dykes, high-level gabbros, foliated gabbros, and compositionally layered gabbros. This stratigraphy is exposed in both the northern and southern limbs of the syncline, but is structurally complicated and thinned along the southern flank by domal uplift from the Ibra Dome (Pallister, 1981; Pallister and Hopson, 1981). Centimetre to metre-sized gabbroic pegmatite dykes and sills intrude the layered gabbros locally, and the entire plutonic crust is intruded by localized, late olivine gabbro and wehrlite series in some localities (Hopson et al., 1981; McCulloch et al., 1981; Pallister and Hopson, 1981; Pallister and Knight, 1981; Pallister, 1981; Rioux et al., 2012).

The sheeted dyke complex in the Ibra Valley is estimated from cross-sections to be approximately 1.2-1.6 km thick (Pallister, 1981) with the volcanic rocks belonging compositionally to the Geotimes unit. Unlike the northern portions of the ophiolite, there is little or no evidence for later, geochemically distinct volcanic rocks in the Ibra Valley (i.e., the Lasail, Alley, clinopyroxene-phyric, ['V2'] and/or Salahi ['V3'] units). A simple, short-lived magmatic history is suggested by the paucity of later volcanics and the presence of only minor intrusions of plutonic rocks

that could be related to these later suites (e.g. ‘V2’ plagiogranites; Haase et al., 2016) into mantle peridotite (Pearce et al., 1981; Smewing, 1981; Alabaster et al., 1982; Amri et al., 1996; Benoit et al., 1996; Kelemen et al., 1997; Python and Ceuleneer, 2003; Tamura and Arai, 2006; Hanghoj et al., 2010; Rioux et al., 2012). The Ibra Valley has traditionally been used as a fast-spreading MOR analogue, interpreted to have formed between ~96.4-95.5 Ma at a fast-spreading ridge with half-rates of 50-100 mm/yr (Rioux et al., 2012).

2.2.2 The Wadi Abyad Crustal Section

The Wadi Abyad section, described as ‘typical’ and relatively uncomplicated, is located in the Nakhl-Rustaq block of the central Oman ophiolite (Figure 2.2) (MacLeod and Yaouancq, 2000). The Abyad section begins in the south with harzburgites which pass up into dunites within a few metres of the sharp, planar contact between peridotites and layered gabbro referred to as the ‘Moho’. The gabbroic crust measures 2.6 km thick at Abyad and consists of layered gabbros (lower 2/3 of the gabbros), foliated gabbros (650 m thick) and varitextured gabbros (upper 200 m) which are overlain by NE-trending sheeted dykes. Orthopyroxene and primary oxide minerals are nearly completely absent from the Abyad section. The layering within the layered gabbros at Abyad is defined by cm- to m-scale variations in the modal proportion of clinopyroxene, plagioclase and olivine (MacLeod and Yaouancq, 2000; Coogan et al., 2002a). The layered gabbros transition upwards over 200 m into the foliated gabbros which are formed of massive non-layered olivine gabbros exhibiting prominent magmatic foliations approximately normal to that of the layered gabbros within the main facies (MacLeod and Yaouancq, 2000; Coogan et al., 2002a). Within ~150 m of the base of the sheeted dykes, the foliated gabbros transition into gabbros exhibiting strong textural, structural, and geochemical heterogeneity (i.e., varitextured gabbros) and an abundance of oxides occur in association with subordinate pegmatitic ferrogabbros. The first characterisation of a fossilised AML horizon, MacLeod and Yaouancq (2000) interpreted these rocks as preserving the lateral edges of an AML characterised by the differentiated end product of a basaltic liquid expelled from the underlying crystal mush.

The ferrogabbroic pegmatites found within the varitextured gabbros at Wadi Abyad were interpreted to represent late-stage basaltic liquids which were able to

locally fractionate *in situ* and back-intrude the mostly crystalline gabbro at the edges of the AML (MacLeod and Yaouancq, 2000). The absence of plagiogranites in the Abyad plutonic section along with the ferrogabbroic fractionation trend was taken by MacLeod and Yaouancq (2000) to suggest that the AML differentiated under relatively water-poor, low fO_2 (i.e., Oxygen fugacity) conditions with little-to-no assimilation of hydrated material from the base of the sheeted dykes. Although the ferrogabbroic pegmatites may form up to 40% of an outcrop in the Wadi Abyad varitextured gabbro horizon, MacLeod and Yaouancq (2000) emphasize that they are always subordinate to the more magnesian, finer-grained isotropic gabbros which are more representative of the facies as a whole. In fact, the combined bulk composition of the Abyad varitextured gabbro horizon is basaltic (Mg# = 65, TiO_2 = 1.1 wt.%) and comparable to the Abyad sheeted dykes that are preserved in discontinuous outcrops within the mouth of the wadi. Further, high-An plagioclase and high-Mg clinopyroxene in the Abyad varitextured gabbros suggest that primitive melts may be delivered to the AML with little modification. Although they address that variations do exist across the ophiolite, MacLeod and Yaouancq (2000) propose that their observations for the Abyad section are generally representative of the ophiolite overall.

CHAPTER 3
QACD: A technique for the quantitative assessment of compositional distribution in geologic materials

3.1 Introduction

In order to fully understand the magmatic and petrogenetic history of an igneous rock, it is critical to obtain a thorough characterisation of the chemical and textural relationships of its mineral constituents. The compositions of minerals in a magma are strongly dependent on the magmatic conditions under which crystallisation occurs (e.g., melt composition, pressure, temperature, and volatile content); hence, mineral compositions have the potential to provide valuable information on the conditions and processes in the magma at the time of crystallisation (Pearce, 1994; see Ginibre et al., 2007 and references therein for a review on the topic). Some elements exhibit a proclivity to be affected by distinct magmatic processes and thus have the potential to record the effects of such processes during magma genesis (Saunders et al., 2014). The common occurrence of compositional zoning with respect to major elements can further elucidate temporal changes in the conditions of crystallisation in a magma.

Traditional microanalytical methods of geological materials (e.g. spot or line profiles by electron probe micro-analyser (EPMA)) obtain chemical compositions of constituent minerals from target locations previously identified by the user during petrographic analysis, under the assumption that the chosen spots are representative of the sample. However, this assumption is difficult to verify, and petrographic selection of spots is prone to a number of pitfalls: (i) chemical zoning is often cryptic (e.g., olivine, pyroxene, amphibole); (ii) there may be bias towards anomalous features which stand out from the representative sample; (iii) it is statistically unlikely that a relatively limited number of spot analyses represent the true distribution of mineral compositions, given that most natural rocks consist of a heterogeneously distributed, diverse assemblage of minerals (Prêt et al., 2010a; Clarke et al., 2001).

Element mapping combines microanalytical techniques that allow for the analysis of major- and minor elements at high spatial resolutions (e.g., electron microbeam analysis) with 2D mapping of samples in order to provide unprecedented detail regarding the growth histories and compositional distributions of minerals. Element maps acquired by EPMA or scanning electron microscope

(SEM) provide a visually powerful presentation of elemental distributions with micrometre to sub-micrometre spatial resolution, allowing for operators to readily recognize chemical features (e.g., compositional zoning within a grain or sample) that would otherwise not be readily visible in thin section or in associated SEM "compositional contrast" images (e.g., backscattered-electrons or BSE) (Newbury, 2006, Prêt et al., 2010a). Element mapping is therefore increasingly used in the geological sciences for qualitative observations of textures, mineral zoning, and element distribution among rock components (Clarke et al., 2001; Friel and Lyman, 2006; de Andrade et al., 2006; Prêt et al., 2010a, b; Ebel et al., 2014).

This contribution presents a method for the acquisition and processing of large area X-ray element maps obtained by energy-dispersive X-ray spectrometer (EDS) to produce a quantitative assessment of compositional distribution (QACD) of mineral populations within geologic materials. Such maps can be used to not only accurately identify all phases and calculate mineral modes for a sample (e.g., a petrographic thin section), but, critically, enable a complete quantitative assessment of their compositions throughout a sample. The QACD method has been incorporated into a python-based easy-to-use graphical user interface (GUI) called Quack. By optimising the conditions at which the EDS X-ray element maps are acquired, we are able to obtain fully quantitative element maps for most major elements in relatively short amounts of time. Although fully quantitative maps of absolute element distributions typically require some form of standardisation prior to analysis, the X-ray element maps acquired by our method can be processed without the analysis of standards to create quantitative maps of major elements and molar ratios (e.g. An, Ca/Ca + Na + K, in plagioclase; Mg#, Mg/Mg + Fe, in pyroxene or olivine) accurate to within a 2σ error of their accepted values. Instead, corrections for individual elements and common element ratios are derived from a growing database of standard analyses and models calculated from first principles. The resulting element ratio maps and chemical population histograms provide a means of determining the full compositional distribution of a sample, from which constraints on the relative compositions and volumes of melts which contributed to the crystallisation history of the rock can be derived. Where previous techniques would require several days to collect a full thin section element map, the QACD method requires significantly shorter times of 6-8 hours. Thus, the QACD method facilitates the rapid collection and processing of large numbers of full-thin section

element maps that is required for the thorough characterisation of geologic units like the AML horizon.

3.2 Developments in element mapping

3.2.1 EDS detectors

In the decades since the first X-ray “dot map” compositional image was first obtained (Cosslet and Duncumb, 1956; Duncumb and Cosslett, 1957), the technique of elemental mapping by electron-beam-excited X-ray emission, or simply element mapping, has become one of the most widely used operational modes of EPMA for the characterization of complex materials and microstructures (Goldstein et al., 2003; Newbury, 2006). Element mapping can be carried out using both energy-dispersive and wavelength-dispersive X-ray spectrometers (EDS and WDS), each with their own set of limitations (see Friel and Lyman, 2006 for a review). For example, the diffracting crystal in a WDS spectrometer is set to a specific wavelength to record the characteristic X-ray intensity of a specific element, thus, the number of elements that can be simultaneously analysed is dependent on the number of WDS spectrometers for a given instrument (Clarke et al., 2001). In contrast, EDS detectors record the entire X-ray energy spectrum for each analysis and therefore do not require for elements to be selected prior to measurement.

In the past, X-ray mapping by EDS suffered from a significant time penalty in part due to the relatively low count rates (<25 cps) achievable with EDS detectors of the time. The efficiency of elemental mapping techniques saw a significant increase with the advent of the silicon (lithium-compensated) energy dispersive X-ray spectrometer (Si(Li)-EDS), which was capable of achieving a maximum count rate of ~2000 cps under ‘best resolution’ operating conditions (i.e., long peaking time constant) (Fitzgerald et al., 1968). The Si(Li)-EDS had an improved energy resolution relative to the flow proportional counter and enabled the simultaneous measurement of elements across the entire range of electron-excited X-ray energies through the use of electronic signal processing. For the statistically sound measurement and quantification of major elements in “point” analyses, spectral measurements would typically require a minimum live time of >10 s (Newbury, 2006).

Significant advances in computing power, speed, and data storage resulted in the development of techniques for the collection of X-ray spectrum images (XSI)

(Gorlen et al., 1984) which allowed for the entire EDS spectrum to be recorded for each beam location, or pixel. During X-ray mapping, the beam is rastered over an array of points at a resolution set by the operator (e.g., 128 X 128). This inevitably has a limiting effect on the dwell time that can be afforded at each pixel. Newbury (2006) approximated the total live time for a 128 x 128 map with a pixel dwell time of 100 ms on a Si(Li) EDS at 1638 s or 27 min. Owing to the combined need for large acquisition times in order to obtain statistically robust data, large data processing times, and standardizations required to obtain fully quantitative concentrations, the technique has often been used for the qualitative visualisation of element distributions and in the calculation and classification of phase distributions for samples at relatively low resolutions, but not for the statistically rigorous quantification of compositional distributions within element maps.

The introduction of the silicon drift detector (SDD) (Struder et al., 1998; Barkan et al., 2004; Newbury, 2005) has radically changed the measurement capabilities of EDS detectors, enabling for precisions and accuracies equivalent to that of an analysis carried out by WDS (Newbury, 2005; Ritchie et al., 2012; Newbury and Ritchie, 2016). For a given detector active area, an SDD can achieve slightly better energy resolution than the conventional Si(Li)-EDS (Newbury, 2005). The biggest advantage of the modern SDD is that, for a given resolution, it can provide significantly higher X-ray throughput count rates relative to a typical Si(Li) detector (see Newbury, 2005 for a detailed comparison of the two types of detectors). The general lack of a physical limitation on the size of SDDs coupled with recent advancements in computer processing capabilities has resulted in increasingly larger detectors being developed which are capable of handling increasingly larger X-ray count rates (e.g. up to 1,000,000 cps). Considering that 100 ms was sufficient for the mapping of major elements with a Si(Li)-EDS at ~2000 cps throughput and assuming a total of 3,276,800 counts for the map (i.e., 2000 cps x 1638s), then the same 128 x 128 map carried out by an SDD-EDS with a modest throughput of ~20,0000 cps would result in a map with a total of 32,768,000 counts. This would suggest that the dwell time could be dropped to as low as 10 ms for the map collected by the SDD-EDS, maintaining an equivalent total number of counts to the Si(Li)-EDS and decreasing the live time to 163.84 s or <3 min. The higher X-ray throughput count rates of modern SDDs (up to >400,000 cps for some EDS systems) has thus enabled the use of lower beam currents and shorter dwell

times in order to achieve statistically sound measurements, further minimising both the dosage of samples and map live time and facilitating the collection of element maps over larger areas (e.g., full thin sections) at higher resolutions (e.g., <15 μm).

3.2.2 Software for processing element maps

Modern SEMs are increasingly being outfitted with SDD-EDS systems for chemical analysis and supplied with software for the collection and analysis of XSIs. The preservation of the full spectrum at each pixel in an XSI allows for the user to perform off-line analysis of the map, whether it be the extraction and quantification of user-defined regions of interest (ROIs), the calculation of phase maps by way of pixel grouping and sorting, or even the mapping of previously unconsidered elements (Liebske, 2015). Owing to a general lack of flexible post-processing functions in vendor-supplied element mapping software, many recent studies (e.g., Cossio et al., 2002; de Andrade et al., 2006; Prêt et al., 2010a, b; Liebske, 2015) have focused on the development of independent post-processing methods for the classification and separation of phases from XSIs or extracted element maps. However, a large proportion of these independently-produced post-processing methods fall short on their applicability to broader research.

Clarke et al (2001) provided a *MATLAB*™-based scripting method for applying the Bence-Albee matrix correction algorithm (Bence and Albee, 1968) to X-ray element maps collected by WDS-EPMA in order to produce oxide weight percent and cation proportion maps limited to 8 major oxides (i.e., SiO_2, Al_2O_3, FeO, MnO, MgO, CaO, Na_2O, and K_2O). The results can be plotted and exported as maps and binary scatter plots with a focus on calculating pressure-temperature conditions of metamorphic assemblages. It is important to note that in order to run the Bence-Albee algorithm, several parameters must be specified beforehand, including pixel counting time, α-coefficient parameters specific to instrument geometry (e.g., Love and Scott, 1978), intensity on standards collected during standardisation β factors derived for the standard compositions, and background parameters if background corrections are required. The Bence-Albee method was also employed in *XRMapAnal* (Tinkham and Ghent, 2005), a standalone Windows executable program focused on applying the algorithm to element maps collected by WDS-EPMA, which included functions for phase identification, modal analysis, and cation calculation. Aside from the ability to plot binary scatter plots, the majority of the

functions present within *XRMapAnal* are usually incorporated into vendor-provided element mapping software. Lanari et al (2014) produced *XMapTools*, a *MATLAB*™-based GUI for processing element maps collected by WDS-EPMA. The XMapTools method, like many other methods, is geared towards estimating P-T conditions of metamorphic rocks by incorporating the method of de Andrade et al (2006) to separate phases using a K-means clustering algorithm (see section 3.5.2 for a description) and quantify mineral structural formulae by using quantified point analyses collected from within the mapped region as standards for correction rather than incorporating the more complicated Bence-Albee algorithm. The method incorporates two separate GUI modules, *Chem2D* and *Triplot3D*, for plotting binary and ternary scatter plots of the derived mineral compositions.

Other methods have focused less on quantifying map compositions and more on accurate phase clustering and identification. Prêt et al (2010a,b) provided a method for thin-section scale phase-mapping which uses maps that have already been quantified by either commercial software or existing methods, thus allowing for both WDS- and EDS-derived maps to be used. The main focus of their method is on accurate phase thresholding for deriving phase modes and semi-quantitative porosity maps. In contrast, Cossio et al (2002) created Petromod, a Windows 95 software package coded in Microsoft Visual Basic 5®. Petromod uses BSE and WDS/EDS maps which have previously undergone signal processing (i.e., correction for probe current drift, normalisation of maps, and smoothing with a 3-by-3 median filter) to create a Microsoft Access® database for calculations. The approximate location of quantitative spot analyses is indicated by the user and used to create semi-quantitative maps intended only for deriving phase maps, determining modal phase abundances, and for discriminating between solid solution endmembers within phases.

The recent efforts of Liebske (2015) produced *iSpectra*, an ‘open-source’ software optimised for analysing XSIs collected by EDS-equipped SEMs which is primarily focused on providing accurate phase identification and modal phase abundance calculations, lacking the ability to further process element maps in order to produce element ratio maps or detailed compositional statistics. *iSpectra* is aimed at producing more accurate phase identification and assignment by requiring the input of the raw 3D data cube (or XSI) for the mapped area in the Lispix format (Bright, 1987; http://www.nist.gov/lispix/). Lispix data sets are a common output

format for commercial EDS systems, consisting of a binary, uncompressed file containing a consecutive sequence of each spectrum with an accompanying file containing information regarding the data type and dimensions of the XSI (Bright, 1987; Liebske, 2015). The uncompressed nature of this format means that it is subject to rampantly large file sizes; assuming that data are stored in a 16-bit format (i.e., whole numbers between ±32,000 that are ~2 bytes each), a 1024x768 map collected on an EDS detector with 2048 energy resolution would produce a data cube containing 1,610,612,736 data points (i.e., 1024x768x2048) and constituting exactly 3 GB of memory. This makes *iSpectra,* although rigorous in its approach to processing by requiring the full raw data cube, difficult to use and apply to large area maps with comparatively large memory requirements. The focus of *iSpectra* on the accurate identification of phases and determination of modal phase abundances in element maps, although useful, effectively limits users from carrying out any further processing of element maps to produce element ratio maps or statistical assessments of compositional variations.

One of the most widely used commercial products for automated rapid quantitative mineral and phase analysis is QemSCAN (Pirrie et al., 2004). QemSCAN was originally designed to provide rapid quantitative modal mineral analyses for the mining industry by using a Carl Zeiss™ SEM outfitted with four light-element EDS detectors to collect X-ray spectra over a user-defined pixel spacing at rapid (e.g., 10 ms per pixel) dwell times. The software automatically compares collected spectra against a database of known spectra to assign a mineral or phase name to each pixel. The software systematically maps the near-surface qualitative composition for each particle, assigns it to a mineral/phase and creates digital phase maps from the data. Using the resulting phase maps, the software has the ability to provide data relating to the shape and size of and the specific density calculated for each particle. Unfortunately, instead of providing the functionality to fully quantify the chemical composition at each individual pixel, QemSCAN opts for a semi-quantitative calculation of the average or bulk chemical composition for a group of pixels identified as a phase. This is acceptable if the user is simply attempting to characterise the modal mineralogy of a sample or carrying out some form of feature analysis, but inappropriate for users who would like to examine the full quantitative chemical distribution within a phase and across a sample. Further, the QemSCAN software package, like many of those described

previously in this section, lacks the functionality for users to modify existing components or create their own application-specific data processing modules for use within the software. Although it was once a unique product in the field of electron microscopy, the basic analytical tools and processing functions of the QemSCAN system have become commonplace amongst the vendor-provided software for EDS detectors (e.g., AztecFeature™ in the Aztec™ software from Oxford Instruments or the COMPASS™ algorithm in the Pathfinder™ software from Thermo Scientific™).

In some cases, investigators have taken advantage of the rapid collection time and high (e.g., 1 µm) resolution of BSE imagery to create compositionally calibrated BSE images for determining the distribution of plagioclase compositions. For example, Cashman and Blundy (2013) used the grayscale variations in BSE images to collect quantitative analyses which bracketed the compositional spectrum of plagioclase hosting melt-inclusions. The BSE images were imported into the ImageJ (http://rsb.info.nih.gov/ij/) image analysis software and the quantitative analyses of plagioclase were used to calibrate the linear grayscale variations in the images according to An content. These images were then used to examine the distribution of plagioclase compositions within the crystals at high-resolution. The high resolution of the BSE imagery means that pixels of surface defects and with electron interaction volumes approaching grain boundaries will have higher error and skew the data, producing an 'Edge' effect. These pixels are generally accounted for by running the maps through median filters which average out the data while preserving edges and grain boundaries (see section 3.5.1 for more information). Though this method produces high-resolution compositional variations for a given phase, it is limited to phases (e.g., plagioclase, olivine, pyroxene) with elements, or more often molar ratios (e.g., An or Mg#), which have a significant effect on the mean atomic number (i.e., the density) of the material. Some of the aforementioned software (e.g., XMapTools and PetroMod) allow for the inclusion of BSE maps for their quantification methods, however, but still require that element maps be imported in order for the processing to be carried out.

Many of the available processing methods and vendor-supplied software lack the ability to efficiently quantify EDS element maps according to mineral-specific standardisations. Map quantification within vendor-provided software (e.g., the Oxford Instruments Aztec software) is designed to quantify the EDS spectrum

stored for each pixel like it would for a typical quantitative spot analysis under normal operating conditions. In quantifying an EDS spectrum, integrated peak intensities for the elements chosen by the user are produced after filtering out the background noise of the energy spectrum surrounding the peaks. These background-corrected peak intensities are compared with those collected on standard reference materials for which the elemental concentration is known (i.e., Castaing's "first approximation to quantitative analysis"; Castaing, 1951). In 'standardless' correction methods, the appropriate intensities of standard reference materials are either derived from a suite of experimental standards measured by the software manufacturer (i.e., fitted standards) or calculated from first principles, considering every aspect of X-ray generation, propagation, and detection (Goldstein et al., 2003). In most analyses, the measured intensities from both the standard and the specimen require a correction for differences in density, energy loss, X-ray cross section, electron backscatter, and absorption within the solid in order to produce truly comparable intensities independent of the material. These effects are commonly referred to as inter-element or matrix effects and are corrected using a matrix correction method. For simplicity, the common matrix effects which must be accounted for are conveniently divided into atomic number (*Z*), X-ray absorption (*A*), and X-ray fluorescence (*F*); hence, every matrix correction (e.g., ZAF, XPP, PAP) at their core is built to correct for the combined matrix effects of *ZAF* (Goldstein et al., 2003). The process of quantifying analytical spectrum by applying background and matrix corrections, although relatively quick for individual spectra, can be time consuming when it is applied to every spectrum in an element map which may contain >1,000,000 pixels. We found that it took approximately four hours for the Aztec software on the Cardiff University EDS-SEM system to produce a quantified compositional map for an element map of ~500,000 pixels collected in approximately six hours. Such long processing times are unacceptable if a user desires to apply standardisations to the map which are specific to mineral phases.

In order to accommodate the large number of full-thin section quantitative element maps needed for our investigation of the AML horizon, we required both a method for the rapid collection of element maps, and software which could facilitate the efficient post-processing of element maps collected by our dual EDS-equipped SEM. In particular, we needed software which would facilitate our post-processing

methods to produce fully quantitative assessments of compositional distributions for element maps without the need of multiple software platforms and allow for the flexibility to easily adapt the software's functionality, which none of the existing platforms provided. The resulting software, a python-based GUI referred to as 'Quack' (see section 3.5 for an overview), facilitates every step of the QACD process from processing for 'bad' pixels and noise in maps through manual/automatic phase identification, calculation of modal phase abundances, quantification of elements and molar ratios without the need for standard analyses, and the production and export of both element/ratio maps and histograms. Most importantly, the Quack software allows for users to quickly quantify elemental concentrations and molar ratios for individual phases instead of having to quantify the entire map with a single broad standardisation or several times over for mineral-specific standardisations. The python code for Quack allows for users to adapt the software to their needs and more readily create new functionality when it is needed, thus aiming to curb the perpetual development of more disparate software methods.

3.3 Developing and optimising the QACD method

The experimental method that was used to determine the optimal conditions for map collection is provided here, in consideration that the optimal conditions for efficiently collecting element maps of sufficient quality for the QACD method will vary between SEMs and detectors. Carbon-coated samples were analysed using the Zeiss Sigma HD SEM outfitted with dual 150 mm^2 active area Oxford Instruments Xmax SDD EDSs in the School of Earth and Ocean Sciences at Cardiff University. The SDDs were controlled and the output from the digital signal processor (DSP) integrated in the Oxford system was processed by the Oxford Instruments Aztec Software package. Optimisation of the mapping procedure was carried out using plagioclase, olivine, and diopside standards from Astimex (see Table 3.1 for compositions). These X-ray maps of the standards were acquired with a constant beam accelerating potential of 20 keV while systematically varying other parameters individually in order to address the effect of each parameter on both the quality of the map output and the total live time needed to collect it (see Table 3.2 for summary of experiments). These parameters include pixel dwell time (e.g., 500, 1000, 5000, 10000, 20000, 50000, and 100000µs), and beam current (e.g., 1,

2.5, and 5 nA). Although the beam current was varied as a parameter, it was kept within limits of that needed to generate adequate X-ray flux to reach a reasonable deadtime (<45%) and a minimum output count rate of >200,000cps (i.e., minimum count rate to achieve robust counting statistics) on a pure copper target as a chosen reference standard. The beam current was measured with a stage mounted Faraday cup. However, due to known difficulties in calibrating stage mounted faraday cups with known current sources (Newbury, 2006), the repeatability was estimated on the independent EDS measurement of the integrated X-ray counts from the Cu standard, and was found to be better than 0.2% relative.

The x-y-counts file for each element were imported into Quack and processed according to the QACD Initialize step (see below), which filters out pixel noise (i.e., statistically bad pixels) by calculating the total intensity at each pixel (i.e., sum of each element intensity) and thresholding the map based on statistical analysis of the totals frequency distribution and applies a 3-by-3 median filter to the maps as is typical of post-processing methods (e.g., Cossio et al., 2002) to ensure that anomalous pixels are removed and that crystal edges become smoothed (Muir et al., 2012). Once imported, all maps are added together to produce the total number of counts at each pixel. Each map is then divided by the total counts map as a means of normalising the data. This process of normalisation allows for spectra collected at various dwell times and beam currents to be directly compared. At this stage in the correction procedure there is still some variation between the spectra normalised peaks of various phases. This variation can be further reduced by calculating the mean atomic number (Z), mean atomic weight (A), and the h parameter ($h = 1.2 \times (A / Z^2)$) of the absorption correction defined by Philibert (1963) for each pixel and multiplying the spectrum normalised elements by h. For the purposes of ratio map calculation, the derivation and application of the h parameter to the spectrum-normalised elements has no negative effect on the resulting element ratios.

Finally, the element ratio maps are quantified using correction equations parameterised based on multiple linear least squares regressions of a growing database of both analyses of reference materials, internal standards and unknowns and theoretical EDS spectra generated using the DTSA-II software package from NIST (Ritchie et al., 2008; Ritchie, 2009). The reference database consists of 222

Table 3.1: Compositions of Astimex standards used for optimisation of the QACD method.

	SiO_2	Al_2O_3	FeO	MgO	CaO	Na_2O	K_2O	An^a
Plagioclase	53.12	29.35	0.34	0.1	11.93	4.36	0.24	59.3
	SiO_2	Al_2O_3	FeO	MgO	CaO	Na_2O		$Mg\#^b$
Diopside	55.34	0.62	0.83	17.76	24.8	0.41		97.4
	SiO_2	FeO	MgO	NiO				Fo^c
Olivine	41.6	7.25	50.97	0.37				92.6

[a]An = 100 Ca/(Ca + Na)

[b]Mg# = 100 Mg/(Mg + Fe^{2+})

[c]Fo = 100 Mg/(Mg + Fe)

spectra (as of August 2016; Table 3.3) which have been previously quantified by traditional matrix correction methods (e.g., the ZAF or XPP methods) and verified against standard reference materials. As with the element maps, integrated element intensities for these spectra were normalised to the total counts in the spectrum to remove the effect of varying dwell times and beam currents. The normalised element intensities were then multiplied by the *h* parameter calculated for each spectrum. A multiple linear least squares method was then used to regress best-fit equations relating the *h*-corrected, normalised peak intensities to their corresponding elemental concentrations by weight percent. Equations were also derived for molar ratios (e.g., An in plagioclase) by regressing best-fit equations relating known values to those calculated using the *h*-corrected, normalised peak intensities (see Figure 3.1 for examples of the regressed lines for the molar ratios). Within the database, general equations are derived which include the entire range of spectra, as well as equations specific to minerals/mineral groups (e.g., feldspars, olivine, pyroxene, garnet, oxides). The process of applying the parameterised correction equations to the map results in a map of quantified pixels. The database and correction equations provide an internal 'fitted standards'-type of standardless correction method to the Quack software. However, unlike most 'fitted standards' correction methods, which are system-specific, this quantification method is designed to not be system-specific (i.e., limited to the Cardiff system) in that it removes the effect of instrumental variations by first normalising the elements to the total counts at each pixel. Over time, we plan to incorporate more spectra collected by a variety of instruments over a range of analytical conditions for various

Table 3.2: Table summarising experimental runs on a copper standard to investigate the effect of varying dwell time, process time, beam current, and map resolution on the length (Realtime) and countrates of element maps.[a]

Map Label	Resolution			Accelerating	Beam	Process	Dwell Time	Livetime			Realtime			Deadtime	Map Sum	Spectrum Count
	Width (px)	Height (px)	N (px)	Voltage (kV)	Current (nA)	Time	(µs)	ms	s	minutes	ms	s	minutes	(%)	Counts	Rate (cps)
EDS 1-1-1000-512 res	512	384	196608	20	1.0	1	1,000	393216.0034	393.216	6.55	415921.5088	415.922	6.93	5.5%	10632625	102256
EDS 1-3-1000-512 res	512	384	196608	20	1.0	3	1,000	393216.0034	393.216	6.55	459084.3048	459.084	7.65	14.3%	10641946	92723
EDS 1-6-1000-512 res	512	384	196608	20	1.0	6	1,000	393216.0034	393.216	6.55	1001021.851	1001.022	16.68	60.7%	10659800	42596
EDS 1-1-500-512 res	512	384	196608	20	1.0	1	500	196608.0017	196.608	3.28	207955.4825	207.955	3.47	5.5%	5318052	102292
EDS 1-3-500-512 res	512	384	196608	20	1.0	3	500	196608.0017	196.608	3.28	229655.5557	229.656	3.83	14.4%	5325116	92750
EDS 1-6-500-512 res	512	384	196608	20	1.0	6	500	196608.0017	196.608	3.28	502839.8895	502.840	8.38	60.9%	5346881	42533
EDS 5-1-500-512 res	512	384	196608	20	5.0	1	500	196608.0017	196.608	3.28	252003.9673	252.004	4.20	22.0%	26209121	416011
EDS 5-3-500-512 res	512	384	196608	20	5.0	3	500	196608.0017	196.608	3.28	409455.0171	409.455	6.82	52.0%	26174053	255696
EDS 5-1-1000-512 res	512	384	196608	20	5.0	1	1,000	393216.0034	393.216	6.55	502839.8895	502.840	8.38	21.8%	51962767	413352
EDS 5-3-1000-512 res	512	384	196608	20	5.0	3	1,000	393216.0034	393.216	6.55	812747.7112	812.748	13.55	51.6%	51832759	255099
EDS 10-1-1000-512 res	512	384	196608	20	10.0	1	1,000	393216.0034	393.216	6.55	623587.7686	623.588	10.39	36.9%	100114931	642187
EDS 10-3-1000-512 res	512	384	196608	20	10.0	3	1,000	393216.0034	393.216	6.55	1581182.251	1581.182	26.35	75.1%	99774910	252406
EDS 10-1-500-512 res	512	384	196608	20	10.0	1	500	196608.0017	196.608	3.28	310285.2631	310.285	5.17	36.6%	49494152	638047
EDS 10-3-500-512 res	512	384	196608	20	10.0	3	500	196608.0017	196.608	3.28	782804.2297	782.804	13.05	74.9%	49521740	253048
EDS 10-3-1000-256 res	256	192	49152	20	10.0	3	1,000	98304.00085	98.304	1.64	385605.0568	385.605	6.43	74.5%	24493174	254075
EDS 10-3-1000-128 res	128	96	12288	20	10.0	3	1,000	24576.00021	24.576	0.41	96390.0795	96.390	1.61	74.5%	6122739	254082
EDS 10-3-1000-64 res	64	48	3072	20	10.0	3	1,000	6144.000053	6.144	0.10	24025.61855	24.026	0.40	74.4%	1526910	254214
EDS 10-3-5000-64 res	64	48	3072	20	10.0	3	5,000	30719.99931	30.720	0.51	120184.2232	120.184	2.00	74.4%	7641139	254314
EDS 10-3-5000-32 res	32	24	768	20	10.0	3	5,000	7679.999828	7.680	0.13	30097.36443	30.097	0.50	74.5%	1911825	254085
EDS 10-1-5000-32 res	32	24	768	20	10.0	1	5,000	7679.999828	7.680	0.13	12052.94323	12.053	0.20	36.3%	1909953	633854
EDS 10-1-5000-64 res	64	48	3072	20	10.0	1	5,000	30719.99931	30.720	0.51	48162.22191	48.162	0.80	36.2%	7617434	632648
EDS 10-3-5000-256 res	256	192	49152	20	15.0	3	5,000	491519.989	491.520	8.19	1909031.982	1909.032	31.82	74.3%	121579503	254746
EDS 15-1-5000-256 res	256	192	49152	20	15.0	1	5,000	491519.989	491.520	8.19	1000024.78	1000.025	16.67	50.8%	197250084	788981
EDS 15-1-10000-256 res	256	192	49152	20	15.0	1	10,000	983039.978	983.040	16.38	1997007.69	1997.008	33.28	50.8%	393707134	788594
EDS 15-1-10000-128 res	128	96	12288	20	15.0	1	10,000	245759.9945	245.760	4.10	499094.6655	499.095	8.32	50.8%	98371919	788403

[a]All runs were carried out with a beam accelerating voltage of 20kV, magnification of 85x, and working distance of 8.5 mm.

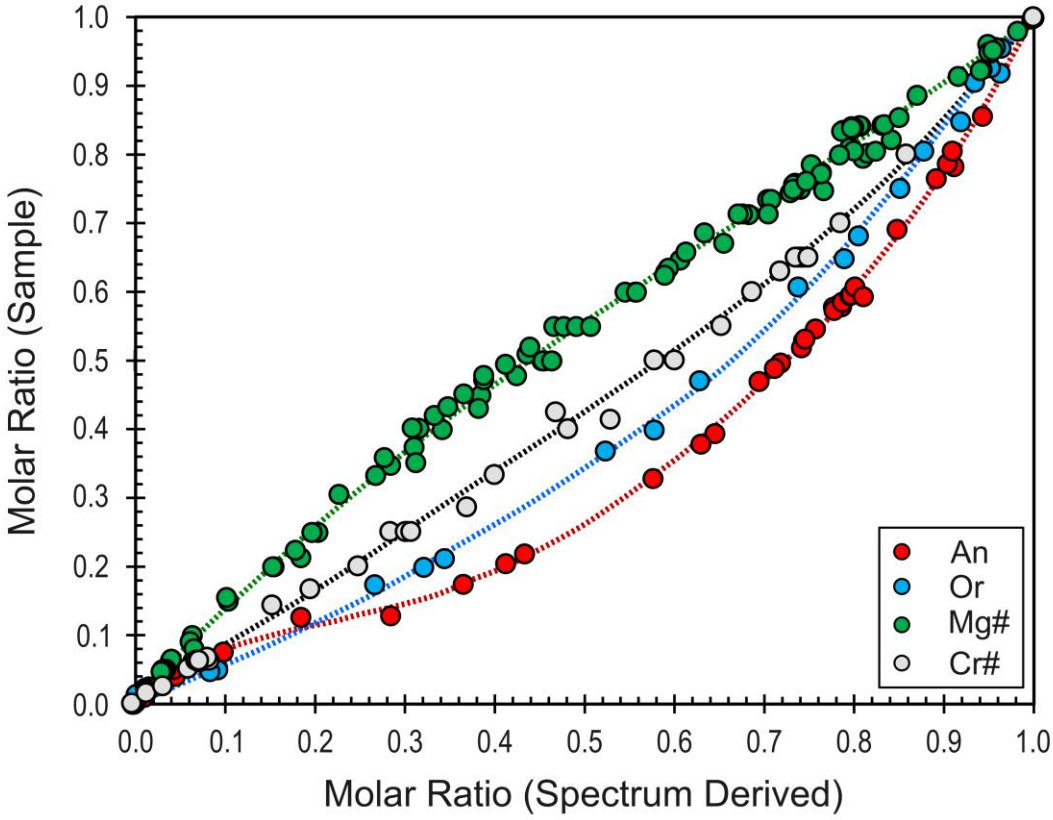

Figure 3.1: Molar ratio as derived from the spectrum (i.e. the molar ratio of background-corrected element intensities normalised to the total number of counts in the spectrum) plotted against the known molar ratio of the analysed sample. An (Ca / (Ca + Na + K)) and Or (K / (Ca + Na + K)) consist of analyses of feldspar standards and unknowns. Mg# (Mg / (Mg + Fe)) and Cr# (Cr / (Cr + Al)) consist of a mixture of olivine, pyroxene, garnet, amphibole, spinel and oxide standards and unknowns.

materials into the database, leading to the development of increasingly accurate corrections for a wider variety of materials (see discussion below for more details).

To optimise the QACD method, the maps of plagioclase, diopside and olivine standards ran under different conditions were processed and corrected to produce molar ratio maps of An in plagioclase and Mg# in diopside and olivine. Histograms of An in plagioclase and Mg# in pyroxene and olivine were produced from the molar ratio maps and used to compare the quality (i.e. peak mean, median and 2σ error) of the resulting compositional peak for each histogram. The lowest energy X-ray measured most often by this method is Na, thus the initial experiments for optimising the QACD method were carried out on the Plagioclase standard. The effects of varying both the beam current and pixel dwell time on the peak quality

Table 3.3: A summary of the mineral analyses included in the QACD correction database for the elements available as of August 2016.

Element	N_{total} *(Element)*	*Pure*	*Feldspar*	*Pyroxene*	*Feldspathoid*	*Olivine*	*Garnet*	*Ilmenite*	*Spinel*	*Rhodonite*	*Quartz*	*Rutile*
Na	94	1	45	39	9							
Mg	141	1	13	42	5	21	36	4	18	1		
Al	165	1	53	42	9		37	5	18			
Si	184	1	53	42	9	21	56			1	1	
K	54	1	44	1	8							
Ca	155	1	51	42	7	13	41					
Ti	66	1		34	5	2	10	5	8			1
Cr	64	1		9			30	2	20			2
Mn	106	1		30		19	44	5	6	1		
Fe	155	1	21	39	8	21	43		18	1		3
Ni	11	1				1			9			
Mg#	116			40		21	36		18	1		
Cr#	47			7			30		10			
An	43		43									
Or	39		39									
N_{total} *(Mineral)*		11	53	42	9	21	56	5	20	1	1	3

of calculated An for maps run at 20 keV and 64x48 resolution are summarised in Table 3.4 with the histograms of those maps presented in Figure 3.2. We found that the mean An of the Plagioclase standard (i.e., 0.593) is even reproduced to within 0.17% of the standard by the map collected with a 10,000 µs dwell time and 1.0 nA beam, indicating that the method is accurate even under relatively challenging analytical conditions. The precision of the An peak produced by a given map is monitored by the standard deviation (σ) of the mean in the histogram, and is improved by increasing pixel dwell time and/or the beam current, resulting in a decrease in overall peak width and increase in the peak height. For a dwell time of 50,000 µs we find that the standard deviation of the An peaks produced decreases between 1.0 nA (σ = 0.019 or 1.9 mol.%) and 3.0 nA (σ = 0.0115 or 1.15 mol.%) resulting in a narrower, taller peak in Figure 3.2 at 3.0 nA that is comparable to the 200,000 µs peak produced at 1.0 nA. Thus, the standard deviation of the produced peak can be minimised by increasing the beam current.

For an accelerating potential of 20 keV and beam current of 2.5 nA, modus operandi for the Cardiff University SEM, a pixel dwell time of 10,000 µs, or 10 ms, and a minimum output count rate of 200,000 cps are required to produce element ratio peaks that fall within a 2σ error of the reported standard value (see Table 3.5, Figure 3.3). We find that for longer pixel dwell times of 100 ms there is a significant increase in both precision (0.0371 at 10,000 µs vs 0.0109 at 100,000 µs) and accuracy (1.10% at 10,000 µs vs 0.37% at 100,000 µs) along with the ability to image lower concentration elements. In the end, we chose to use a standard pixel dwell time of 20 ms which, when compared to the 10 ms dwell time, more accurately reproduced the standard compositions (% error = 0.20%) within the range of accuracies achieved by longer dwell times; thus, optimising the balance between map quality and total run time. Figure 3.4 provides histograms of Mg# derived from maps of the olivine and diopside standards collected with a beam current of 2.5 nA, dwell time of 20 ms, a 64x48 resolution resulting in peaks of 0.928 and 0.968 with standard deviations of 0.0038 and 0.0085 and errors of 0.22% and 0.59% relative to the standard values of 0.926 and 0.974 for the olivine and diopside standards, respectively.

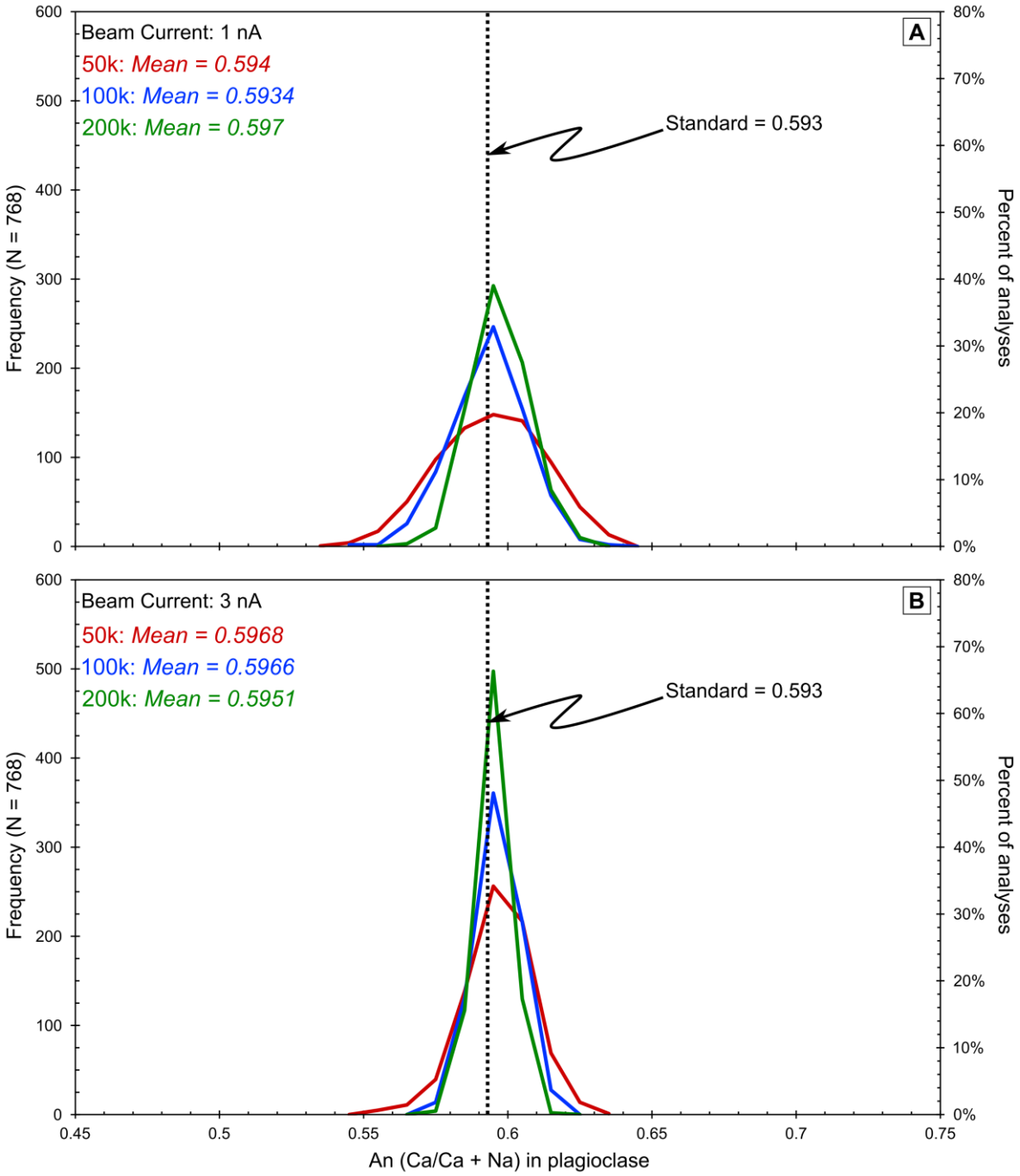

Figure 3.2: Histograms of An (Ca/Ca + Na) in plagioclase for maps carried out at varying dwell times (50k = 50 ms; 100k = 100 ms, 200k = 200 ms) and (**A**) 1.0 nA and (**B**) 3.0 nA beam currents.

Table 3.4: Compariosn of peak quality for An derived from element maps of the Plagioclase standard at variable beam current and dwell times.

Map[a]	Current (nA)	Process Time	Resolution			Dwell Time (µs)	Anorthite				
			Width (px)	Height (px)	N (px)		Mean	Median	σ	RSD(%)[b]	% error[c]
1nA_50k_32res	1.0	1	32	24	768	50,000	0.594	0.5942	0.019	3.2%	0.17%
1nA_100k_32res	1.0	1	32	24	768	100,000	0.5934	0.5944	0.0131	2.2%	0.07%
1nA_200k_32res	1.0	1	32	24	768	200,000	0.597	0.597	0.0097	1.6%	0.67%
3nA_50k_32res	3.0	1	32	24	768	50,000	0.5968	0.5971	0.0115	1.9%	0.64%
3nA_100k_32res	3.0	1	32	24	768	100,000	0.5966	0.5965	0.0077	1.3%	0.61%
3nA_200k_32res	3.0	1	32	24	768	200,000	0.5951	0.5951	0.0056	0.9%	0.35%

[a] All runs were carried out with a beam accelerating voltage of 20kV, magnification of 500x, a process time of 1 and working distance of 8.5 mm.

[b] RSD(%) = (100 x σ) / Mean

[c] % error = 100 x (Measured - Certified) / Certified

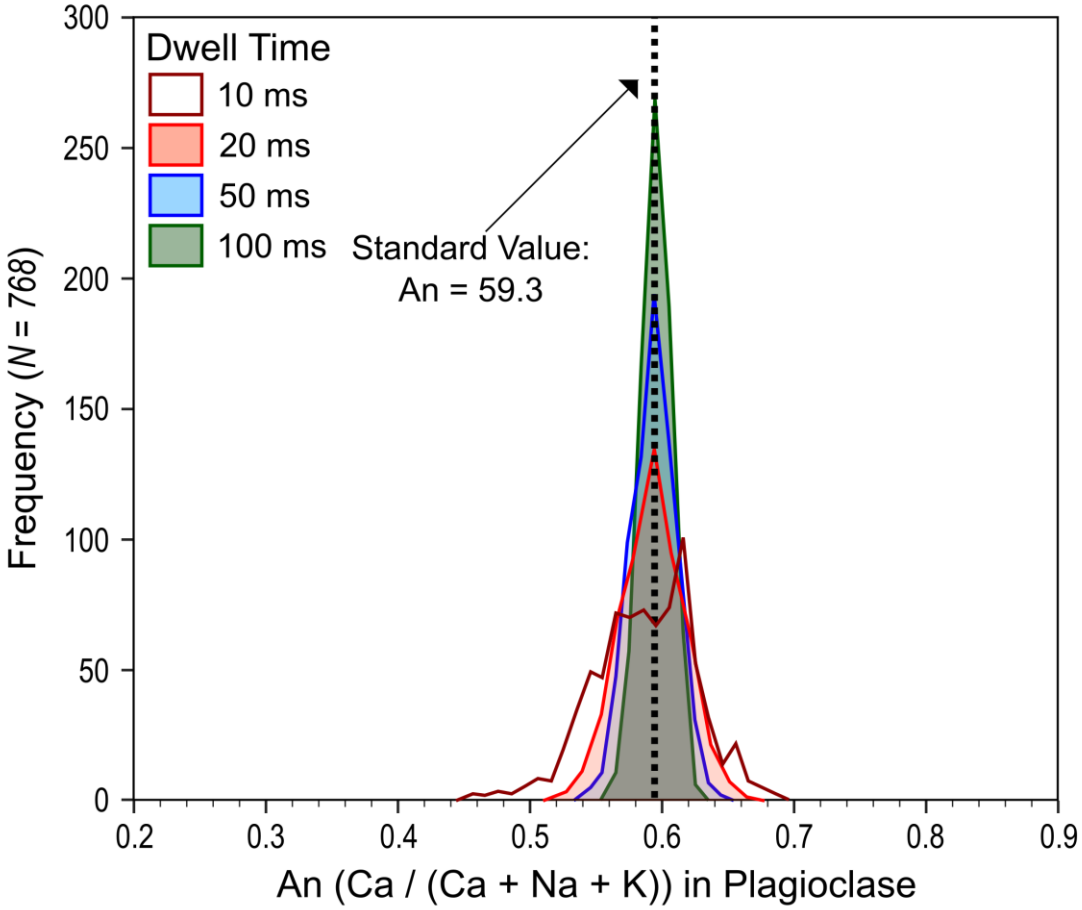

Figure 3.3: A histogram of An in plagioclase (SPI/ASTIMEX Plagioclase/Labradorite standard) derived from element maps with varying pixel dwell time. The element maps were run at 20 keV with a set resolution (32x24 pixels) and set current (2.5 nA). See table 3.5 for statistics on each of the histograms presented here.

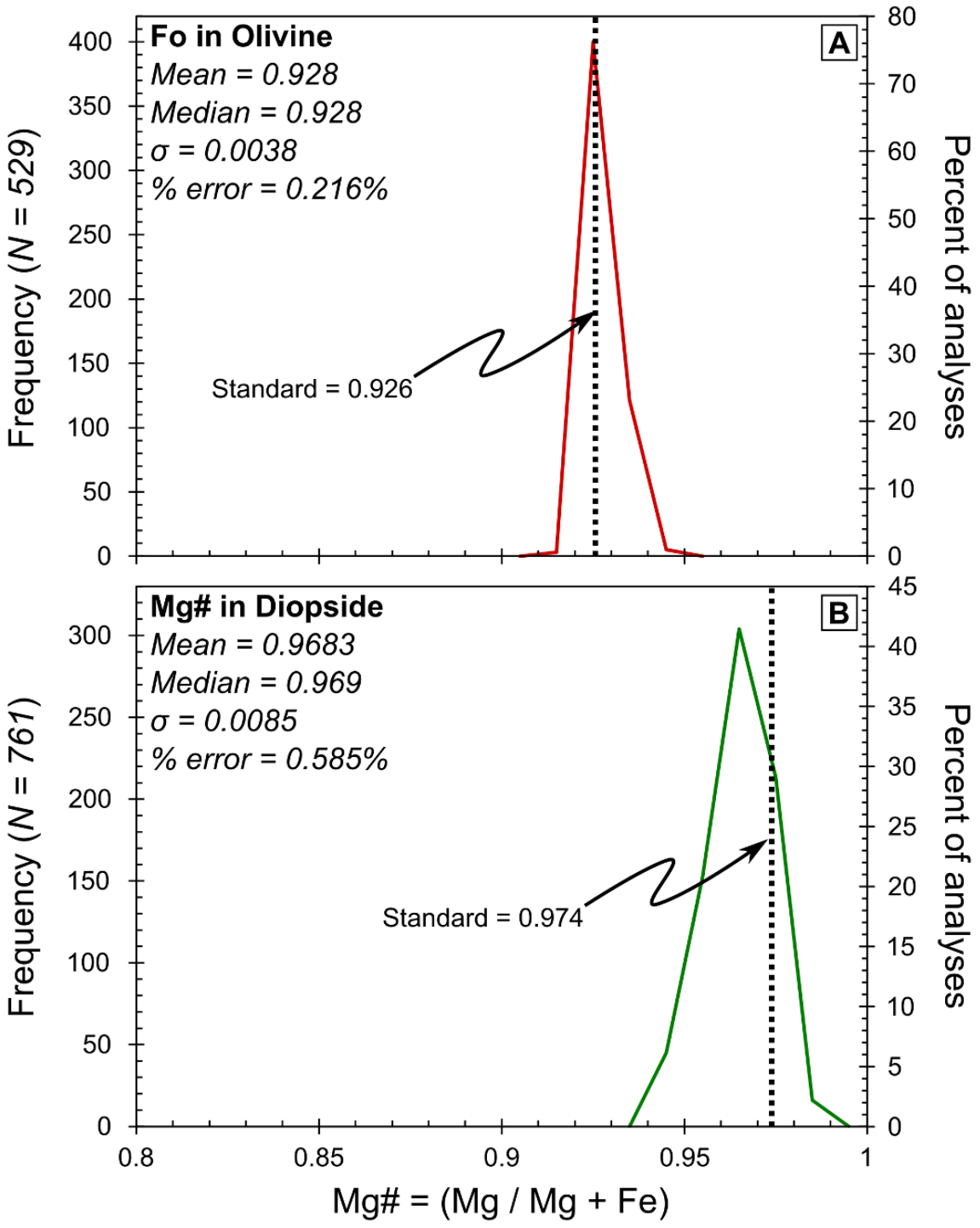

Figure 3.4: Histograms of Mg# (Mg/Mg + Fe) derived from maps of the (**A**) Olivine and (**B**) Diopside standards.

Table 3.5: Compariosn of peak quality for An derived from element maps of the Plagioclase standard at variable dwell times.

Map[a]	Current (nA)	Process Time	Resolution			Dwell Time (µs)	Anorthite				
			Width (px)	Height (px)	N (px)		Mean	Median	σ	RSD(%)[b]	% error[c]
Plag_2.5nA_10k	2.5	1	32	24	768	10,000	0.5865	0.5877	0.0371	6.3%	1.10%
Plag_2.5nA_20k	2.5	1	32	24	768	20,000	0.5918	0.5925	0.0254	4.3%	0.20%
Plag_2.5nA_30k	2.5	1	32	24	768	30,000	0.5941	0.5935	0.0194	3.3%	0.19%
Plag_2.5nA_50k	2.5	1	32	24	768	50,000	0.5937	0.5946	0.0169	2.8%	0.12%
Plag_2.5nA_100k	2.5	1	32	24	768	100,000	0.5952	0.5958	0.0109	1.8%	0.37%

[a] All runs were carried out with a beam accelerating voltage of 20kV, magnification of 500x, a process time of 1 and working distance of 8.5 mm.

[b] RSD(%) = (100 x σ) / Mean

[c] % error = 100 x (Measured - Certified) / Certified

3.4 Proof of concept: zoned plagioclase

A large proportion of studies focusing on the interpretation of crystal zoning in magmatic systems to date have been carried out on plagioclase, leading to the identification and classification of a variety of crystal morphologies and zoning patterns (see Ginibre et al., 2007 for a short review). Owing to the nature of plagioclase to reflect chemical variations through its optical properties, many of the previous studies of plagioclase zoning have been primarily carried out with polarizing light optical microscopes. In recent decades, studies of plagioclase zoning have benefited from the use of increasingly more detailed and efficient techniques based on the collection of BSE imagery and element maps by SEM or EPMA; hence, a natural sample containing zoned plagioclase was chosen for the initial testing of the QACD method.

Dolerite sample JC21-73R-7 from the Hess Deep Rift, Equatorial Pacific Ocean (see Figure 2.1c for an approximate location of dive 73) was chosen after a petrographic investigation determined that it contained an abundance of optically zoned plagioclase phenocrysts. A phenocryst which exhibited a minimum of two distinct chemical zones and minor oscillatory zoning patterns was chosen for targeted mapping (Figure 3.5). After collecting a BSE image of the target phenocryst and the surrounding material (Figure 3.5A), a portion of the crystal which contained an approximate 50:50 proportion of two distinct, nearly homogeneous chemical zones was chosen for point analysis and element mapping. The quantitative point analyses determined the core and rim to be of An_{79} (n=5) and An_{69} (n=5) rim, respectively. The area was mapped at a magnification of 1000x and a resolution of 64 x 32 pixels with an accelerating potential of 20 keV and a current of 2.5 nA. The resulting An map can be seen in Figure 3.5B and the resulting An histogram in Figure 3.5C. The resulting histogram (bulk mean An = 0.74; $\sigma = 0.11$) exhibits two peaks with medians centred around 0.69 and 0.79, both of which match the population peaks for the two previously determined compositional zones.

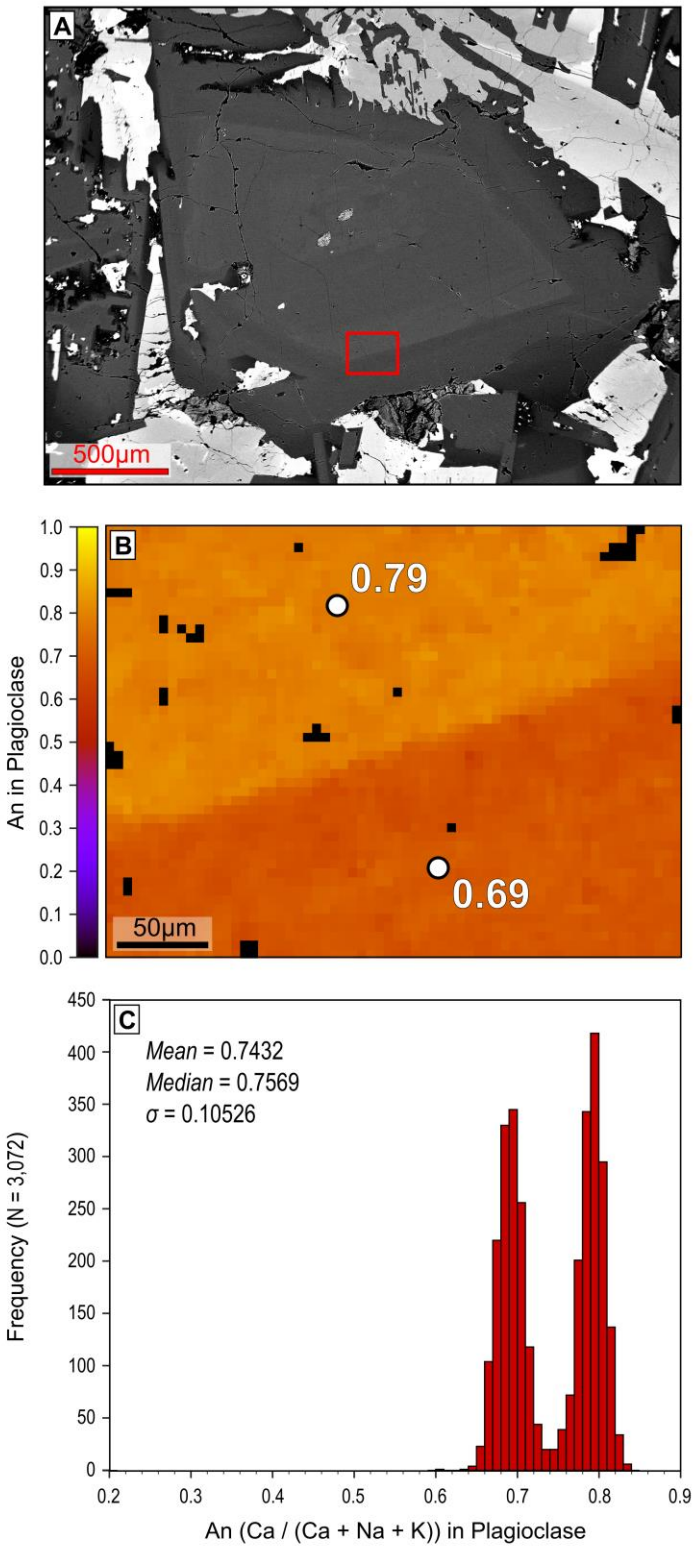

Figure 3.5: (**A**) A Back-scattered electron image of a zoned plagioclase phenocryst chosen for element mapping in dolerite 73R-7. The red box constitutes a zone with an approximate 50:50 distribution of plagioclase zonation chosen for isolated mapping. (**B**) A ratio map and (**C**) histogram of An in plagioclase has been derived from the map outlined in the BSE image. The locations of quantitative point analyses of the core (An_{79}) and rim (An_{69}) are indicated by white circles.

Next, an element map was collected over the entirety of the phenocryst and the surrounding area represented in the BSE image of Figure 3.5A. Figure 3.6 provides the resulting phase-separated map (A) and histogram (B) of An in plagioclase for the phenocryst and the surrounding dolerite matrix material. Note that although the previous analysis focusing on the two distinct zones within the plagioclase phenocryst resulted in a significantly 'cleaner' compositional histogram, it lacks information regarding the presence of both subtle changes in the internal zonation of the plagioclase phenocryst and the strong zonation in the grain as it approaches the grain boundaries.

The low-An tail which is present within the histogram for the full plagioclase phenocryst in Figure 3.6B is representative of the portions of the plagioclase grain within the mapped area that are in contact with the surrounding phases. If this map had been created by using a calibrated BSE image, then the low-An tail could be considered as an 'Edge' effect, however, the geometry and distribution of the zoning combined with our use of a 3-by-3 median filter to smooth or average out the data while preserving grain boundaries instils confidence that this tail is more or less related to actual zoning in the plagioclase as it approaches the grain boundaries.

Thus, we have successfully developed a method for the rapid collection and processing of whole-thin section quantitative element maps. We have demonstrated that, with the QACD method, we can determine the full, quantitative compositional distribution of plagioclase, pyroxene, and olivine compositions with the required accuracy and precision from these maps.

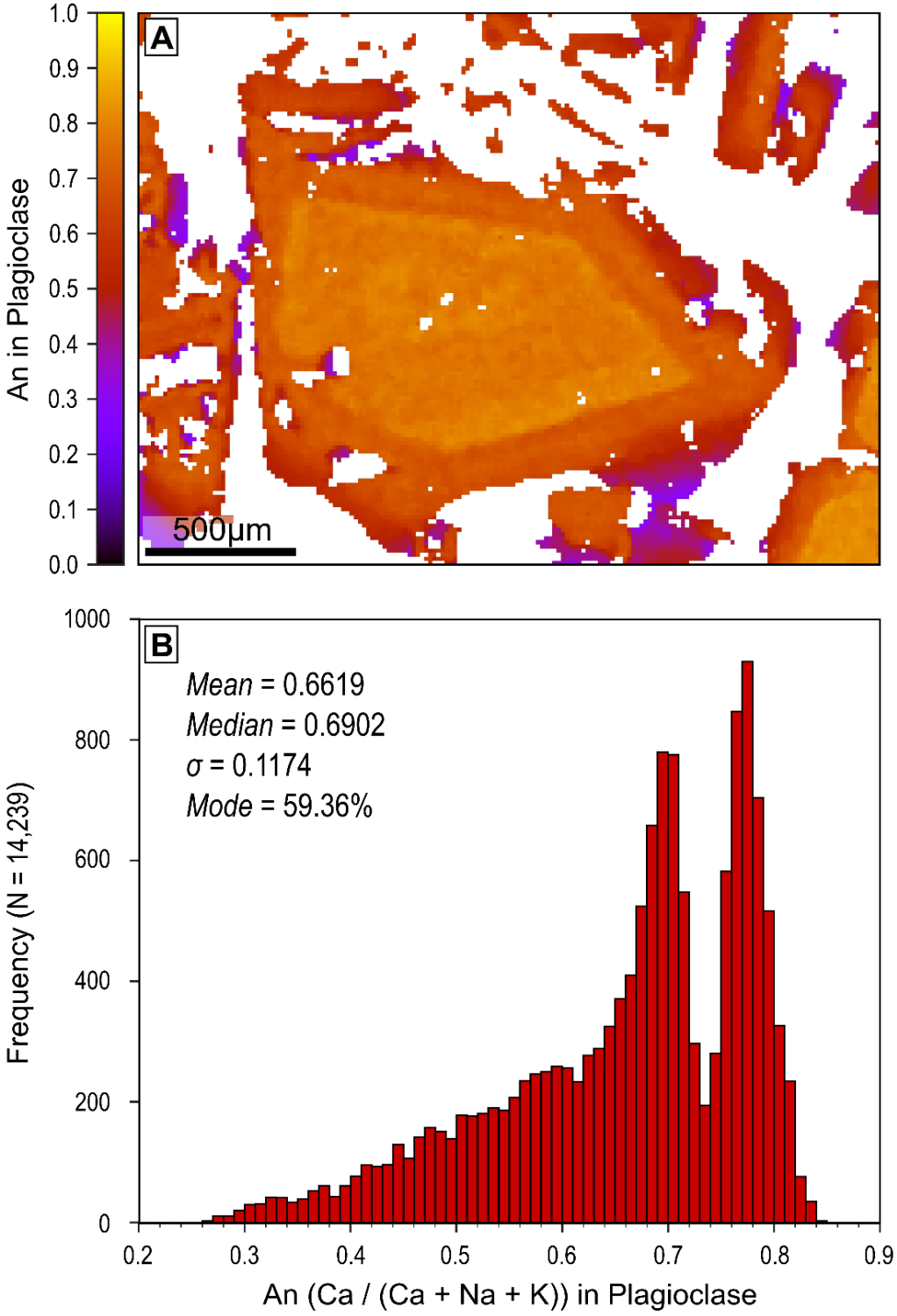

Figure 3.6: (**A**) A ratio map and (**B**) histogram of An in plagioclase derived from a 179x134 element map of a zoned plagioclase phenocryst in dolerite 73R-7.

3.5 Quack: software for QACD

The QACD method has been incorporated into a software package with a user-friendly graphical user interface (GUI) called Quack, which can be run with Python version 2.7 (see Quack user-manual in the electronic Appendix E3 for a list of required plugins) and requires no prior knowledge of the Python coding language (i.e., no requirement for command line input). The program is structured into four main parts: Initialise, Phase, Ratio and Results (Figure 3.7). The first step (Initialise), starts by loading the maps. The user will determine what type of filters, if any, they would like to apply to the maps and the overall dataset. Next (Phase), the user has a choice regarding how they want to go about identifying phases in their dataset and creating phase masks. The third step (Ratio), allows the user to calculate element ratio maps and apply quantitative corrections. The final step (Results), allows the user to create and plot element/ratio histograms and maps. All of the functions used in these different stages are explained below and relevant software environment-specific explanations of the modules can be found in the Quack user-guide (electronic Appendix E3).

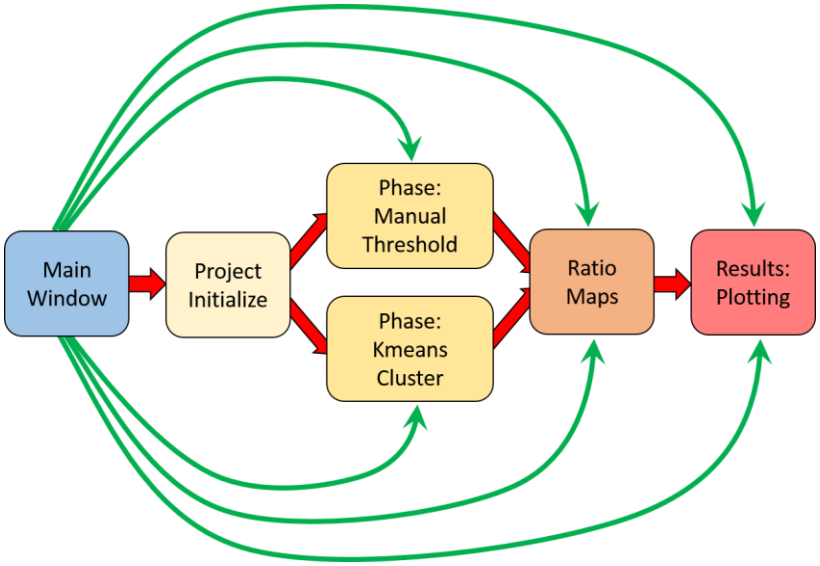

Figure 3.7: A flowchart of the QACD method as it has been incorporated into the QACD software.

3.5.1 Raw data treatment (Initialise)

Previous methods for processing quantitative X-ray element maps have included ways to process the raw map data including the ability to calculate and remove backgrounds from the map (i.e. peak fitting) and correct for spectrometer dead-time (e.g. Tinkham and Ghent, 2005). Like most vendor-provided EDS

software, the Oxford Instruments Aztec Software package on the Cardiff system already provides a built-in method for correcting raw X-ray map data which is optimised for their detectors, known as TruMap. Since all EDS users have this ability, we have not included such options within the QACD processing method, and instead, we rely on the vendor-provided software to perform these intensive corrections. The resulting background-corrected element maps are each exported from Aztec as comma-separated format text files (.csv) and used as the primary data input for Quack. These files do not include a header and consist of simple matrices of X-ray intensity data corresponding to the number of collected photons per analysed element per pixel, with a single column of zeros at the far right of the matrix.

Upon executing the Initialize section of Quack, the user is prompted to pick the working directory in which the CSV files are located and create a project file within this directory. This project file, an HDF5 or hierarchical data formatted file, is structured like a tree and serves as a storage location for the data to be processed throughout the session (Figure 3.8). Next, the user is prompted to pick the CSV files that they would like to process and load them into the project file. The CSV files are read into matrices and, if the data is indicated as being from the Aztec Software, the column of zeros at the end of the matrix is removed. The user is now asked if they would like to apply a ‘Pixel Totals’ filter, a 3-by-3 median filter, or both to each map in the dataset. The ‘Pixel Totals’ filter simply stacks the individual element maps and adds together the total photon count rates for each pixel. A histogram is created from the resulting matrix of totals and a threshold created from statistical analysis of the totals peak to remove salt-and-pepper noise from the map. The threshold is then applied to all of the element maps, thus removing pixels with statistically anomalous total counts. The 3-by-3 median filter smooths the maps using an algorithm that replaces the central value of a 3-by-3 pixel area with the median value of all the nine points within the area. This ensures that anomalous pixels (e.g. those resulting from irregularities in crystal surface or polish) are averaged out while preserving crystal edges (Muir et al., 2012). The resulting maps are saved and stored under a new ‘Filtered’ node within the project file. The filtered maps are flattened into vectors and two ‘stacks’ are created for use in various calculations in later steps: a stack of 5 pre-defined common elements (i.e., Mg, Al, Si, Ca, and Fe), and a stack of all of the loaded element maps. The latter is then

used to calculate the mean atomic number (Z), mean atomic weight (A), and the *h* parameter of the absorption correction defined by Philibert (1963) for each pixel.

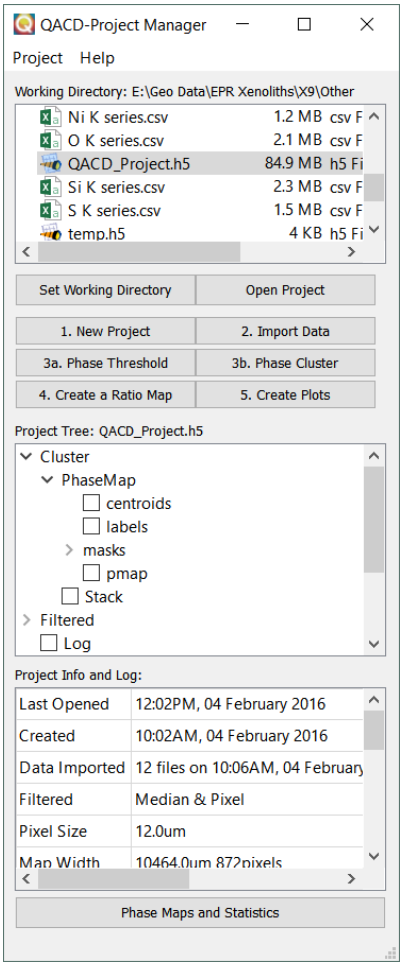

Figure 3.8: A screenshot of the main project manager window for the QACD software. A detailed view of the project tree can be seen in the centre of the window.

3.5.2 Phase identification (Phase)

Once the maps have been filtered and saved to the project file, the user begins the process of identifying mineral phases. The aim of image processing is to segment an original image (or set of images) into a classified image by assigning a mineral identity to each pixel (cf. Higgins, 2006). This can be done by simple IF/AND/OR mineral-specific algorithms (e.g., Muir et al., 2012) or more complex methods based on statistical algorithms (e.g., de Andrade et al., 2006; Lanari et al., 2014; Liebske, 2015). The QACD method contains two types of phase identification that the user can choose from. The first allows the user to define individual phases by simple thresholding relative to the amounts of key elements; thresholding is done by sliders, which interactively update the map to reflect the current threshold, allowing for precise phase maps to be created that are specific to the compositions

in any given sample. Once the key elements and their thresholds have been determined, the user names and creates a phase mask which is stored in the project under the 'Phase' node (Figure 3.9). This results in maps that display the X-ray intensity data for pixels that lie solely within the boundaries of the phase of interest.

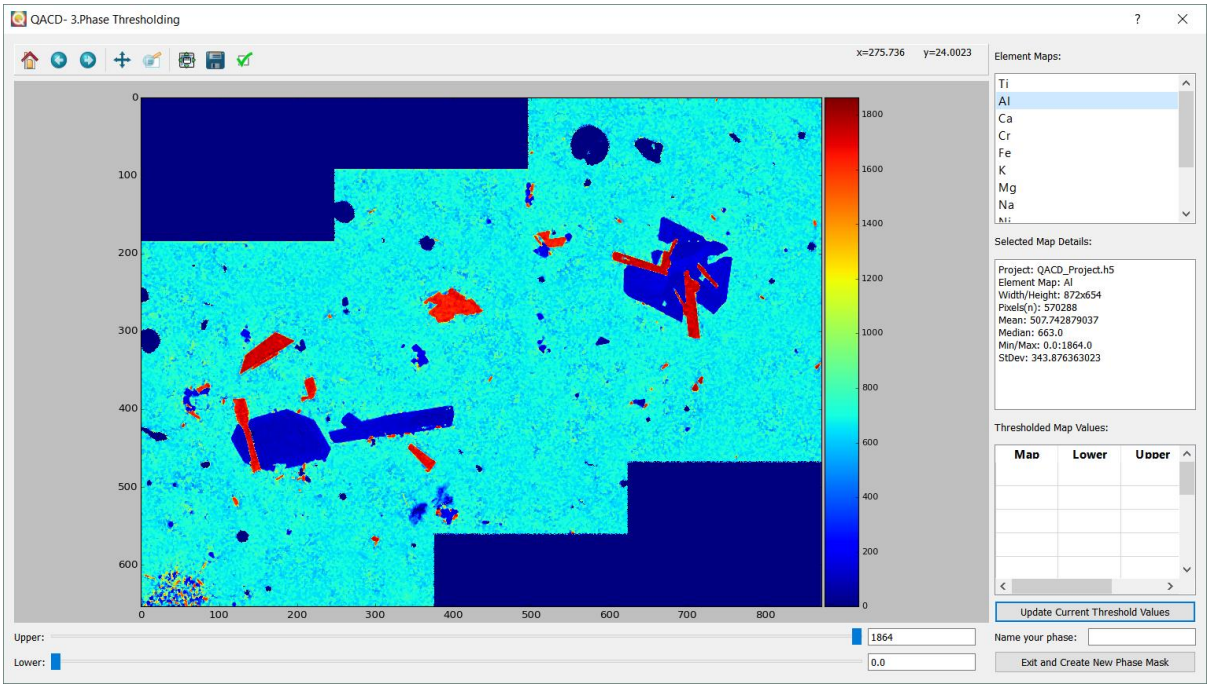

Figure 3.9: A screenshot of the phase thresholding window for the QACD software.

The second method is an advanced adaptation of a k-means clustering algorithm, an iterative process which assigns *n* observations (i.e., pixels) to exactly one of *k* clusters defined by centroids (Lloyd, 1957). Each observation is assigned to the cluster defined by a centroid with the nearest mean to the observation. Essentially, given a sequence of observations (x_1, …, x_n), the k-means algorithm partitions the observations into *k* (≤*n*) groups S = (S_1, …, S_k) by minimising the sum of squares within each cluster. The sum of squares within each cluster is defined as the sum of the distance functions for each observation in the cluster relative to the centroid.

$$\sum_{i=1}^{k} \sum_{x \in S_i} \|x - \mu_i\|^2$$

The centroids are randomly selected by the algorithm and *k* is defined by the user before the algorithm is executed. Because this method is automated and can be influenced by slight variations in minor elements, the user has the choice between

using either of the two stacks (5 common major elements or all loaded elements) created in the initialization process. After choosing which stack to use, the user is prompted to provide a range for the possible number of phases. For example, if five main phases were identified during petrographic analysis, then the user might provide a range of five to nine for this step in order to account for potential variations in alteration phases or zoning within minerals or any accessory phases. The software then carries out a series of k-means clustering operations across the range of provided minimum and maximum numbers of phases. The user is then presented with the resulting maps to choose the most appropriate result for further editing, providing an opportunity for the user to edit the results by way of merging, deleting, and renaming the phases. The final phase masks are saved and stored in a 'Cluster' node within the project file under the phase name provided by the user. The clusters can be returned to for further editing, and the process can be repeated and stored under a separate and numbered cluster node.

Both the clustering and the thresholding methods for phase separation have their strengths and uses. The sensitivity of the k-means clustering method to slight elemental variations makes it useful for simple bulk phase mask creation and modal abundance calculations. For this reason, we have included features for calculating modal maps within the phase clustering portion of the software. The thresholding method allows for finer control over phase separation by the user, thus it is less optimised for calculating bulk sample phase maps and more towards single phase masking. Although the thresholding method is not set up for producing modal phase maps, statistics are produced for each phase mask which include the total number of pixels in a phase; allowing for the user to record and determine modal proportions for masked phases with ease.

3.5.3 Molar ratio and concentration map calculation (Ratios)

In addition to the processing of element maps and phase identification, Quack facilitates the interactive manipulation and visualisation of element maps and the calculation of elemental concentration maps and geochemically useful element ratio maps. Several common presets (e.g., An, Mg#) have been included in the ratio map calculator for ease of use, and custom ratios can be calculated according preset formats (i.e., A / B or A / (A + B) or A / (A + B + C)). For quantifying a single element, a preset is provided which is referred to as 'single', as in single element.

The window contains a list and several dropdown menus that are populated with the names of the imported elements. Upon selecting a preset ratio, a label displays details on what the ratio is and the dropdown boxes for the elements are automatically updated to reflect the chosen ratio. The user can choose to change these elements as well as provide a custom name for the calculated map. After pressing the calculate button, a dialog appears asking for the user to specify what phase, if any, they would like the ratio map to be calculated for; this determines which equations from the database will be used to calculate the map. Whenever a new map is imported or created, statistics are calculated for the map data (i.e., range, mean, median, and standard deviation of the selected ratio) and stored as metadata when the map is saved to the project file.

3.5.4 Figure creation and export (Results)

The software has the ability to display/create and export element maps and histograms of map data (Figure 3.10). These can be carried out on any of the element maps, including the original filtered element intensity maps, within a project. The figure export window contains options for controlling the size, dpi (exported resolution), file type and name of the exported file as well as the figure title and whether or not to include an annotation with statistical information for histograms. Histograms are generated from the chosen map data upon launching the histogram export window. For molar ratio maps, the histograms are calculated with 1 mol.% wide bins. For element intensity or concentration maps, the software calculates the bin size for 100 bins between the minimum and maximum of the dataset. The bins cannot currently be changed or specified by the user; this feature will be incorporated in the next release of the software along with the ability to produce other potential statistical plots. Upon exporting a histogram, the user has the option to save a .csv file under the same name containing the bins and frequencies corresponding to the figure.

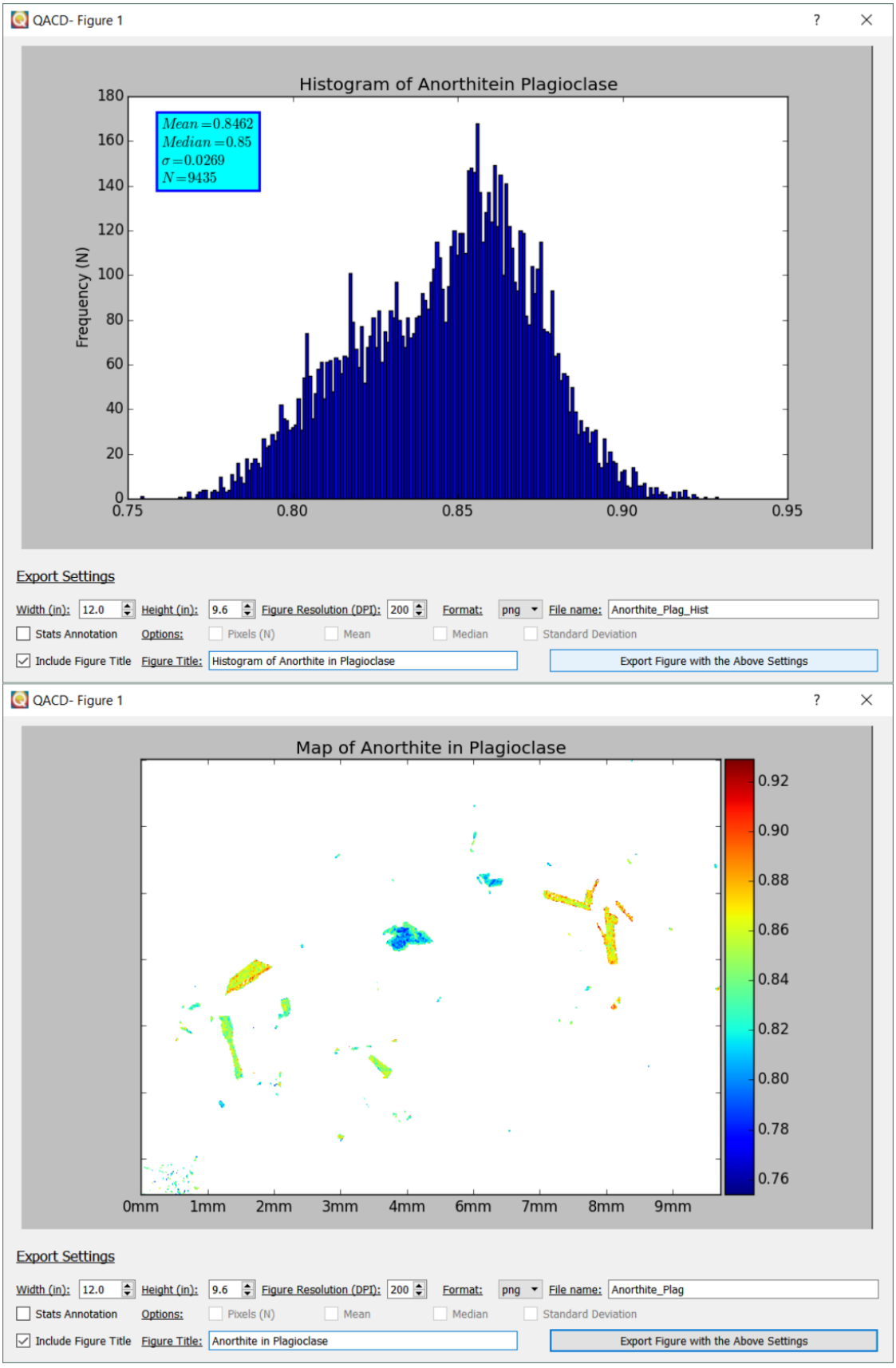

Figure 3.10: A screenshot of the figure export window for a (**A**) histogram and an (**B**) element map from the QACD software.

Aside from visualising data for export as maps and histograms, the Quack software also allows for the user to export data in the form of text files. Under the file menu portion of the Project Manager window the user can select the option to export various maps and data from the project as .csv files for use in other post-processing software (Figure 3.11). Currently the software supports the export of phase masks, filtered and processed maps, user-created ratio maps, and the project log file.

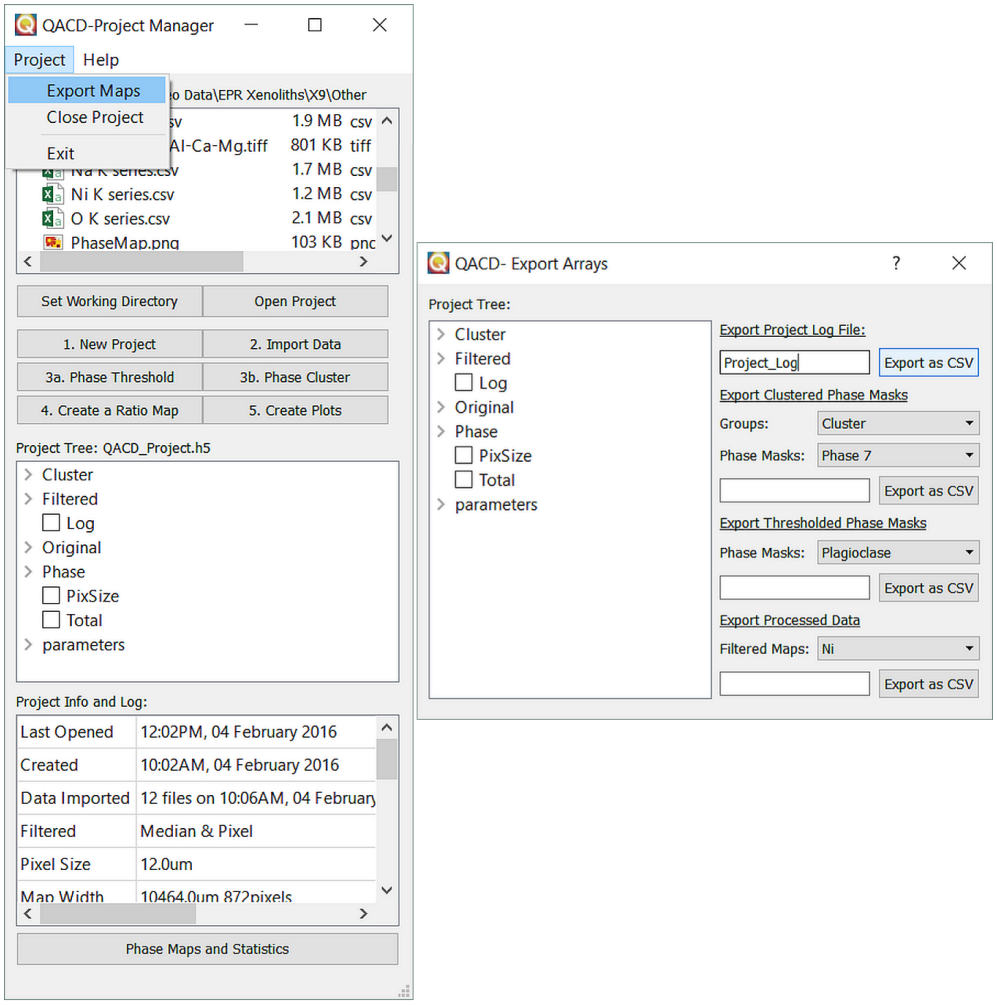

Figure 3.11: (**A**) A screenshot of the project manager window highlighting the location of the map export function. (**B**) A screenshot of the map export window, where users can export various maps and metadata from the project as .csv or .txt files.

3.6 Discussion

The QACD method has been optimised for the rapid collection for full-thin section quantitative element maps on any EDS equipped SEM. The previous processing methods outlined in section 3.2.2 were focused on post-processing of element map data derived primarily by WDS-EPMA. Those published methods which do allow for data derived from EDS systems as well as WDS-EPMA fall short

of being able to accommodate both the full range of processing from data filtration through quantification, molar ratio calculation, and statistical analysis of the data and, in particular, are not optimised for the processing of the large map sizes that are required for full thin section element maps.

3.6.1 WDS vs EDS element mapping

The problem of these software methods lacking the ability to process full-thin section element maps may be rooted in the specific nature of how mapping is conducted by WDS-EPMA. Element mapping with WDS requires a fixed beam due to the tendency of the spectrometer to experience defocusing when the beam is rastered outside of the focal region of the spectrometer (typically a narrow band within the centre of the field of view). A fixed beam means that each pixel in a map has to be collected by manually moving the stage from point to point; a method which we will refer to as stage mapping. Stage mapping results in longer run times for element maps due to delays in stage movement caused by stage communication and backlash corrections (on some systems, up to 0.75 s delays between controller input and stage movement; Newbury, 2006). A 64x32 resolution map (2,048 pixels) run with a 100 ms dwell time could experience up to 25 minutes and 36 seconds of delay time for stage movement on top of the expected 3 minutes and 25 seconds of live time that is actually spent collecting data at each spot, resulting in a full run time of 29 minutes and 1 second for the map. Further, the number of elements which can be collected for a WDS-EPMA map at a given time is limited to the number of WDS spectrometers that the machine is outfitted with (e.g., a 4 spectrometer EPMA can only analyse 4 elements at a time). Things become more complicated when collecting maps intended for quantification which require robust counting statistics typically achieved by longer dwell times (100-300 ms vs 40 s m.o.) and/or higher beam currents (100nA vs 10nA *modus operandi*) that can be damaging to certain materials.

If a user wanted to collect a 1200x700 (840,000 pixels) full-thin section element map of 8 major elements (e.g., Si, Ti, Al, Fe, Mg, Ca, Na, K) using the WDS-EPMA method with a 100 ms dwell time, a single pass would require a live time of 23 hrs and 20 min with up to 175 hrs of time needed for stage movement, assuming a system with a 0.75 s stage delay. Even if the system had a shorter stage delay of 0.1 s, the time required for stage movement would be 23 hrs and 20

minutes, resulting in a single pass of 66 hrs and 40 minutes (2 days 18 hrs and 40 min). Furthermore, because the WDS configuration limits the number of elements that can be analysed, two passes will be required in order to collect the full map. In total, the map would take 5 days 13 hrs and 20 min to finish. It is no surprise, therefore, that the previously published methods that focused on processing WDS-EPMA element maps were not practically considering the processing of such large maps.

In contrast, our optimised method for collecting full thin section element maps by EDS facilitates the collection of the entire energy range for every pixel with lower beam currents (e.g, 1-3 nA) and a minimum dwell time of 20 ms. With an ideal spectrometer throughput achieved at ~35% deadtime on our EDS system, a 64x32 resolution map ran at 100 ms would require a 3 min 25 s live time and result in a 4 min 37 s run time. Further, the same 1200x700 (840,000 pixel), 100 ms dwell time, full thin section map that took more than 5 ½ days to run by WDS-EPMA would only take 1 day 7 hrs 30 min. Using the minimum 20 ms dwell time achieved by the QACD method, the map would instead require a 4 hr 45 min live time resulting in a total run time of 6 hrs 18 min. The QACD method and Quack software is designed to capitalise on these advanced capabilities of EDS-SEM systems.

3.6.2 Advantages of the Quack software

As previously discussed in section 3.2.2, the existing processing software which is designed for EDS element maps is limited in capability. Each of the methods capable of handling EDS-derived element maps is primarily focused on accurate phase identification and the calculation of modal abundances, with no room for adaptation. In contrast, the Quack software has been designed to allow for user modification. The software is currently built for processing large maps, calculating molar ratio maps, and plotting histograms of the maps data, allowing for users to export any of the data that is generated by the method into text files and images. Thus, the user is not limited to the software in its current state and can even modify the code of the python-based software to suit their own research needs.

The long term goal is to maintain the established GitHub (https://github.com/mloocke/QACD-quack) repository for the software, so that it would serve as a place for users to (i) obtain the most up-to-date version of the

software, (ii) provide feedback regarding software bugs, (iii) request new features, and (iv) provide their own custom-coded features and modules for addition to the software. The GitHub repository will eventually also serve as a home for the QACD quantitative correction database. The database has currently only received spectra and analyses derived from the Cardiff University SEM that are limited to the standards and unknowns and optimised operating conditions of the Cardiff SEM lab. Like the experimental petrology database at the core of the MELTs modelling software (Ghiorso and Sack, 1995), the long term goal of the QACD database is to incorporate spectra acquired by users on their own EDS-equipped SEM under various conditions for a wide variety of standard and unknown compositions. Over time, these will facilitate the derivation of increasingly more accurate and precise correction models for a larger variety of elements, molar ratios, and mineral phases than is currently available to us. The QACD method has thus been designed to be a bespoke 'living' method that is easily updated and adapted with time.

3.7 Conclusion

The QACD method and the Quack software provide a new method for the rapid collection of full-thin section quantitative element maps and a new post-processing tool for calculating mineral modes, producing element intensity/concentration and molar ratio maps, and quantifying full-sample compositional distributions. For the first time, a series of samples can feasibly be mapped in full to provide a thorough compositional characterisation of a rock or rock unit, allowing for full histories of igneous rocks to be reconstructed. Using the traditional method of map collection by WDS-EPMA, an investigation seeking to characterise the bulk compositional distribution of an igneous rock unit based on 10 thin sections would require more than 55 days of run time to complete; hence, full-thin section quantitative element mapping is not common for petrological studies. Using the QACD method, the same 10 thin sections could be mapped over the course of two to three days (i.e., 2 days 15 hrs or 63 hours). Thus, the QACD method facilitates the incorporation of element mapping into the *modus operandi* of a geochemist or petrologist with access to EDS-equipped systems.

CHAPTER 4
Application of the QACD method to natural samples

4.1 Introduction

The first application of the QACD method after initial testing and development on standard reference materials was full thin section element maps of six natural samples: (i) the same dolerite with zoned plagioclase phenocrysts from Hess Deep as was used for the initial tests (JC21-73R-7); (ii) a crystal-rich intermediate tuff from Almeria, Spain (ALM1) with a complex crystal assemblage exhibiting a variety of plagioclase zoning patterns and at least two distinct compositions of clinopyroxene; (iii) a basalt from the Gakkel Ridge, Arctic Ocean (HLY0102-D45-3) characterised by a large number of phenocrysts and glomerocrysts constituting approximately 20 modal percent of the rock in hand sample; (iv) an olivine gabbro (90R-6 126-129) and (v) an oxide-bearing olivine gabbro (80R-6 121) from ODP hole 735B.

4.2 Plagioclase zonation in a dolerite

The first successful full-thin section quantitative element map collected by the QACD method was that of dolerite sample JC21-73R-7 (Figure 4.1), in which previous testing of the method had been carried out on a compositionally zoned phenocryst. After collecting a full thin-section BSE image (Figure 4.1B), an element map was carried out at an accelerating potential of 20 keV, a beam current of 2.5 nA, a pixel dwell time of 20ms and a pixel step-size of 15 µm. The resulting An map can be seen in Figure 4.1C and the resulting An histogram in Figure 4.2. A total of ~100 phenocrysts were counted in the map, of which 60 crystals are larger than ~1 mm. An examination of both the BSE image and the An map of the phenocrysts reveals several interesting features within the sample that were not readily apparent in plain- or cross-polarised light microscopy. (i) Two plagioclase phenocrysts have higher-An cores (~An_{87}) than the rest of the sample; one just to the left of the map centre, and the other in the upper portion of the map, just to the right of centre. These two grains differ in zoning pattern with the central grain being characterised by a large high-An core and thin lower-An rim, and the upper-right grain being characterised by a smaller high-An core with slightly concentric zoning out to the lower-An rim. The likelihood of an analyst picking these grains for probing based on petrography is ~2% (2 out of 100) for the bulk phenocryst population and ~3%

(2 out of 60) if they are focusing on characterising the larger grains. (ii) Only a small number of the larger phenocrysts (6 out of 60 or ~10%, of the phenocrysts) preserve a narrow reverse zone before transitioning into the normally-zoned rim. The likelihood that these grains would be chosen for analysis is 6% (6 out of 100) for the overall phenocryst population and 10% for the larger sub-population. Even if the analyst happened to choose those grains, such subtle features may not be readily apparent in spot traverses, unless a BSE map had been made beforehand. (iii) The matrix plagioclase is observed to cover a wide range of An compositions. The bulk of the matrix plagioclase have compositions which appear to be in equilibrium with phenocryst rims and exhibit zoning over short distances towards lower An.

The histogram derived from the map (Figure 4.2) provides quantitative constraints on the nature of how An is distributed across the sample with the phenocryst cores (~An_{80}) making up a comparatively smaller peak to that of the phenocryst rims and more primitive of the matrix compositions (~An_{66-67}). The range of matrix compositions observed in the map is reflected in the the lower-An tail of the histogram. Further, subtle zoning features observed within phenocrysts in the map represent a statistically insignificant proportion of the overall population, and are thus not readily apparent when examining the bulk population histogram. For example, the higher-An phenocryst cores are represented by very small bars in the histogram, while the subtle reverse zoning identified in a handful of phenocrysts from the map is lost in the bulk compositional distribution.

This sample illustrates the need for combining the use of element maps and histograms for reconstructing the full petrogenetic histories of rocks. The element maps provide constraints on compositional and textural variations and can reveal a lot about the true nature and histories of a sample without context as to how they relate to the overall compositional distribution. The histograms then allow for the overall compositional distributions to be quantified. Thus, element maps and histograms employed by the QACD method inform one another and prevent the user from acquiring incomplete or unrepresentative data and potentially erroneous interpretations.

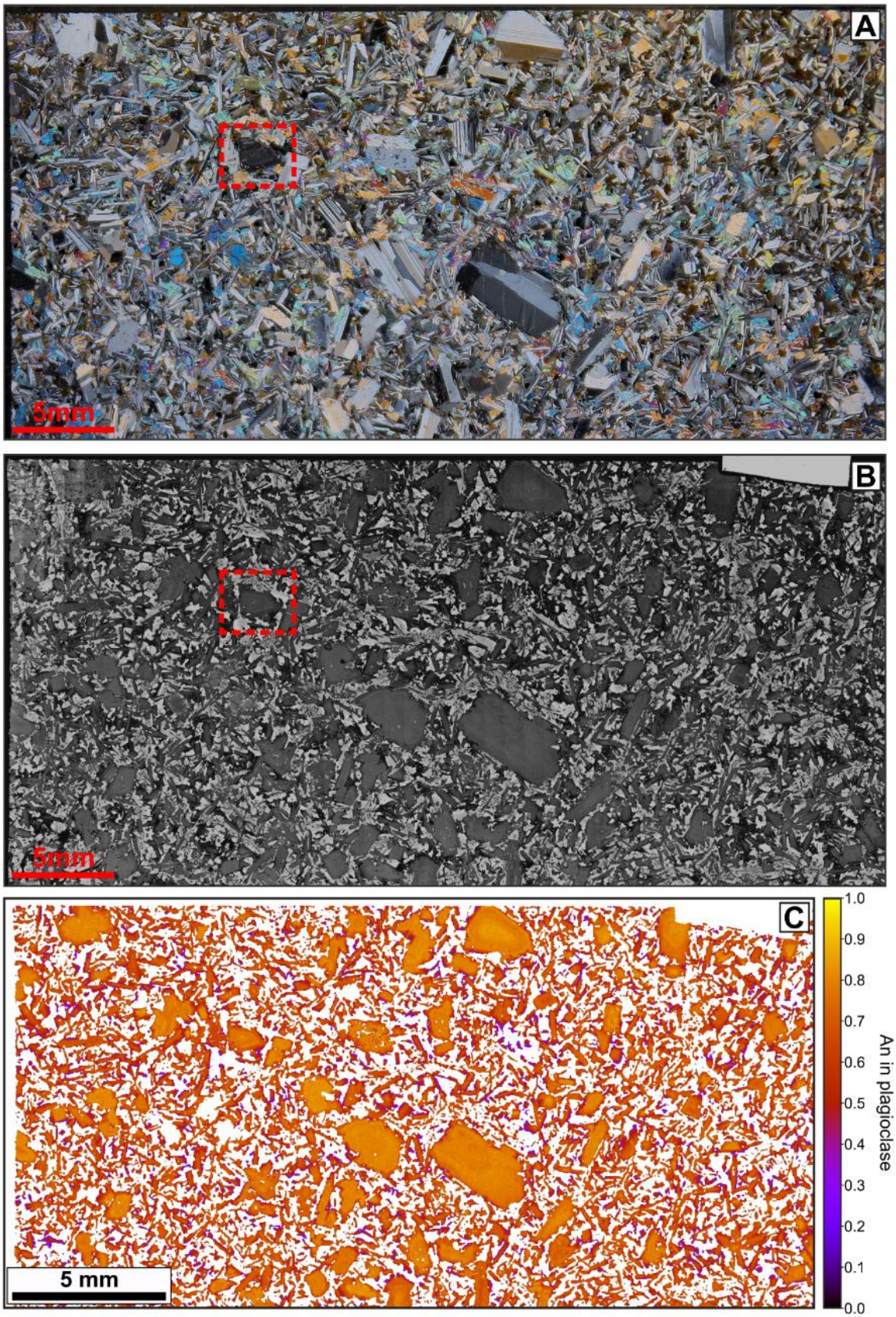

Figure 4.1: A (**A**) cross-polarised light photomicrograph, (**B**) back-scattered electron map and (**C**) molar ratio map of An for the JC21-73R-7 thin section. The red box in each panel indicates the location of the grain chosen for detailed element maps in Section 3.5.

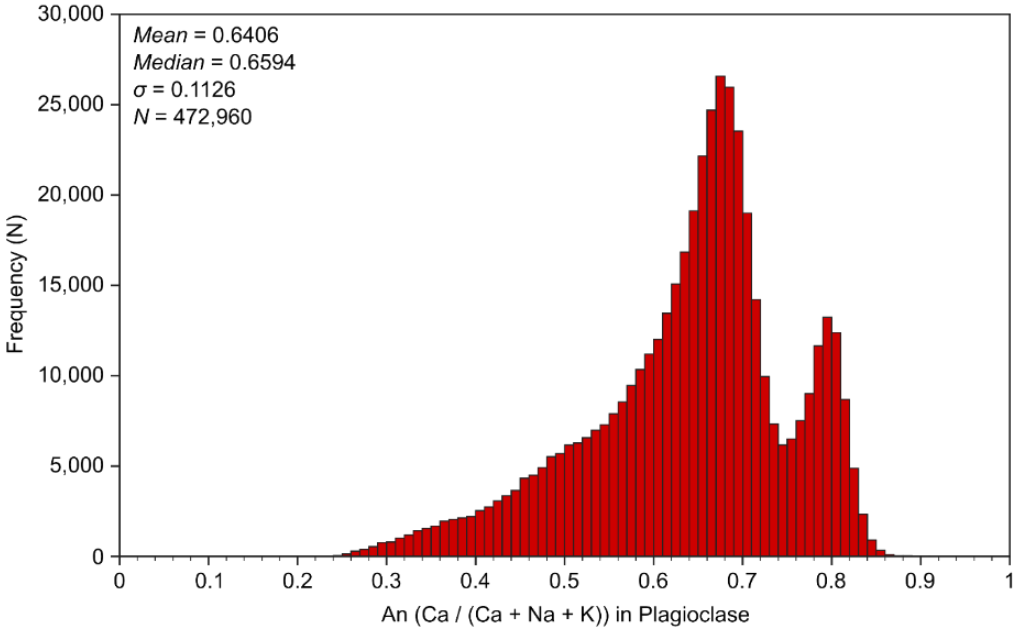

Figure 4.2: Histogram of An in plagioclase corresponding to the full thin section map of 73R-7 displayed in Figure 4.14C.

4.3 Feldspar and pyroxene phenocrysts in a tuff

A single thin section of a crystal-rich intermediate tuff (ALM1) containing abundant plagioclase, amphibole and pyroxene crystals of variable morphologies was chosen for further application of the QACD method. ALM1 was sampled from a stream bed to the north-northwest of the town of Rodalquilar along the southeastern coast of Spain (Figure 4.3). The catchment of the stream is located in the northeastern portion of the Rodalquilar caldera complex within the Miocene Cabo de Gata volcanic field (Cunningham et al., 1990; Rytuba et al., 1990). The precise origin of the sampled mafic tuff within the caldera complex is unknown, but not of importance to this study.

Petrographic analysis of the ALM1 thin section (Figure 4.4) reveals a cargo dominated by large hornblende, orthopyroxene, and quartz grains, plagioclase with a range of morphologies, various fragments of coarse grained xenoliths composed of mostly plagioclase and clinopyroxene, and a single large clast of tholeiitic basalt containing phenocrysts of clinopyroxene and plagioclase with similar morphologies and zonation patterns to crystals found throughout the tuff. A full thin section element map was collected with an accelerating potential of 20 keV, a current of 4.0 nA, a pixel dwell time of 20 ms, and a pixel step size of 15 μm. Phase masks were created for plagioclase (703,259 pixels or 23.61 modal %) and pyroxene (148,226 pixels or 4.98 modal %) and the resulting An in plagioclase and Mg# in

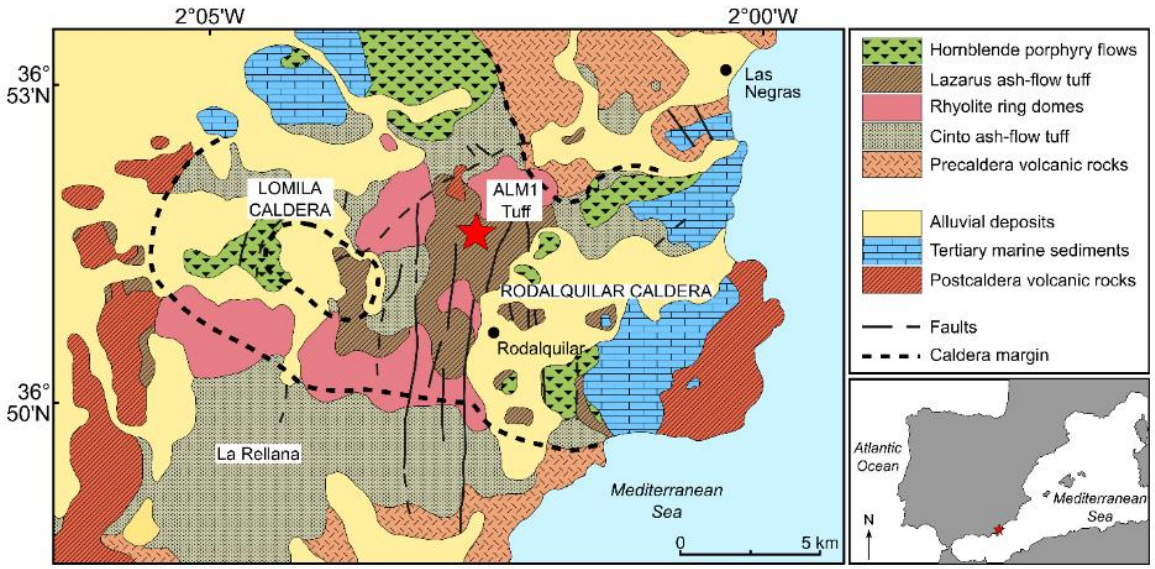

Figure 4.3: A geologic map of the Roalquilar and Lomilla calderas along the southeastern coast of Spain (modified after Rytuba et al., 1990). The bottom right panel indicates the approximate location of the Rodalquilar caldera with a red star. The red star on the main geologic map indicates the approximate sample location for the ALM1 tuff.

pyroxene maps and histograms can be seen in Figure 4.5. The bulk thin section maps and histograms for the ALM1 tuff further illustrate the strengths of using such figures in the interpretation of complex materials.

The map of An in plagioclase for the ALM1 tuff (Figure 4.5A) exhibits a range of grain morphologies, zoning styles, and textural relationships that can be used to further constrain the history and origin of the rock. Overall, there is an impressive array of variability in plagioclase zoning patterns; some completely primitive (high-An), some completely evolved (low-An), and some which fall somewhere in between, displaying predominantly normal zoning (i.e., evolving from core to rim) with the exception of a small percentage of larger grains which contain a reversely zoned core and normally zoned rim. Only an element map will allow for the user to appreciate the extreme variability in plagioclase composition and zoning across the ALM1 tuff, providing constraints on the potential origin of the incorporated materials. At first glance, one may be compelled to assume that the variety in crystal zoning and grain shape would result in a histogram with relatively distinct peaks for each of the dominant zones. However, the corresponding histogram reveals very little else regarding the plagioclase crystal population aside from the bulk range and primary concentration of An across the sample. There are at least three readily identifiable peaks/bumps in the histogram, with the most obvious located at approximately An_{78} and An_{69} and a subtle bump located around An_{55}.

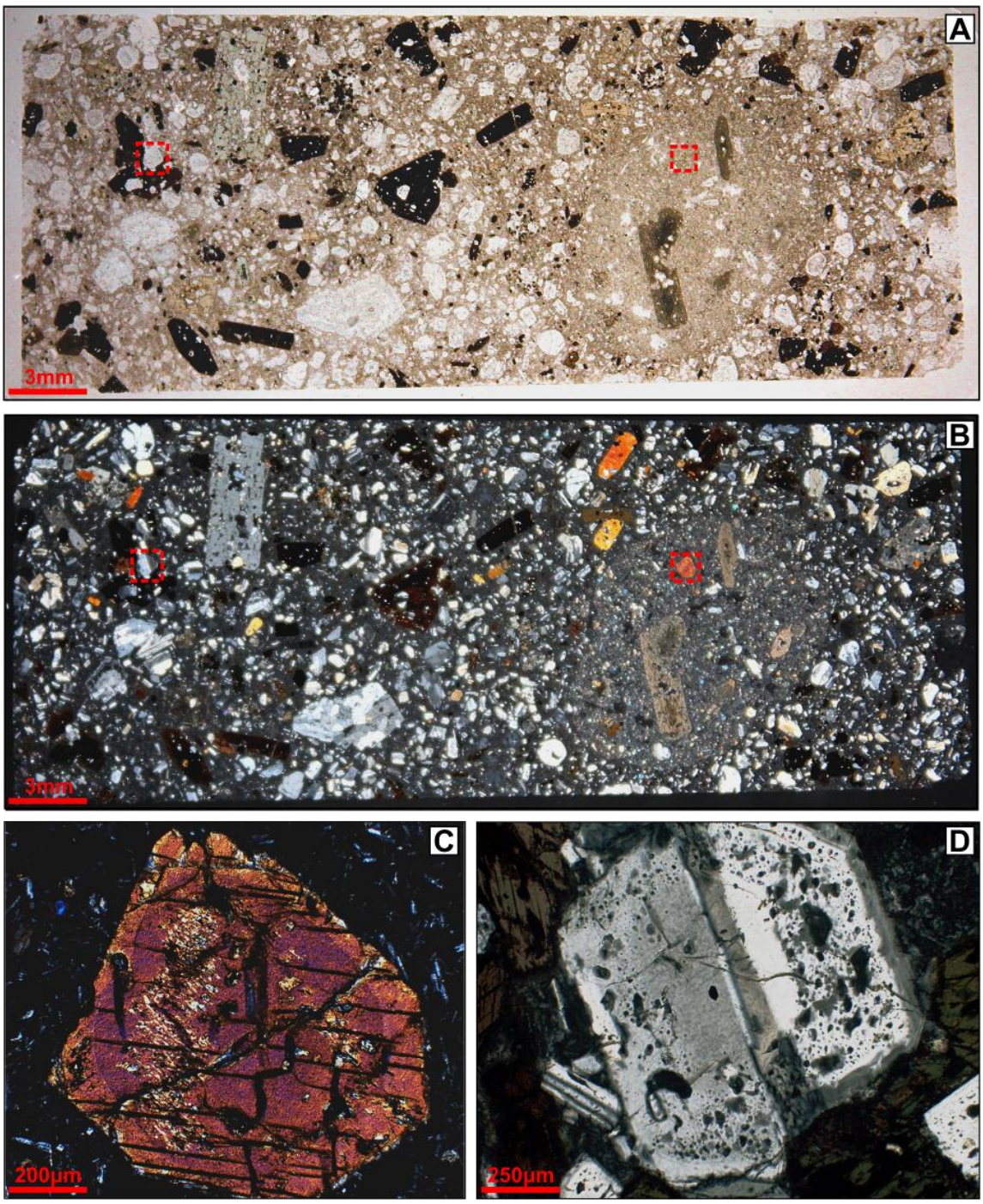

Figure 4.4: A (**A**) plain-polarised light photomicrograph and a (**B**) cross-polarised light photomicrograph of the ALM1 thin section. A cross-polarised light photomicrograph of the (**C**) clinopyroxene and (**D**) plagioclase grains chosen for detailed element maps. The locations of the clinopyroxene and plagioclase grains are indicated in panels A and B by the dashed red boxes.

In contrast to the plagioclase, the element map of Mg# in pyroxene reveals that there are clearly two distinct populations of pyroxene within the sample, a higher-Mg# population exhibiting regular zonation and a lower-Mg# population. The largest concentration of the higher-Mg# pyroxene is within the large basaltic clast in the right half of the map. The presence of individual higher-Mg# pyroxenes within

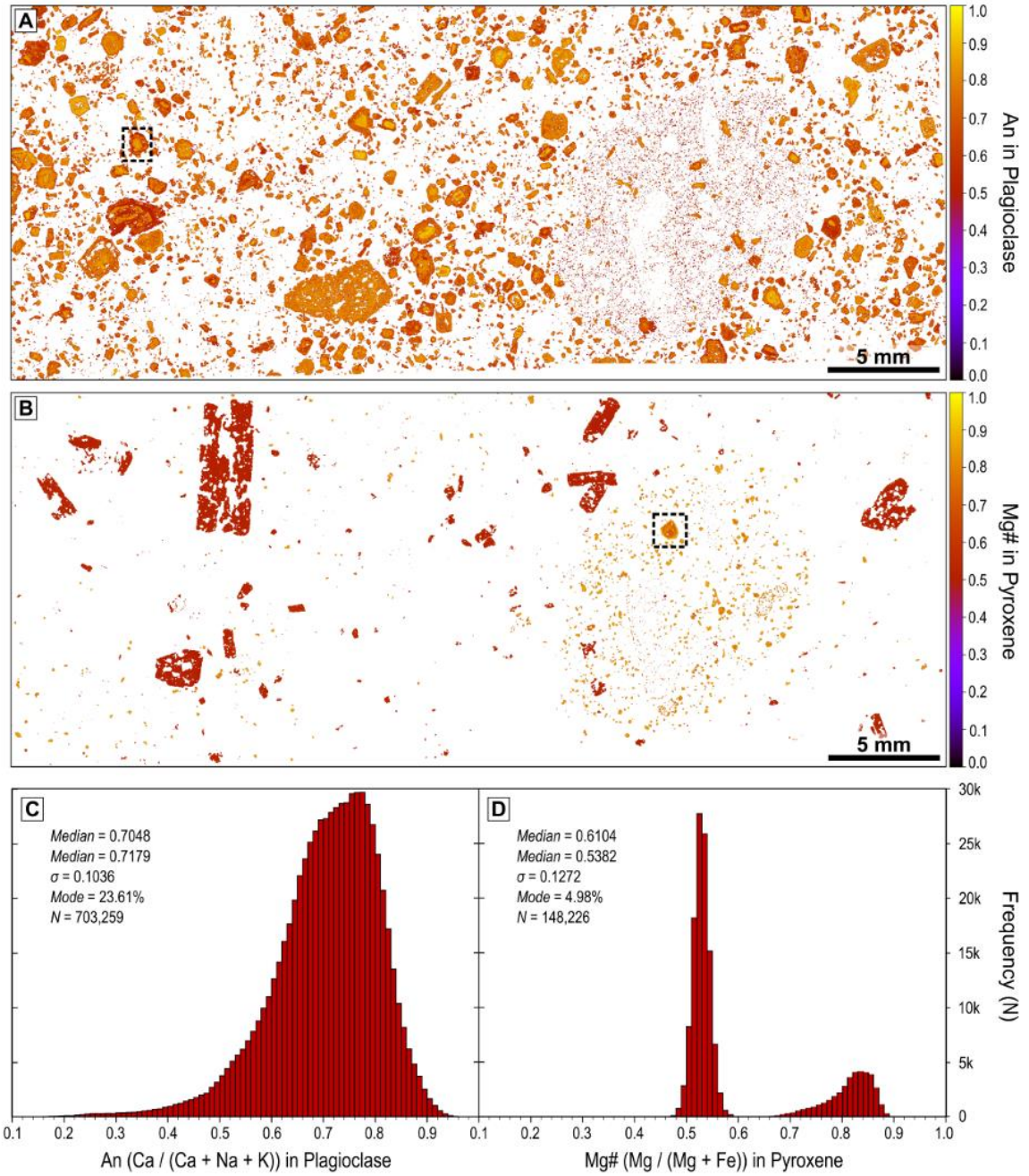

Figure 4.5: Full thin section element maps (2725 x 1093 pixels) of An in plagioclase (**A**) and Mg# in clinopyroxene (**B**) and their corresponding histograms (**C,D**) derived from the ALM1 tuff. The black boxes in panel A and panel B indicate the locations of the maps displayed in Figure 13B and A respectively.

the matrix of the tuff outside of the basaltic clast suggests that the tuff was not only picking up basaltic fragments, but also crystals sourced from these basalts. The corresponding histogram of Mg# in pyroxene reveals two dominant peaks related to the two distinct populations identified in the map. A large, tight peak in Mg# around 55 reports to a low-Ca pyroxene (orthopyroxene) characterised by large, tabular, euhedral grains amongst the main matrix of the tuff. The second, broader

peak in Mg# around 85 corresponds to the smaller, chemically-zoned Ca-rich clinopyroxenes found amongst the matrix and in the clast of tholeiitic basalt.

Two grains (one clinopyroxene and one plagioclase) exhibiting zonation were chosen for higher resolution element maps (Figure 4.6). The zonation pattern of each grain is readily apparent in both the ratio maps and histograms for each element map. In comparing the histogram of Mg# in pyroxene in Figure 4.6c with that of the bulk thin section in Figure 4.5d, the range of Mg# in the small grain is seen to cover the entire range of the clinopyroxene mapped over the bulk sample. This provides a great deal of information regarding the range in composition for the bulk sample, but the degree of detail reflected in the element map of the isolated grain is lost in the background when examining the crystal populations within the rock as a whole. This is further exhibited by the two peaks in An in plagioclase for the element map of the plagioclase grain. Although the histogram of An in plagioclase for the isolated grain in Figure 4.6d easily covers the range of An in plagioclase for the bulk thin section, the two peaks are reflected as little more than slight bumps in the bulk histogram.

A complex sample such as the ALM1 tuff has the potential to pick up phenocrysts and clasts from a variety of sources. In such a situation, the histograms can be used to narrow down the compositional ranges from which the phenocrysts and clasts were incorporated, and the information regarding chemical zoning patterns and crystal morphologies gleaned from the element maps can further be used to narrow down the sources of the populations within the sample. In the ALM1 sample, for example, the observation that the high-Mg# pyroxene is present both within the basaltic fragment and as individual grains amongst the matrix suggests that the tuff was picking up both crystals and basaltic fragments; this information is critical when attempting to reconstruct the geological history of such a complex sample. The ALM1 element map essentially provides a window into the full history of the Rodalquilar caldera, including its basaltic stage. This is another example of a situation where the element map is critical with the histograms serving a more subsidiary, complimentary role in the overall analysis and interpretation.

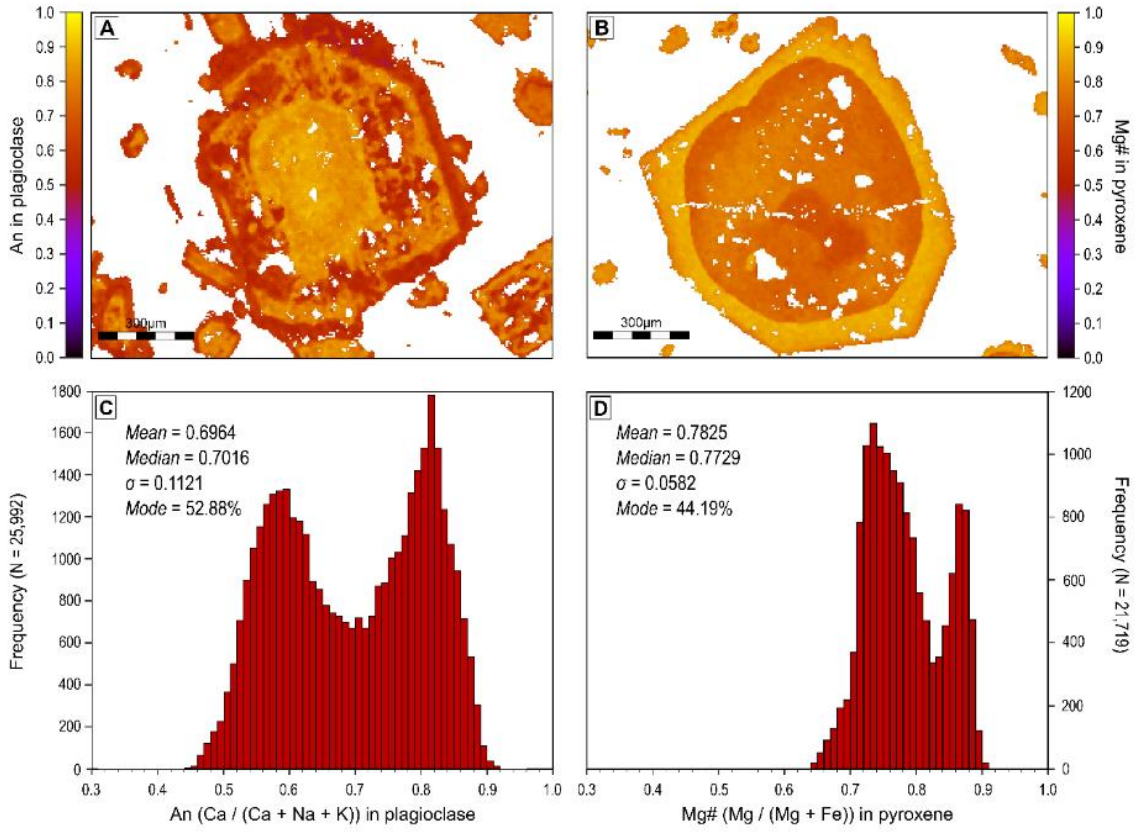

Figure 4.6: (**A-B**) Ratio maps and (**C-D**) histograms of An and Mg# in plagioclase and pyroxene, respectively, derived from 256 x 192 pixel element maps of two separate grains within the ALM1 tuff. The location of the two element maps is indicated in Figure 4.5A and B.

4.4 MORB phenocryst populations

As a contrast to the compositional range and complexity of the ALM1 tuff, two MORB samples, characterised by distinctly high and low modal proportions of phenocrysts, were chosen for analysis by the QACD method. Where the ALM1 tuff is derived from a setting and eruptive process which is expected to result in a complex phenocryst population derived from a wide variety of source compositions within the Rodalquilar complex, MORB typically record simpler histories. Textural and compositional variations in the phenocryst populations of MORB samples likely reflect variations in both the composition of and magmatic processes within the source of the phenocrysts; hence, we can use them to extract information regarding the nature of the magmatic plumbing system at MORs.

Collected from the Gakkel Ridge, an ultraslow spreading MOR located in the Arctic Ocean (Figure 4.7; Michael et al., 2003), HLY0102-D45-3 (86.0217°N, 25.0783°E) is an olivine-, clinopyroxene-, plagioclase-phyric basalt dredged from a small volcanic edifice within the sparsely magmatic zone of the Ridge. Sample HLY0102-D45-3 (D45-3) is characterised by a phenocryst population (~20 modal

%) with an abundance of clinopyroxene, no Cr-spinel, and glomeroporphyritic textures (i.e., phenocrysts tend to clump together).

An element map (2281x17580 pixels) was collected on a thin section of sample D45-3 using an accelerating potential of 20 keV, a beam current of 2.5 nA, a pixel dwell time of 20 ms, and a pixel step size of 10 µm (Figure 4.8). Out of a map of 4,009,998 pixels, a total of 786,769 pixels (19.62 modal %) were determined to belong to the phenocryst population. The phenocryst assemblage of D45-3 lacks any systematic variability in grain size and morphology for the primary phases. Plagioclase (~68% of the phenocrysts) grains tend to be elongate with skeletal features occasionally appearing within grain interiors. Olivine (~20% of the phenocrysts) displays skeletal textures with euhedral to subhedral grains. Both plagioclase and olivine are found as single phenocrysts and associated with glomerocrystic clumps. Clinopyroxene (~12% of the phenocrysts) is rarely found outside of glomerocrystic clumps and is characterised by euhedral to subhedral grains which can be oikocrystic to plagioclase and olivine.

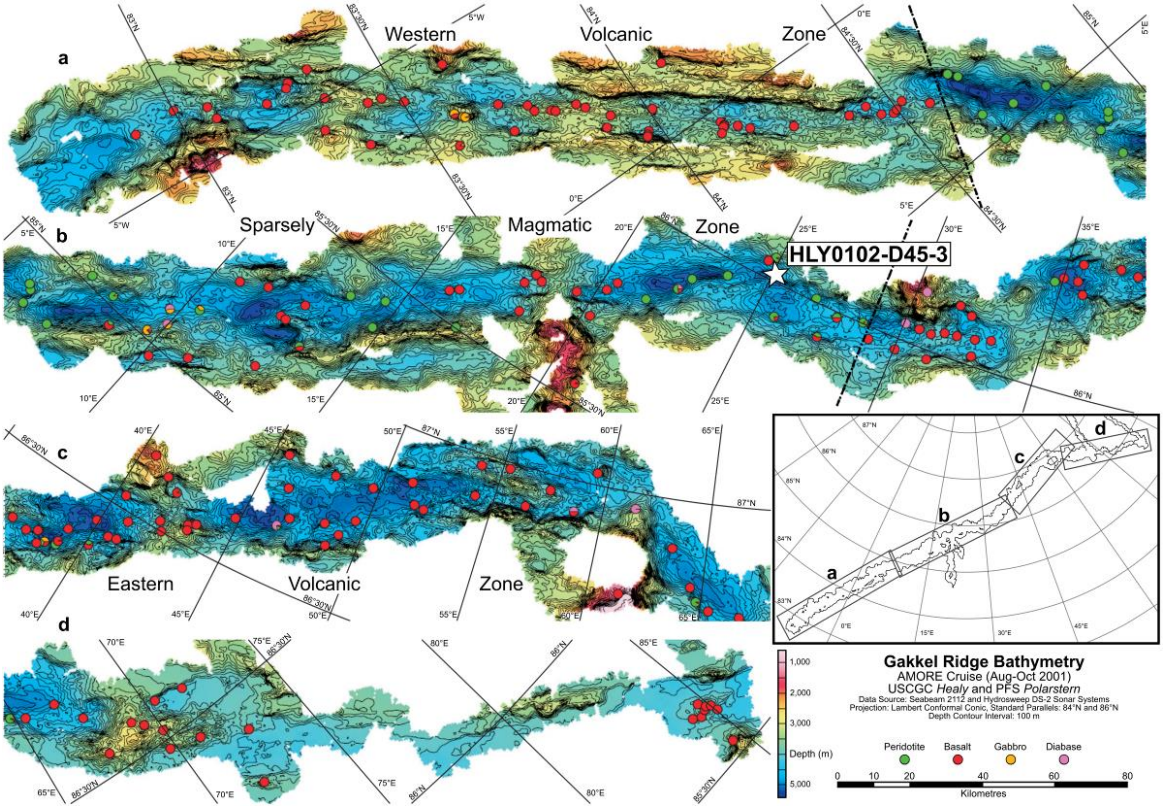

Figure 4.7: A bathymetric map of the Gakkel Ridge separated into the 3 main magmatic zones of the ridge (after Michael et al., 2003). Sampling locations are indicated by circles and colour-coded according to their dominant lithology.

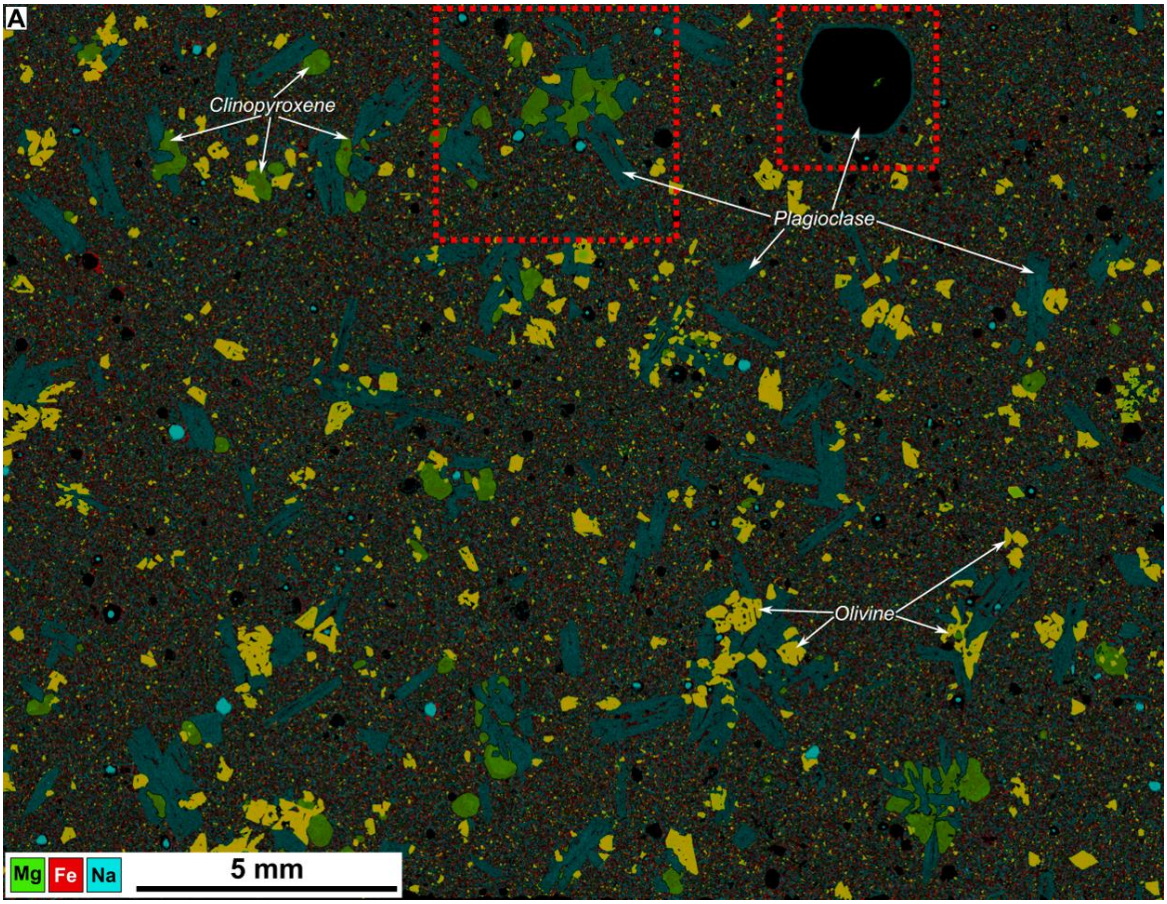

Figure 4.8: A false-coloured, layered element map of a selected portion of the HLY0102-D45-3 sample. As in Figure 4.8, the predominantly black and red regions in the sample are vesicles and cracks containing alteration and products of oxidative weathering. The red boxes indicate the approximate locations of the higher-resolution maps provided in Figures 4.13 (left) and 4.15 (right).

For the overall sample (Figure 4.9), plagioclase is predominantly characterised by an overall narrow range of An variability with a mixture of non-systematic, oscillatory and sector zoning patterns which do not correlate with crystal habit. Such complex zoning patterns were not visible during petrographic analysis of the thin section. A single large phenocryst of resorbed plagioclase with a complex internal zonation pattern and a rim in equilibrium with the bulk plagioclase phenocrysts is present in the upper right quadrant of the element map. Like the plagioclase grains, the clinopyroxene grains span a relatively narrow range of compositions, exhibiting a complex mixture of oscillatory and sector zoning across the sample (discussed below). Although the larger clinopyroxene grains exhibited vague hints of oscillatory zonation petrographically, there was no evidence for such complex zonation patterns in thin section. Very small grains of primarily lower An plagioclase and lower Mg# clinopyroxene are also found to be scattered throughout the matrix material. Olivine grains are found to primarily exhibit minor concentric zoning, even across skeletal morphologies, over a narrow

range of Mg# with the exception of two grains which contain high-Mg# cores and a single phenocryst which contains a lower-Mg# core similar to the average smaller olivines found within the matrix of the sample. These anomalous olivine grains do not appear texturally different from the overall population, and lack any petrographic evidence for such zonation in thin section.

The histogram of An in plagioclase found in Figure 4.10a complements the An maps, revealing a relatively narrow range of An contents across the glomerocrystic clumps and phenocrysts (average ~An_{54}) with the single, large phenocryst of resorbed plagioclase making up the whole of the peak from ~$An_{70\text{-}84}$. We note that the tail of low An displayed in Figure 4.10a is associated with smaller phenocrysts and larger matrix plagioclase. The clinopyroxene grains display a relatively small range of Mg# (average ~69; Figure 4.10b) with the small clinopyroxene grains within the matrix material constituting the low Mg# tail of the primary clinopyroxene peak. Olivine grains are found to have a narrow Mg# range of 72-78 (average ~74; Figure 4.10c) with the two grains exhibiting high Mg# cores represented by barely visible bars between ~84-87 and matrix olivines covering the range between the primary peak and a minimum Mg# of 60.

An element map (4738x4646 pixels) was collected on a representative glomerocrystic clump (left red box in Figure 4.8) under the same conditions as used for the larger map, but with a pixel step size of 5.75 µm (Figure 4.11). Plagioclase (143,749 pixels) and olivine (13,458 pixels) phenocrysts within the clump primarily exhibit oscillatory zoning patterns with narrow ranges of An and Mg# (Figure 4.12a & c) which fall within the range of those seen in the overall section (Figure 4.10a & c). As we noted in the overall map, the matrix plagioclase, which is more readily visible in the glomerocryst map (Figure 4.11), falls towards lower An, constituting the low An tail exhibited in Figure 4.12a. In contrast to the plagioclase and olivine, the clinopyroxene crystals within the clump exhibit primarily oscillatory zoning with evidence for sector zoning occurring within the interior of the larger, oikocrystic clinopyroxene (Figure 4.11b).

A second element map (317x333 pixels) was collected over the large resorbed plagioclase phenocryst (right red box in Figure 4.8) under typical running conditions with a 10 µm pixel step size and a slightly longer dwell time of 30 ms (Figure 4.13). The map reveals a complex zoning pattern in An with a vaguely

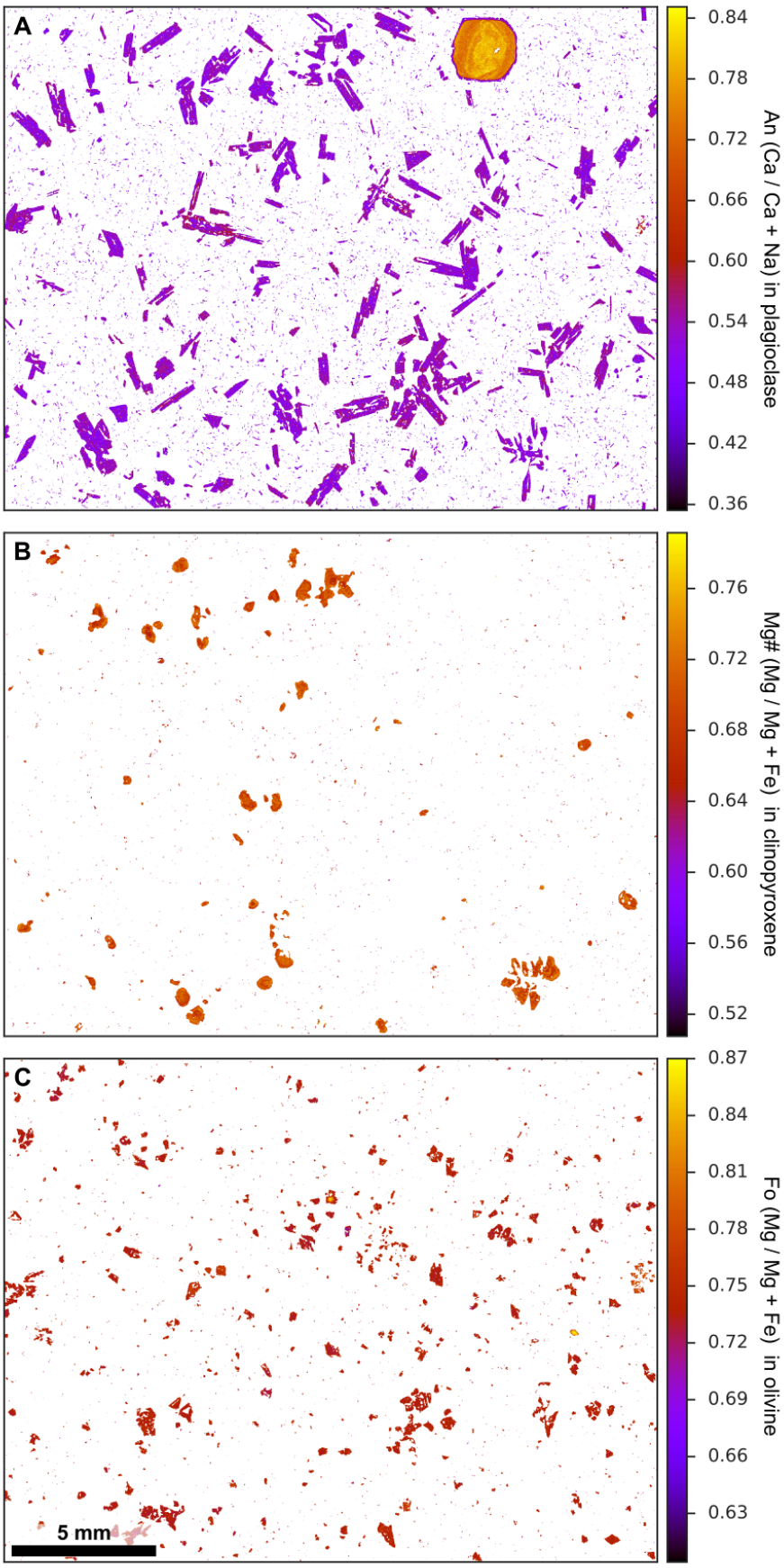

Figure 4.9: Molar ratio maps of (**a**) An in plagioclase and Mg# in (**b**) clinopyroxene and (**c**) olivine calculated from the element map of HLY0102-D45-3 displayed in Figure 4.10.

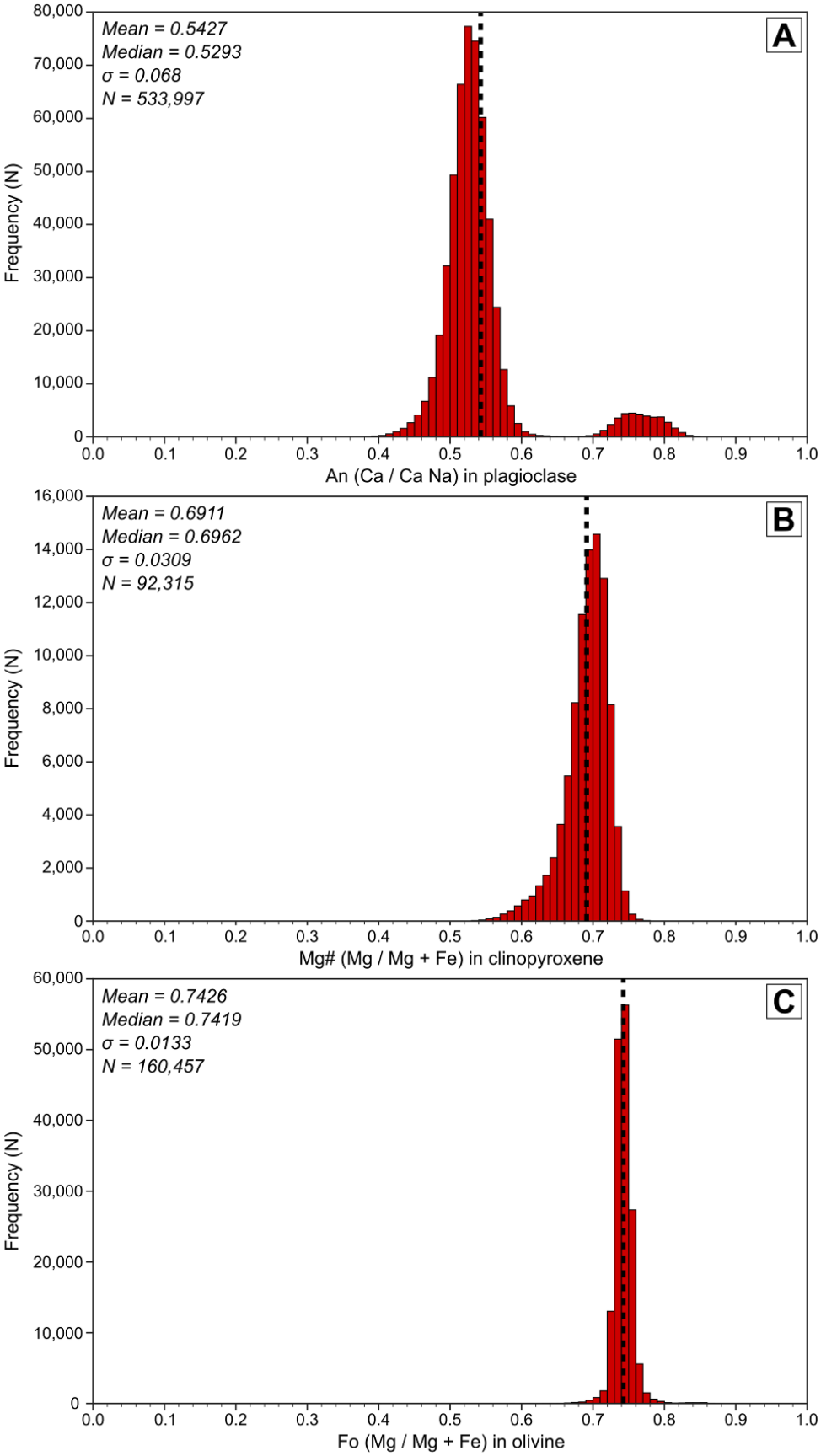

Figure 4.10: Frequency distribution histograms derived from the molar ratio maps of (**a**) An in plagioclase and Mg# in (**b**) clinopyroxene and (**c**) olivine of Figure 4.11.

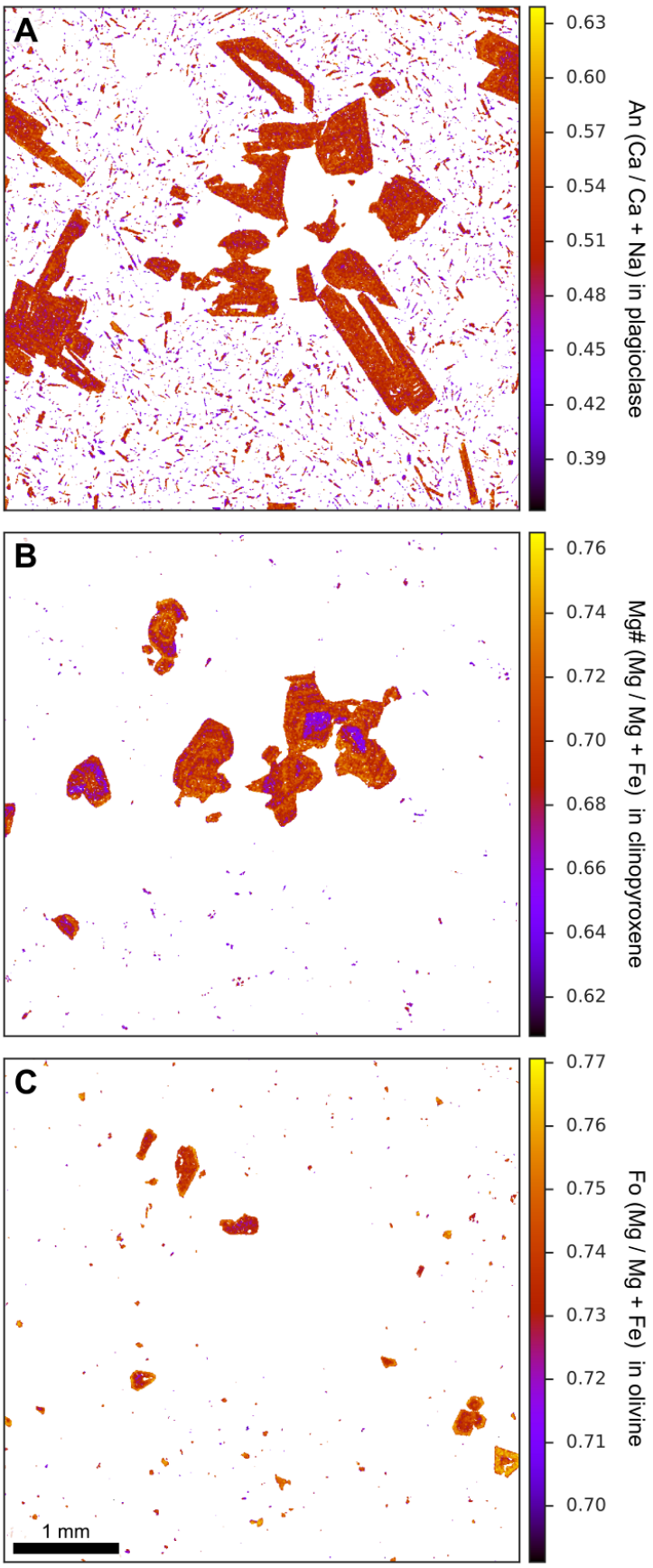

Figure 4.11: Molar ratio maps of (**a**) An in plagioclase and Mg# in (**b**) clinopyroxene and (**c**) olivine calculated for the high-resolution map of a phenocryst clot indicated by the left-most red box in Figure 4.10.

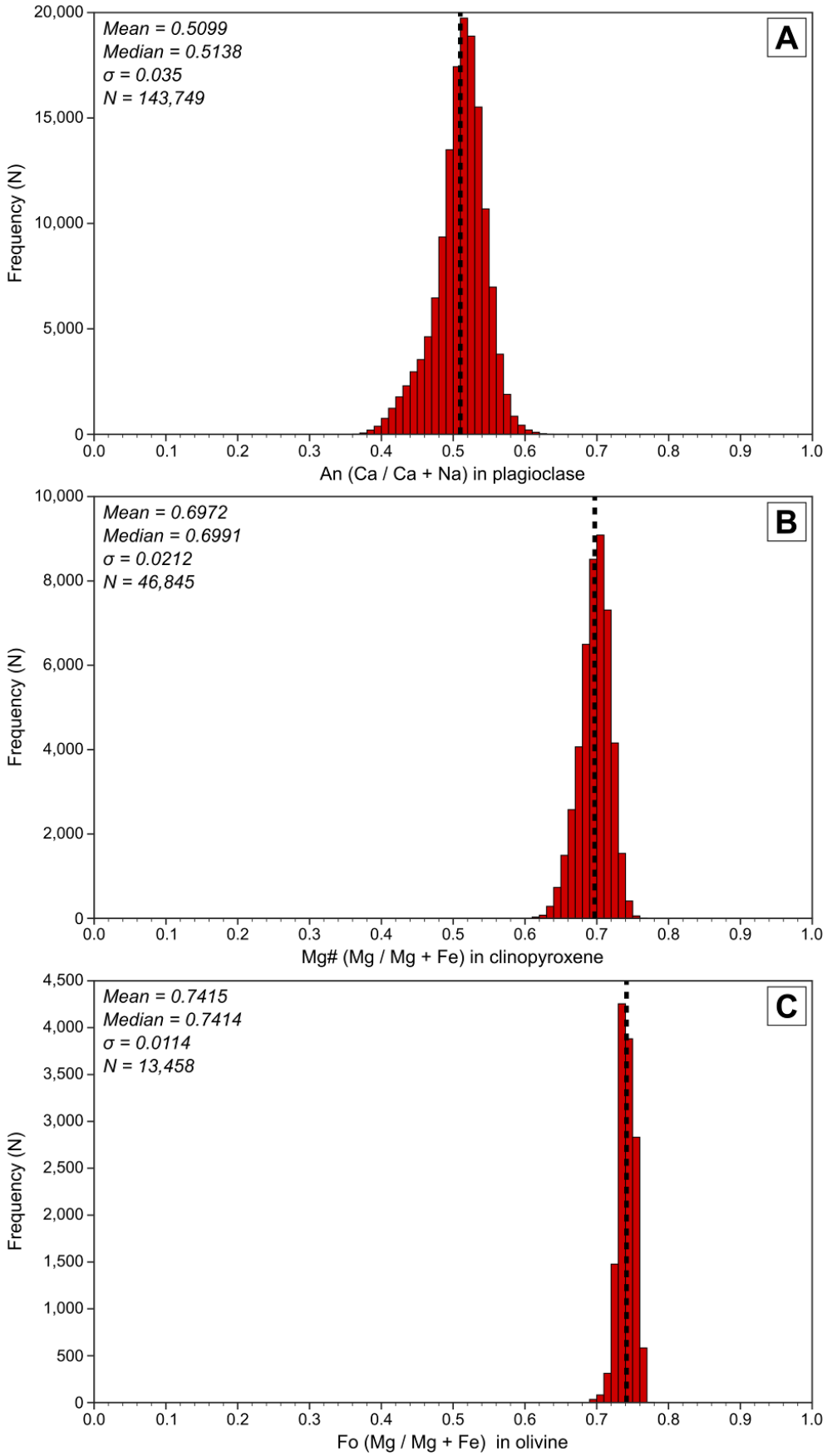

Figure 4.12: Frequency distribution histograms derived from the molar ratio maps of (**a**) An in plagioclase and Mg# in (**b**) clinopyroxene and (**c**) olivine of Figure 4.13.

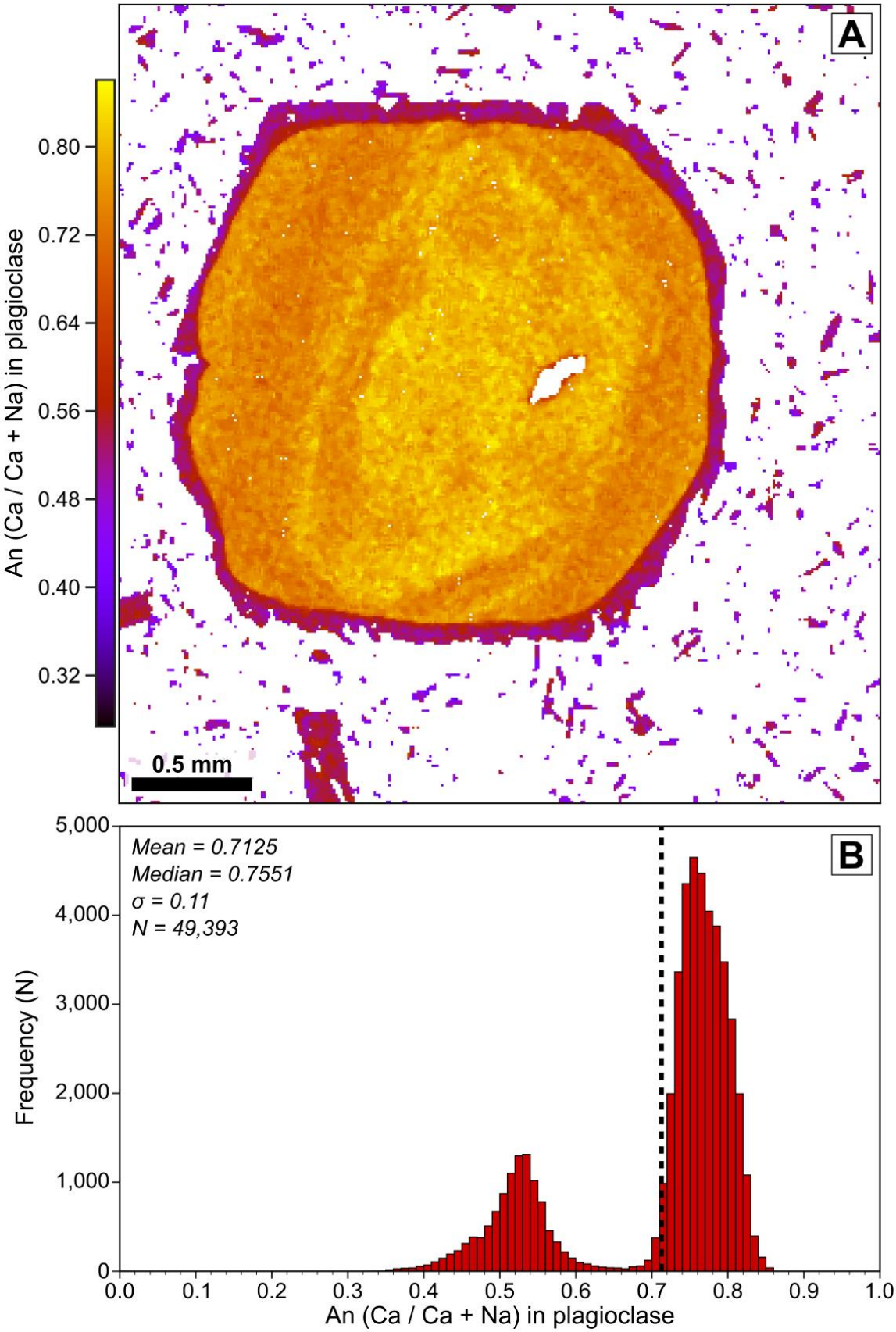

Figure 4.13: Molar ratio (**a**) map and (**b**) frequency distribution histogram of An in plagioclase for the high-resolution map of a resorbed plagioclase phenocryst indicated by the right-most red box in Figure 4.10.

euhedral ~An_{81} core that is concentrically zoned outward towards ~$An_{74\text{-}76}$ compositions. The overall zoning pattern is interrupted by a smooth, rounded, resorbed edge overgrown with a euhedral rim of low An plagioclase (average ~An_{54}) which is in equilibrium with the bulk of the phenocrysts and matrix plagioclase of the overall sample.

The overall relatively homogeneous nature of the D45-3 phenocryst assemblage suggests that the bulk of the phenocrysts are likely derived from the same or similar material to the glomerocrystic clumps. The smooth nature of the transition in molar ratios between the phenocrysts and the matrix materials suggests that they are likely derived from a liquid with a similar composition and petrogenetic history; it is possible that such phenocrysts crystallised from the host magma at depth prior to eruption. The complex nature of the resorbed plagioclase phenocryst suggests that it and the high-Fo olivines are most likely derived from a source which is disparate to that of the bulk of the sample's phenocrysts (i.e., xenocrystic). These xenocrystic grains exhibit overgrowth rims with compositions in equilibrium with the host magma, suggesting that they have resided within the host magma long enough to at least nucleate and crystallise new material. We might interpret these results to suggest that these xenocrystic grains were incorporated by the magma prior to a period of crystallisation where the magma was allowed to cool for long enough to develop larger phenocrysts/glomerocrysts prior to eruption. Regardless of the interpretation of such minor details, we can be certain that the phenocryst populations of D45-3 suggest some form of a longer period of cooling and crystallisation prior to eruption.

The nature of and relationships between crystal morphology, composition and zoning patterns within the D45-3 phenocryst populations is subtle and not readily observable in transmitted light microscopy, a contrast to the readily apparent complexity observed previously in the ALM1 tuff. The relatively narrow range of melt compositions that is expected for MORB magmas means that observations of compositional zoning and textural and morphological relationships between phases from element maps hold more clout over the process of determining the petrogenetic history of a given sample. Observations of compositional and textural variations between phenocrysts and glomerocrysts within the element maps of D45-3 have provided constraints regarding the magmatic (e.g., crystallisation) and mechanical (e.g., incorporation and transport) processes relating to the origin of

the crystal populations in the host magma. In support of the element map observations, the histograms provide us with a quantification of the compositional distribution of the crystal populations within the sample, allowing for us to assess how the compositions of the phenocryst populations relate or differ to that of the host magma.

4.5 Mid-ocean ridge gabbros

Two thin sections of coarse-grained gabbroic rocks have been chosen to illustrate the application of QACD to plutonic rocks. Thin sections 90R-6 126-129 and 80R-7 121 (referred to further as 90R-6 and 80R-7) are an olivine gabbro and oxide-bearing olivine gabbro sampled from ODP hole 735B which drilled 1508 m into gabbroic rocks unroofed at the Atlantis Bank core complex on the slow/ultraslow-spreading (15.7 mm/yr; Baines et al., 2007) Southwest Indian Ridge (Dick et al., 2000). Petrographic analysis revealed that both thin sections contained subtle evidence suggestive of zonation within the plagioclase, but deformation has obscured most of it; therefore, the full extent to which the plagioclase is zoned could not be readily determined in thin section. Further, there was no apparent zonation observed in the clinopyroxene and olivine of both thin sections.

4.5.1 Sample 90R-6 126-129

Thin section 90R-6 (Figure 4.14) is characterised by very large, subhedral to anhedral, granular plagioclase (~10-20 mm long) and olivine (~1-8 mm) with interstitial, anhedral clinopyroxene (~5-15 mm long). Grain boundaries between plagioclase and olivine are noted to be curved. A full-thin section element map was acquired using an accelerating potential of 20 keV, a beam current of 2.5 nA, a pixel dwell time of 20 ms, and a pixel step size of 25 µm (Figure 4.14). The resulting map of 1,125,183 pixels was found to consist of 70.6% plagioclase (794,377 pixels), 10.4% clinopyroxene (116,765 pixels), and 13% olivine (145,709 pixels) with ~6% of the mode being constituted by minor oxide and alteration phases.

Maps of An in plagioclase and Mg# in clinopyroxene and olivine for 90R-6 are provided in Figure 4.15. Contrary to petrographic observations of the sample, the plagioclase grains of 90R-6 are found to exhibit a variety of complex zoning patterns (Figure 4.15a). In fact, the high degree of variation in the geometry and intensity of zoning between individual plagioclase grains suggests that an analyst would have a hard time picking a grain and vector to collect a ‘representative’ profile

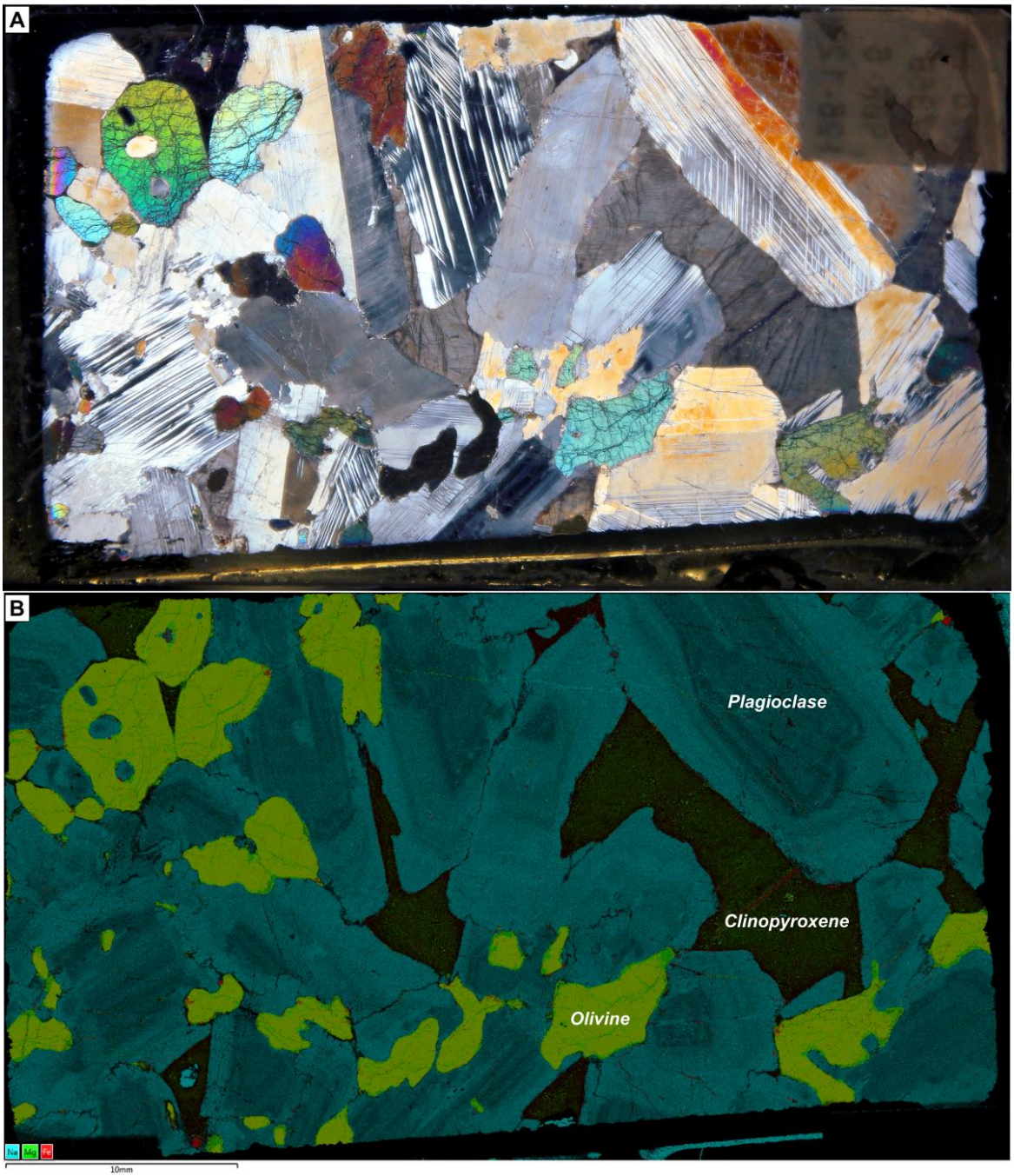

Figure 4.14: A (**A**) cross-polarised light photomicrograph and a (**B**) false-coloured, layered element map of the of 90R-6 126-129 thin section.

from, even with the aid of an element map. The complexity of the plagioclase in 90R-6 provides vital information regarding the magmatic history of the sample and can only be fully appreciated with an element map. In contrast to plagioclase, olivine in 90R-6 exhibits no obvious compositional zonation (Figure 4.15c). The curved olivine-plagioclase grain boundaries are found to often cut across compositional zoning patterns in plagioclase, suggesting that the anhedral olivine grains may have crystallised from a later, reactive intercumulus melt. The 90R-6

clinopyroxenes (Figure 4.15b) are interstitial to both plagioclase and olivine, suggesting that they were the last phase to crystallise. The clinopyroxene exhibits minor compositional zonation within each grain without any obvious preferential geometry, suggesting that this zonation may primarily be related to changes in melt composition associated with normal crystallisation. The element map revealed two compositional features that were invisible in thin section, and would have been unlikely to have been revealed by conventional EPMA studies. First, thin, dark clinopyroxene films observed along some of the olivine and inter-plagioclase grain boundaries in the layered element map for the sample (Figure 4.14) were revealed during processing to be more primitive (higher-Mg# of ~88) interstitial clinopyroxene (lighter-colours regions outlining inter-grain junctions in the left portion of Figure 4.15b). Second, one interstitial clinopyroxene has markedly lower Mg# (~78) than the other clinopyroxenes.

The histograms for the 90R-6 element maps support observations from the element maps for compositionally complex plagioclase and comparatively simple clinopyroxene and olivine (Figure 4.16). Plagioclase is found to range in composition from An_{55-81}, with primary peaks representing the average cores and rims at ~An_{70} and ~An_{62}, respectively. Several of the larger plagioclase with regular, concentric zoning are observed to have thin, higher-An zones occurring approximately at the boundary between their cores and more evolved rims in the element maps, these higher-An zones are represented in the histogram as a small tail skewed towards An_{80}. In contrast, the clinopyroxene (Mg# 75-88, average 83) and olivine (Mg# 78-84, average 81) cover relatively narrow compositional ranges, suggesting that they likely crystallised from smaller batches of interstitial melt within a plagioclase framework that is suggested by the complex zoning patterns to have been derived from multiple melt batches.

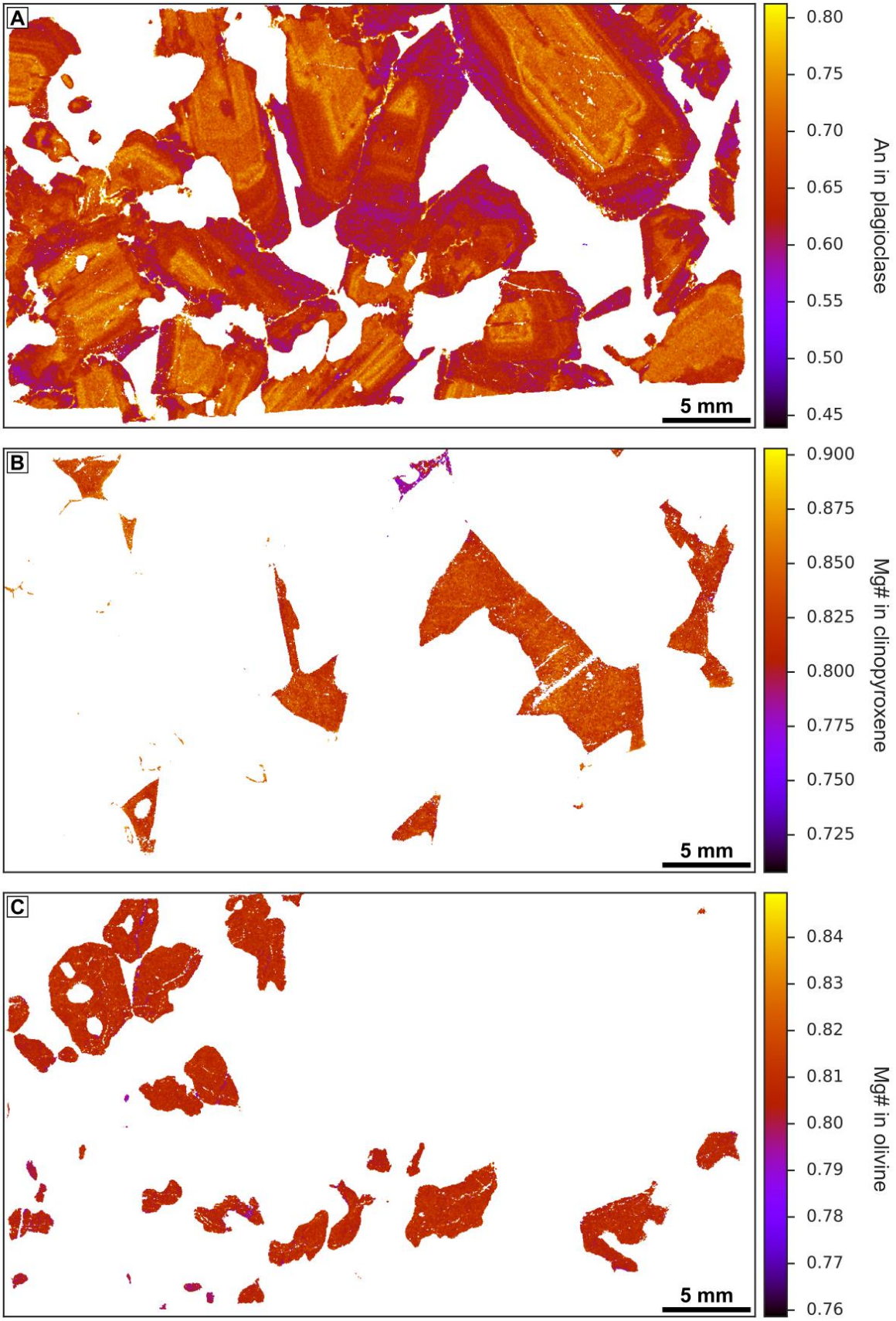

Figure 4.15: Molar ratio maps of (**a**) An in plagioclase and Mg# in (**b**) clinopyroxene and (**c**) olivine calculated from the element map of 90R-6 126-129 displayed in Figure 4.16.

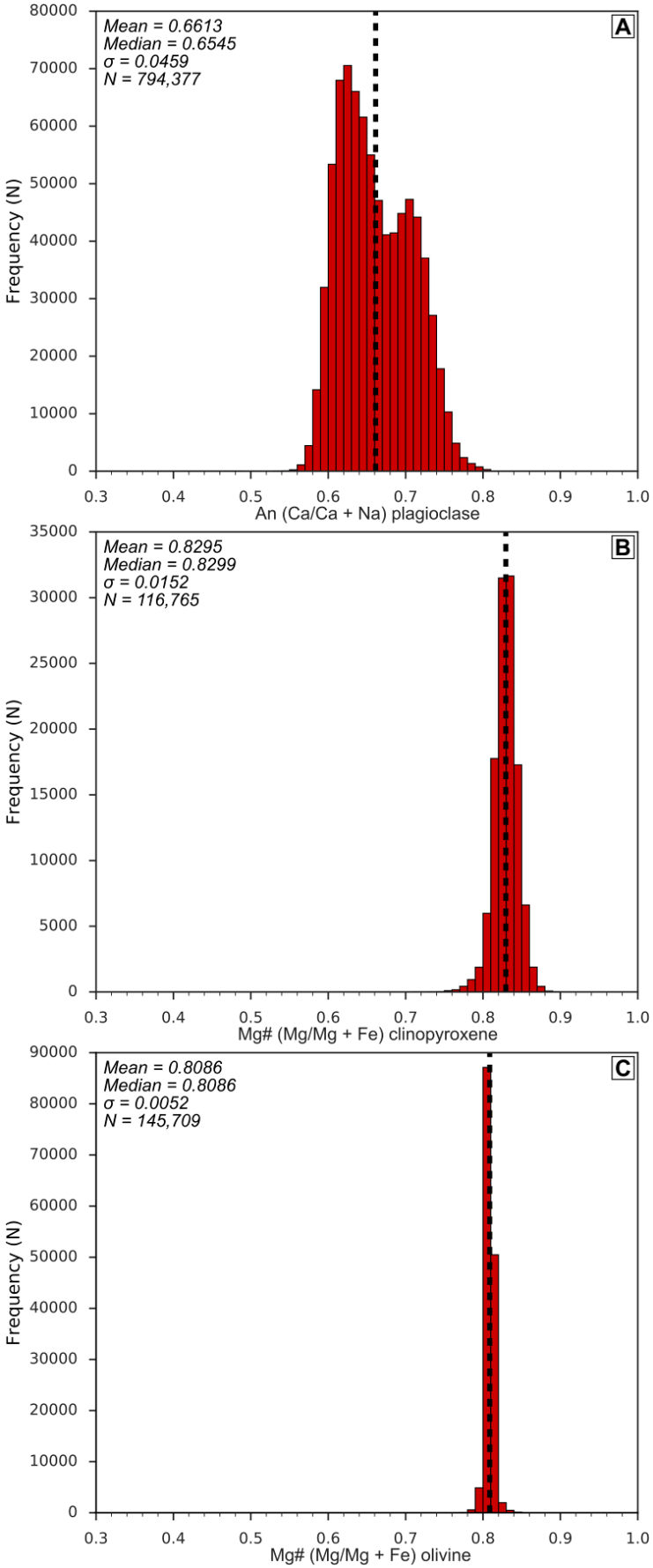

Figure 4.16: Frequency distribution histograms derived from the molar ratio maps of (**a**) An in plagioclase and Mg# in (**b**) clinopyroxene and (**c**) olivine in 90R-6 126-129 presented in Figure 4.17.

4.5.2 Sample 80R-7 121

Thin section 80R-7 (Figure 4.17) is characterised by very large, subhedral to anhedral, granular plagioclase (~5-15 mm long) and intergranular, anhedral to subhedral olivine (~5-7 mm) with granular to intergranular, anhedral to subhedral clinopyroxene (~5-20 mm). A full-thin section element map was acquired of this sample using an accelerating potential of 20 keV, a beam current of 2.5 nA, a pixel dwell time of 20 ms, and a pixel step size of 40 μm (Figure 4.17). The resulting map of 499,552 pixels (447,451 after removing the epoxy) was found to consist of 39.4% plagioclase (176,351 pixels), 38.5% clinopyroxene (172,190 pixels), and 9.5% olivine (42,715 pixels) with ~12.6% of the mode being constituted by oxide, apatite and alteration phases.

A thick zone in the left portion of the thin section contains plagioclase and clinopyroxene which are characteristically more enriched in Na and Fe, respectively. The plagioclase found in this portion of the thin section tends to be more heavily affected by deformation. Oxides (1.5%) and apatites (0.3%) within the sample are primarily associated with the enrichment zone, forming along the periphery of the enriched plagioclase. The Na and Fe enrichment along grain boundaries is observed to decrease in relative intensity with distance away from this zone. In the rest of the sample, straight to slightly curved, well-equilibrated plagioclase-clinopyroxene grain boundaries are observed in contrast to the more chaotic, seriate boundaries and deformation observed within the enrichment zone. Aside from the high concentration of accessory phases and deformation, petrographic observations of the thin section do not suggest any difference in compositional zonation associated with the enrichment zone. The concentration of Na decreases away from the enriched zone, resulting in a gradual increase in the overall plagioclase An. Both olivine and clinopyroxene cut across An zonation in plagioclase, suggesting that these phases reacted with the plagioclase during crystallisation. We see a comparable trend in clinopyroxene Mg# (Figure 4.18b) to An in plagioclase, with Mg# decreasing towards the centre of the enrichment zone (Mg# from ~80 to 60). The core Mg# of clinopyroxene is nearly constant across the sample (Mg# ~80) with all grains exhibiting some degree of zonation towards lower Mg# at their rims. The net intensity of core to rim Mg# zonation in clinopyroxenes decreases with distance away from the enrichment zone and varies relative to orientation, with more intense zonation occurring in grain boundaries which face

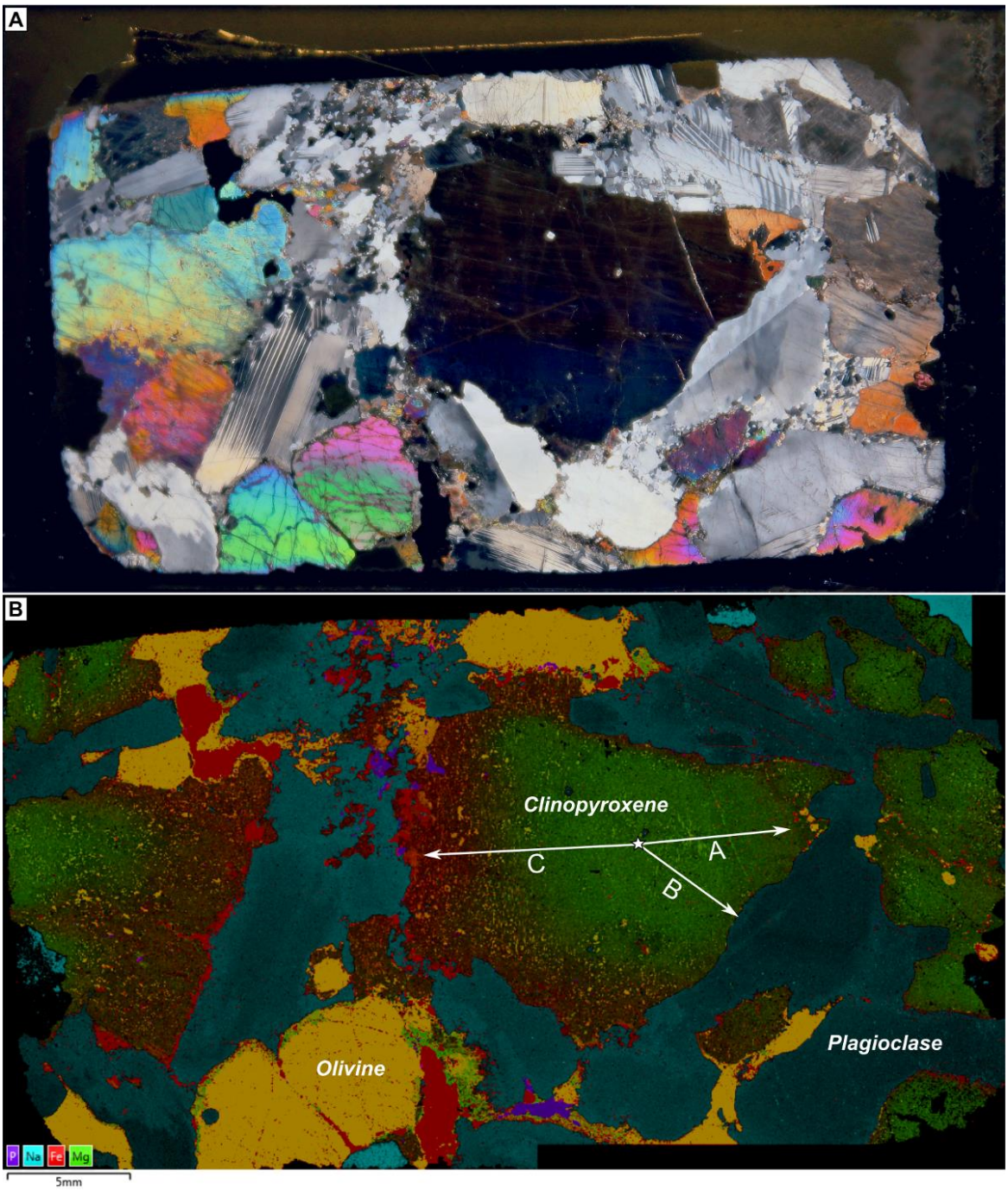

Figure 4.17: A (**A**) cross-polarised light photomicrograph and a (**B**) false-coloured, layered element map of the of 80R-7 121 thin section. White lines A, B and C represent examples of core to rim analysis profiles discussed in the text and plotted in Figure 4.22.

the direction of the enrichment zone (discussed below). Olivine does not display any marked zonation in Mg# within individual grains (Figure 4.18c), but vary between regions of the thin section, with the lowest Mg#s (median ~54) present amongst the most evolved plagioclase and clinopyroxene in the upper-left portion of the section, slightly less-

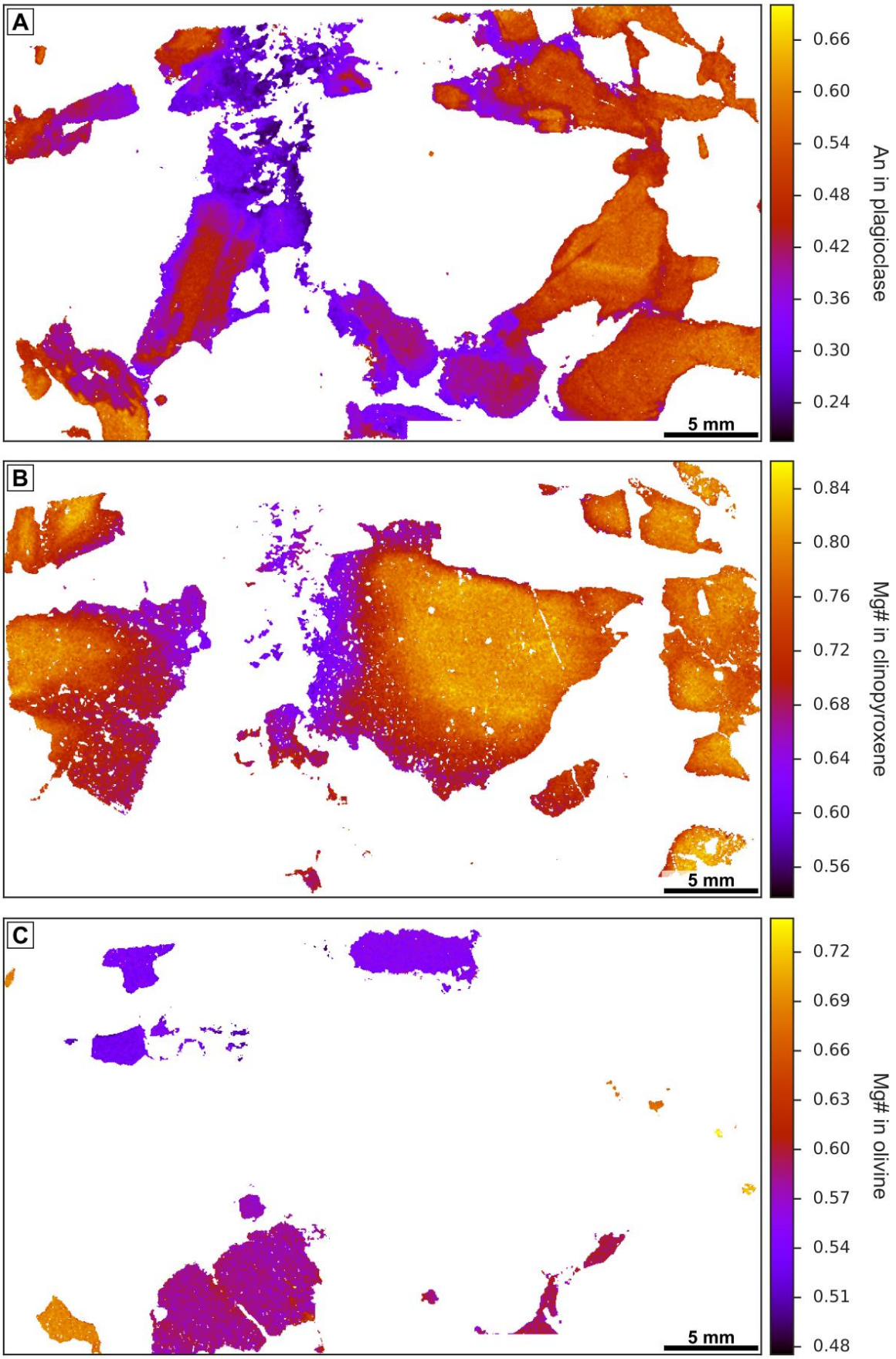

Figure 4.18: Molar ratio maps of (a) An in plagioclase and Mg# in (b) clinopyroxene and (c) olivine calculated from the element map of 80R-7 121 displayed in Figure 4.19.

evolved Mg#s (median ~58) associated with correspondingly less-evolved plagioclase and clinopyroxene in the lower and middle portions of the section, and the most primitive Mg#s (median ~68) being found in grains associated with the 'normal' portions of the sample outside of the periphery of the enrichment zone.

Plagioclase is found to exhibit gradual, concentric zonation in An which is most apparent in the right portion (~An_{60} to An_{48}) of the thin section (Figure 4.18a). Both the minimum and bulk An of plagioclase grains is observed to plummet within the left portion of the thin section (~An_{40} to An_{30}), reaching its lowest values in the upper-left portion of the thin section (~An_{25}) where the concentrations of accessory and alteration phases become most abundant. As in the layered element map, the

Histograms of the ratio maps (Figure 4.19) exhibit comparatively complex compositional distributions over a wide range of compositions, with overall plagioclase An ranging between $An_{20\text{-}65}$ and Mg# in clinopyroxene and olivine ranging from 57-85 and 48-74, respectively. Overall, the histogram of An in plagioclase reflects the transitional nature of An across the sample with the four main peaks reflecting the gradual step down in the average core An composition for each of the compositional zones from the outer portions of the sample (peak at ~An_{52}), into the edges of the enrichment zone (slight peak at ~An_{48}), the bulk of the enrichment zone (peak at ~An_{39}), and the most evolved portion in the centre of the enrichment zone (peaks at ~An_{34}). The compositional segmentation in olivine Mg# observed between the regions of the section is reflected in the corresponding histogram, with peaks at Mg#s of ~68, 58, and 55 reflecting the transition from the less-affected portions of the sample gradually into the core of the enrichment zone. The histogram of Mg# in clinopyroxene reflects the overall distribution of similar Mg# cores across the sample (peak at Mg# ~80) with a second peak (Mg# ~69) representing the average or most abundant rim composition across the sample. The most extreme evolved rims found immediately adjacent to the enrichment zone are represented by the tail that is skewed towards lower Mg#s on the left side of the secondary peak.

We interpret the enrichment zone in the sample to represent a pathway for the focused transport of evolved melt which reacted with the surrounding gabbroic material to produce highly evolved (i.e., low An and low Mg#) plagioclase, clinopyroxene, and olivine and an abundance of accessory oxides and apatites. The effects of this reactive process diminish with distance away from the primary

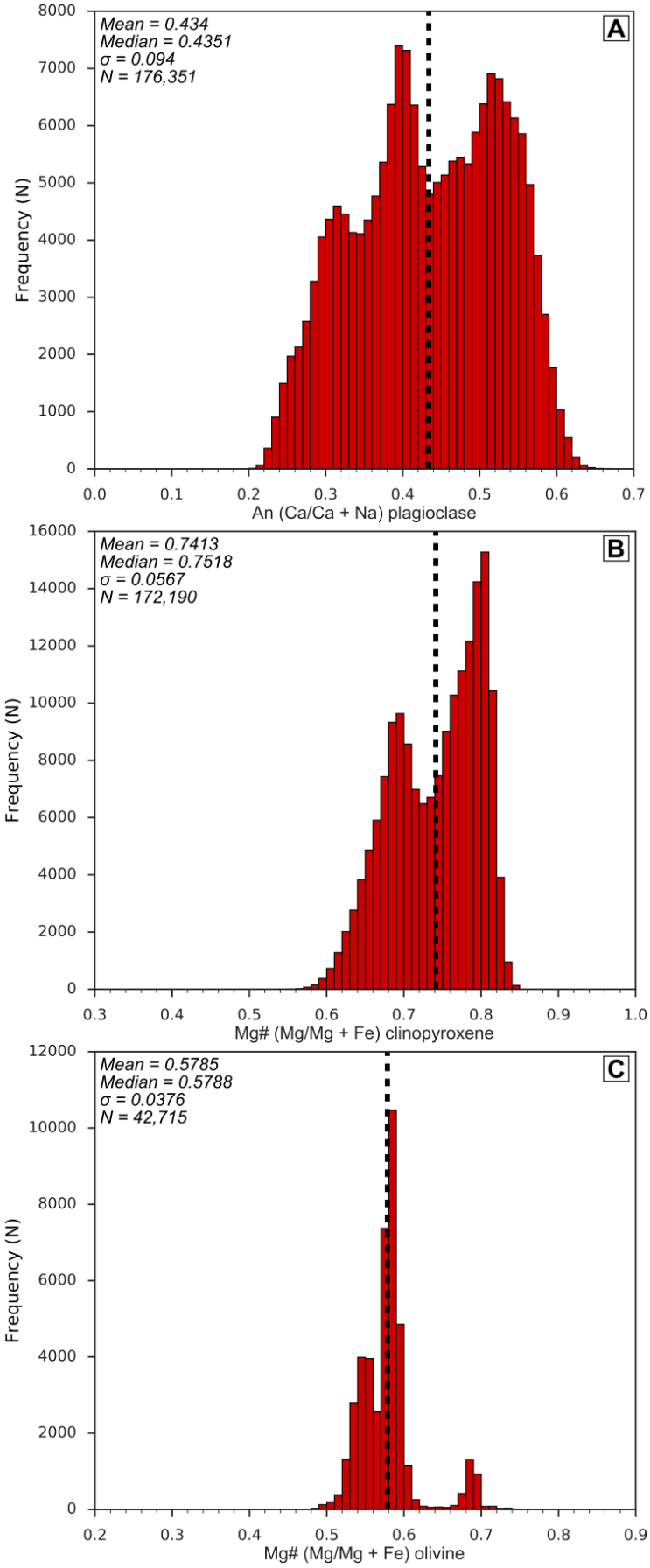

Figure 4.19: Frequency distribution histograms derived from the molar ratio maps of (a) An in plagioclase and Mg# in (b) clinopyroxene and (c) olivine in 80R-7 121 presented in Figure 4.20.

reaction zone, resulting in a range of zoning profiles across grains. This is most apparent in the large clinopyroxene grain at the centre of the element map. The white lines labelled A, B, and C in Figure 4.17 represent 3 possible vectors that could be chosen for collecting representative zonation profiles for the sample based on petrography only. The results of these profiles for Mg# in clinopyroxene are provided in Figure 4.20 where it becomes apparent just how evolved the rims adjacent to the reaction zone have become. The lack of evidence for compositional zonation in transmitted light microscopy of the sample means that without the aid of an element map, an analyst would need to rely on choosing the most optimal vector from core to rim in relation to the grain shape, likely resulting in profiles A and B due to presence of less alteration on the right side of the grain. Profile A maximises the distance covered to the outer extensions of the grain covering a range of Mg# between 82 and 75 over a distance of ~8 mm, while profile B follows the shortest path to the grain boundary with a range of Mg# between 82 and 78 over a distance of ~5.5 mm. In contrast, profile C covers a wide range of Mg# between 82 and 66 over a distance of ~10 mm. Simple probing based on petrographically-determined optimal analytical locations has a significant chance of missing the presence of the melt-rock reaction feature within the 80R-7 sample. Similar to sample 90R-6, even with representative profiles like that of profile C in Figure 4.20, the analyst would lack the appreciation for the degree of compositional and textural complexity and variability for the sample. This is best illustrated by the olivine grains, of which each has a different composition and lacks any zonation. If a thorough petrologist had probed each of the olivine grains, they would not know how to appropriately interpret the results without some sort of context. The element maps provide the analyst with contextual information which is key to appropriately interpreting a sample.

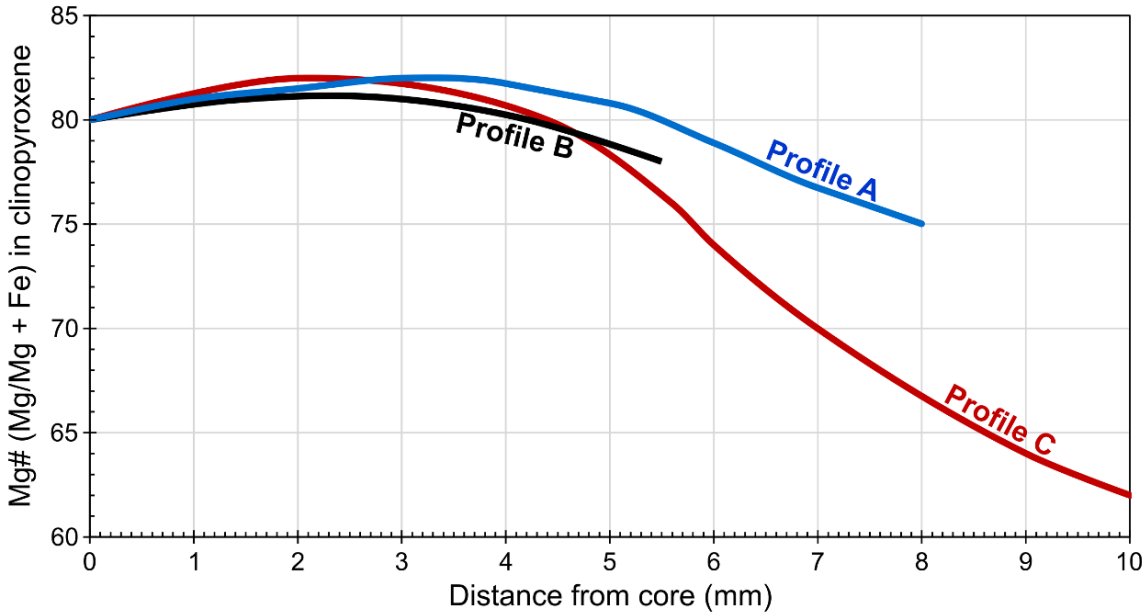

Figure 4.20: Representative core to rim profiles of Mg# in clinopyroxene derived from vectors indicated by white lines in Figure 4.19.

4.6 Discussion

The QACD method offers a number of important advantages over conventional microanalysis by EPMA, which are critical in the interpretation of igneous rocks: 1) it reveals the full range of mineral compositions present; 2) it reveals the complete variability in zoning patterns present; 3) it provides textural context for the variations in compositions and zoning patterns; 4) it is statistically rigorous, precluding bias. These four advantages are discussed in turn below using examples from this study.

4.6.1 Full range of mineral compositions

Each sample which we have applied the QACD method to has been revealed to contain primary mineral phases which cover a range of compositions and typically display some degree of variability across the sample. A volcaniclastic sample like the ALM1 tuff is expected to have incorporated crystals and clasts from a wide range of source compositions. In such samples, a thorough characterisation of the sample can provide important constraints on both the total range of source compositions of the source material incorporated into the tuff and the compositions of the sources which contributed the bulk of the material to the sample. This is illustrated by the histogram of An in plagioclase for the ALM1 sample (Figure 4.5c) in which we observe that the entire compositional range found in the sample covers $An_{16\text{-}94}$ with the bulk of the distribution falling around three primary peaks at An_{78},

An_{69}, and An_{55}. We interpreted the full range of the ALM1 An in plagioclase to indicate that it is sampling materials from across the full magmatic history of the Rodalquilar caldera complex with the primary peaks (as well as a clast and crystals from a tholeiitic basalt) indicating primary sampling of the basaltic stage of the caldera.

4.6.2 Complete variability in zoning patterns

The element map collected for the 90R-6 126-129 gabbro is an example of a sample which exhibited little petrographic evidence for compositional zoning (partly obscured by deformation) or even compositional variability across the sample, but was revealed through element mapping to exhibit extremely complex zoning patterns for An in plagioclase (Figure 4.15a) which varied substantially between individual grains. Such samples cannot be accurately represented by a handful of petrographically-chosen analytical profiles, and thus require the collection of a full-thin section quantitative element map in order to fully appreciate the nature and degree of complexity in compositional zoning for the sample.

4.6.3 Textural framework

Sample 80R-7 121 is an example of a sample which can easily be misrepresented by careful choosing of representative locations by an analyst, and thus requires a thorough assessment of the compositional variability for the sample in order to fully appreciate its complexity. This was partly illustrated by the representative line profiles in Figure 4.20 which found that the full range of compositional zoning in the clinopyroxene was revealed only by choosing a profile in the opposite orientation to those deemed appropriate according to petrographic observations. The resulting histograms for 80R-7 allow for the user to track the bulk changes in mineral compositions as seen in the element maps between the normal portions of the sample and the gradually more evolved, melt-rock reacted portions of the sample. The need for textural context is best illustrated by the nature of the olivine grains in 80R-7 121 (Figure 4.18). As we previously noted, a thorough petrologist might probe each of the olivine grains, finding that each one has a different composition and lacks any zoning without any context. It is only by collecting an element map that the analyst has the true context of how a particular grain or composition relates to the overall sample, thus facilitating an appropriate interpretation of the data.

4.6.4 Statistically rigorous

Element maps such as those presented above provide information which is valuable in determining both the quantitative (e.g., histograms) and qualitative (e.g., molar ratio maps) nature of compositional distributions within and across geologic samples. For example, such information can prove valuable in determining whether oscillatory zonation in a plagioclase crystal is the result of either large-scale, repeated changes in externally controlled growth conditions or kinetic effects at the crystal-melt interface; two types of processes with distinct implications for growth environment dynamics (Pearce, 1994; Ginibre et al., 2007). This suggests that although element maps are, in themselves, a visually powerful tool for the examination of elemental distributions over large areas, the information which they provide can be misleading to the human eye when examined from a qualitative point-of-view.

Consider the map of An in plagioclase presented in Figure 4.1: the eye is naturally drawn to the large, high An grains of the sample, and thus one might predict that such compositions would constitute a significant portion of the sample and form a large peak when compared with the rest of the plagioclase in the map. Although the histogram for that map, which is displayed in Figure 4.2, does exhibit a peak for those high-An grains, that peak is not so large as to eclipse the rest of the sample in the histogram. We critically note that, more often than not, during the development of the QACD technique, we found ourselves making such mistakes and over-estimating our own predictions of the modal proportions of specific compositional ranges and features present in element maps. Such a mistake as this can lead to a preferential choice by a user to only analyse specific portions of the map that may stand out from the rest of the sample (e.g., high An cores and low An rims), but may not be fully representative of the sample as a whole. If a user were to carry out point analyses on just the extremes of An composition for the mapped plagioclase phenocrysts in Figure 4.2 (i.e., means of ~An_{69} and ~An_{80}), then the resulting data would fail to reveal the presence of a second major peak at $An_{69.6}$, which is actually the major peak of the sample, and the general nature of the transition between the extreme ends of An zonation. For example, if we consider the range of An found in the phenocryst cores (i.e., $An_{74.5\text{-}83.5}$), then analyses of the phenocryst cores would only be representative of ~17% of the

plagioclase present in the sample (i.e., 82,378 pixels out of the total 472,960 plagioclase pixels in Figure 4.1).

The potential for bias in the choice of targets for spot analysis is effectively removed by treating every pixel of a quantitatively-optimised element map as a single analysis. Further, by quantifying element maps for useful element ratios, like An, and deriving histograms of the data, vital information can be gleaned regarding both the map-scale variations in chemical zonation and crystal morphologies, inherently qualitative features which invite error on the part of human operators, and the relationship of such chemical variations to the overall distribution of chemical populations within the sample.

4.7 Conclusions

Element mapping is critical in reconstructing the full histories of igneous rocks. We have demonstrated here that QACD provides four major distinct advantages over conventional element map processing, (i) providing a statistically rigorous method, precluding operator bias, for revealing (ii) the full range of mineral compositions and (iii) the extent and distribution of compositional zoning (iv) within the textural context of the sample. Although we have primarily presented applications for the QACD method with respect to primary mafic phases (e.g., plagioclase, pyroxene, olivine), the application of the method is not limited to these phases. We have included corrections for oxides and garnets in the QACD software which allow for its application to other rock types, including metamorphic rocks. The ability of the software to be easily modified and adapted means that new applications for the QACD method can be developed by users.

CHAPTER 5
The paradox of the axial melt lens at fast-spreading mid-ocean ridges

5.1 Introduction

Here we present the first comprehensive study of the AML horizon at a fast-spreading MOR (Hess Deep, equatorial Pacific Ocean). We show that plagioclase and pyroxene within the AML are much too evolved to be in equilibrium with MORB, with mean An (54.85) and Mg# (65.01) consistent with derivation from basaltic andesite to andesite melts (Mg# 43-26). Primitive compositions (i.e., An≥80 and Mg#≥85) are critically under-represented within the AML, constituting ~0.26% of plagioclase and ~0.02% of pyroxene. We propose that, in between decadal eruptions, the AML is predominantly crystal mush and is fed by small volumes of evolved interstitial melts. Short-lived, focused injection of primitive melt leads to mixing of primitive melts with the extant highly fractionated melt, and triggers eruptions. This model reconciles the paradoxical compositional mismatch between the volcanic and plutonic records with the geophysical characteristics of the AML, the short residence times of Pacific MORB phenocrysts, and the incompatible trace element over-enrichments in MORB.

5.2 Methods

The JC21 Dive 78 hand samples are varitextured to the degree that they cannot be fully represented by a single 2.8 x 4.8 cm thin section. Seventeen (three dolerites and fourteen gabbronorites) of the twenty-three samples collected by dive 78 were slabbed for subsampling. A series of locations which adequately represented the range of textural variability of each sample were mapped onto the surfaces of the slabs (Figure 5.1) and cut to produce thin sections for microanalysis. A total of sixty serial thin sections were produced from the seventeen slabbed samples. The number of serial thin sections cut from each sample varied according to its degree of textural variability. For example, one to two sections were cut for samples which exhibited markedly lower degrees of textural variability while some of the most variable samples had six or seven sections cut from them.

5.2.1 The QACD method

The complex nature of the dive 78 samples presented a challenge for documenting the full range and distribution of compositions within the AML at Hess Deep by traditional microanalytical techniques (e.g., point by point EPMA analysis).

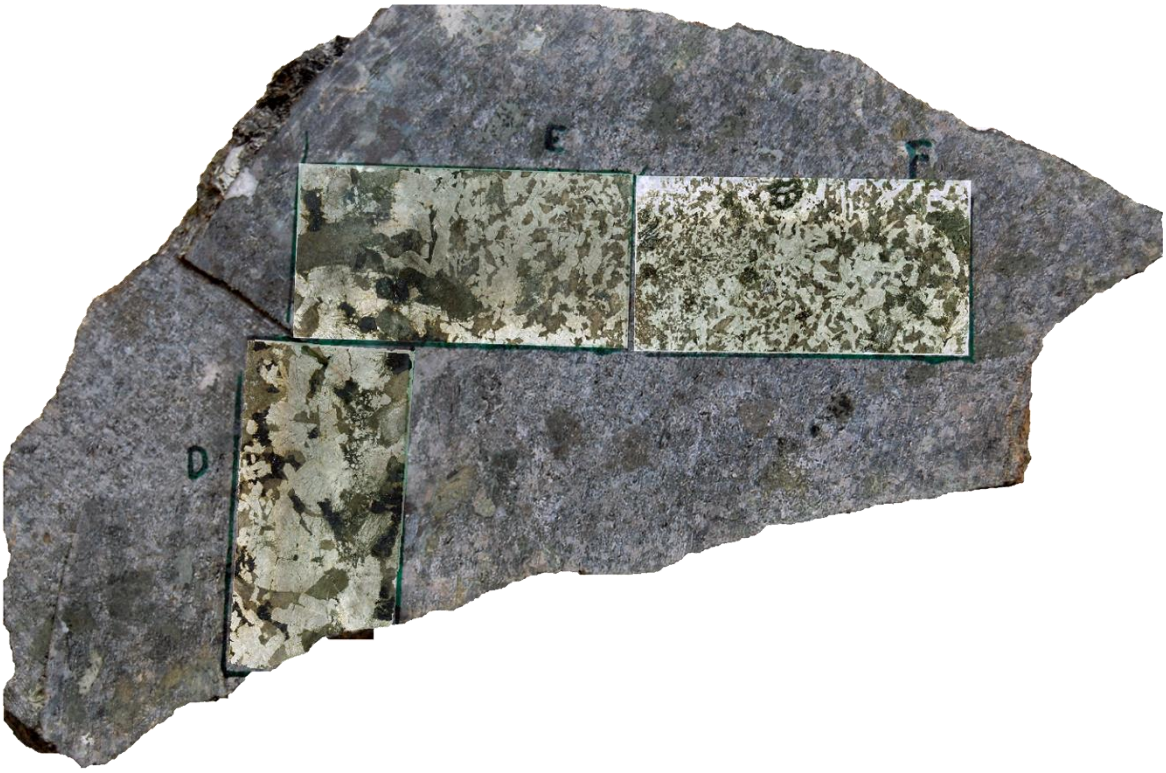

Figure 5.1: A photograph of the slab from which thin sections 78R-5D, 78R-5E, and 78R-5F were samples. Photomicrographs of the serial thin sections have been superimposed the slab to illustrate their original orientation and the range of textural changes exhibited across the sample.

To obtain a rigorous characterisation of the composition of the AML horizon at Hess Deep, we have developed a methodology for the collection and processing of full thin section quantitative element maps (see Chapters 3 & 4) (thin section ratio maps and frequency distribution histograms are provided in the electronic appendices of this thesis).

A total of thirty-four thin sections across seventeen samples from the dive 78 suite were deemed appropriate for element mapping based on petrographic observations (i.e., minimal alteration and satisfactory polish). Full thin section quantitative multi-element maps were collected on a Zeiss Sigma HD analytical scanning electron microscope equipped with two 150 mm^2 active area EDS detectors in the School of Earth and Ocean Sciences at Cardiff University. Typical pixel step-sizes of 25 µm with a dwell time of 20 ms and a minimum output count rate of 200,000 counts per second were used. The resulting element maps were post-processed using a python-based script (i.e., the Quack software; see Chapter 3 for a description of the method).

In order to track the degree of evolution of the melts parental to the AML gabbros, we have focused on An (=Ca / [Ca + Na] in plagioclase) and Mg# (=Mg /

[Mg + Fe] in clinopyroxene). The precision of An and Mg# calculated by this method have been determined on plagioclase and diopside standards to be ~3 and 2 mol% (2σ), respectively. Phase masks for plagioclase and pyroxene were calculated from the element maps using simple IF/AND/OR statements to classify each mineral. The resulting phase masks were used to segment calculated molar ratio maps of An and Mg# for plagioclase and pyroxene respectively. Histograms with 0.01 (i.e., 1 mol%) wide bins were calculated for each map and combined to produce bulk sample histograms and a bulk AML histogram. The corresponding ratio maps and frequency distribution histograms for the individual samples are provided in the electronic appendix.

5.2.2 Modelling melt differentiation

A series of fractional crystallisation models were carried out to investigate and parameterise the relationship between An in plagioclase, Mg# in clinopyroxene and the corresponding Mg# of the parent melt. Using MELTS (Ghiorso and Sack, 1995), fractional crystallisation models of a least-squares regressed parental EPR MORB composition (Lissenberg et al., in revision), all assuming perfect fractional crystallisation, were carried out with oxygen fugacities between the quartz-fayalite-magnetite buffer and 1 log unit below at 1 kbar under dry conditions.

5.3 Results

Petrographic analysis (see Table A.1) of the sixty serial thin sections reveals that the varitextured nature of the hand samples is often reflected to a further extent both within and across serial thin sections. Sample 78R-6, for example, was described in handsample as a medium grained, equigranular disseminated oxide gabbro with moderate to strong magmatic foliation lacking any obvious textural variability. In fact, serial thin sections 78R-6A, 6B and 6C were found to contain 3 identifiable textural domains and rare olivine grains (up to 5-7 mm) (see Figure 5.2 for descriptions of the domains). The degree of textural variability exhibited by sample 78R-6 on the scale of a single thin section, though a little less than most, is qualitatively representative of the dive 78 samples analysed by this study.

The An and Mg# maps produced from the dive 78 thin sections represent a total of more than 13 million and 12 million spot analyses of plagioclase and pyroxene, respectively. An average of 400,000 pixels of plagioclase and 350,000 pixels of pyroxene where analysed in each thin section which, using a 25 um pixel

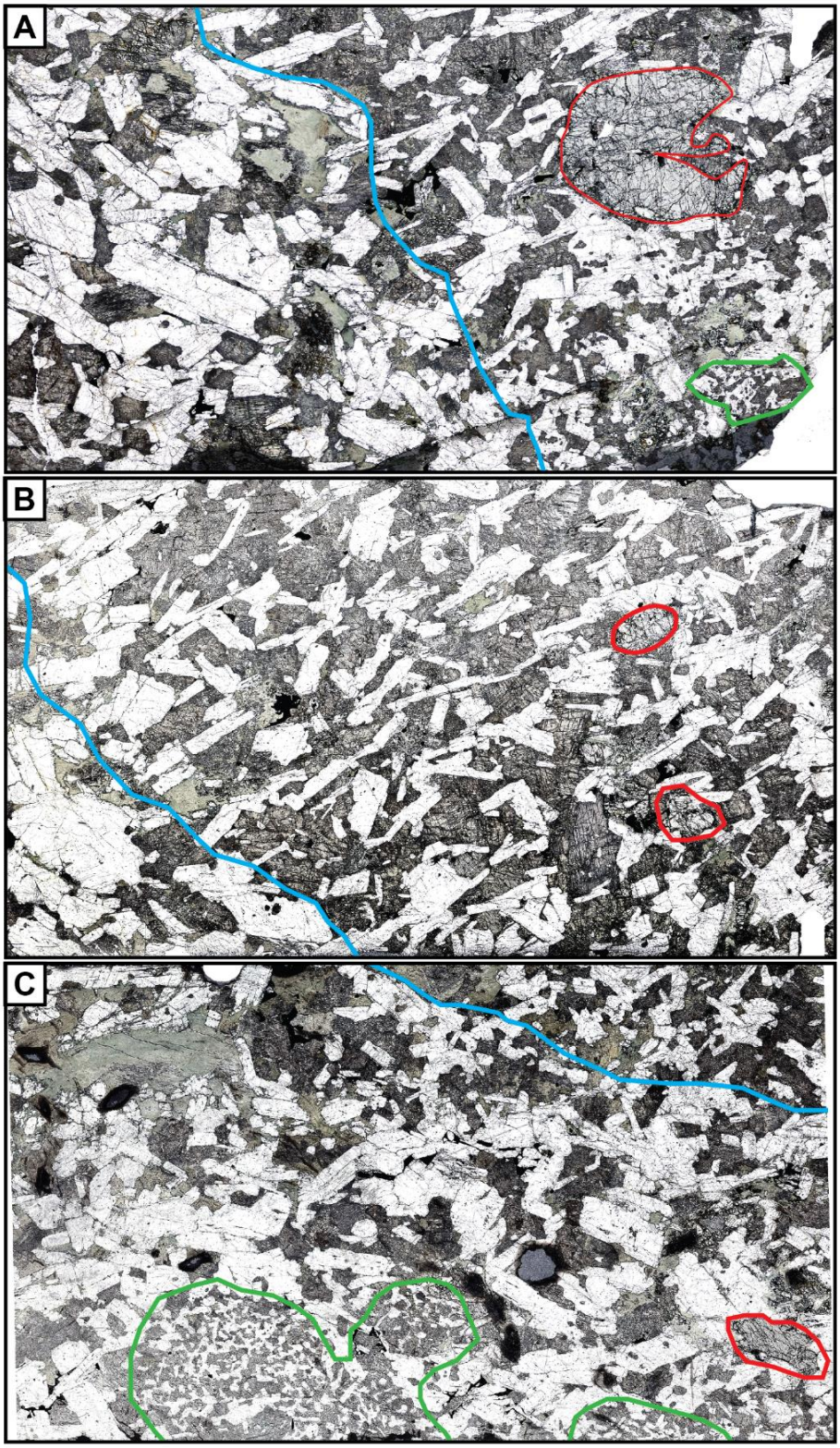

Figure 5.2: Photomicrographs of serial thin sections (**A, B** and **C**) for 78R-6, a disseminated oxide olivine-bearing gabbronorite which reflect the average range of variability encountered in the gabbroic rocks of dive 78. Isolated grains of olivine (outlined in red) occur dispersed throughout the sample. The blue line demarks a textural change between a domain of large, blocky plagioclase with a weak to moderate foliation towards the top left of the thin sections and a more pyroxene-rich domain containing long, acicular plagioclase with a strong foliation towards the bottom left of the sections. Rounded hornfelsic domains composed of equigranular plagioclase and clinopyroxene (outlined in green) can be found in some of the Dive 78 samples exhibiting sharp, non-gradational contacts with the surrounding material.

step-size translates to approximately 250 and 220 mm^2, respectively. In the case of plagioclase, for a specific composition to represent 1%, 5% or 10% of the sample it would need to constitute ~2.5, 12.5 or 25 mm^2 of the mapped plagioclase. Similarly, for a specific pyroxene composition to represent 1%, 5% or 10% of the sample it would need to constitute ~2.2, 10.9 or 21.9 mm^2 of the mapped pyroxene. Extrapolating to the bulk of the AML, for a plagioclase composition to represent 1%, 5% or 10% of the AML it would need to constitute ~81.25, 406.25 or 812.5 mm^2 while a pyroxene composition would need to constitute ~75, 375 or 750 mm^2 across the analysed samples.

There is no evidence to suggest that there is any systematic compositional variability between textural domains in a majority of the thin sections. This is reflected in section 78R-6A where the molar ratio maps of An (Figure 5.3A) and Mg# (Figure 5.3B) exhibit no apparent variation between the three textural domains highlighted previously in Figure 5.2A. Plagioclase is consistent across the 78R-6A textural domains with normal binary zoning between an ~An_{58} core and an ~An_{50} rim (Figure 5.3C) while pyroxene mostly have an average Mg# of 72.5 (Figure 5.3D) with occasional larger grains exhibiting zoning towards a more primitive core. This would seem to suggest that the various textural domains encountered at the scale of a thin section are likely derived from the same melt or melts of similar composition by varying physical processes. The only samples which exhibit any systematic compositional variability between textural domains are those which contain pegmatite veins. The pegmatite veins in samples like 78R-5x4B (Figure 5.4) tend to be significantly evolved and often exhibit a strong gradation towards more primitive compositions away from their margins and into the rest of the sample.

Sample 78R-14, like 78R-5x4B, contains a prominent pegmatite vein which is more evolved than the surrounding gabbroic material (Figures 5.5 and 5.6). The evolved pegmatite vein in 78R-14A is represented in Figure 5.5C by a large peak at ~An_{45}. The main distinguishing characteristic between the pyroxene in the pegmatite and the rest of 78R-14A is the presence of a lower Mg# peak at ~50 (Figure 5.6C) which corresponds to small purple pixels adjacent to patches of alteration in the molar ratio map (Figure 5.6A). Section 78R-14E (Figure 5.5B and 5.5D) was sampled away from the pegmatite vein and exhibits a main peak around ~An_{54} for the matrix material and slight zoning towards more evolved compositions

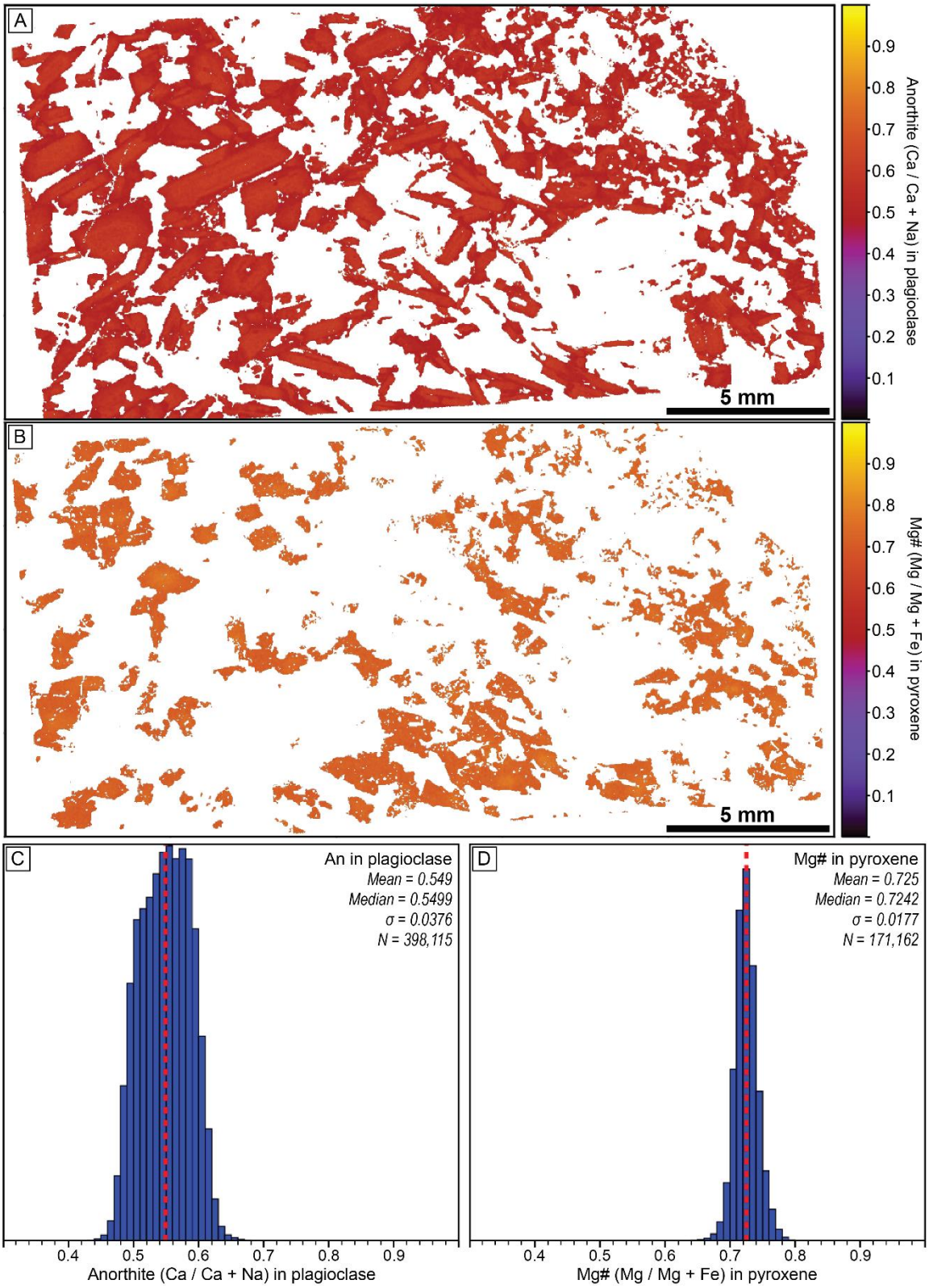

Figure 5.3: Molar ratio maps of (**A**) An in plagioclase and (**B**) Mg# in pyroxene derived from thin section 78R-6A and their associated frequency distribution histograms (**C-D**).

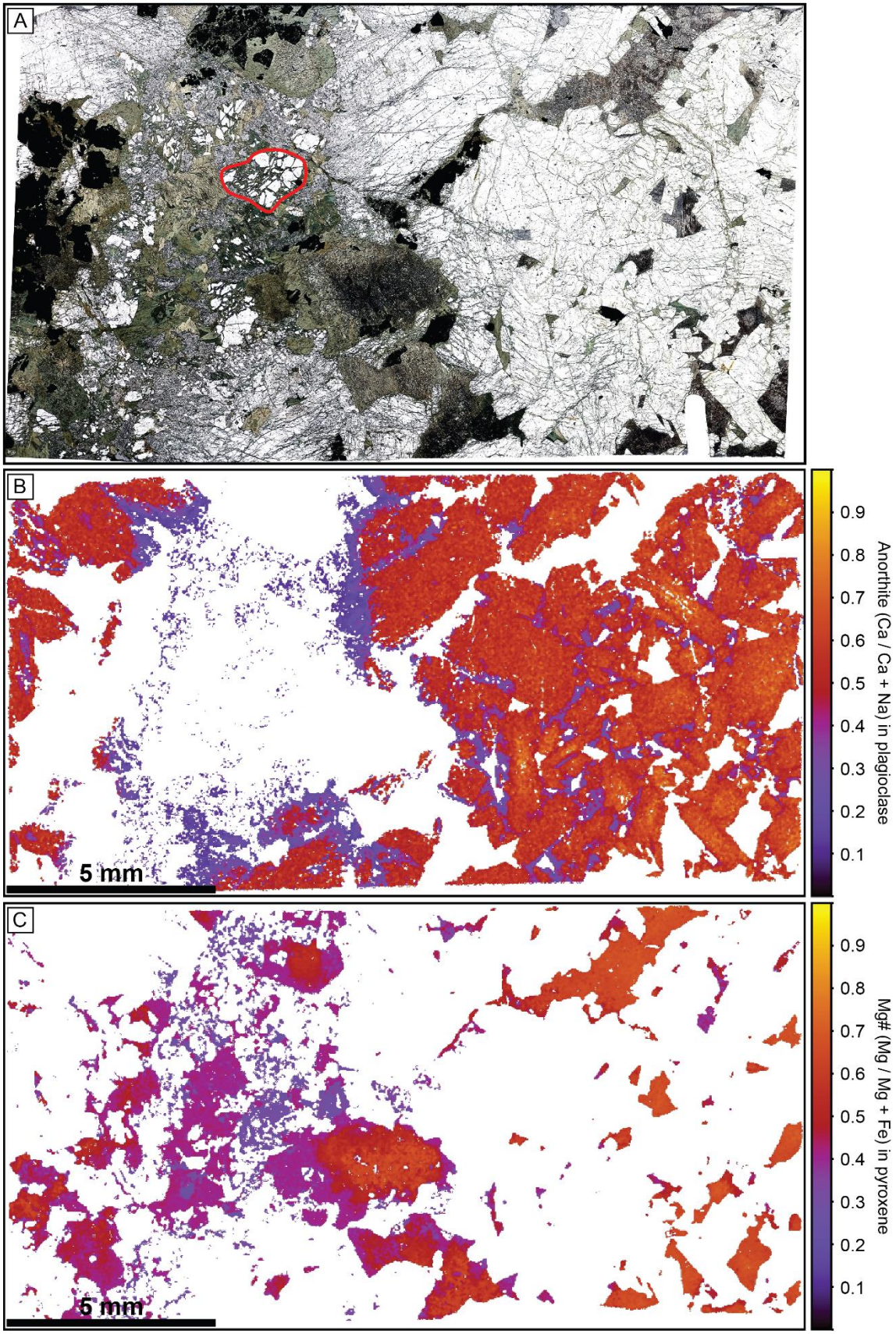

Figure 5.4: A (**A**) photomicrograph of and the molar ratio maps of **(B**) An in plagioclase and (**C**) Mg# in pyroxene produced from thin section 78R-5x4B, an oxide gabbronorite containing a prominent pegmatite vein. Quartz (outlined in red in panel A) is often found within dive 78 pegmatite veins.

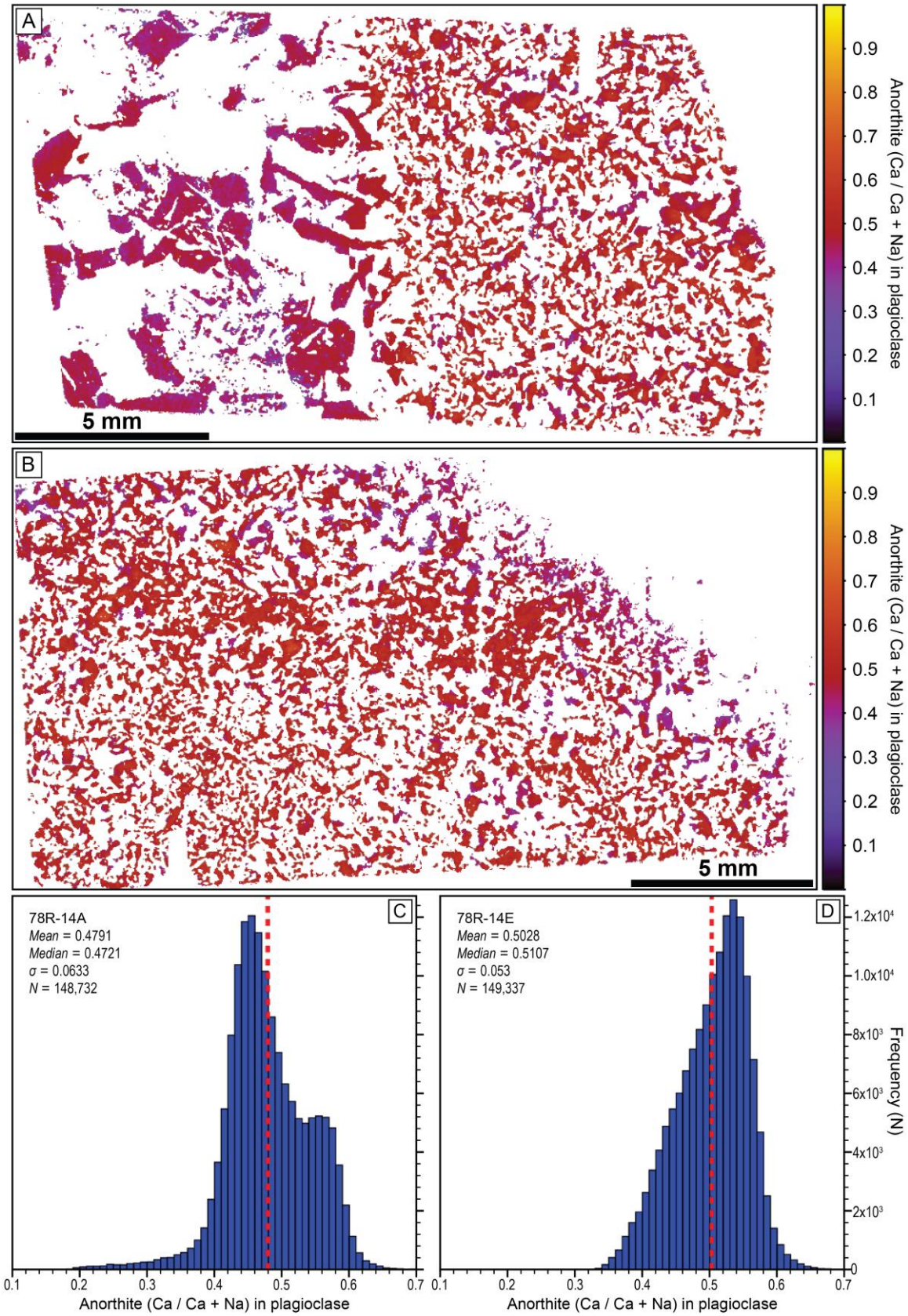

Figure 5.5: Molar ratio maps of An in plagioclase and their associated frequency distribution histograms for thin sections 78R-14A (**A, C**) and 78R-14E (**C, D**).

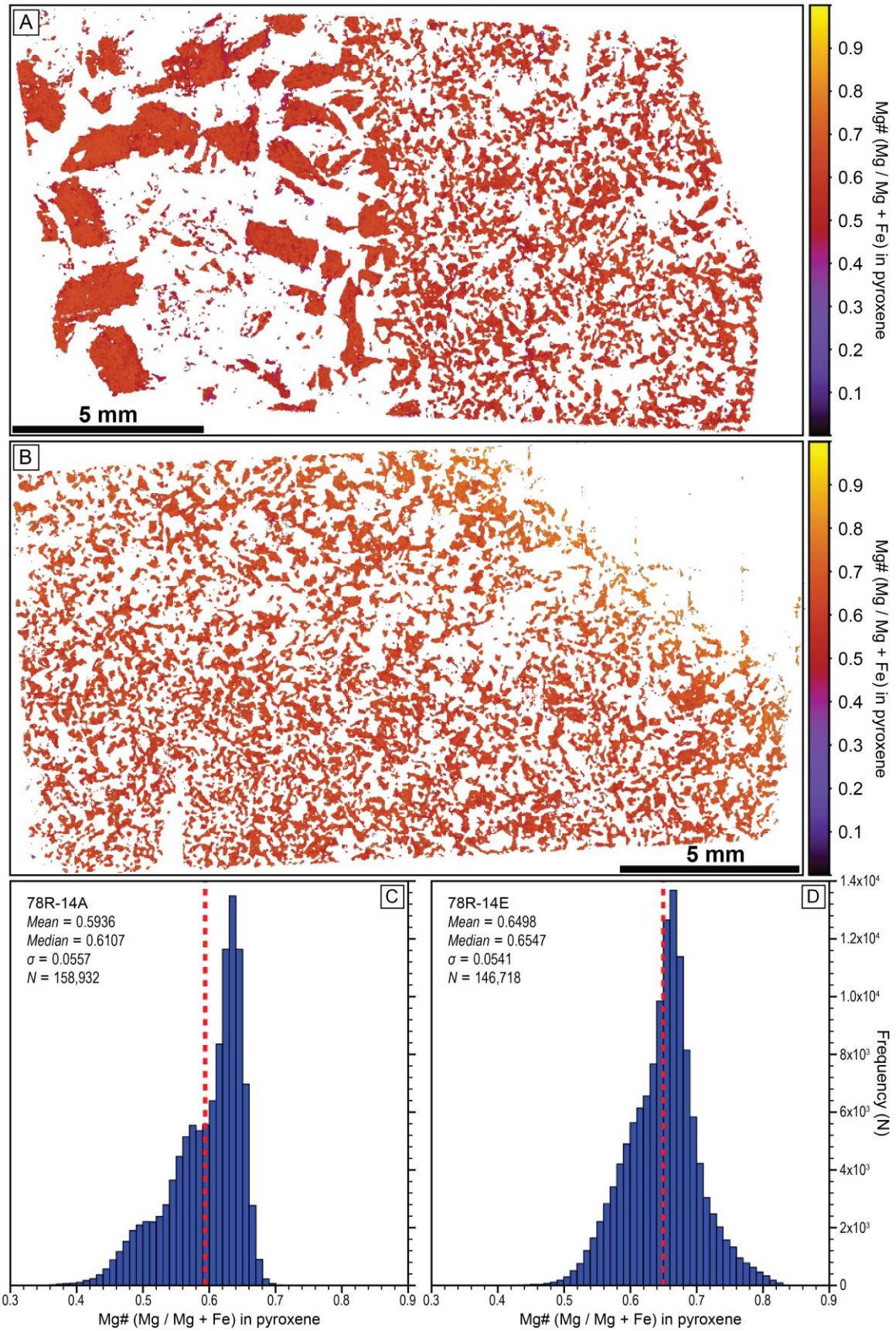

Figure 5.6: Molar ratio maps of Mg# in pyroxene and their associated frequency distribution histograms for thin sections 78R-14A (**A, C**) and 78R-14E (**C, D**).

which indicate cryptic amounts of pegmatite-related material within the section. No apparent peak can be found at a Mg# of 50 for 78R-14E (Figure 5.6D) but a large tail towards high Mg#s is present which is the result of a poor polish in the upper right corner of the thin section.

The histograms of the ratio maps for all of the serial thin sections were combined on a sample by sample basis to produce bulk compositional distribution histograms of each sample. For example, in the case of sample 78R-14 (Figure 5.7) the combined bulk histograms of the two serial thin sections reveal An distributions with a mean of An_{49} and two prominent peaks at ~An_{45} and ~An_{54} which represent the pegmatite and the rest of the sample, respectively. The Mg# distributions reflect the low Mg# bits found in the pegmatite and the bulk pyroxene zonation observed throughout the sample in Figure 5.6B. The 'strip-a-grams' presented in Figure 5.8 are an attempt to present all of the bulk thin section histograms on a single, informative plot for direct comparison. The 'strip-a-gram' plots heatmaps of the calculated probability density functions of each An and Mg# histogram as horizontal strips; hence the name 'strip-a-gram'. Although we lack accurate depth estimates for our AML samples in this study, the y-axis of the 'strip-a-gram' could be adapted to plot samples according to depth. The overall distribution of An compositions in Figure 5.8A clusters approximately between An_{50} and An_{60} with two prominent samples peaking around An_{45} (sections 78R-2B and 78R-2F) and a handful of samples broadly distributing above An_{60} with the highest being 78R-5F. The overall distribution of Mg# in Figure 5.8B clusters between Mg#s of 65 and 70 with a group of three sections (78R-5D, 78R-5x4B and 78R-5x4C) clustering around a mode of 40-42 and three prominent sections at the top of the plot (78R-6A, 78R-6B and 78R-6C) clustering around a mode of 70 to 73.

Combining all of the samples together, the bulk AML was found to have a mean An of 54.85 and Mg# of 65.01 (Figure 5.9). The overall distribution is skewed towards more evolved An and Mg#, which likely reflects extreme fractionation during closed system crystallisation, or 'fossilisation', of the AML. Primitive plagioclase and clinopyroxene compositions are scarce (An≥80: ~0.26%; Mg#≥85: ~0.02%) across the thin sections, with 78R-8A containing the only identifiable coherent domains of primitive plagioclase. In 78R-8A the primitive plagioclase constitutes ~0.4% (i.e., 700 out of 174980 analyses) (Figure 5.10) and occurs as discrete resorbed cores (~$An_{80\text{-}85}$; <1mm) in larger (up to 2mm in length) evolved

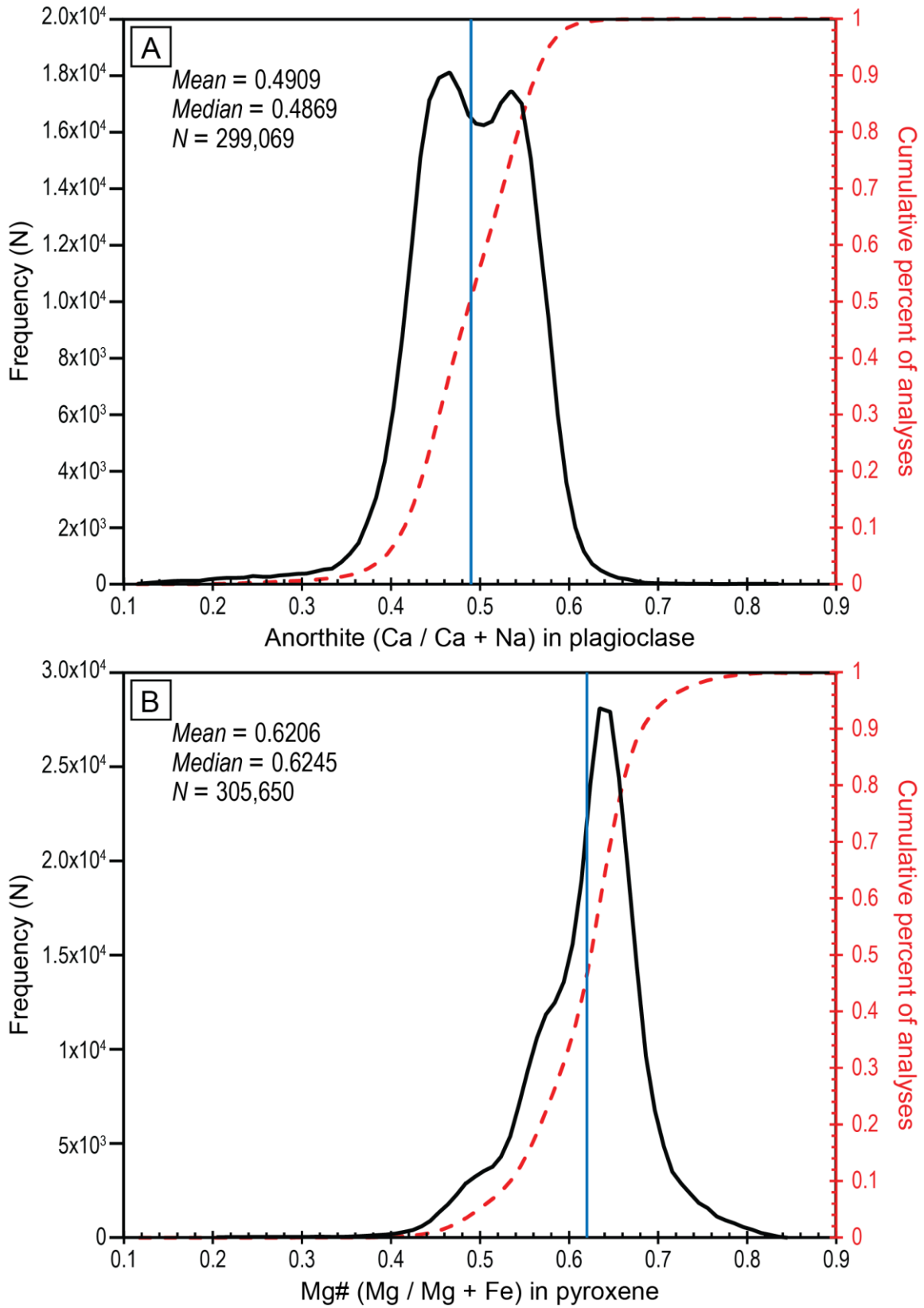

Figure 5.7: Combined bulk sample histograms of (A) An in plagioclase and (B) Mg# in pyroxene for sample 78R-14.

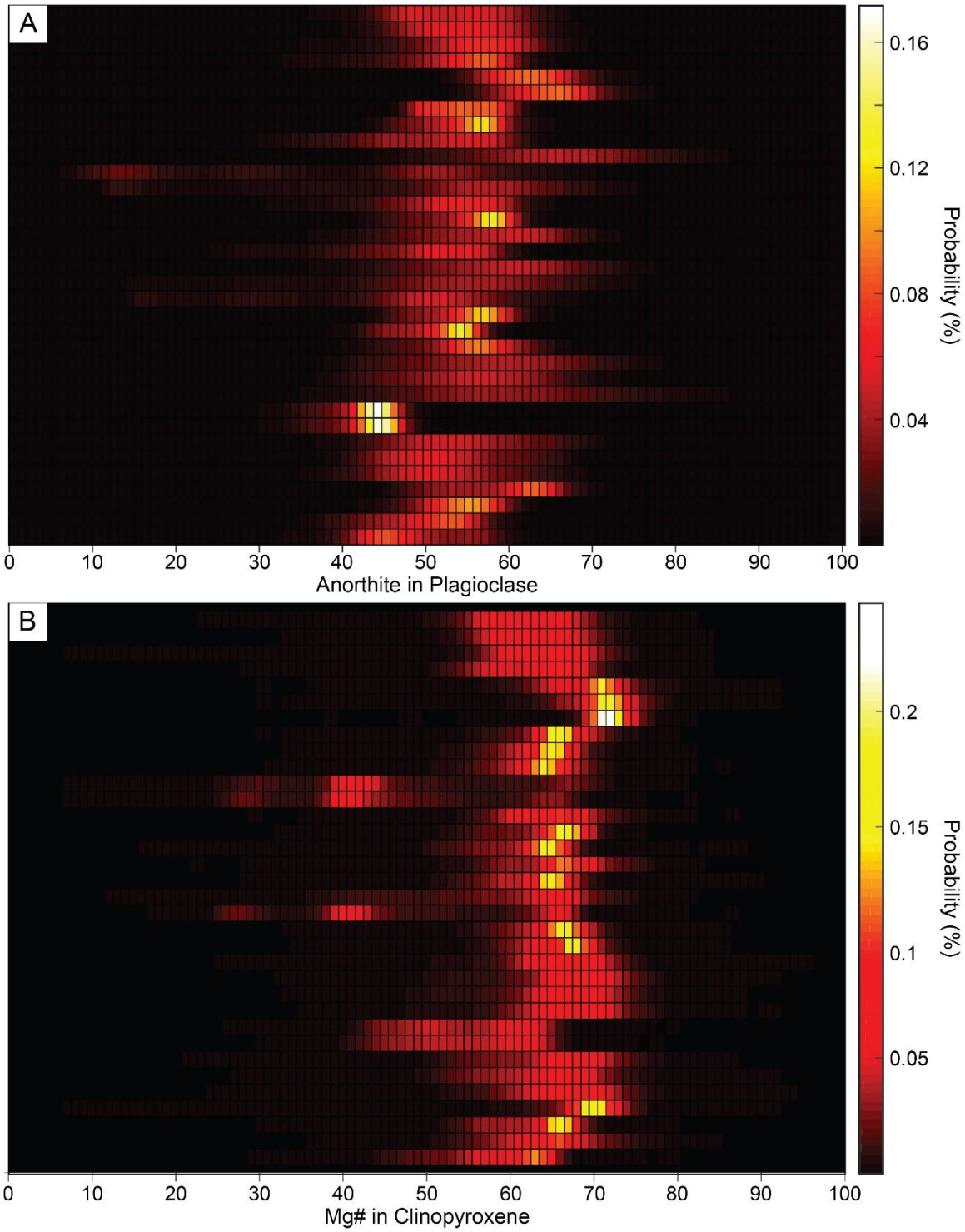

Figure 5.8: Strip-a-grams of probability (%) density distributions for (**A**) An in plagioclase and (**B**) Mg# in pyroxene for the bulk samples of dive 78. Each strip represents the combined results of each serial thin section for all of the analysed samples.

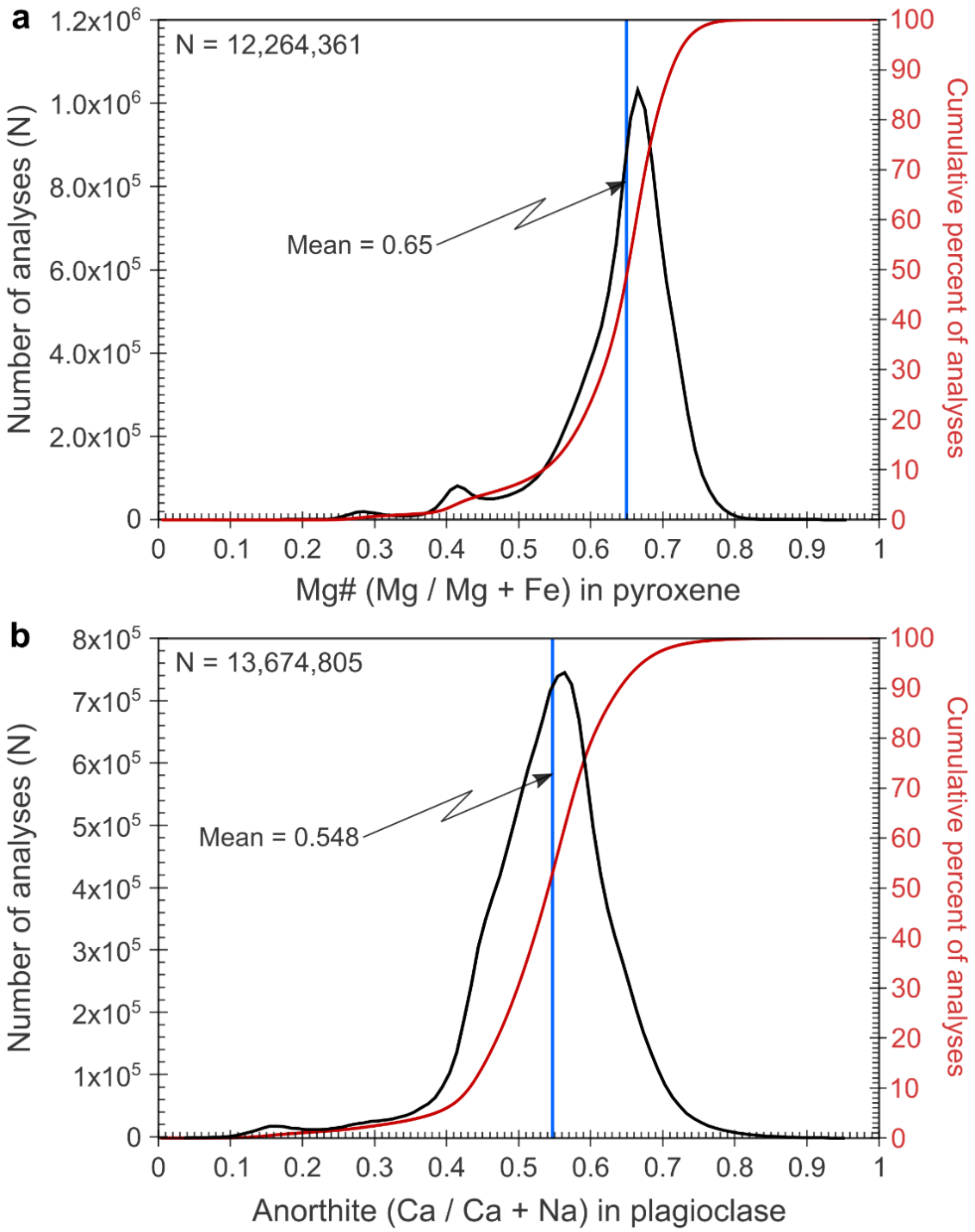

Figure 5.9: Frequency (black lines) and cumulative (red lines) distribution histograms for (**a**) An in plagioclase and (**b**) Mg# in pyroxene.

plagioclase grains. The bulk of the 78R-8A plagioclase are characterised by an ~An_{57} core and an ~An_{50} rim. The plagioclase grains which contain the primitive cores exhibit concentric zoning from the ~An_{82} core through an ~An_{57} zone to an ~An_{50} rim, suggesting that the primitive cores did not crystallise from, and were likely entrained within, the parent melt of the bulk of the sample.

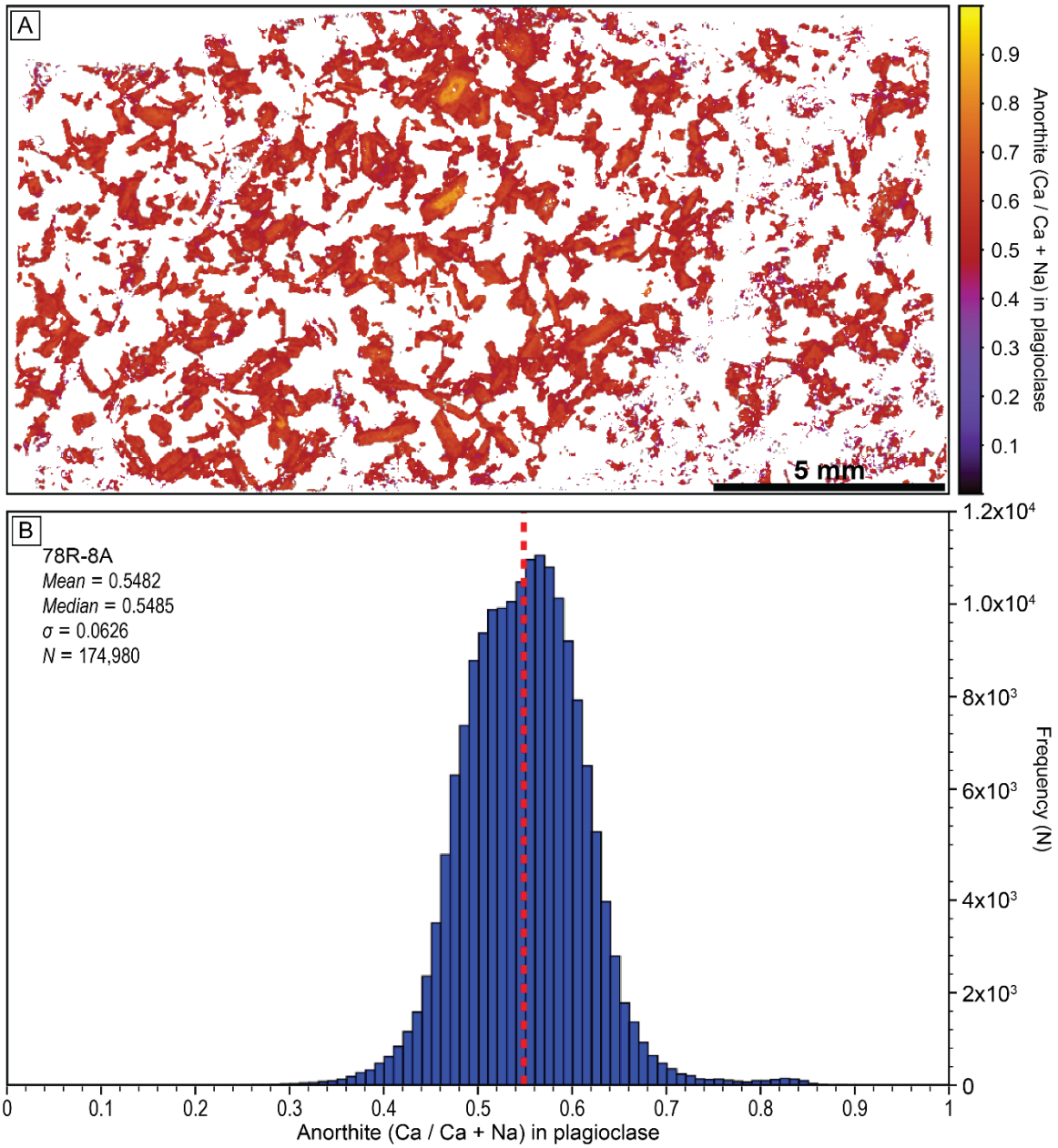

Figure 5.10: (**A**) Molar ratio map of An in plagioclase and (**B**) the associated frequency distribution histogram for thin sections 78R-8A.

5.4 Discusison

5.4.1 Melt composition within the AML

We have parameterised the measured An and Mg# distributions against melt compositions using a MELTS (Ghiorso and Sack, 1995) fractional crystallisation model of a primary EPR MORB (Lissenberg and MacLeod, in revision). Results (Figure 5.11) show that the bulk AML mean $An_{54.85}$ and clinopyroxene Mg# of 65.01 would equate to a melt Mg# of 43 and 26, respectively, with melt compositions of basaltic andesite and andesite: hence, the gabbros are derived from melts substantially more evolved than mean EPR MORB (mean Mg# 58) (Lissenberg and

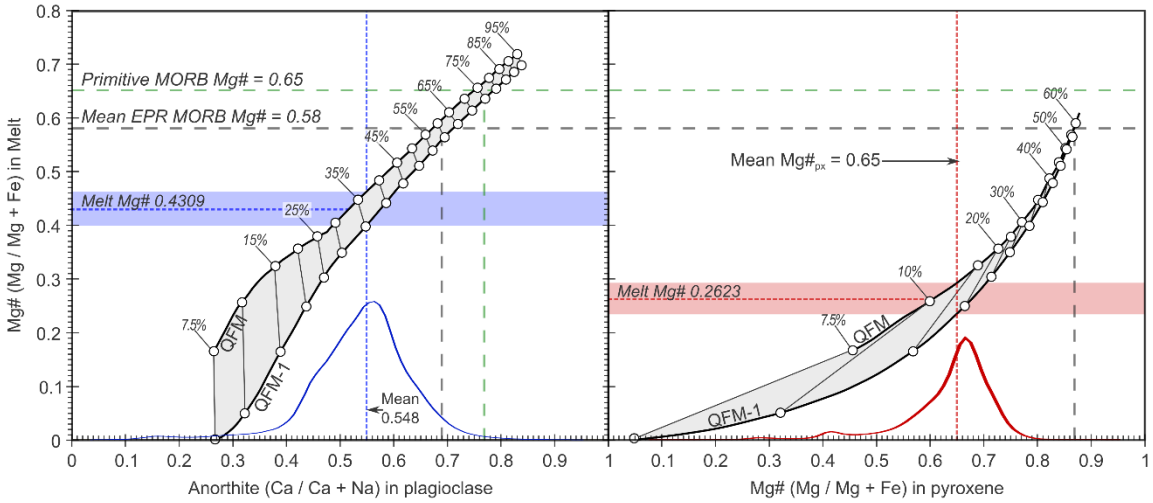

Figure 5.11: Melt Mg# versus (**a**) An in plagioclase and (**b**) Mg# in clinopyroxene. The representative probability distributions for each molar ratio are plotted along the x-axis in each panel for reference. Fractional crystallisation MELTS (Ghiorso and Sack, 1995) models (black lines) of a parental EPR MORB (Lissenberg et al., in revision) have been plotted for oxygen fugacities between the quartz-fayalite-magnetite buffer and one log unit below it. The remaining melt fraction is plotted at 5% intervals (white circles). See the Methods section for details on the modelling. The shaded blue and red regions represent the range of melt Mg# in equilibrium with the means of the plagioclase and clinopyroxene datasets, respectively.

MacLeod, in revision). Only 3.77% of plagioclase and 0.01% of pyroxene within the AML samples have compositions primitive enough (An≥69, Mg#≥87) to have been derived from mean EPR MORB, and only ~0.55% of plagioclase has An≥77 and therefore could be in equilibrium with primitive (Mg#≥65) MORB. Although the precise percentages will vary depending on assumed primary melt composition and fractional crystallisation model, the bulk AML plagioclase An and clinopyroxene Mg# is consistently more evolved than that which is predicted to be in equilibrium with mean to primitive EPR MORB compositions.

According to our parameterised model, the calculated bulk mean An and Mg# compositions equate to drastically different equilibrium melt Mg#s, suggesting that there is a compositional gap between the two phases. While this could be considered a reflection of the phases fractionating at different points during the parent melt's evolution, there is a simpler explanation for the compositional gap. Plugging the mean pyroxene Mg# of 72.5 for section 78R-6A (Figure 5.3D) into the parameterised MELTs model returns a plagioclase (An_{50} to An_{55}) in equilibrium with the plagioclase rims found within the section. This would suggest that the more primitive plagioclase cores crystallised from a more primitive melt, forming a framework, and the plagioclase rims and evolved interstitial pyroxenes crystallised from an evolved interstitial melt.

The data presented here are paradoxical: that although geophysical evidence indicates that the AML is the proximate source of MORB, the plutonic rocks that occur at this level are too evolved to be in equilibrium with MORB. Hence, the plutonic and volcanic records do not tally.

5.4.2 A conceptual model for the axial melt lens

Any petrological model for the AML, in addition to resolving this paradox, must be able to account for: (i) the observations of generally high crystal (<40% melt; Marjanović et al., 2015; Xu et al., 2014) content of the AML and its fine-scale along-axis segmentation in melt proportions (Marjanović et al., 2015; Carbotte et al., 2015); (ii) the short (30-90 days) residence times of Pacific MORB phenocrysts (Pan and Batiza, 2002, 2003; Moore et al., 2014); (iii) the indication of melt mixing as a major process prior to eruption based on the presence of a number of distinct compositional groups in lava phenocrysts (Pan and Batiza, 2002, 2003; Goss et al., 2010; Moore et al., 2014); (iv) clinopyroxene trace elements for the dive 78 samples indicating crystallisation from melts with strongly enriched and fractionated trace element patterns, which has been interpreted as a signature of reactive porous flow of interstitial melt in the lower crustal crystal mush (Lissenberg et al., 2013); (v) the presence of incompatible trace element over-enrichments in MORB (O'Neill and Jenner, 2012; Lissenberg et al., 2013).

We propose that the AML is characterised by protracted, mush-dominated periods where it is fed by evolved interstitial melts extracted from the underlying lower crustal crystal mush (Figure 5.12A and 5.12C), undergoing slow cooling and crystallisation which may lead to the development of fine-scale segmentation of the AML horizon (Singh et al., 1998; Carbotte et al., 2013; Marjanović et al., 2015). These small volumes of melts would be over-enriched in trace elements and highly fractionated as a result of reactive porous flow through the crystal mush beneath (Lissenberg et al., 2013). In the few months leading up to decadal eruption events (Pan and Batiza, 2002, 2003; Goss et al., 2010; Moore et al., 2014) (Figure 5.12B), primitive melt is injected into the AML in large, focused volumes where it undergoes rapid mixing with small volumes of the extant evolved melt to produce a hybridised MORB with over-enriched incompatible trace elements. The rapid emplacement of the primitive melt likely contributes to triggering of a diking or eruption event (Goss et al., 2010; Moore et al., 2014), thus limiting the mixing and residence time of

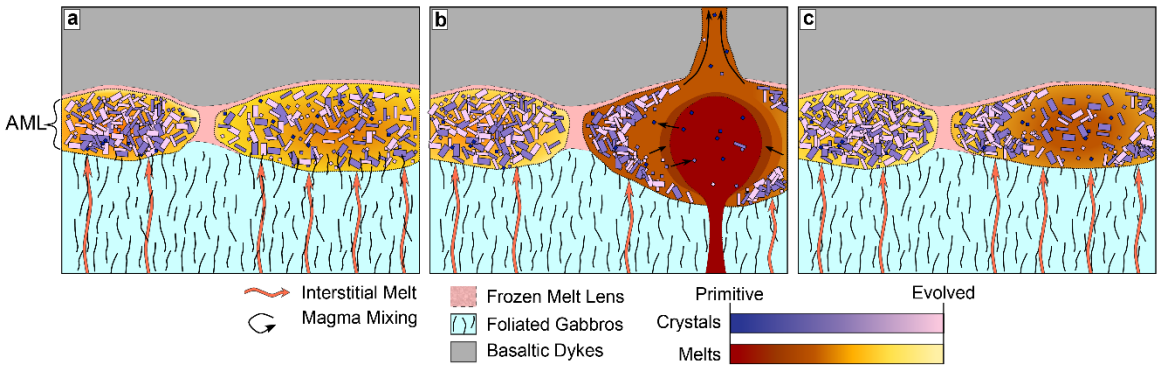

Figure 5.12: Along-axis cartoon representation of the model for the evolution of the AML developed in this paper. (**a**) An inter-eruption, mush-dominated period where the AML horizon is recharged by small volumes of evolved, interstitial melt extracted from the underlying crystal mush (pale red arrows). The AML undergoes slow cooling and crystallisation. Pale pink regions in the diagram represent frozen portions of the melt lens. On a decadal timescale (**b**), large volumes of primitive melt from the lower crust are injected into the AML where they undergo rapid mixing with the highly-fractionated, evolved extant melt (black arrows). These injection events are likely to occur within 30-90 days of eruption events, playing a leading role in triggering these eruptions. (**c**) After an eruption has drained the AML of large volumes of hybridised magmas, the remaining melt will begin to slowly cool and crystallise as the dominant mechanism of melt delivery returns to that of the evolved interstitial melt as in panel a.

magma with MORB compositions in the AML, and the amount of material contributed by it to the plutonic record. Any primitive melt remaining in the AML after eruption will continue to mix with the extant fractionated melt to produce a hybrid, evolved abyssal tholeiite liquid (Natland and Dick, 2009) with a low crystallisation temperature and the capability to produce a two pyroxene assemblage (i.e., a gabbronorite) (Walker et al., 1979). This model accounts for the general lack of primitive compositions in the AML and the abundance of orthopyroxene in the upper gabbros of the Hess Deep plutonic section. Hence, the evolved nature of the plutonic rocks in the AML does not in itself require that MORB bypasses the AML horizon altogether, as has been suggested previously (Natland and Dick, 1996, 2009). Further, the geophysical observation of variations in melt content and distribution over scales of a few hundred metres (i.e., smaller distances than the length of fine-scale AML segments) (Marjanović et al., 2015) suggests that the focused nature of primitive melt delivery to the AML horizon could lead to the preservation of evolved pockets of melt which lack interconnectivity (e.g., pale pink region between the AML segments in Figure 5.12) with the broader AML horizon. With increasing crystallisation and occlusion of porosity, strong crystal networks form in these lower-temperature segments of the AML (Pan and Batiza, 2003), isolating and thus preserving pockets of evolved material within the horizon, now represented by the skew towards low Mg# and An (Figure 5.9).

5.5 Conclusions

Our holistic model for the role of the AML at fast-spreading MORs reconciles the paradoxical compositional mismatch between the volcanic and plutonic records with the geophysical characteristics of the AML, the short residence times of Pacific MORB phenocrysts, and the incompatible trace element over-enrichments in MORB. It is also consistent with detailed examinations of the changes in magmatic chemistry during the repose time between the 1991-1992 and 2005-2006 eruption events of the EPR region around 9°50'N. During this period, the underlying AML was gradually recharged with more evolved residual liquids originating from the underlying mush zone (Goss et al., 2010). Focused replenishment of primitive magma to the AML ~6 weeks prior to eruption may have played a major role in triggering the eruption event (Moore et al., 2014).

The data presented in this paper are difficult to reconcile with previous models in which primitive melts fed from the mantle enter and reside in the AML and crystallise significant gabbroic material (e.g., the gabbro glacier model) (Morgan and Chen, 1993; Coogan et al., 2002a). We instead propose that while the AML is an active player in the development of MORB, permitting the fractionation and storage of evolved melts from the underlying crystal mush and recording the mixing of that material with primitive melt, it fulfils more of a passive role with respect to lower crustal accretion (Pan and Batiza, 2002, 2003).

Future work should seek to establish whether the evolved compositions determined at Hess Deep are a general feature of AML plutonic rocks elsewhere. Given the segmentation of mid-ocean ridge axes (Carbotte et al., 2015), as well as the AML itself (Carbotte et al., 2013; Marjanović et al., 2015), some degree of variability is likely to occur (Perk et al., 2007), although the Pito Deep plagioclase and pyroxene compositions in the shallow gabbros overlaps those described herein from Hess Deep. However, we can rule out that the evolved nature of the Hess Deep AML is the result of its putative location near a segment end (Stewart et al., 2005; Rioux et al., 2012a), since the Hess Deep crust has a bulk Mg# of 74.29 (i.e., that of a primary mantle melt), and the gabbroic rocks beneath the melt lens have steeply dipping foliations and lineations. These observations indicate delivery of primary melt to the Hess Deep section and a crustal accretion mechanism involving vertical (i.e., within-section) melt and/or mush transport.

CHAPTER 6
An evolved melt lens in the northern Ibra Valley, southern Oman Ophiolite

6.1 Introduction

In order to further constrain the characteristics of the AML horizon in support of our investigation of the *in situ* Hess Deep AML sample suite (Chapter 5), we have mapped and sampled in detail this horizon in an 'undisturbed' section of the Oman ophiolite (Wadi Saq) located in the north-eastern Ibra Valley, Wadi Tayin Massif, southern Oman Ophiolite (Figure 2.4). The mapping location was chosen based on the abundance of relatively continuous outcrops from the foliated gabbros through the DGT into the sheeted dykes. Continuous outcrops of the AML horizon are uncommon due to preferential meteoric alteration relating to the prevalence of fractures, igneous contacts and lithological heterogeneity within the horizon (France et al., 2009). The good exposure and near-continuous outcrop within the mapping area provided a natural laboratory to observe the complex nature of the AML across a range of scales (i.e., from pluton- down to sub-centimetre-scale). The observations of the mapped section have provided analogous constraints for our Hess Deep investigation regarding the three-dimensional nature and distribution of the rocks which formed in the AML, while providing vital information regarding the nature and variability of the DGT in the Oman ophiolite.

6.2 Structure of the Wadi Saq upper gabbros

We selected an area to the east of the Wadi Saq, near the village of Farigh along the northern limb of the Ibra valley for detailed study on the basis of continuous exposure from the foliated gabbros up through the base of the sheeted dykes; herein referred to as the Wadi Saq section (Figure 6.1). The general stratigraphy of the section follows a roughly N-S trend from lower crust to upper crust, with mapping covering the top of the foliated gabbros, through high-level gabbros and into the base of the sheeted dykes (Figure 6.2). Continuous outcrop becomes lost within the sheeted dykes, which outcrop discontinuously in the gravel plains to the south, before passing into scattered Geotimes lava outcrops and thence, 4km to the south, into a window of underlying (Hawasina) shelf sediments and a recumbent fold/thrust complex (Hopson, 1981; Pallister, 1981; Pallister and Hopson, 1981). The dominant lithologies based on field observations, and referred to by their descriptive field names are as follows: foliated gabbros, patchy isotropic

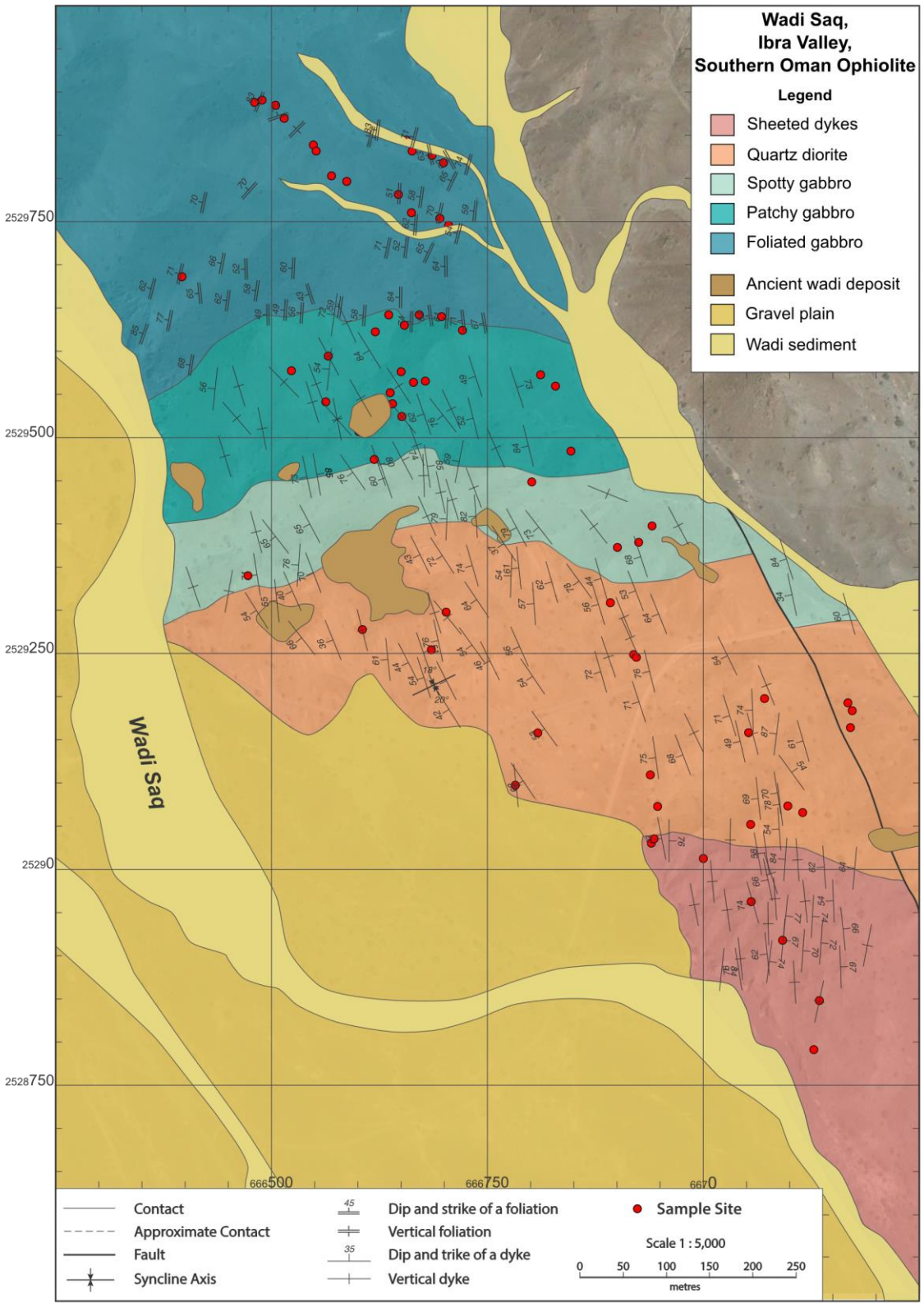

Figure 6.1: A 1:5,000 geologic map of the hills to the east of the village Farigh where the Wadi Saq enters the gravel plains. Roughly 1km of true stratigraphic thickness has been mapped from the upper foliated gabbros up through the base of the sheeted dykes.

gabbros, spotty gabbros, quartz diorites, sheeted dykes, and cross-cutting dykes.

The Ibra area lacks good exposure of bedded volcanic rocks or interbedded/overlying pelagic sediments, therefore, one must rely on the attitude of lithologic contacts or cumulus layering in the plutonic rocks in order to correct for the Ibra Valley syncline in restoring the stratigraphy to horizontal (Pallister, 1981). The crust/mantle boundary along the crest of Jabal Dimh (~30 km E-W extent) has a southerly dip of ~30-35° (Pallister, 1981; Pallister and Hopson, 1981). Assuming that layering in the upper gabbros formed horizontally, Pallister (1981) constructed a series of cross-sections perpendicular to the fold axis defining the fold symmetry by the attitudes of cumulus layering and unit contacts in the upper gabbros. We employed this same technique for reconstructing the approximate unit thicknesses reported in this chapter. A cross-section line was defined through the centre of the mapped area and used to calculate the distance from the fold hinge, as defined by Pallister (1981), to each of the unit contacts. These distances were used to calculate the variation in the expected dip of the contacts assuming a dip for the crust/mantle boundary of ~30° and checked against estimates from the field and the derived cross-sections for accuracy. The resulting dips (25-20°) and average unit thicknesses were then used to estimate the original stratigraphic thicknesses. Figure 6.4 provides a stratigraphic cartoon using these calculated thicknesses and summarising the field observations presented below. A range of representative field photographs of the mapped units are provided in Figures 6.3-8, with high resolution versions of these figures provided in the electronic appendix. For each unit, summaries of petrographic descriptions have been provided in Appendix A (Table A.2) and full-thin section scans are provided in the electronic appendix (E5) for reference.

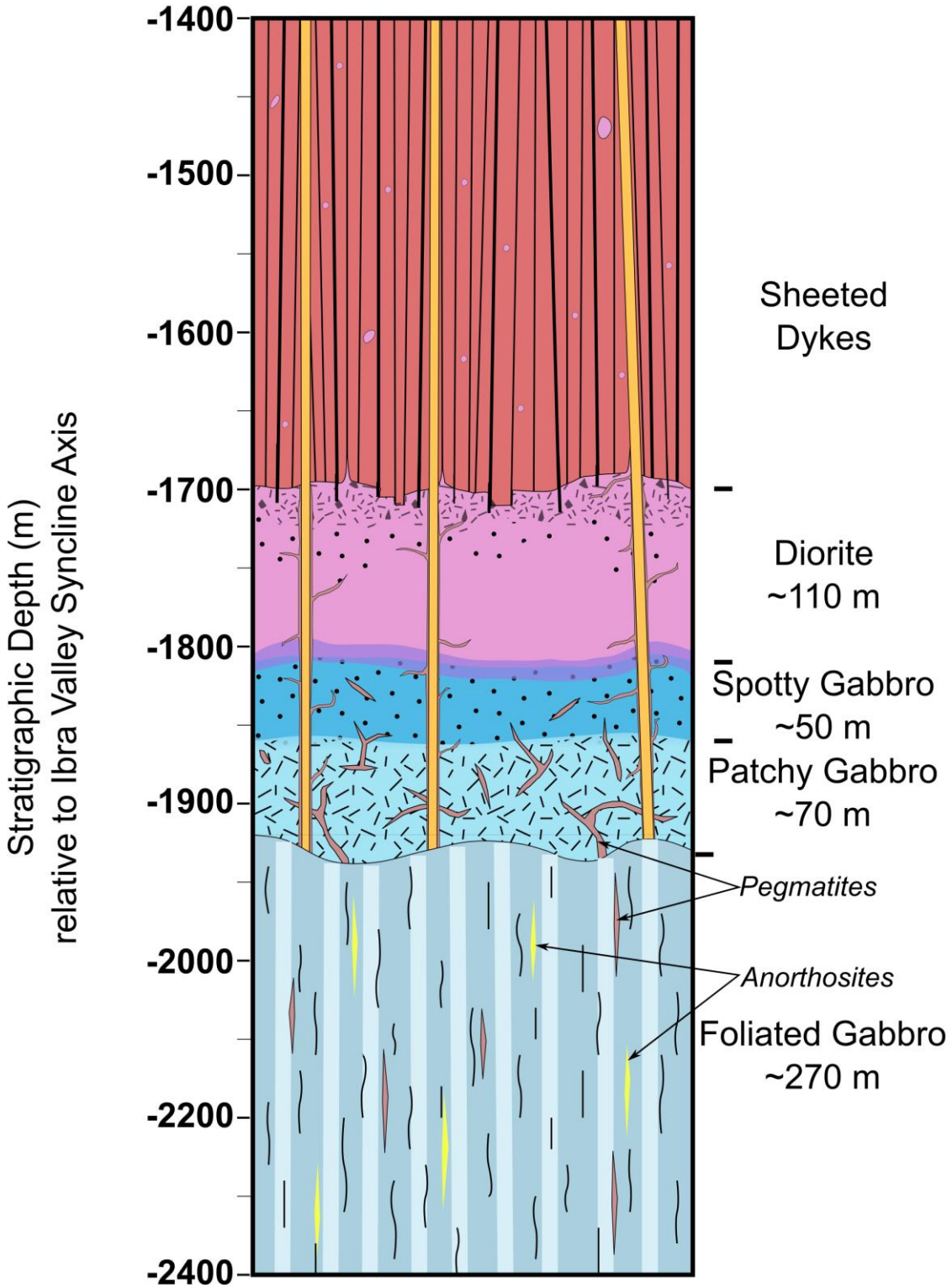

Figure 6.2: A simplified cartoon of the representative mapped stratigraphy of the Wadi Saq section based on field observations as described in the text of section 6.1. The foliated gabbros at the base of the column contains lenses of anorthosite (yellow) and pegmatite (red). Pegmatites also appear in the patchy and spotty gabbros as veins and patches and are found intruding along the margins of cross-cutting dykes (orange) into the diorite unit. The varitextured nature of the diorite becomes more intense at the base of the sheeted dykes (black patterns). Xenoliths of the diorite can be found throughout the sheeted dykes.

6.2.1 Foliated gabbros (Figure 6.3)

The upper portions of the foliated gabbros mapped by this study (~270 m thick) consist of a series of subfacies that, unlike other sections in Oman (e.g., Wadi Abyad; MacLeod and Yaouancq, 2000), can vary significantly perpendicular to the foliation (i.e. palaeo-horizontal) on the scale of an outcrop (Figure 6.3A). Though these subfacies usually exhibit prominent magmatic foliations (average strike of 005° and dip of 66° to the NW), it is not uncommon for portions of the outcrop to exhibit a range of fabric intensities from very strong to weak (or non-existent in the case of pegmatite lenses) (Figure 6.3D and 6.3F). The dominant subfacies of the unit is a medium grained (2-5 mm), granular gabbro with a range of modal phase proportions between more leucocratic (50-60% plagioclase) and more melanocratic (40-50% plagioclase) bands (Figure 6.3A, 6.3B and 6.3F). This dominant subfacies comprises the bulk of the outcrop and consist of anywhere from 0.2-1 m wide bands in which plagioclase is typically euhedral/subhedral and blocky to tabular with slight variability in grain size, while pyroxene is generally subhedral and lacking in grain size variation (even in the more melanocratic facies) and minor olivine, where present, is generally subhedral, altered, and variable in grain size. Olivine is present throughout the mapped portion of the foliated gabbros as predominantly altered, oxidised grains in outcrop that increase in abundance with depth in the section.

Other identified subfacies include anorthositic leucogabbros gradational to anorthosites (Figure 6.3E-F), foliated olivine gabbro, and foliation-parallel lenses of pegmatites (Figure 6.3A and 6.3D). In several cases, most or all of these subfacies can be observed occurring in a single 5-10 m wide outcrop (Figure 6.3A). The anorthositic subfacies is dominated by subhedral, rounded, blocky to tabular plagioclase ranging from <0.1 mm up to ~0.5 mm in length with rare patches of interstitial oxide or pyroxene appearing in the wholly anorthosite endmembers. The anorthosites are typically found as thin (<0.2 m) bands that are gradational to the other subfacies, but one band was documented as having sharp contacts with the surrounding foliated gabbros (sample ML98). The foliated olivine gabbro subfacies occurs as 0.5-1.5 m wide bands and resembles the dominant granular gabbro (*sensu stricto*) subfacies but also containing abundant, large (up to 1 mm), subhedral to euhedral granular olivines. Foliation-parallel pegmatite lenses within

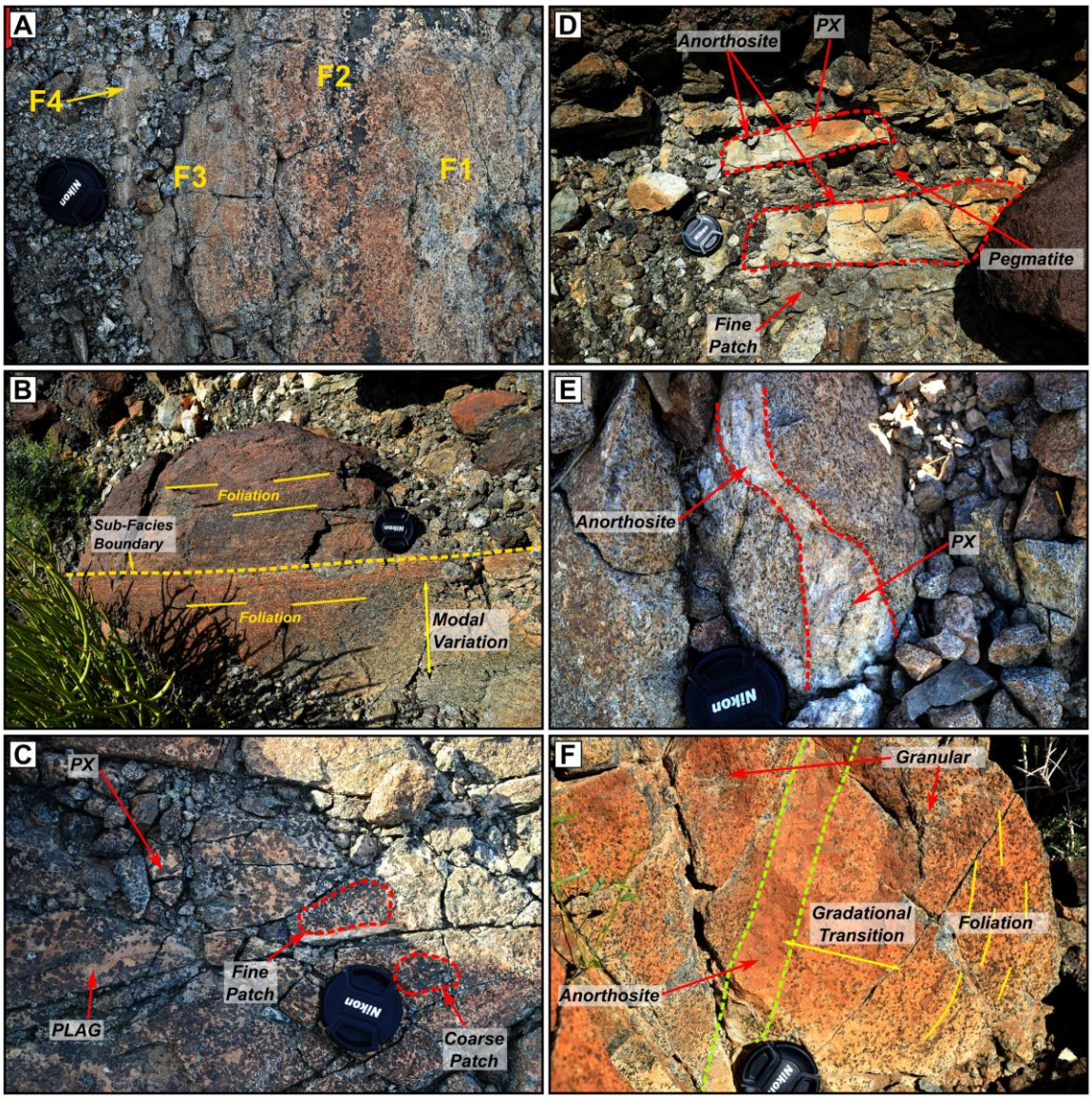

Figure 6.3: Representative field photographs of foliated gabbros from Wadi Saq. (**A**) Four subfacies of the foliated gabbros in a single outcrop, including (F1) a strongly foliated, medium-grained granular subfacies cut by (F2) lenses and veins of pegmatite which grades into (F3) a finer-grained subfacies with (F4) wispy veins of anorthosite. (**B**) Modal layering parallel to the foliation. (**C**) Strongly foliated granular pyroxene clots in a plagioclase matrix with extreme modal variation. (**D**) Anorthosite strips amongst pegmatite lenses ~1 m to the south of the modal layering in panel B. (**E**) Wispy strips of anorthosite with undulating margins near the contact with the patchy gabbros. (**F**) Outcrop containing 3 subfacies of the foliated gabbros including (from left to right) (i) a granular, melanocratic subfacies with a weak fabric, (ii) an anorthositic strip with mafic stringers, and (iii) a moderately foliated granular subfacies.

the foliated gabbros tend to occur as ~5-10 cm wide bands that span the length of outcrops but may not be readily traced between outcrops. The pegmatites are characterised by large (up to 2.5 cm), euhedral plagioclase surrounded by interstitial green and brown amphibole, clinopyroxene (where primary mineralogy is preserved), and occasional oxides (up to ~1 cm). Two other subfacies were identified higher up in the section near the contact with the patchy gabbro. These

facies include intergranular to subophitic patches within the more dominant granular leuco- and melagabbro subfacies, and anorthositic leucogabbros with spot-like, weathered clots of pyroxene ± oxide ± amphibole oikocrysts (up to ~0.5 cm in diameter).

Overall, the foliated gabbros exhibit subhedral granular to intergranular, moderately well-equilibrated textures with gently curved plagioclase grain boundaries. In most samples, plagioclase grains are elongate (>2:1 aspect ratio), tabular, anhedral to subhedral grains. Clinopyroxene, though appearing granular in some outcrops, tends to be interstitial (sometimes poikilitic) to plagioclase. When present, olivine is granular, anhedral to subhedral, and forms either large (up to 5 mm), solitary grains or granular clusters interstitial to plagioclase. Both oxide and brown amphibole, though major phases in pegmatitic lenses within the unit, are typically found occurring as minor, late, interstitial phases in a large number of samples.

We note a characteristic absence of cross-cutting dykes within the foliated gabbro section. The contact between the foliated gabbros and the isotropic or patchy gabbros is gradational, with strong foliations transitioning into the isotropic matrix of the patchy gabbro over ~5-7 m. It is along the foliated-patchy gabbro contact in the patchy gabbro that the first cross-cutting dolerite dykes occur in the section. Several cross-cutting dykes were observed cutting along the foliated-patchy gabbro contact horizontally from the East before abruptly cutting up-section into the patchy gabbros trending ~005°. These cross-cutting dykes can be traced through the entire section into the sheeted dykes where they become lost between discontinuous outcrops. The origin of these cross-cutting dykes is discussed further in section 6.4.5.

6.2.2 Patchy gabbros (Figure 6.4)

The patchy gabbro (~70 m thick) consists of a subophitic fine to slightly medium grained (1.5-4 mm), ‘50:50’ (i.e., 50% pyroxene, 50% plagioclase) gabbro that lacks any observable fabric (i.e., isotropic) and is characterised by patches and networks of pegmatites (Figure 6.4). The distribution of pegmatite patches is heterogeneous within the patchy gabbro, ranging from outcrops with little (<1 modal %) or no patches to outcrops dominated by patches (>50 modal %) which. The pegmatites of the patchy gabbro resemble those found within the

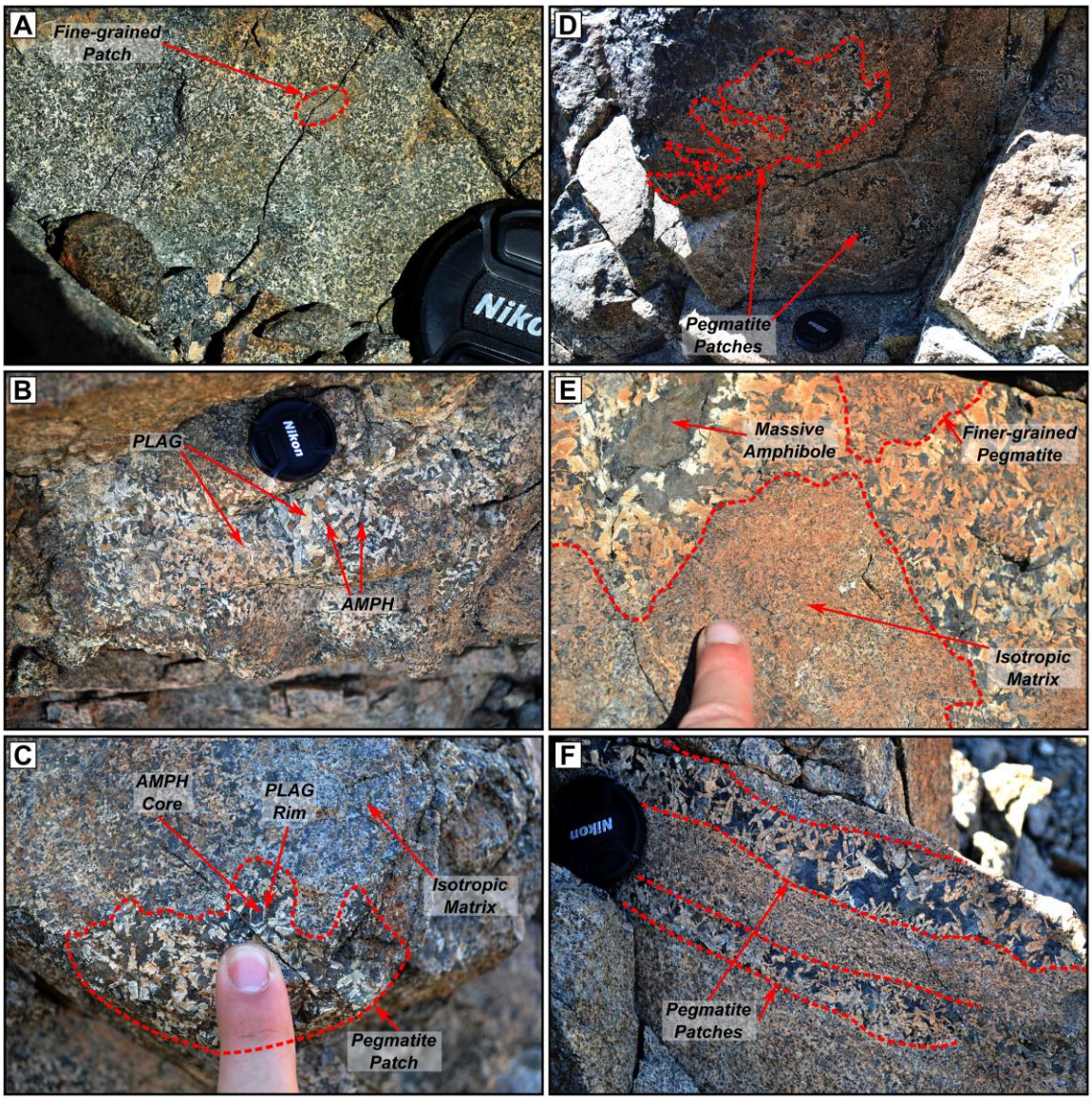

Figure 6.4: Representative field photographs of patchy gabbros from Wadi Saq. (**A**) Typical, isotropic, featureless patchy gabbro matrix. (**B**) An example of a pegmatitic patch within the patchy gabbro. (**C**) A pegmatite patch within the patchy gabbro approximately 1.5 m to the east of panel B. (**D**) Typical network of pegmatite patches within the patchy gabbro. (**E**) Pegmatite patches within the patchy gabbros exhibiting minor grain size variation in the matrix material. (**F**) A patchy gabbro from the transition with the foliated gabbros containing pegmatite patches aligned parallel to the foliated gabbros.

foliated gabbros, characterised by large (0.2-20 mm) euhedral to subhedral plagioclase grains surrounded by interstitial green and brown amphibole with variable abundances of oxides (from <1% up to >10%). Pegmatites in outcrops which contain a smaller mode of patches tend to be characterised by sharp boundaries with the background subophitic gabbro and maintain the typical intersertal pegmatite textures as seen in the foliated gabbro pegmatites. Those pegmatites which dominate the mode of outcrops tend to form complicated networks with diffuse margins that grade into and interact with the surrounding host

gabbro, leading to more complex 'varitextured' relationships and a general decrease in the pegmatite grain size. There are no major subfacies identified with the exception of some more leucocratic patches and more transitional subophitic to ophitic textured gabbros, both of which appear near the upper contact with the spotty gabbro. The bulk of the cross-cutting dykes in the patchy gabbros exhibit strongly chilled margins with an average trend parallel to ~345°. Oxide and brown amphibole are more abundant within the patchy gabbros, most often appearing within pegmatitic patches, but also found as late interstitial phases within the subophitic matrix of the samples where they can account for up to 5% of the mode. Some thin sections are slightly varitextured, however, such textural complexity is not readily apparent in hand sample, and is not observed in outcrop outside of the vicinity of pegmatite patches.

The contact between the patchy gabbro and the spotty gabbro roughly parallels the trend of the foliated-patchy gabbro contact, deeper in the section. The contact is gradational in some places while in others there is a definite high-temperature contact defined by the sharp boundary of pegmatite patches and veins intruding up into the spotty gabbro. In the upper 5-10 m of the patchy gabbro, the spotty gabbro begins to appear in channels and layers roughly parallel to the trend of the contact. Hence, we believe that the spotty gabbro unit is related to the patchy gabbro with the intruding pegmatite veins and patches along the contact being related to the main pegmatites of the patchy gabbro unit.

6.2.3 Spotty gabbros (Figure 6.5)

The spotty gabbro (~ 50 m thick) gets its name from characteristic clots of oikocrystic pyroxene ± oxide ± amphibole that give it a 'spotty' appearance in outcrop (Figure 6.5). The size and concentration of the spots (average of 5-10 mm) varies quite significantly within the unit, increasing in concentration in the vicinity of the contacts with the units above and below. The matrix surrounding the spots is typically characterised by a mantle of adcumulus, subhedral plagioclase (~0.5-1.5 mm) which grades out into the rest of the sample at its edges. The unit is heavily varitextured with respect to both the mode and grain size of phases, and thus there are no discernible subfacies observed. However, some outcrops and thin sections

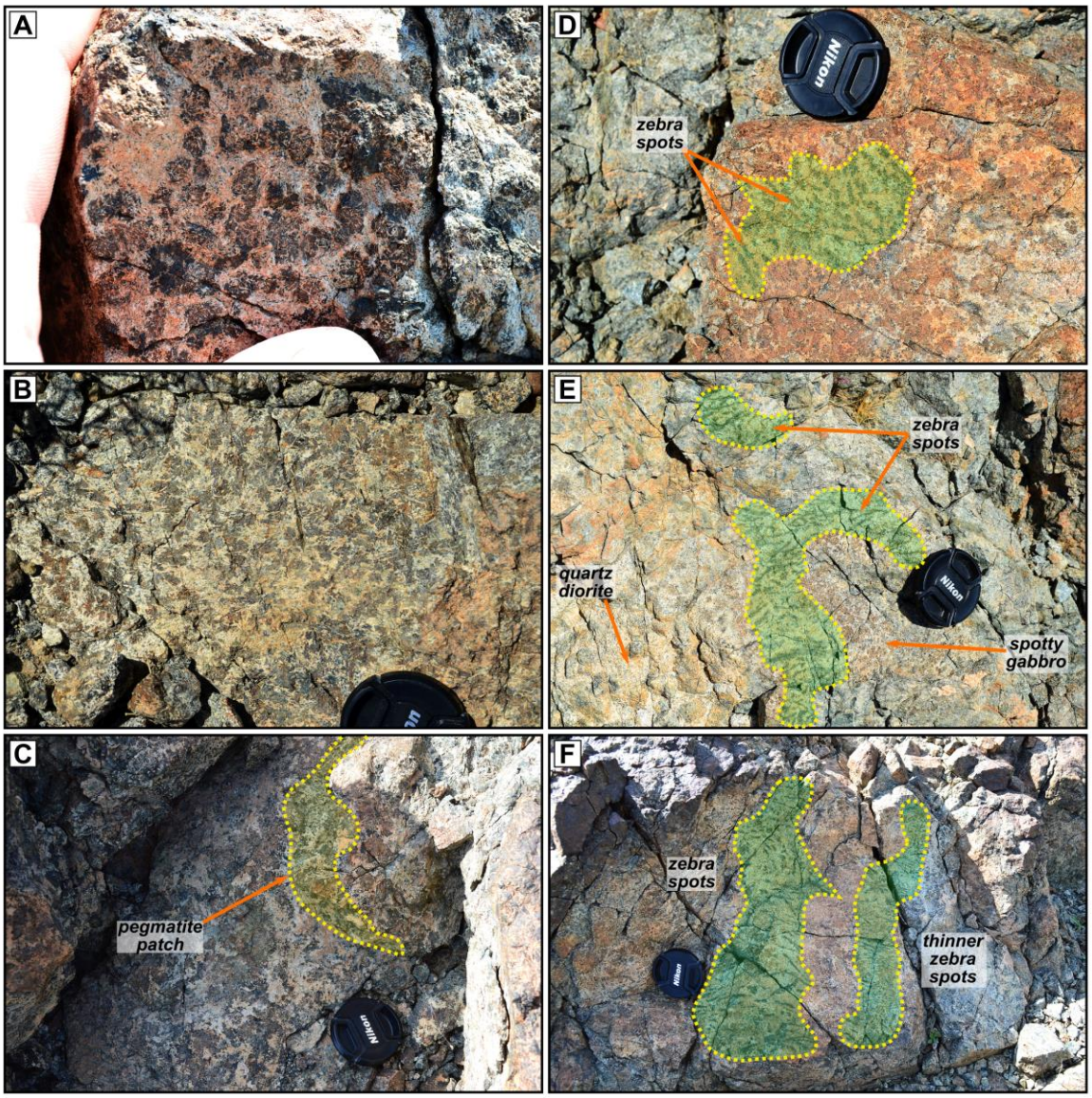

Figure 6.5: Representative field photographs of spotty gabbros from Wadi Saq. (**A**) Typical characteristic spots of the spotty gabbros made up of clinopyroxene clots containing acicular plagioclase within a matrix dominated by plagioclase. (**B**) An example of the typical texture of subophitic clinopyroxene clots within a plagioclase matrix that characterises the spotty gabbros. (**C**) A small patch of diffuse, coarse-grained pegmatitic material within a varitextured portion of the spotty gabbro. (**D**) Elongate 'zebra' spots of amphibole distributed between patches of more typical clinopyroxene spots. (**E**) Patches of 'zebra' spots within the gradational contact with the Diorite unit. (**F**) 'Zebra' spots surrounding a fine-grained leucocratic patch near the contact with the diorite.

reveal textural features within the spotty gabbros that vaguely resemble portions of the patchy gabbro (i.e., the subophitic host gabbro with diffuse networks of pegmatites) and subfacies of the foliated gabbros (i.e., anorthositic patches with >70% plagioclase and interstitial pyroxene and oxide; granular leuco- to melagabbros with clinopyroxene dominantly interstitial/intergranular to plagioclase). Overall, the spotty gabbro could be classified as a '50:50' gabbro with local modal variations on the order of ±10-15% in plagioclase and clinopyroxene.

Like the patchy gabbro, oxide and brown amphibole are common across the spotty gabbro unit and not limited to pegmatitic or coarse-grained patches. Though oxides are observed to occasionally display more granular morphologies (e.g., within coarse-grained pegmatite patches), they predominantly occur alongside brown amphibole as a late interstitial phase to both the dominant granular plagioclase and intergranular/interstitial clinopyroxene. No olivine is observed within the spotty gabbros.

Crosscutting dykes (~0.5-1m wide) continue through the spotty gabbro unit as in the patchy gabbro beneath, exhibiting strongly chilled margins. Although obscured in many cases by the cross-cutting dykes, the spotty gabbro-quartz diorite contact is observed as being dominantly gradational. We note that often within 5 m of the contact, the spotty gabbro is observed to contain diffuse patches of more elongated spots, referred to as ‘zebra’ spots in the field (Figure 6.5D-F). These ‘zebra’ spots are characterised by elongated (up to 1.5 cm long) amphibole oikocrysts. We interpret the ‘zebra’ spots and the gradational contact between the units as suggesting that, as with the patchy-spotty gabbro contact, the bulk of the spotty gabbros and quartz diorites are magmatically related. Pegmatites intrude along the margins of cross-cutting dykes and out into the main spotty gabbro along joints and fractures, implying that the host was likely cool during dyke intrusion. The cross-cutting pegmatite veins are likely associated temporally with the same group of later pegmatites identified throughout the deeper units of the section; hence, we believe that these pegmatites may post-date the main phase of magmatism at the ridge axis. We also note that more leucocratic patches, suggestive of possible xenoliths of the quartz diorite but lacking in abundant amphibole, are observed as occurring within the upper ~1-2 m of the spotty gabbro. These patches could represent felsic enclaves resulting from high-temperature magmatic interactions between the two units or, if they are xenoliths, they could represent pieces of a more crystalline diorite that was stoped into a still partially molten spotty gabbro.

6.2.4 Quartz diorite (Figures 6.6 & 7)

The quartz diorite unit (~110 m thick) forms the top of the plutonic section, and consists predominantly of two grain-size varieties, each containing their own

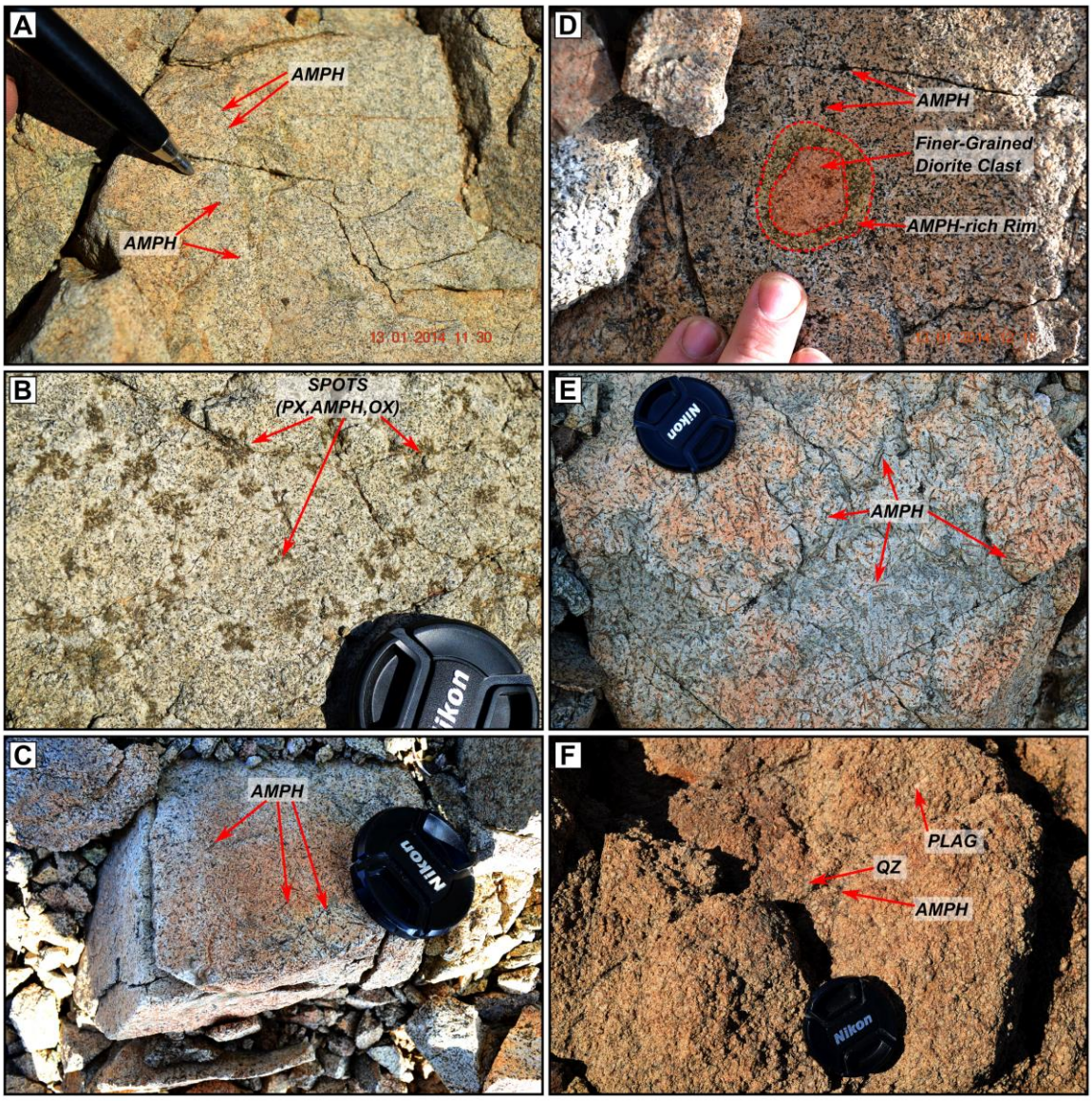

Figure 6.6: Representative field photographs of the dominant facies within the quartz diorite unit from Wadi Saq. (**A**) An example of the typical fine-grained subfacies of the diorite unit containing occasional small (< 0.5mm) amphiboles. (**B**) An example of the spotty diorite subfacies consisting of up to 1 cm in size clots of amphibole with inclusions of acicular plagioclase. (**C**) An example of the typical medium-grained subfacies which contains abundant acicular amphiboles. (**D**) An example of the medium-grained subfacies which is dominated by blocky amphibole instead of acicular amphiboles. (**E**) An example of the typical coarse-grained version of panel C with large acicular amphiboles. (**F**) An example of the coarser-grained, quartz-rich diorite which contains blocky to tabular amphiboles and is found often cross-cutting the main body of the quartz diorite and intruding up into the base of the sheeted dykes.

subfacies: the first ranging from fine (<1 mm) to medium grained (2-4 mm) and a second variety which is coarse grained (up to 7 mm) (Figure 6.6). Overall the quartz diorite contains notable amounts of quartz, oxides and other minor phases with extreme textural variabilities akin to the high-level ‘varitextured’ gabbros described in Wadi Abyad (Coogan et al., 2002a; MacLeod and Yaouancq, 2000) (Figure 6.7). Quartz is often found in close association with plagioclase, forming

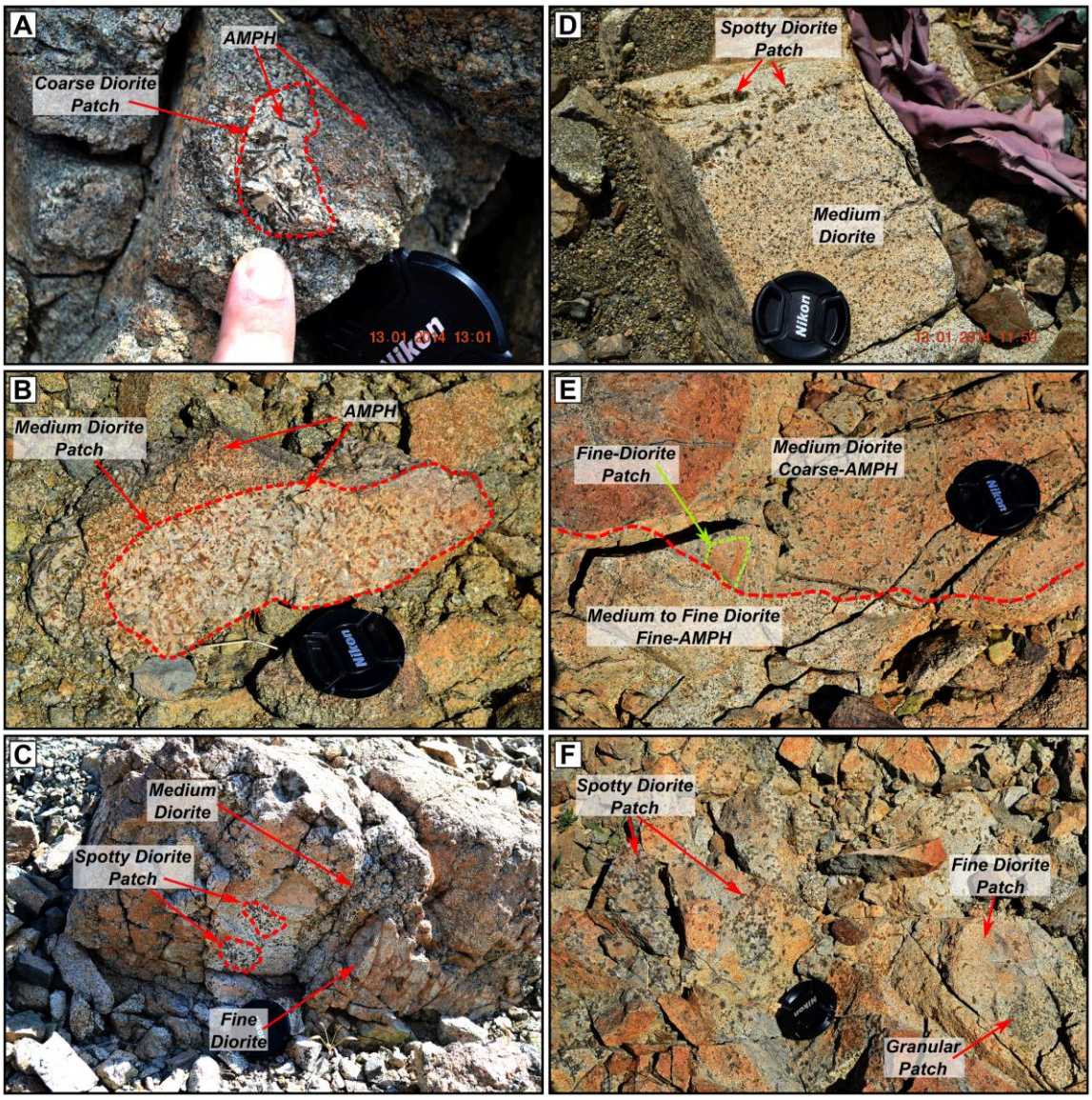

Figure 6.7: Representative field photographs of varitextured outcrops within the quartz diorite unit from Wadi Saq. (**A**) Patches of coarser diorite with acicular amphibole within typical medium-grained diorite with blocky amphibole. (**B**) Pods of medium-grained, acicular amphibole diorite within varitextured patches of finer-grained material dominated by higher concentrations of amphibole. (**C**) A mixed matrix of fine and medium-grained diorite with concentrated patches of spotty diorite containing oxides. (**D**) Tabular outcrop of medium-grained diorite with diffuse patches of spotty diorite. (**E**) Complicated mixture of fine-grained diorite with diffuse patches of slightly coarser material containing abundant elongate clusters of acicular amphibole and oxide. (**F**) As in panel E, another complex mixture near the base of the sheeted dykes that also contains concentrated patches of spotty diorite.

both granular masses and myrmekitic intergrowths of quartz and plagioclase interstitial to larger plagioclase grains. Small (up to 10 cm wide patches) ‘spotty’ diorites are characterised by 3-6 mm clots of pyroxene ± oxide ± amphibole, like that observed in the spotty gabbros (Figure 6.6B), within both grain-size varieties of the unit. Petrographic examination of these ‘spotty diorite’ clots reveals them to be clasts of granular to subophitic material dominated by amphibole. Both of the

grain-size varieties are found to contain subfacies that are characterised by abundant acicular amphiboles (Figure 6.6C and 6.6D). An extremely quartz-rich subfacies of the coarse-grained unit with grain sizes of up to 7 mm is commonly observed in the vicinity of the roots of the sheeted dykes (Figure 6.6F). As in the spotty gabbro, crosscutting dykes in the quartz diorite have strongly chilled margins (Figure 6.8A) with pegmatitic veins, accompanied by greenschist-facies alteration, often observed protruding into the quartz diorite along joints and fractures from the margins of the cross-cutting dykes.

6.2.5 Sheeted dykes (Figure 6.8)

The top of the quartz diorite is defined by the base of sheeted dykes, which is characterized by a complex relationship between dyke roots and later coarse-grained diorites intruding the dykes. The overall grain size of the diorite unit tends to fine towards the base of the sheeted dykes with outcrops of dyke roots exhibiting magmatic flow fabrics and grain-size reduction from the surrounding fine-grained diorite over a distance of several cm into the core of the dyke roots (Figure 6.8D). We suggest that these are equivalent features to the 'foliated microgabbros' described by MacLeod and Rothery (1992) and MacLeod and Yaouancq (2000) within the sheeted dyke-gabbro transition. Abundant acicular amphibole phenocrysts and both dioritic xenoliths and xenocrysts occur throughout the mapped portion of the sheeted dykes (Figure 6.8F), further suggesting that the sheeted dykes are rooting in and being sourced from the diorite unit (see section 6.4).

The sheeted dykes have a predominantly N-S strike as defined by their chilled margins and are dominantly lighter in colour (Figure 6.8C) compared to the darker cross-cutting dykes that can be tracked from the top of the foliated gabbros into the sheeted dyke complex. The cross-cutting dolerite dykes manifest in a markedly different way on hillslopes with dark and rubbly weathering (Figure 6.8A and 6.8B), and a slight green-coloured tinge likely related to greenschist-facies hydrothermal alteration. They form several metre-wide groups, however, outside of these groups the dolerite dykes tend to form distinct anastomosing dykes within the larger packages of lighter-coloured dykes. These generally seem to follow and intrude along the joints and fractures of the lighter-coloured dykes.

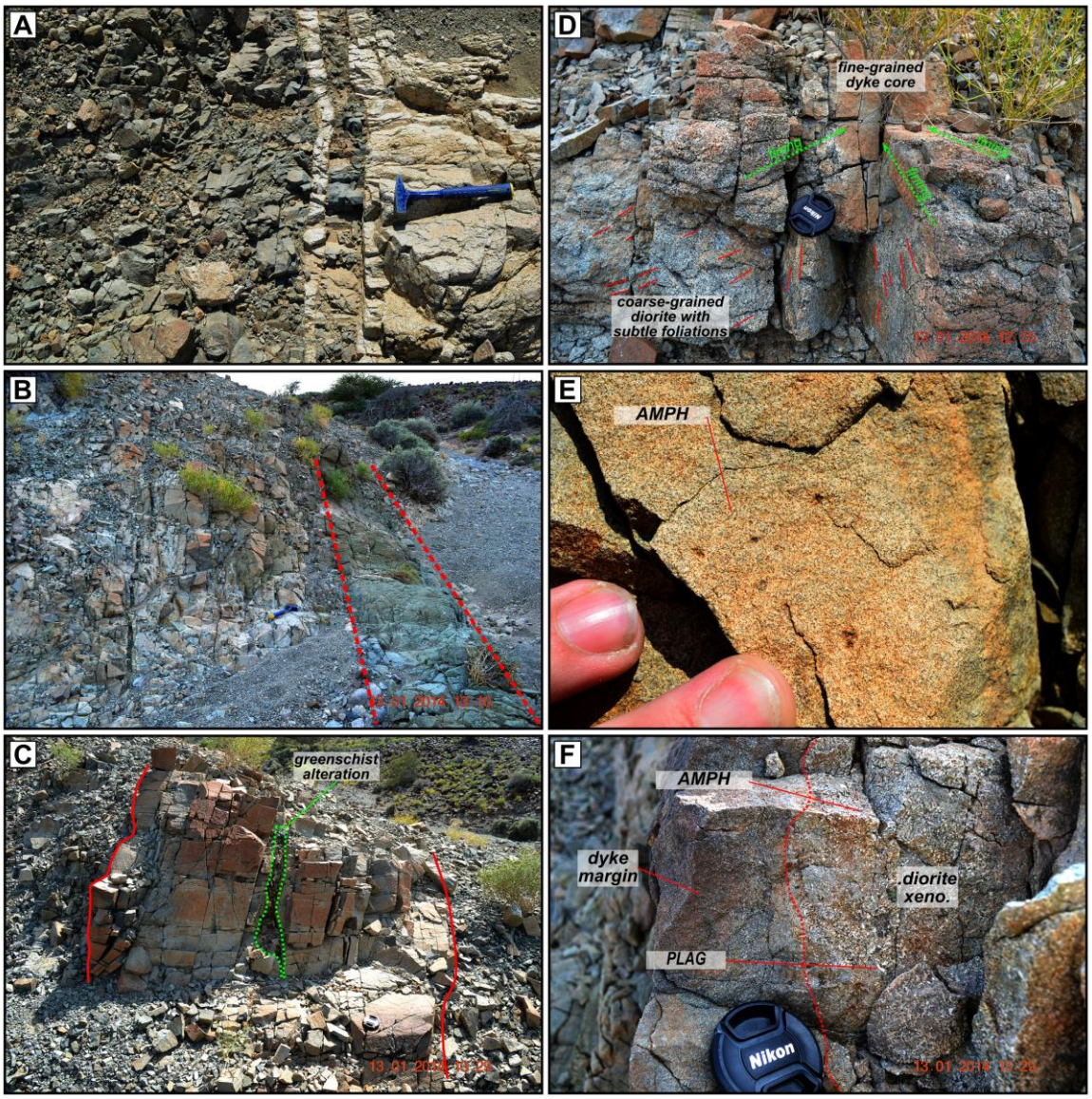

Figure 6.8: Representative field photographs of sheeted and cross-cutting dykes from Wadi Saq. (**A**) Greenschist facies-altered dolerite dykes splitting and anastomosing around blocks and strips of coarse-grained diorite. The dolerite dykes exhibit chilled margins against the diorite. (**B**) An outcrop of the sheeted dykes containing abundant light-coloured dykes cut by highly greenschist facies-altered dolerite dykes (e.g., outlined by the red lines). (**C**) A typical tabular/blocky outcrop of intact, light-coloured sheeted dykes. Red lines indicate approximate locations of dyke margins. Note the presence of a thin zone of alteration in the centre of the dyke. (**D**) A sheeted dyke keel observed rooting in medium-grained diorite at the base of the sheeted dykes. A continuous grain size gradation is observed between the diorite and the keel of the fine-grained dyke. Subtle magmatic foliations defined by plagioclase and amphibole in the coarser material are oriented towards the dyke keel. (**E**) An example of the interior of a typical light-coloured sheeted dyke. (**F**) An example of a disaggregated dioritic xenolith found in the core of a light-coloured dyke high in the sheeted dykes.

6.3 Whole-rock geochemistry

Whole-rock geochemistry was carried out to determine the geochemical composition of each of the units and assess their origins and relationships to each other. The stratigraphic section described above was sampled systematically at a variety of scales, where possible, to assess smaller-scale variability within the units.

A total of 104 samples (i.e., 27 foliated gabbros, 15 patchy gabbros, 11 spotty gabbros, 17 quartz diorites, 14 sheeted dykes, and 20 cross-cutting dykes) were collected across the Wadi Saq section. Although variable degrees of outcrop degradation within the patchy gabbros, spotty gabbros, and particularly the quartz diorite unit hindered more detailed sampling of small-scale variabilities within the units, great care was taken to collect representative samples of the textural range within each unit for geochemical and petrographic analysis. All 104 samples were processed and analysed for whole-rock major and trace element chemistry by inductively coupled plasma-optical emission spectrometry (ICP-OES) and -mass spectrometry (ICP-MS) in the School of Earth and Ocean Sciences at Cardiff University (see Appendix B for description of the analytical methods). Average bulk rock major element and trace element data for each unit is provided in tables 6.1 and 6.2, respectively, with the full ICP-OES and ICP-MS datasets being provided in tables C.1-6 and C.7-12, respectively, of Appendix C.

6.3.1 Alteration effects

The major element compositions of the lavas, dykes, and upper plutonics from the Oman ophiolite have been affected to some degree by low-grade metamorphism (e.g., greenschist facies assemblages in the sheeted dykes) related to seafloor hydrothermal circulation (Pearce et al., 1981; Alabaster et al., 1982; Lippard et al., 1986; Miyashita et al., 2003; Umino et al., 2003; MacLeod et al., 2013). This alteration is most commonly reflected in the compositions of fluid-mobile elements (e.g., Na, K and Ca) with other elements like Si, Fe, and Mg having the potential to be mobilised to some extent. Loss on ignition (LOI) measured for the whole rock powders provide relatively low averages for most of the units (see Table 6.1) with the cross-cutting dykes, commonly observed in the field as having abundant greenschist facies alteration, having the highest values (2.74%). The lowest LOIs on average are found in the diorites (1.44%) with the bulk of the gabbros and the sheeted dykes falling between ~2.0-2.1%. As a whole, we found good correlations against Zr, an immobile incompatible element often used as an index of fractionation, for all elements except Rb, Cs, Ba, and, in the diorite and cross-cutting dykes, K; Pb, and Sr exhibit reasonably good correlations (Figure 6.9), and CaO and SiO_2 do not appear to be significantly affected (Figure 6.10).

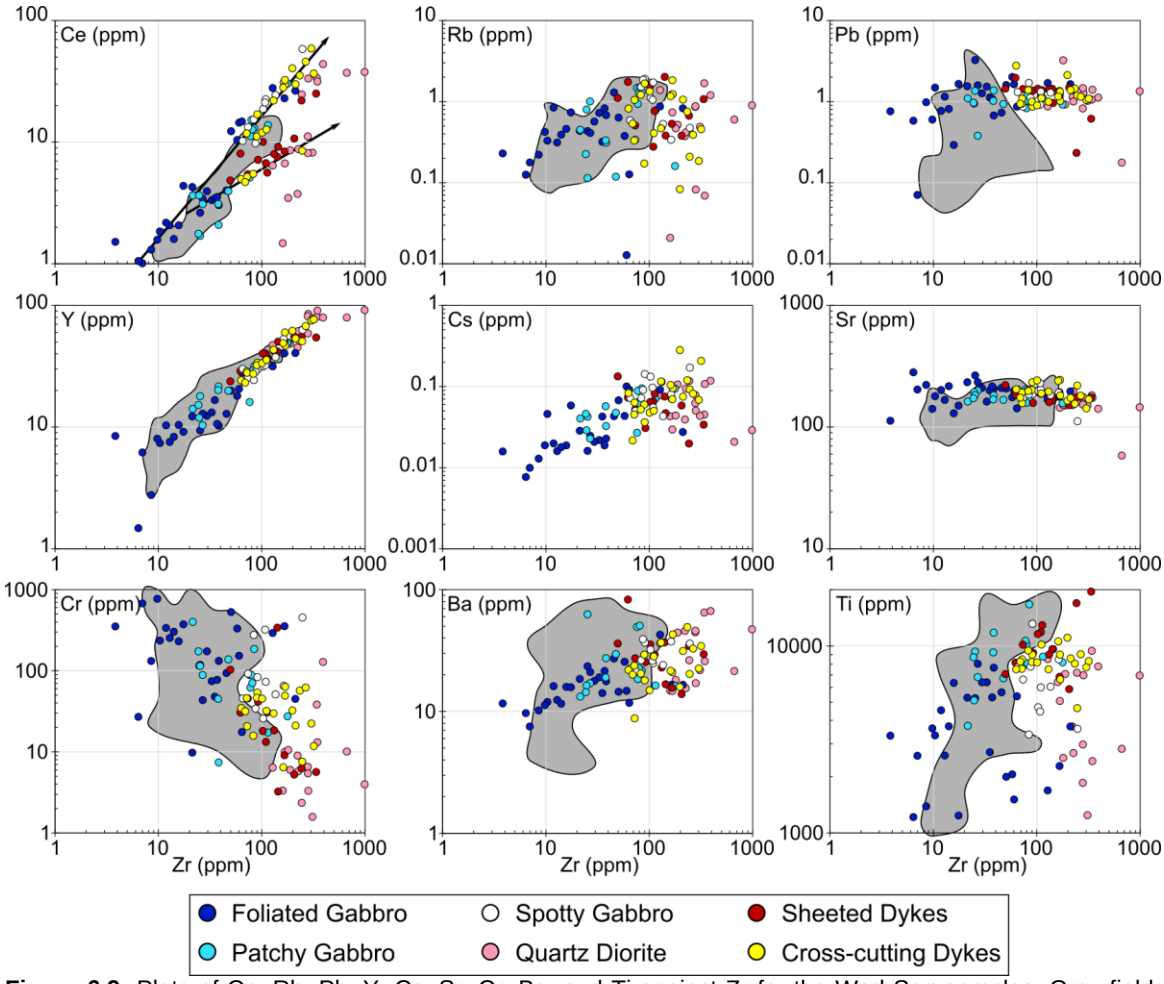

Figure 6.9: Plots of Ce, Rb, Pb, Y, Cs, Sr, Cr, Ba, and Ti against Zr for the Wad Saq samples. Grey fields represent data for the Wadi Abyad section (MacLeod and Yaouancq, 2000).

Coherent trends for the majority of the major oxides plotted against Zr and Mg# (100 x Mg / (Mg + Fe)) (Figure 6.10) suggest that their overall concentrations, if altered in any way, mirror their original compositions, reflecting comagmatic variations. Despite the relatively consistent correlations for most elements and in accordance with previous investigations (e.g., Lippard et al., 1986; Miyashita et al., 2003; MacLeod et al., 2013), we mostly consider a subset of the major elements and immobile trace elements (i.e., HFSE and REEs) in our interpretations of the petrogenetic histories for the Wadi Saq samples.

Table 6.1: Average, standard deviation (Stdev) and relative standard deviation (RSD) of major elements for each Wadi Saq unit.[a]

	Diorite (*N = 17*)			Foliated Gabbro (*N = 27*)			Patchy Gabbro (*N = 15*)			Spotty Gabbro (*N = 11*)			Sheeted Dykes (*N = 14*)			Cross-cutting Dykes (*N = 20*)		
	Average	Stdev	RSD[c] (%)	Average	Stdev	RSD (%)	Average	Stdev	RSD (%)	Average	Stdev	RSD (%)	Average	Stdev	RSD (%)	Average	Stdev	RSD (%)
Major elements (wt. %)																		
SiO_2	66.82	5.39	8.06	47.38	1.61	3.39	48.20	1.53	3.17	49.14	1.55	3.16	54.10	3.79	7.00	50.94	4.39	8.62
TiO_2	0.76	0.39	51.43	0.45	0.20	45.61	1.38	0.59	42.66	1.07	0.47	43.71	1.59	0.34	21.60	1.41	0.23	16.54
Al_2O_3	13.62	1.18	8.67	19.20	3.59	18.67	15.25	2.03	13.28	15.83	1.96	12.38	14.70	0.54	3.68	14.93	0.50	3.36
Fe_2O_3(T)	6.59	2.37	35.87	5.98	1.82	30.53	11.48	2.81	24.47	9.66	2.72	28.17	11.09	1.37	12.38	11.10	3.67	33.03
MnO	0.07	0.04	61.60	0.10	0.03	32.43	0.18	0.04	21.69	0.14	0.05	32.53	0.11	0.04	33.17	0.14	0.04	30.03
MgO	1.07	0.62	58.45	7.93	3.03	38.15	7.08	1.35	19.08	7.49	1.93	25.84	4.27	2.05	48.16	5.90	1.50	25.48
CaO	3.18	1.15	36.26	14.36	1.55	10.78	11.02	1.56	14.19	11.65	2.23	19.15	6.52	1.45	22.17	9.15	2.95	32.18
Na_2O	5.75	0.95	16.56	2.32	0.82	35.23	3.14	0.74	23.42	3.04	0.81	26.68	5.21	0.95	18.16	3.44	1.20	34.80
K_2O	0.17	0.12	71.80	0.10	0.07	66.10	0.17	0.08	47.68	0.19	0.07	40.45	0.22	0.14	61.11	0.20	0.11	52.61
P_2O_5	0.20	0.13	64.62	0.03	0.02	63.89	0.07	0.04	58.44	0.07	0.03	41.97	0.25	0.08	34.27	0.14	0.03	24.09
LOI	1.44	0.47	32.90	2.11	0.68	31.94	2.02	0.74	36.81	2.05	0.48	23.59	2.01	0.80	39.57	2.74	1.04	37.86
Mg#[b]	24.74	8.55	34.55	73.00	8.94	12.24	58.23	7.33	12.58	63.09	10.27	16.28	43.90	10.68	24.32	54.50	9.33	17.12

Notes:

[a] Full results tables for each unit are reported in Appendix III

[b] Mg# = Mg / Mg + Fe^{2+} assuming Fe^{3+}/Fe^{2+} = 0.12

[c] RSD (%) = [100 x Stdev] / Average; see Appendix II for more information

Table 6.2: Average, standard deviation (Stdev) and relative standard deviation (RSD) of trace elements for each Wadi Saq unit.a+B37:AB67

	Diorite (*N = 17*)			Foliated Gabbro (*N = 27*)			Patchy Gabbro (*N = 15*)			Spotty Gabbro (*N = 11*)			Sheeted Dykes (*N = 14*)			Cross-cutting Dykes (*N = 20*)		
	Average	Stdev	RSD[b] (%)	Average	Stdev	RSD (%)	Average	Stdev	RSD (%)	Average	Stdev	RSD (%)	Average	Stdev	RSD (%)	Average	Stdev	RSD (%)
Trace elements (ppm)																		
V	15.0	13.1	87.1	154.1	53.2	34.5	364.0	166.7	45.8	293.9	116.9	39.8	216.2	100.0	46.3	302.7	78.3	25.9
Cr	14.7	29.9	203.4	228.1	199.0	87.2	106.2	95.2	89.6	136.8	143.9	105.2	46.8	86.5	184.7	32.8	17.2	52.4
Co	6.7	2.9	43.5	30.0	10.4	34.6	41.8	7.5	17.9	39.0	8.9	22.8	24.3	9.4	38.5	38.9	18.4	47.2
Ni	35.4	40.5	114.3	134.1	80.4	60.0	157.1	110.1	70.0	106.9	55.7	52.1	148.3	278.8	188.0	260.6	765.3	293.7
Cu	16.6	12.3	73.7	42.9	29.7	69.4	51.1	29.4	57.5	36.1	21.6	59.8	28.8	26.5	92.2	44.0	53.8	122.2
Zn	27.9	20.5	73.6	34.3	16.8	49.1	78.3	33.0	42.1	56.5	21.0	37.2	38.5	22.8	59.3	70.8	62.5	88.3
Ga	20.1	2.0	10.1	13.1	2.0	15.3	15.3	1.4	9.4	14.5	1.9	13.1	18.6	2.1	11.1	16.6	1.8	11.1
Rb	0.8	0.5	65.9	0.4	0.3	68.1	1.0	0.6	56.6	0.8	0.4	51.1	0.9	0.6	69.9	0.7	0.5	65.3
Sr	141.5	40.0	28.2	193.1	37.9	19.6	171.2	21.8	12.7	187.8	33.1	17.6	183.5	29.0	15.8	197.2	50.3	25.5
Y	83.7	17.0	20.3	9.4	3.5	37.4	22.9	7.1	30.9	20.5	6.9	33.8	50.6	14.5	28.6	34.2	11.2	32.8
Zr	410.3	189.8	46.2	18.8	11.5	61.3	56.3	24.4	43.3	58.9	28.8	48.9	194.2	79.2	40.8	113.3	80.1	70.7
Nb	8.5	1.6	19.1	0.6	0.3	57.1	1.6	0.8	50.5	1.5	0.8	54.6	5.2	2.2	41.7	2.7	1.4	50.1
Cs	0.1	0.1	64.2	0.0	0.0	76.2	0.1	0.0	48.1	0.1	0.0	31.7	0.1	0.0	48.7	0.1	0.0	33.3
Ba	40.3	21.2	52.5	15.2	5.0	33.1	30.7	25.3	82.4	19.9	5.9	29.8	29.7	14.0	47.1	21.2	10.8	50.9
La	13.3	3.9	29.3	0.9	0.4	42.5	2.4	0.8	32.9	2.5	1.2	48.5	7.7	2.7	35.1	4.7	2.0	42.9
Ce	37.2	9.9	26.6	2.6	1.1	42.5	6.9	2.4	34.1	7.2	3.3	46.4	21.0	7.0	33.6	13.1	5.5	42.0
Pr	6.0	1.4	24.0	0.4	0.2	42.1	1.2	0.4	35.5	1.2	0.6	46.1	3.5	1.1	32.5	2.1	0.9	41.4
Nd	28.0	5.6	20.1	2.4	0.9	38.5	6.2	2.0	32.2	6.2	2.6	41.7	16.9	5.4	32.1	10.5	3.9	37.5
Sm	8.5	1.7	20.0	0.9	0.3	38.3	2.2	0.7	33.6	2.1	0.8	36.9	5.5	1.7	31.6	3.5	1.2	33.1
Eu	2.1	0.3	14.6	0.5	0.1	24.3	0.9	0.2	24.0	0.8	0.2	27.8	1.7	0.5	30.8	1.2	0.2	18.9
Gd	10.1	1.7	17.4	1.2	0.4	36.7	2.9	0.9	31.8	2.6	0.9	32.7	6.4	1.8	28.8	4.2	1.2	28.1
Tb	1.9	0.4	18.9	0.2	0.1	38.3	0.5	0.2	31.5	0.5	0.2	34.2	1.2	0.3	28.8	0.8	0.2	29.5
Dy	13.0	2.6	19.7	1.6	0.6	37.3	3.7	1.1	30.9	3.4	1.2	34.4	8.0	2.2	27.7	5.4	1.6	30.3
Ho	2.7	0.5	19.9	0.3	0.1	36.8	0.8	0.2	32.0	0.7	0.2	33.8	1.6	0.5	27.9	1.1	0.3	30.2
Er	8.4	1.8	21.1	0.9	0.3	38.6	2.2	0.7	31.6	2.0	0.7	34.8	4.8	1.4	28.7	3.3	1.0	31.9
Tm	1.4	0.3	21.4	0.1	0.1	39.5	0.4	0.1	32.5	0.3	0.1	35.6	0.8	0.2	28.9	0.5	0.2	33.1
Yb	9.1	2.1	22.8	0.9	0.3	38.4	2.3	0.7	32.8	2.1	0.8	37.1	5.0	1.4	27.8	3.5	1.2	34.1
Lu	1.4	0.3	22.5	0.1	0.1	39.0	0.3	0.1	32.3	0.3	0.1	36.3	0.8	0.2	28.6	0.5	0.2	37.1
Hf	9.6	3.9	40.6	0.5	0.3	56.9	1.5	0.6	39.1	1.4	0.6	44.8	4.3	1.6	37.5	2.6	1.7	63.6
Ta	0.6	0.2	25.5	0.0	0.0	56.5	0.1	0.1	67.1	0.1	0.1	52.5	0.3	0.1	35.0	0.2	0.1	43.9
Pb	1.2	0.4	31.5	1.2	0.7	59.9	1.2	0.4	29.9	1.4	0.6	40.6	1.1	0.4	34.1	1.2	0.3	25.8
Th	1.2	0.4	35.8	0.1	0.2	154.9	0.2	0.1	38.7	0.2	0.1	44.9	0.5	0.2	37.5	0.3	0.2	54.1
U	0.4	0.1	34.4	0.0	0.0	91.1	0.1	0.0	43.4	0.0	0.0	73.9	0.2	0.1	42.3	0.1	0.1	67.7

Notes:

[a] Full results tables for each unit are reported in Appendix III

[b] RSD (%) = [100 x Stdev] / Average; see Appendix II for more information

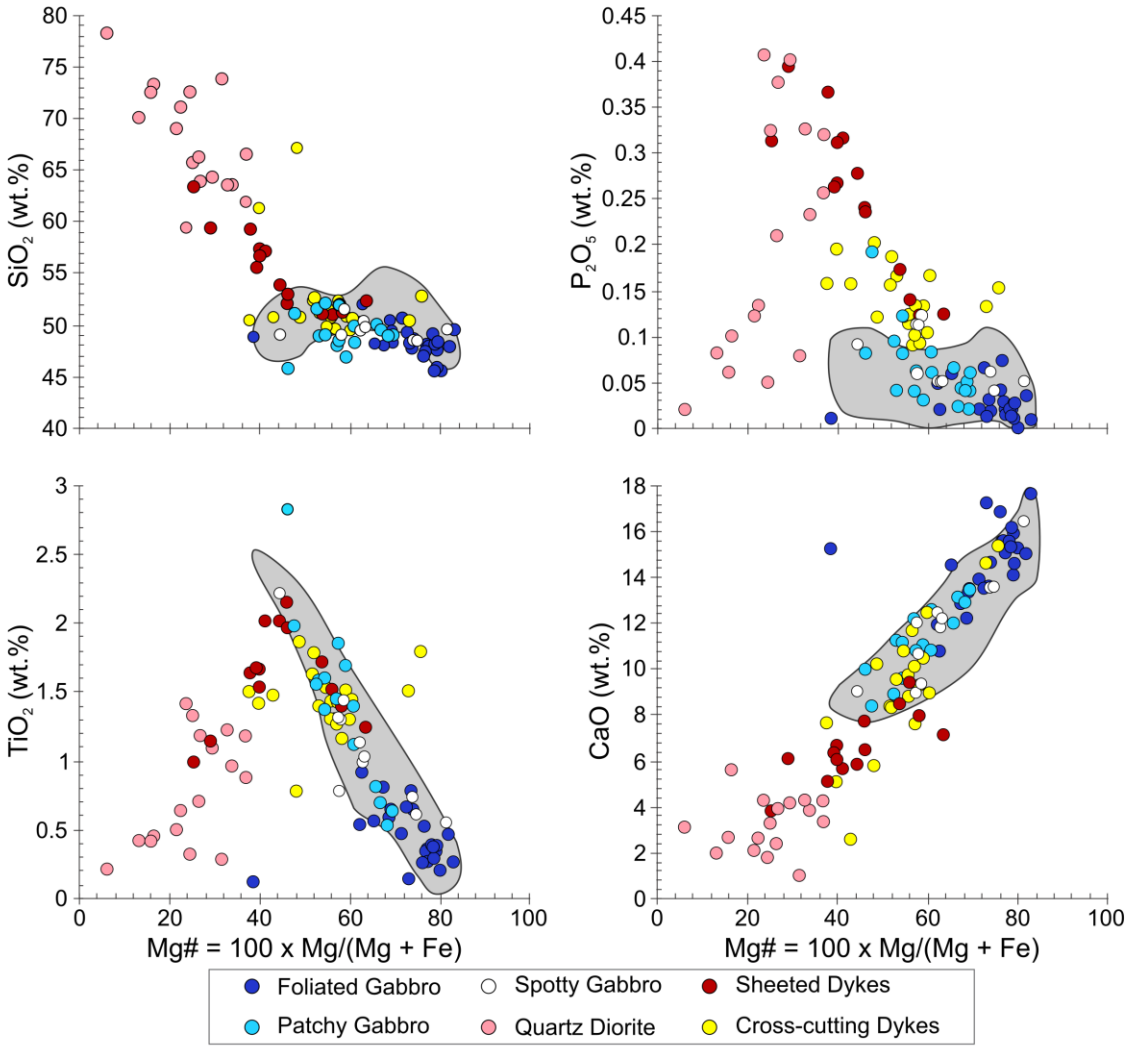

Figure 6.10: Whole rock Mg# plotted versus (**a**) SiO_2, (**b**) TiO_2, (**c**) P_2O_5 and (**d**) CaO for each of the units in the Wadi Saq area. Data from the Wadi Abyad section (MacLeod and Yaouancq, 2000) is plotted for comparison in the grey fields.

6.3.2 Foliated gabbros

The foliated gabbros cover the Mg# range of the gabbroic section but are characteristically more primitive (38.5-83.1, average 73.0) with relatively low incompatible element contents (e.g., TiO_2: 0.12-0.91 wt.%, average 0.45 wt.%) and variable, but mostly positive Eu anomalies (0.43-1.91, average 1.02) indicative of a cumulate origin. On average, the foliated gabbros display a marked increase in minimum Mg# and both minimum and maximum TiO_2 contents up section (Figure 6.11). We note that the Wadi Saq foliated gabbros share very little overlap with the known compositional range of the Ibra Valley volcanic crust as found in the Oman DB due to their likely cumulate origin (MacLeod et al., 2013) (Figure 6.11). For the most part, the range of subfacies within the foliated gabbros can be considered as a continuous range of modal

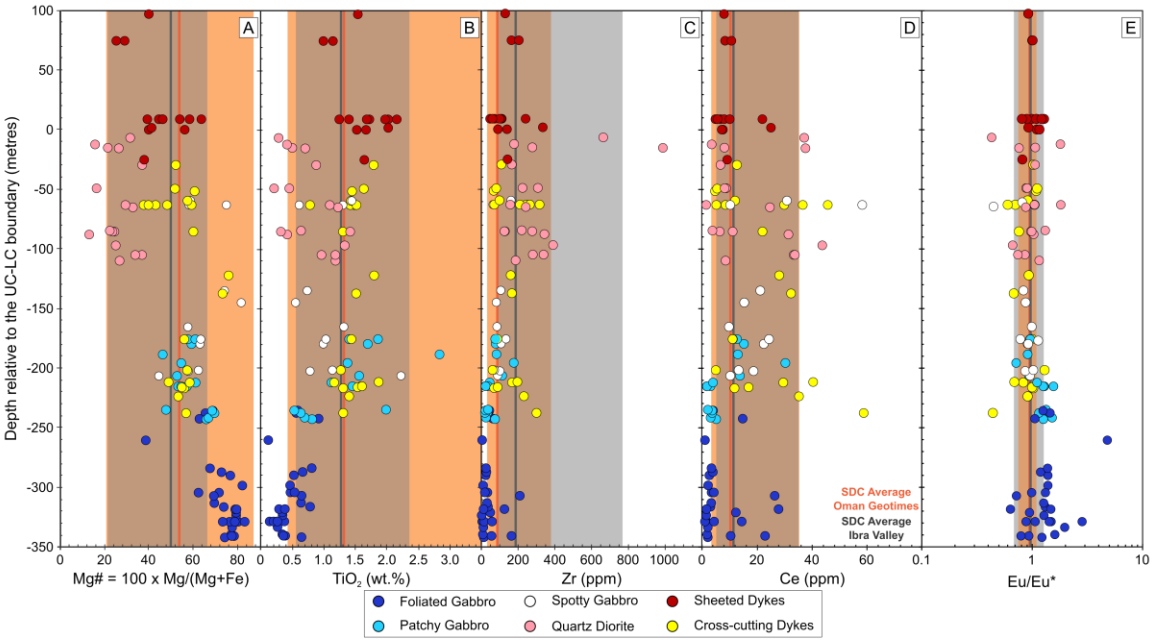

Figure 6.11: Variations in whole rock (**a**) Mg#, (**b**) TiO2, (**c**) Zr and (**d**) Ce (**e**) and Eu/Eu* anomaly plotted against sample depth relative to the upper crust-lower crust (UC-LC) boundary, or the base of the sheeted dykes.

variations with the exception of anorthosite and pegmatite lenses; hence, we consider the gradational range of subfacies as a whole (FG) and the anorthosites (FG-A) and pegmatites (FG-P).

The main FG group (18 samples) is characterised by moderately primitive Mg# (65.4-83.1, average 75.2) with low TiO_2 concentrations (0.2-0.79, average 0.47) and more positive Eu anomalies (0.63-1.97, average 1.26) relative to the bulk of the unit, reflecting a relatively plagioclase-rich cumulus nature.

The FG-A group (3 samples), which includes samples which were determined petrographically to have modes which fall in the transition between pure anorhtosite and the main FG group, is characterised by lower Mg# (38.5-78.6, average 63.4), lower TiO_2 concentrations (0.12-0.36, average 0.21), and strong positive Eu anomalies (1.43-4.79, average 3.02) relative to the bulk unit, reflecting its plagioclase-rich cumulate nature.

The FG-P group (6 samples) is characterised by moderate Mg#s (62.3-79.4, average 71.3) with enriched TiO_2 concentrations relative to the bulk foliated gabbros (0.25-0.91, average 0.51) and moderately positive Eu anomalies (0.72-1.47, average 1.04). The range of Eu anomalies likely reflects variability in plagioclase content for FG-P cumulates.

Rare earth element (REE) patterns for the foliated gabbros (Figure 6.12) cover almost the entire range of concentrations of the plutonic section and have positive Eu anomalies with the exception of a single sample from the FG group and 3 samples from the FG-P group. The range of REE-patterns in the FG-P group likely reflects variations in the degree of fractionation of the parental melt. The FG-P group is enriched in Ce (average 14.1 ppm) and depleted in Zr (average 13.7 ppm) relative to the FG-A (Ce = 1.3 ppm; Zr = 16.0 ppm) and FG (Ce = 5.2 ppm; Zr = 20.9 ppm) groups, suggesting that the FG-P on average is more fractionated than the rest of the foliated gabbros. This is most obvious in Figure 6.13 where the FG-P, with the exception of 1 sample, is enriched in most elements relative to the rest of the foliated gabbros. Some of the foliated gabbros, particularly the FG-P, are depleted in Cr, Ti and V, suggesting that they have fractionated spinel and oxides. Interestingly, the Wadi Abyad foliated gabbros show no signs of oxide accumulation or fractionation.

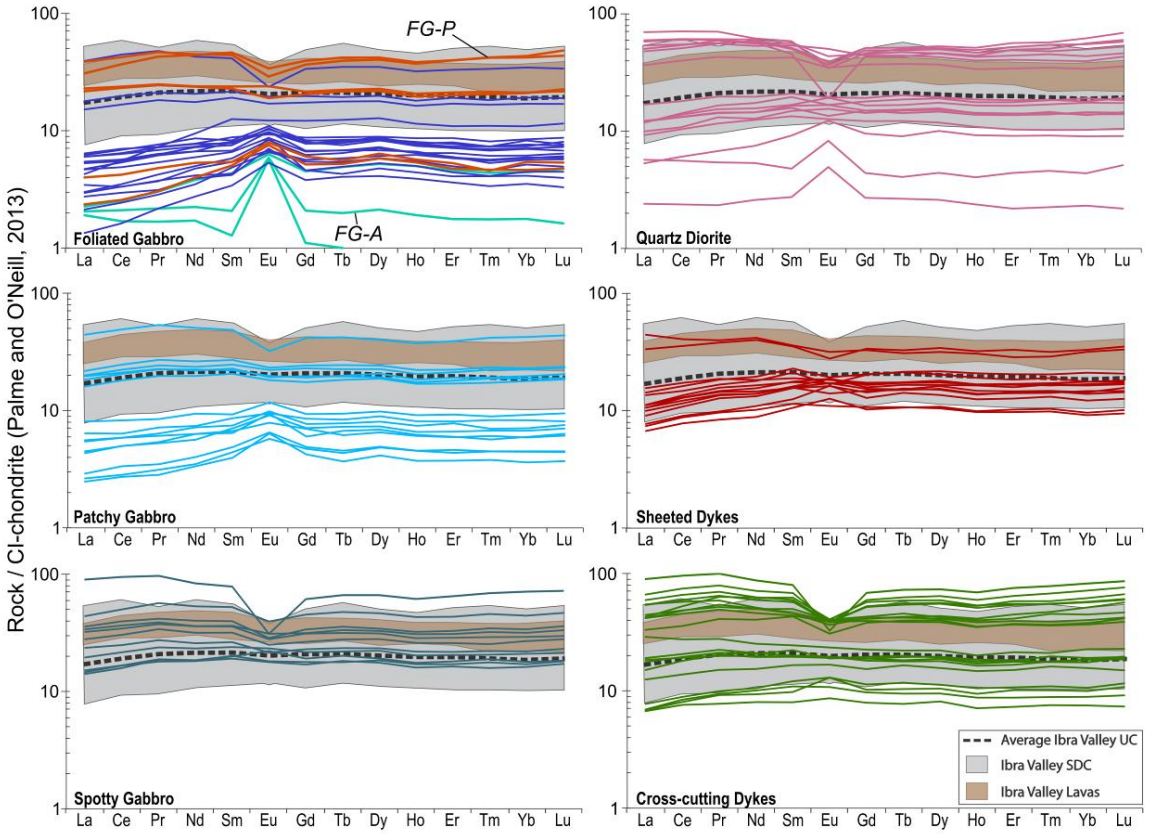

Figure 6.12: Whole rock REE plots by lithologic unit. The range of analyses of Ibra Valley sheeted dykes from the Oman DB (MacLeod et al., 2013) are plotted for comparison.

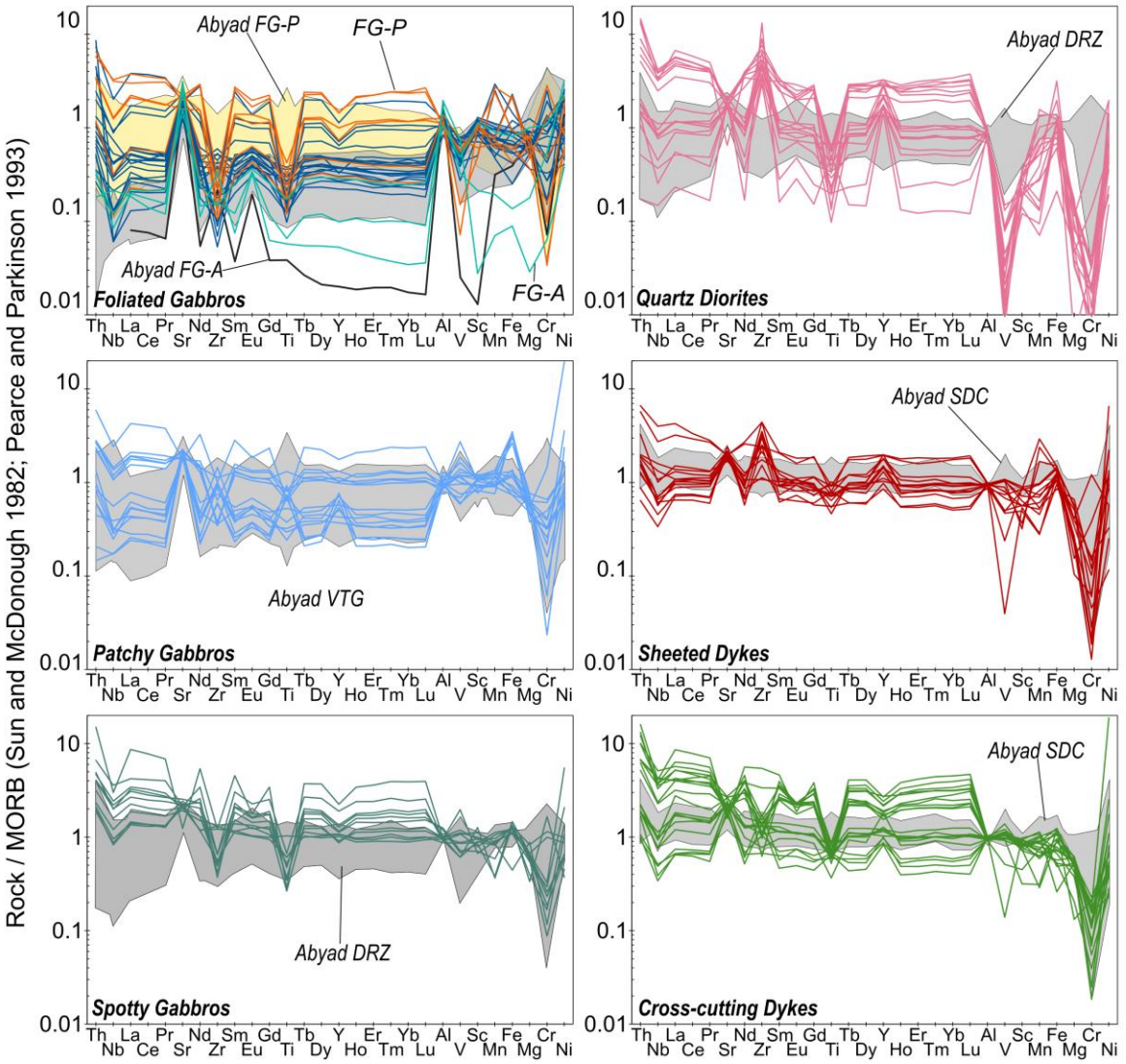

Figure 6.13: MORB-normalised (Sun and McDonough, 1982; Pearce and Parkinson, 1993) extended spider diagrams for the Wadi Saq section. Data from the Wadi Abyad foliated gabbros (FG) including anorthosites (FG-A) and pegmatites (FG-P), varitextured gabbros (VTG), dyke rooting zone (DRZ), and sheeted dyke complex (SDC) were provided by Christopher MacLeod.

6.3.3 Patchy gabbros

The patchy gabbros have more moderate Mg#s relative to the foliated gabbros (46.3-70.1, average 58.2), a range of incompatible element concentrations (e.g., TiO_2: 0.52-2.78, average 1.38) which increase in samples with more abundant pegmatite patches, and moderate Eu anomalies (0.72-1.56, average 1.14). In contrast to the foliated gabbros, the patchy gabbros fall within the known compositional ranges for both the Ibra Valley volcanics (Figure 6.11) and some of the Wadi Abyad upper plutonics (Figure 6.10), implying that the patchy gabbros likely crystallised from melts which were within the compositional range of the Ibra valley dykes and the high-level Wadi Abyad gabbros. Compared to the FG-P group, the patchy gabbros have higher Mg#s on average (i.e., 58 versus 71) and are more

highly enriched in high-field strength elements (e.g., Zr, average 56.3 ppm) than in REEs (e.g., Ce, average 6.9 ppm), suggesting that (i) the parental melts of the patchy gabbros have yet to fractionate zircon and (ii) the more fractionated parental melts of the FG-P group likely occurred later, assuming the gabbroic section evolved from a relatively homogeneous melt composition. The most depleted REE patterns of the patchy gabbros in Figure 6.12 belong to samples collected from the transition between the foliated and patchy gabbros and samples which contain an abundance of very large pegmatite patches. Samples with REE patterns falling towards the middle of the range (i.e., OM14-ML50, 51, 54, 57, and 93) lack any Eu anomalies and are found to contain an abundance of smaller, more diffuse pegmatite patches mixed with the background isotropic gabbro in thin section; suggesting that these REE patterns are the result of mixing between these two textural endmembers. In fact, those samples containing a larger proportion of or nearly pure pegmatite patches (found predominantly towards the top of the unit) are found to have more negative Eu anomalies relative to the more positive Eu anomalies of those samples with larger proportions of the host isotropic gabbro (Figure 6.11), suggesting that the pegmatite patches may be former liquids and the relatively patch-free isotropic gabbros may be cumulates. The most REE-enriched pattern (OM14-ML95) is found to contain more of the background isotropic gabbro in thin section with occasional pegmatites forming more diffuse, gradational patches. In Figure 6.13, we find that all of the patchy gabbros have either accumulated or fractionated oxides and the pegmatites tend to be more Fe-rich, comparable to the ferrogabbro pegmatites found within the varitextured gabbros of Wadi Abyad (MacLeod and Yaouancq, 2000).

6.3.4 Spotty gabbros

Relative to the stratigraphically lower patchy gabbros, the spotty gabbros cover a wider range of Mg# (44.0-81.3, average 63.1) with moderate incompatible trace element contents (e.g., TiO_2: 0.53-2.20, average 1.07) and, with the exception of OM14-ML11 (Eu/Eu* = 0.45), slightly positive to no Eu anomalies (0.45-1.28, average 0.88). Although they plot entirely within the compositional range of the Wadi Abyad upper gabbros (Figure 6.10), the spotty gabbros completely cover and partially overlap the range of TiO_2 contents and Mg#, respectively, for the Ibra Valley volcanics (Figure 6.11). The average trace element contents of the spotty

gabbros are very similar to those of the patchy gabbros (e.g., Ce, average 7.2 ppm; Zr, average 58.9 ppm) with REE patterns plotting towards more enriched compositions (Figure 6.12). Like the patchy gabbros, the enrichment in Zr likely indicates an evolved liquid which has yet to fractionate zircon. Cumulate textures in thin section suggest that the enriched compositions and relatively smooth REE patterns of the spotty gabbros are the result of mixing (i.e., crystals and intercumulus liquid) and not crystallisation from a pure liquid. The extended spider diagram in Figure 6.13 shows that all of the spotty gabbros, like the patchy gabbros, have either fractionated or accumulated oxides. In comparison, the high-level gabbros from Wadi Abyad show evidence for oxide accumulation but not fractionation (MacLeod and Yaouancq, 2000).

6.3.5 Quartz diorites

The quartz diorite unit is characterised by low Mg# (5.4-36.9, average 24.7), moderate incompatible element concentrations (e.g., TiO_2: 0.22-1.37, average 0.76) and variable Eu anomalies (0.43-1.81, average 1.02); compositions which share little to no overlap with upper plutonics of the Wadi Abyad section (Figure 6.10) and partially overlap with the Ibra Valley sheeted dykes in major element chemistry (Figure 6.11). On average, the quartz diorite unit is significantly enriched in trace elements (e.g., Ce, average 37.2 ppm; Zr, average 410.3 ppm) with REE patterns covering the bulk of the range for the Wadi Saq plutonics (Figure 6.12). Based on the extreme textural variability found within the quartz diorite unit in outcrop, hand sample, and thin section, we suggest that the resulting compositions and REE patterns are a reflection of mixing across such variability and do not attempt to decipher the data further. The diorites can be seen in Figure 6.11e to cover a similar range of Eu anomalies across the entire thickness of the unit. Samples which plot toward more positive Eu anomalies tend to have significantly less extreme textural variability, instead displaying gradual changes across samples with occasional discrete textural domains. All of the diorites in Figure 6.13 show evidence for either fractionation or accumulation of oxide with some samples exhibiting highly fractionated patterns with enriched Zr. The Ce vs Zr plot in Figure 6.9 suggests that there are two trends leading to the Zr enrichment which are likely related to a mixture of extreme fractionation and accumulation of zircon.

6.3.6 Sheeted and cross-cutting dykes

The sheeted dykes are characterised by moderately low Mg# (24.4-62.6, average 43.9), moderately high incompatible element concentrations (e.g., TiO_2: 0.97-2.15, average 1.59), and little to no Eu anomalies (0.81-1.13, average 1.02); compositions which partially overlap with the upper plutonics of the Wadi Abyad section (Figure 6.10) and fall towards the most enriched end of the known range for the Ibra Valley sheeted dyke complex (Figure 6.11). The major element chemistry of the sheeted dykes bridges the gap between the quartz diorite and gabbroic units, as it overlaps with the two disparate compositional groups in Figure 6.11. On average, the sheeted dykes are enriched in trace elements, falling approximately halfway between the average compositions of the quartz diorite and the gabbroic units (e.g., Zr, average 194.2 ppm; Ce, average 20.9 ppm) with REE patterns plotting mostly around the middle of the range of the Wadi Saq units and within the range of the Ibra Valley volcanics (Figure 6.12). Some of the sheeted dykes exhibit negative V anomalies (Figure 6.13), suggesting that, unlike the Wadi Abyad sheeted dykes (MacLeod and Yaouancq, 2000), they have fractionated oxide. We also note the presence of positive anomalies in Zr for the sheeted dykes (Figure 6.13), which plot approximately half-way between those of the extremely enriched quartz diorites and the other units. Positive Zr anomalies are characteristic of the quartz diorites whereas the spotty gabbros have strong negative anomalies and the foliated and patchy gabbros have more variable concentrations.

The cross-cutting dykes have slightly higher Mg# (37.6-75.2, average 54.5), slightly lower incompatible element contents (e.g., TiO_2: 0.77-1.86, average 1.41), and similar Eu anomalies (0.44-1.29, average 0.89) relative to the sheeted dykes. These compositions cover the compositional range of the Ibra Valley volcanics with some samples expanding the Ibra Valley range to both more primitive and more evolved compositions (Figure 6.11). On average, the cross-cutting dykes are more depleted in trace elements, relative to the sheeted dykes (e.g., Zr, average 113.3 ppm; Ce, average 13.1 ppm) and have REE patterns which cover a large portion of the range of the Wadi Saq units (Figure 6.12). The cross-cutting dykes within the plutonic section have similar, albeit slightly more depleted, compositions relative to the sheeted dykes. Two samples are found to have negative V anomalies in Figure 6.13, consistent with oxide fractionation. Unlike the sheeted dykes, the cross-cutting dykes in Figure 6.13 have variably positive and negative Zr anomalies

consistent with those seen in the patchy gabbros, but with concentrations akin to those of the spotty gabbros. The cross-cutting dykes include enriched compositions which more similar to those of the spotty gabbros than to the quartz diorites, suggesting they might represent a late stage of the axial sequence which was unable to mix with the more fractionated melt typically hosted within the quartz diorite melt lens. Further, the appearance of these cross-cutting dykes parallel to and along the foliated-patchy gabbro contact suggests along-strike lateral propagation of melts.

6.4 Discussion

6.4.1 The anatomy of the dyke-gabbro transition

The gradational boundaries and consistent geochemical trends observed across the lithological units of the Wadi Saq section suggest that the units share a common magmatic lineage, likely forming around the same time beneath the ridge axis. Although the cumulate foliated gabbros exhibit lateral modal and textural variability, the bulk of the samples within the unit follow a coherent trend towards more evolved compositions (e.g., lower Mg#, higher TiO_2; Figure 6.11 & 10)) up section with pegmatitic lenses occurring throughout the unit with fractionated and evolved compositions. The contact between the foliated and patchy gabbros is complex with a large portion of the contact appearing gradational. One sample from the patchy gabbro side of the contact between the two units (ML71) contains patches of olivine-bearing foliated gabbro within the coarse-grained subophitic matrix characteristic of the patchy gabbro, suggesting that the melt which sourced the patchy gabbro was expelled from the underlying foliated gabbros. This is further supported by (i) an overlap between the most primitive, relatively patch-free patchy gabbros and the more evolved foliated gabbros and (ii) the apparent continuous trend towards more evolved compositions up section between the units. As with the foliated gabbro-pegmatites, the pegmatite patches within the patchy gabbro appear to have relatively evolved, fractionated, liquid-like compositions. These compositions along with the tendency of the pegmatites to form diffuse networks and isolated patches may suggest that they were partly derived from late-stage trapped liquids within the isotropic, subophitic gabbro host. The spotty gabbro shares a generally gradational boundary with the patchy gabbros that is reflected in the complete compositional overlap between the two units (Figure 6.11 & 10).

The spotty gabbros are highly varitextured, typically characterised by more evolved compositions with higher concentrations of REEs and strong, consistent depletions in Zr and Ti relative to the patchy gabbros (Figure 6.13). The REE patterns for the spotty gabbros (Figure 6.12) suggests that they are comparable to the more REE-enriched patchy gabbros which typically contain greater proportions of pegmatite patches and occur towards the top of the patchy gabbro unit. We infer that the spotty gabbros are cumulates with higher proportions of fractionated liquids derived from the underlying patchy gabbro.

The quartz diorite unit is completely gradational with the spotty gabbro, suggesting that, although the diorite is evolved in composition, it is comagmatic with the more primitive gabbroic portions of the section. The major element compositions of the quartz diorite continue the evolutionary trends established by the gabbros (Figures 6.11 & 10) and exhibit REE patterns which cover the entire range of those seen in the gabbros (Figure 6.12). The gradational boundary between the quartz diorite and spotty gabbro coupled with the complete overlap between the most REE-enriched samples of both units suggests that they are likely cogenetic and derived from the same evolved melt. Magmatic flow fabrics occur between the diorite and dyke keels at the base of the sheeted dykes, and suggest that the dykes are sourced from the quartz diorite. This is supported, in part, by the observation of the sheeted dykes bridging the compositional gap between the gabbros and the diorites and the presence of strong, positive Zr anomalies for the sheeted dykes in Figure 6.13, which are characteristic of the quartz diorite. Thus, we interpret the quartz diorite as the fossilised AML for the Wadi Saq section. With our combined field- and geochemical evidence we have thus documented a continuous series of cumulates to evolved liquids comprising the upper portions of a magmatic system that fed the sheeted dykes of the Wadi Saq section (Figure 6.2).

6.4.2 The role of hydrous partial melting

Oceanic ‘plagiogranites’, a non-descriptive field term encompassing tonalities, trondhjemites, and granodiorites in predominantly mafic systems (defined in Coleman, 1977 and Koepke et al., 2007), are thought to be a common feature at the base of the sheeted dyke complex in ophiolites (Pallister and Hopson, 1981; Koepke et al., 2004, 2007; France et al., 2010). Though many potential

origins have been suggested, the two predominant processes suggested for producing such magmas are (i) extended fractional crystallisation of a MORB magma (e.g., Beccaluva et al., 1977; Coleman and Donato, 1979; Malpas, 1979; Aldiss, 1981; Dubois, 1983; Lippard et al., 1986; Amri et al., 1996; Floyd et al., 1998; Selbekk et al., 1998; Beccaluva et al., 1999; Niu et al., 2002; Rao et al., 2004; Bonev and Stampfli 2009; Rollinson, 2009), which has been verified in experimental studies (Dixon-Spulber and Rutherford, 1983; Berndt et al., 2005; Feig et al., 2006) and (ii) 'hydration melting' of hot gabbros or sheeted dykes initiated by influx of seawater-derived hydrothermal fluid from active shear zones (e.g., Malpas, 1979; Gerlach et al., 1981; Pederson and Malpas, 1984; Flagler and Spray, 1991; Spray and Dunning, 1991; Koepke et al., 2004, 2007; Wanless et al., 2010; France et al., 2010). The 'hydration melting' process has been proposed by many recent studies of these types of rocks in ophiolites (France et al., 2010), with such an anatectic origin being interpreted from trace element modelling and or observations of discrete patches of hornfelsic/granoblastic material within the AML horizon; this granoblastic material is often interpreted to represent the restites of partial melting of stoped pieces of the base of the sheeted dykes (Koepke et al., 2007, 2008, Nicolas et al., 2008; France et al., 2009, 2010, 2014). Some studies have even gone on to infer that the 'hydration melting' process has a main control on MORB geochemistry (e.g., Koepke et al., 2008; France et al., 2009, 2010)

A means for distinguishing between these two processes was proposed by Brophy (2009) based on the REE-SiO_2 systematics of mafic to felsic magmas in MOR environments. For liquids greater than ~62 wt. % SiO_2, hydration melting yields a negative to flat correlation between REE abundances and increasing SiO_2, while fractional crystallisation should yield a positive correlation (Brophy, 2009; Brophy and Pu, 2012). The quartz diorite unit exhibits a positive correlation between REE concentration and SiO_2, indicating a fractional crystallisation origin (Figure 6.14). The continuous trend which can be seen in SiO_2-La and SiO_2-Yb between the quartz diorite, sheeted dykes, and gabbroic units is consistent with field and geochemical observations suggesting that the unit is not a late intrusive, but is rather an extreme differentiate of the magmatic system. This is further supported by positive correlations between Ce (a light-REE) and Nb (Figure 6.15) and Zr (Figure 6.9) (incompatible trace element), which are continuous with the rest of the mapped units, and the correlations between Mg# and TiO_2 and SiO_2 (Figure

6.10A and 6.10B), which are both continuous with the rest of the mapped units and consistent with fractional crystallisation.

In considering the possibility of a 'hydrous melting' origin, we carried out a simple mass balance model wherein we took the results of partial melting experiments of altered sheeted dykes from the Oman ophiolite published by France et al. (2010) (Table 6.3) and calculated the equivalent thickness of dyke material that would need to be melted to create a 1x1x120 m tall column of the Wadi Saq diorite unit, and what volume of restite would be left after such a process (Table 6.3). The thickness of the diorite unit (Z_{DRT} = 120 m) is divided by the corresponding volume percent (F_{liq}) of liquid which most closely matches the diorite composition, resulting in the thickness of dykes (Z_{SD}) needed to be incorporated and melted in order to produce the observed 120 m thickness of the diorite unit:

$$Z_{SD} = \frac{Z_{DRT}}{F_{liq}}$$

The volume percent of restite left in the diorite after partial melting (F_{res}) is calculated as:

$$F_{res} = \frac{(Z_{SD} - Z_{DRT})}{Z_{SD}}$$

The results of this calculation (Table 6.3) show that a thickness of >12 km of sheeted dykes would need to be partially melted in order to produce a 120 m thick diorite unit with comparable Mg# to that of the Wadi Saq average (24.74), leaving behind a total restite thickness of 11,880 m (99 vol.%) in the field area. This is quite improbable as (1) we did not stumble across an 11.88 km thick body of granoblastic restites in the Wadi Saq area and (2) the average upper crustal (i.e., lavas + sheeted dykes) thickness in Oman is ~1.5-2 km (Nicolas et al., 1996). Further, the thickness of dykes required to produce a melt with the maximum Mg# found in the Wadi Saq diorite (i.e., 36.9) would be ~444 m and result in 73 vol.% (~ 324 m) of restites. Critically, we did not find any field evidence for patches of granoblastic material in the quartz diorite unit or within the rest of the Wadi Saq section. France et al. (2010) present this model in such a way that it seems perfectly viable for producing leucocratic melts; however, this model does not account for the extreme range of compositions or textures found in the Wadi Saq quartz diorite. The observation of the sheeted dykes rooting into the diorite body, and the diorite having a gradational rather than sharp contact with the spotty gabbro below it argues for a

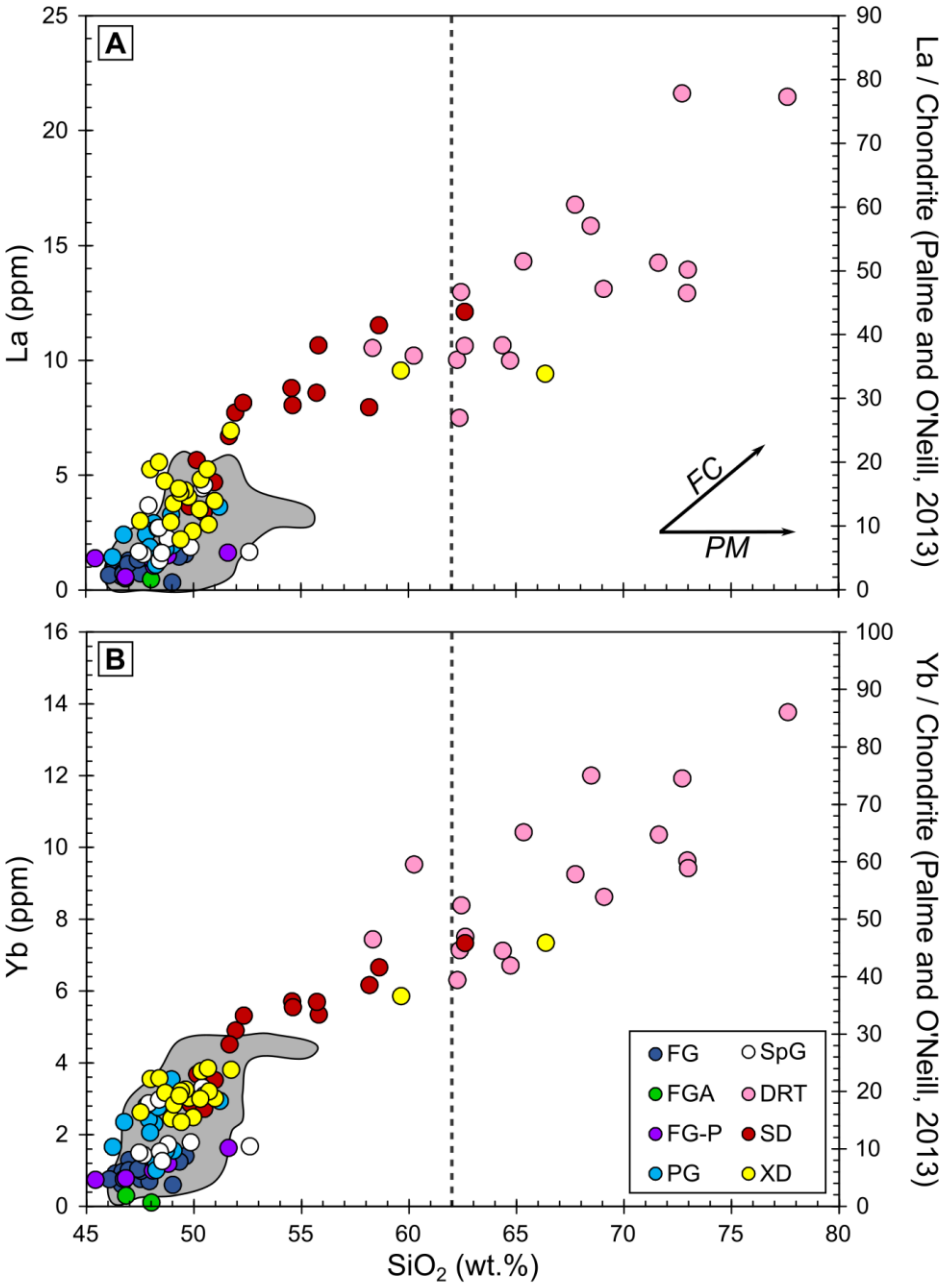

Figure 6.14: Plots of bulk-rock (**a**) La and (**b**) Yb versus SiO_2 (wt.%) for the Wadi Saw upper crustal section. The axes on the right side of the diagrams provide the values for La and Yb normalised to Chondrite values of Palme and O'Neill (2013). Grey fields represent the range covered by the Wadi Abyad section (MacLeod and Yaouancq, 2000).

comparatively simpler origin for the diorite unit. On this basis alone, the 120 m thick quartz diorite unit mapped in the Wadi Saq area could not have been formed solely or dominantly by stoping and re-melting of the base of the sheeted dykes. Hence, both the field- and geochemical data indicate that an origin of the quartz diorite by hydrous partial melting is very unlikely.

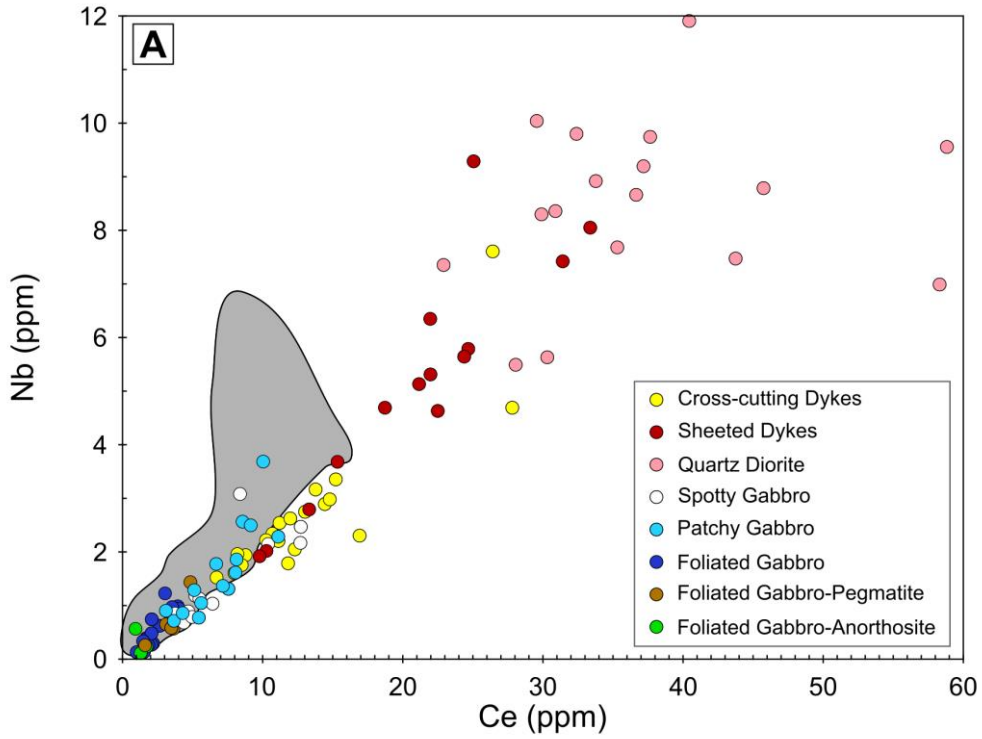

Figure 6.15: Plot of bulk-rock Nb versus Ce for the Wadi Saq units. The generally positive slope of the trend is consistent with fractional crystallisation. Grey fields represent the range covered by the Wadi Abyad section (MacLeod and Yaouancq, 2000).

A third, often overlooked mechanism for producing such evolved rocks in MORB-like environments is the presence of water in the parental melt. MELTs modelling (see the figure caption for 6.16 for model conditions) provided by MacLeod et al (2013) found that increasing concentrations of water in a melt accelerates Si enrichment in the liquid line of descent (Figure 6.16). This catalytic effect of water leads to the development of substantially more evolved and fractionated melts at a given melt fraction for moist melts compared to dry melts. Therefore, the point at which a melt reaches oxide saturation will be earlier in wetter melts, leading to larger volumes of more evolved liquids. This is illustrated in Figure 6.16b, where the addition of 0.1% H_2O results in oxide saturation (i.e., the peak in TiO_2) at ~20% liquid, a difference of 7% compared to the dry system. The presence of abundant brown amphibole in the Wadi Saq section suggests that the magmatic system was being fed by a moist melt. However, the most compelling evidence for a moist parental magma at Wadi Saq is in the abundance of Ti and V anomalies in extended spider diagrams (Figure 6.13) indicative of oxide accumulation and fractionation for all of the Wadi Saq units. This is critical when compared to the

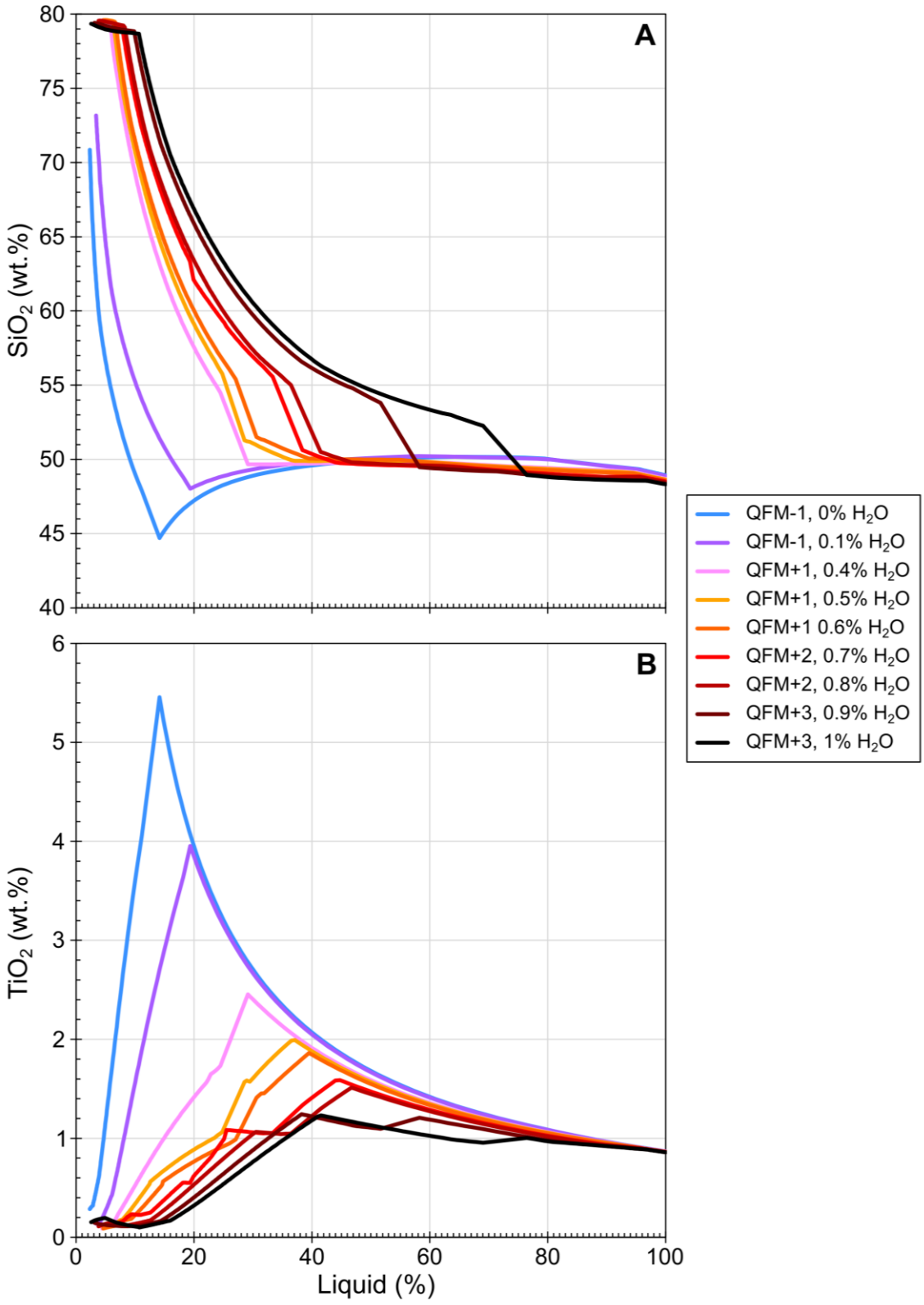

Figure 6.16: Plots of (**A**) SiO_2 and (**B**) TiO_2 versus melt fraction (liquid %) for MELTs models (Ghiorso and Sack, 1995) derived by MacLeod et al (2013). The models use a MORB parental melt composition (Kinzler and Grove, 1993) modified with lower initial TiO_2 (0.7 wt.%) to match the depletion observed in Oman. Fractional crystallisation models were carried out at 2 kbar with initial oxygen fugacity at the quartz-fayalite-magnetite buffer. Initial H_2O concentrations were varied progressively between 0 and 2 wt.% (MacLeod et al., 2013).

Table 6.3: Results of mass balance calculations for a hydrous melting origin of the quartz diorite unit

Experiment[a]	M 1030	M 1000	M 970	M 955	M 940	M 910	M 880	M 850
T (°C)	**1030**	**1000**	**970**	**955**	**940**	**910**	**880**	**850**
Melt SiO_2	55.5	59.2	63	64.4	69.3	69.3	71.2	72.6
Melt Mg#	48.9	49.0	46.8	43.8	38.0	33.9	32.9	26.3
F_{liquid} (vol%)	93	70	50	40	27	7	2	1
Calculated Values[b]								
Z_{SD} (m)	129	171	240	300	444	1714	6000	12000
$F_{restite}$ (vol%)	7	30	50	60	73	93	98	99

[a] Experimental runs from France et al (2010)

[b] As in the text, all values are calculated assuming a 120 m thickness of quartz diorite is created

Wadi Abyad section which shows no sign of either oxide accumulation or fractionation in the foliated gabbros or sheeted dykes, but does have oxide accumulation in the ferrogabbro pegmatites of the high-level gabbros (MacLeod and Yaouancq, 2000). The difference in oxide abundance between the Wadi Saq and Wadi Abyad sections raises key questions about where and when oxides have crystallised and reacted/precipitated and their effective mass balance. Unfortunately, these questions are outside of the scope of this investigation.

6.4.3 An evolved melt lens

The quartz diorite and sheeted dykes at Wadi Saq fall towards more evolved compositions compared to data for the entire Wadi Abyad section (Figure 6.10). We previously noted that the sheeted dykes trend towards more evolved compositions which are consistent with the range of extant data for the Ibra Valley volcanics (Figure 6.13; MacLeod et al., 2013) and suggests that Wadi Saq is not simply an anomalously evolved section within the Ibra Valley. In fact, the Wadi Saq section lies at the most fractionated end for the Oman Ophiolite. The MELTs models used in Figure 6.16 further support the idea that the units can be related by simple progressive fractional crystallisation of a moist (up to 0.6 wt.% H_2O; MacLeod et al., 2013) Geotimes melt composition. Such a moist parental magma might explain both the ubiquitous amphibole within the section, appearing even in the deepest portions of the foliated gabbros sampled by this study, and the abundance of quartz (both granular and in myrmekitic associations), Fe-Ti oxides, and amphibole within the quartz diorite unit. The fractional crystallisation models (Figure 6.16) show that increasing water contents within the starting melt results in

progressively earlier saturation of oxides (e.g., 0 wt. % H_2O, Fe-Ti oxide saturation at F = 0.16; 0.6 wt. % H_2O, Fe-Ti oxide saturation at F= 0.32), which roughly coincides with the saturation of phases like amphibole and quartz. This means that for a relatively dry system, oxides, amphiboles, and quartz might not be expected until there is only 15% melt left of the starting volume compared to 32% in a system with ~0.6 wt. % water; effectively doubling the volume of fractionated and evolved material that is produced. Therefore, a moist parental melt composition should result in an overall more evolved and fractionated upper crustal section.

The role of the quartz diorite in the Wadi Saq AML becomes apparent when we consider (i) the field observations of magmatic flow fabrics between the quartz diorite into the keels of dykes within the dyke-gabbro transition, (ii) the magmatic, gradational contacts between the quartz diorite and spotty gabbro units and (iii) the TiO_2, Fe_2O_3, and trace element (e.g., Zr) enrichments exhibited by the unit. Further, the Wadi Saq dykes are most similar in composition to the Geotimes volcanics (Figure 6.17), suggesting that they are not anomalous relative to the rest of the Oman ophiolite. However, while the plutonic portion of the Wadi Saq section lies at the fractionated end of the spectrum for the Oman ophiolite, the sheeted dykes at Wadi Saq have below average TiO_2 concentrations relative to that of the Geotimes lavas and dykes of the OmanDB database (Figure 6.11; MacLeod et al, 2013). The lower TiO_2 concentrations may reflect the comparatively high amount of oxides found in the upper plutonics at Wadi Saq. Thus, the relatively evolved nature of the Wadi Saq upper gabbros compared to those of Wadi Abyad (MacLeod and Yaouancq, 2000; Coogan et al., 2002) might be, among other factors, a function of higher concentrations of water in the parental melt and/or temperature variations along the paleo-ridge axis (MacLeod et al., in prep).

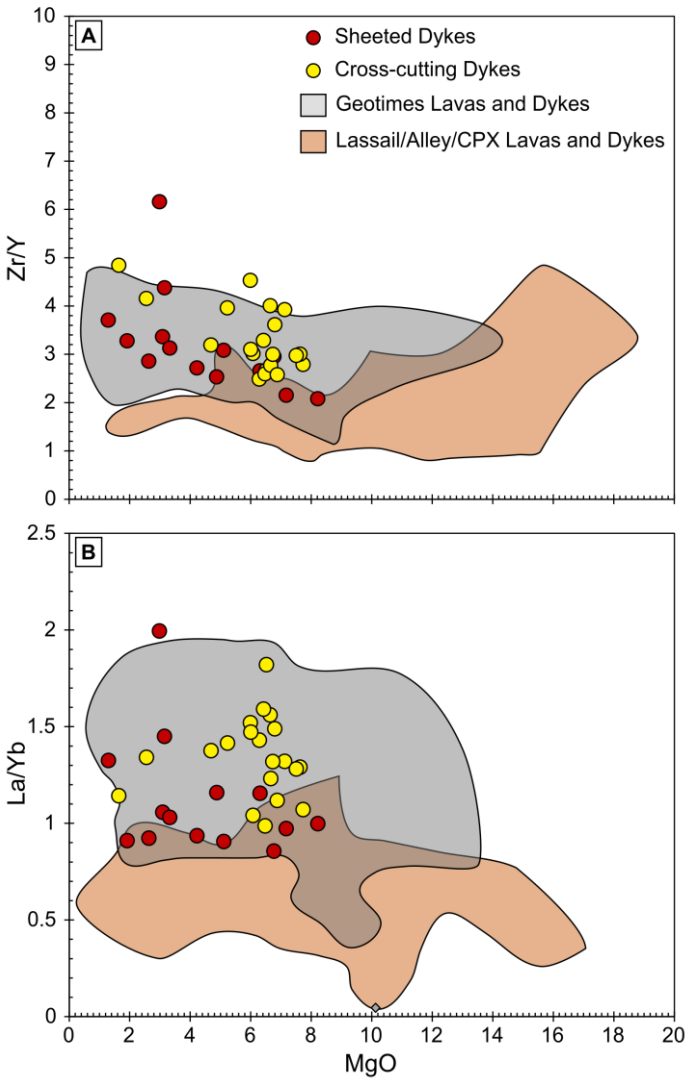

Figure 6.17: Bulk-rock (**a**) Zr/Y and (**b**) La/Yb versus MgO in Wadi Saq sheeted and cross-cutting dykes plotted relative to combined lavas and dykes for the Geotimes (i.e., 'V1') and Lassail/Alley/CPX-phyric (i.e., 'V2') volcanics in the OmanDB database (MacLeod et al., 2013).

6.5 Conclusions

Detailed mapping and sampling of the Wadi Saq DGT, north-eastern Ibra Valley, southern Oman Ophiolite has revealed a plutonic complex separating the sheeted dykes and the foliated gabbros comprised of three distinct units: an ophitic gabbro with pegmatitic patches (patchy gabbro; 70 m), overlain by a varitextured spotty gabbro (50 m), capped by an extremely varitextured quartz-diorite (120 m). The sheeted dykes are observed rooting in the quartz-diorite, and contacts between the plutonic units are gradational and subhorizontal. All of the units, except for the foliated gabbros, are isotropic, lacking any strong fabrics, and primary igneous amphibole and oxides are ubiquitous throughout the section, increasing in modal abundance towards the base of the sheeted dykes and indicating extensive

differentiation and/or the presence of small amounts of water in the primary liquid. Geochemical data, supported by field observations, suggest that all of the units can be related by simple progressive fractional crystallization of a moist Geotimes melt composition. The field relationships, as well as the relatively evolved composition of the overlying sheeted dykes and the bulk Ibra Valley volcanics, suggest that the Wadi Saq AML accommodated the formation of highly evolved melts relative to other sections like Wadi Abyad. We rule out a substantial role for hydrous partial melting in the origin of evolved melts at Wadi Saq, and instead suggest that small concentrations of water in the parental melt had a catalytic effect in accelerating the fractionation of the system. This is primarily based on (i) the lack of patches of granoblastic material in the field area, suggested to represent the restites of partially melted pieces of the sheeted dykes (France et al., 2010) and (ii) the composition of the quartz-diorite unit.

We see a gradual evolution up section in Wadi Saq which is consistent with observations provided from Wadi Abyad, however, the extremely evolved nature of the Wadi Saq dyke-gabbro transition contrasts with the more primitive AML and sheeted dyke complex documented in Wadi Abyad, suggesting that there is lateral variability in the AML along the Oman ridge axis. While Wadi Saq shows evidence for some degree of oxide accumulation and fractionation in every unit, the Wadi Abyad section only shows evidence for oxide accumulation in the ferrogabbro pegmatites within the varitextured gabbros. Further work is needed in order to determine exactly where and when oxides have crystallised and their effective mass balance in both sections.

Any working model for the Wadi Saq AML must address the evolved nature of the quartz diorite unit while taking into account those observations which suggest that it was derived from the same parental melts as the gabbroic units. Future work will require detailed major and trace element analyses of minerals for the various units in order to fully constrain the magmatic history of the section. The often complex, varitextured nature of the Wadi Saq gabbros and diorites will require the application of an element mapping technique (e.g., QACD) in order to confidently reconstruct these histories. Element maps of the Wadi Saq samples can then be used to inform the selection of locations for trace element analyses. Such data will be critical in assessing the role of the AML at Wadi Saq compared to Hess Deep.

CHAPTER 7
Summary and Conclusions

7.1 The QACD method

In seeking to fully characterize the petrologic and geochemical nature of the AML horizon at fast-spreading MORs, we have developed and optimised a method for the rapid collection and processing of full-thin section quantitative element maps to produce a quantitative assessment of compositional distribution (QACD). The QACD method and the Quack software, in which the method is incorporated, provide a new method for the rapid collection of full-thin section quantitative element maps and a new post-processing tool for calculating mineral modes, producing element intensity/concentration and molar ratio maps, and quantifying full-sample compositional distributions.

We have demonstrated that element mapping is critical in reconstructing the full histories of igneous rocks, with the QACD method, in particular, providing four major advantages over conventional methods for element map processing by (i) precluding operator bias as a statistically rigorous method and (ii) revealing the full range of mineral compositions and (iii) the extent and distribution of compositional zoning (iv) within the textural context of the sample. Our optimisation of element map collection for the QACD method has reduced the minimum amount of time expected for a quantitative element map from several days by WDS-EPMA down to 6-8 hours (Cardiff University SEM) on an EDS equipped SEM or EPMA; for the first time, making feasible the collection of element maps for a full suite of samples. The QACD method thus facilitates the incorporation of element mapping into the modus operandi of a petrologist for reconstructing the full histories of igneous rocks. Further, the open-source development of the Quack software with the Python coding language allows for users to readily modify and the adapt the software for to suit their own particular research.

7.2 The Wadi Saq AML

Although our analysis of the Wadi Saq AML horizon in the Oman ophiolite suggests that (i) water in the parent melt likely played a major role in the development of the system and (ii) the Wadi Saq AML fed the overlying sheeted dykes, the varitextured and evolved nature of the horizon together with the evolved composition of the overlying sheeted dykes and Ibra Valley volcanics suggest that

the Wadi Saq AML accommodated the formation highly evolved melts. The degree to which the Wadi Saq dyke-gabbro transition (DGT) is evolved contrasts with the more primitive, but still evolved, dyke-gabbro transition documented previously at Wadi Abyad in the Nakhl-Rustaq block further north in the Oman ophiolite (MacLeod and Yaouancq, 2000; Coogan et al., 2002a). This would suggest that there is lateral variability in the AML along the Oman ridge axis, which is consistent with recent geophysical observations (e.g., Marjanović et al., 2015; Carbotte et al., 2015) at modern fast-spreading MORs which suggest a discontinuous, segmented AML along the length of the ridge axis. The next logical step in understanding the processes which formed the Wadi Saq section is to collect detailed mineral major- and trace element data on the samples by EPMA and laser ablation (LA)-ICP-MS analysis, respectively.

7.3 The Hess Deep AML

In applying the QACD method to the Hess Deep AML sample suite, we have presented the first comprehensive investigation of the AML horizon at a fast-spreading MOR. Considering the results of our investigation at Hess deep together with our observations from the Oman ophiolite and geophysical and petrological constraints on the properties of the AML at modern fast-spreading MORs, we are able to address the first-order questions regarding the nature and role of the AML in oceanic crustal accretion posed in section 1.2 of this thesis.

7.3.1 What are the compositions of melts being delivered to the AML?

Our application of the QACD method to the Hess Deep AML sample suite revealed that plagioclase and pyroxene within the AML are much too evolved to be in equilibrium with MORB, with mean An_{55} and Mg# of 65.01 which are consistent with derivation from andesitic melts (Mg# <43). A critical lack of more primitive compositions within the Hess Deep AML suggests that if primitive melt is delivered to the AML, then it likely does not remain within the AML long enough to contribute extensive amounts of material to the horizon. Considering the highly fractionated, incompatible element enriched signatures of the clinopyroxenes analyzed in a few of the Hess Deep AML gabbros by Lissenberg et al. (2013), we propose that the AML receives and accommodates the storage and fractionation of highly evolved melts expelled from the underlying crystal mush.

7.3.2 What implications do these findings have for crustal accretion models?

Lissenberg et al (2013) report an overall upward fractionation of the plutonic sequence at Hess Deep that reaches its maximum in the AML horizon. Further, our data strongly suggest that the AML mostly crystallises from evolved, migrating interstitial melts. Together, these observations are difficult to reconcile with previous 'gabbroic glacier' models in which primitive melts fed from the mantle/lower crust are injected into and reside within the AML and crystallise significant gabbroic material (Morgan and Chen, 1993; Coogan et al., 2002). Thus, we conclude that the AML is not an active player in the accretion of the lower gabbroic crust. Instead, it is a passive player in lower crustal accretion, serving as a natural collection point for melts migrating upwards through the lower crust in response to buoyancy and compaction of the crystal mush (Lissenberg et al., 2013).

7.3.3 Is the AML an active or passive player in the development of MORB?

The compositions reported by our investigation are simply too evolved to be in equilibrium with mean EPR MORB. The evolved nature of the AML suggests that it plays an active, but subsidiary role in feeding the upper crust. This is consistent with the hypothesis that primitive MORB may be delivered to the AML where it reacts and mixes with the resident reacted, incompatible element enriched melt prior to eruption (Goss et al., 2010; Lissenberg et al., 2013). A rapid mixing and reaction between injections of large volumes of primitive MORB and the evolved extant melt of the AML could account for (i) the critical lack of primitive material in the AML horizon, (ii) the geochemical observations of phenocrysts populations in MORB lavas indicating melt mixing prior to eruption (Pan and Batiza, 2002, 2003; Goss et al., 2010; Moore et al., 2014) and (iii) the observed over-enrichments of incompatible trace elements in MORB (O'Neill and Jenner, 2012; Lissenberg et al., 2013).

7.4 A holistic model for the role of the AML at fast-spreading MORs

The AML, as suggested by the data presented in this thesis, is evolved in composition and accommodates the storage and fractionation of highly evolved melts. We propose a model wherein, between decadal eruptions, the AML is predominantly a crystal mush, fed by small volumes of evolved interstitial melts expelled from the underlying crystal mush. Short-lived, focused injection of primitive

melt in the months preceding eruption events leads to mixing of primitive melts with the extant highly fractionated melt, and triggers eruptions. This holistic model for the role of the AML at fast-spreading MORs reconciles the paradoxical mismatch between the volcanic and plutonic records with the geophysical constraints of the AML, the short residence times of Pacific MORB phenocrysts, and the observed incompatible trace element over-enrichments in MORB.

7.5 Future work

Our investigation, though comprehensive, only characterised the AML horizon sampled from the Hess Deep rift. If there is any lateral variability in the AML along axis as is suggested by geophysics and our analysis of the Wadi Saq section of the Oman Ophiolite, then it is likely that the compositions and processes that characterise the Hess Deep AML may not be representative of the AML horizon as a whole; thus, we cannot and should not assume that the nature of the AML is fully understood. Further comprehensive investigations of similar AML horizons from other locations along fast-spreading mid-ocean ridges are required if we are to fully understand the complex nature of the AML and the potential role(s) that it plays in the accretion of fast-spreading MOR crust. Such investigations should seek to establish whether the evolved compositions determined at Hess Deep are a general feature of the AML along MORs and address questions such as:

- How is the AML affected by variations in primary melt composition (e.g., water)?
- How is the AML affected by variations in mantle temperature along-axis?
- How is the AML affected by along-axis variations in melt volume?

APPENDIX A
Sample locations and petrography

A1 Hess Deep: JC21 Dive 78

Table A1 contains the locations and thin section descriptions (including modal phase estimates) for the JC21 Dive 78 thin sections which were analysed for element maps by this study. Naming conventions for lithological classification follow IODP procedures as indicated in the annotation for Table A1 and are as follows:

- Lithology
    - Gabbro: < 5% orthopyroxene
    - Gabbronorite: > 5% orthopyroxene
    - Troctolite: > 5% olivine
    - Trondhjemite: > 20% quartz and < 1% K-feldspar
    - Totally altered: no igneous relics
    - Breccia: mixed lithologies
- Modifiers
    - Troctolitic: 5% < clinopyroxene < 15%
    - Olivine: 5% < olivine
    - Olivine-bearing: 1% < olivine < 5%
    - Orthopyroxene-bearing: 1% < orthopyroxene < 5%
    - Disseminated oxide: 1% < oxides < 2%
    - Oxide: 2% < oxides
    - Anorthositic: 80% < plagioclase

Table A.1: Sample locations and their respective thin section descriptions for Hess Deep Dive 78 thin sections mapped by this study.

Sample	Lat (N) (*WGS 84*)	Lon (W) (*WGS 84*)	Water depth (*mbsl*)	Lithology[a]		Modal phase abundances[b]					Alteration (~%)	Accesory minerals	Notes on thin section
				Handsample	Thin Section	Ol	Pl	Cpx	Opx	Ox			
JC21-78R-1A	2.3081	101.5225	3160	disseminated oxide gabbronorite	disseminated oxide gabbronorite	-	45	44	**10**	1	20	Sulphide, apatite, minor brown amphibole	Weak shape preferred orientation in felsdpars; Evidence for minor subgrain formation and rotation in feldspars. Oxides are late and disseminated over the area of the thin section. One grain may be a heavily altered and exsolved opx, but at first glance, there are no other possible opx. Boundaries of interstitial cpx with plag are rarely embayed or shown signs of reequilibration. Many cpx have occasional small plagioclase grains in them, but not enough that
JC21-78R-1B	2.3081	101.5225	3160	disseminated oxide gabbronorite	disseminated oxide gabbronorite	-	47	47	**5**	1	25	Sulphide, apatite, minor brown amphibole	Little to no fabric. Varitextured with evidence for clinopyroxene symplectite textures. Brown amphibole present as very low abundance interstitial phase. Orthopyroxene is mostly altered out.
JC21-78R-1D	2.3081	101.5225	3160	disseminated oxide gabbronorite	disseminated oxide gabbronorite	-	46	46	**7**	1	30	Sulphide, apatite, zircon minor brown amphibole	Like 1B; kink banding in cpx and evidence for sub-grain rotation
JC21-78R-2B	2.3078	101.52257	3132	oxide gabbro	oxide melagabbro	-	35	55	-	10	50	5% brown amphibole, apatite, zircon, sulphide	Very altered- lots of amphiboles, chlorite, and secondary cpx. Possible clinopyroxene symplectite textures.
JC21-78R-2F	2.3078	101.52257	3132	oxide gabbro	oxide melagabbro	-	30	60	-	10	45	Brown amphibole, apatite, sulphide	Like 2B but with larger plagioclase grains and more clinopyroxene. Also heavily altered
JC21-78R-3	2.3073	101.5228	3117	oxide gabbronorite		-	45	35	15	5	30	Brown amphibole, apatite, sulphide	Like sample 78R-2 but with some possible fresh Opx; Cpx symplectites present.
JC21-78R-3A	2.3073	101.5228	3117	oxide gabbronorite	disseminated oxide gabbronorite	-	55	40	5	2	25	Amphibole and quartz alteration, maybe apatite	Well developed foliation defined by blobky to tabular plagioclase. Oxide is a large interstitial phase. A lot of pyroxene exsolution; opx present as large, altered, random grains. Larger opx grains are some what poikilitic/subophitic. Cpx symplectite textures abound.
JC21-78R-3C	2.3073	101.5228	3117	oxide gabbronorite	oxide gabbronorite	-	45	50	5	3	25	Amphibole and quartz alteration, apatite, zricon	Like 3A but with more plagioclase and vague hints of former fabrics of various orientations across the sample. A lot of pyroxene exsolution; opx present as large, altered, random grains. Larger opx grains are some what poikilitic/subophitic. Abundant, well-developed Cpx
JC21-78R-3D	2.3073	101.5228	3117	oxide gabbronorite	disseminated oxide gabbronorite	-	45	50	5	2	20	Amphibole and quartz alteration, apatite, zricon, some sulphide	Like 3C but lacking a well-developed fabric. A lot of pyroxene exsolution; opx present as large, altered, random grains and as exsolution lamellae in cpx. Larger opx grains are some what poikilitic/subophitic. More abundant cpx symplectite textures.
JC21-78R-4	2.3077	101.52287	3116	gabbronorite	oxide gabbronorite	-	60	30	8	2	30	Brown amphibole	Pretty altered sample exhibiting abundant Cpx symplectites. Mixture of plagioclase between larger blocky to subhedral grains and smaller, more rounded and randomly oriented grains.
JC21-78R-4C	2.3077	101.52287	3116	gabbronorite	oxide gabbronorite	-	45	50	5	5	25	Brown amphibole, apatite, sulphide	Vague fabric present in plagioclase. Pretty altered sample. A lot of pyroxene exsolution; opx present as large, altered, random grains. Larger opx grains are some what poikilitic/subophitic. Some of the larger opx oikocrysts contain small rounded cpx within them. At least two

[a]lithological classification follows IODP procedures (see Expedition 335 Scientists (2012). Methods. In: Teagle, Ildefonse, Blum and the Expedition 335 Scientists, Proc. IODP 335, doi:10.2204/iodp.proc.335.102.2012)

[b]phase abbreviations as follows: Ol = olivine, Pl = plagioclase, Cpx = clinopyroxene, Opx = orthopyroxene, and Ox = oxide

Table A.1: continued

Sample	Lat (N) (*WGS 84*)	Lon (W) (*WGS 84*)	Water depth (*mbsl*)	Lithology[a]		Modal phase abundances[b]					Alteration (~%)	Accesory minerals	Notes on thin section
				Handsample	Thin Section	Ol	Pl	Cpx	Opx	Ox			
JC21-78R-5D	2.3077	101.52283	3116	oxide gabbronorite	oxide gabbronorite	-	50	30	5	15	40	Quartz 2%; apatite, zircon; sulphides	Heavily altered with remnants of symplectite reaction texture in clinopyroxenes. Pegmatitic texture and grain size with quartz associated with alteration of plagioclase and amphibole. Oxides are large and lobate. Brown amphibole is associated with interstitial reactive phase in
JC21-78R-5E	2.3077	101.52283	3116	oxide gabbronorite	oxide leucogabbronorite	-	55	30	10	5	35	Brown amphibole, sulphide, apatite, and zircon; Quartz 2%	Abundant symplectite forming within cpx grains along cleavage and exsolution lamellae. Symplectite reaction with brown amphibole sometimes results in formation of a new cpx within the original grain.
JC21-78R-5F	2.3077	101.52283	3116	oxide gabbronorite	oxide gabbronorite	-	45	47	5	2	25	Brown amphibole, sulphides, apatite, and zircon	Abundant symplectites. Two primary textural domains. Finer-grained domain has a granular texture with abundant curved plagioclase grain boundaries and extremely complex inter-clinopyroxene grain relationships. Clinopyroxene symplectite texture is pervasive within the
JC21-78R-5x1A	2.3077	101.52283	3116	gabbronorite	disseminated oxide gabbronorite	-	45	45	10	<1	25	Brown amphibole, sulphides	Possible fabric in large blocky plagioclase. occasional large interstitial plag with extinction radiating out from center upon rotation (zoned?); areas in plag aggregates with well-developed subgrain boundaries; cpx in hornfelsic domain has low birefringence and small lobate grains…plag anhedral, small lobate/elongate' maybe some fresh opx
JC21-78R-5x2B	2.3077	101.52283	3116	gabbronorite	oxide gabbronorite	-	45	50	5	2.5	30	Brown amphibole, sulphide, apatite	Patches of grungy altered plag and px (stippled)… possibly cuneiform?; more symplectite; mostly granular to subophitic texture; some very large ophitic OPX (with smaller round CPX inside) and some even smaller opx; As you approach the lower right corner, plag have slight foliation with more developed granular texture
JC21-78R-5x3A	2.3077	101.52283	3116	gabbronorite	oxide gabbronorite	-	40	45	15	3	20	Brown amphibole, sulphide	Left side portion and parts of rest of TS have a more developed granular texture in patches; opx is larger oikocrysts with both plag and rounded cpx within; weak plag orientation in background has been overprinted; more symplectites
JC21-78R-5X4A	2.3077	101.52283	3116	oxide gabbronorite	oxide gabbronorite	-	40	40	20	2	35	Quartz, brown amphibole, apatite, zircon	Outside of TS scan on right middle side-- small bleb of hornfelsic texture; px and plag grain size becomes small and more lobate/irregular(re-EQ); possible small relict CPX (~300 microns); some heavily altered grains of parallel extinction mineral with cpx 9altered opx?); Large number of plag oriented towards top right, even more with twins parallel to this direction; OPX (large grains) brown and heavy alteration-- on left side, align vertical; rest of section alligned
JC21-78R-5X4B	2.3077	101.52283	3116	oxide gabbronorite	oxide gabbronorite	-	40	50	10	8	45	Quartz, brown amphibole, apatite, zircon	Quartz in altered opx/amph vein; plag heavily altered there (qtz diorite); within some cpx grains small splintery grains oriented perpendicular to cleavage
JC21-78R-5X4C	2.3077	101.52283	3116	oxide gabbronorite	oxide melagabbronorite	-	30	55	15	3.5	45	Quartz, brown amphibole, apatite, zircon	Lots of zircons in amph portion; quartz is nasty seriate to rounded edges; large blocky plag, very fractured with very irregular boundaries; quartz often nastily intergrown and reaction with plag; highly strained plag with oscilatory twining (zoning?) some cpx symplectite.
JC21-78R-5X4D	2.3077	101.52283	3116	oxide gabbronorite	oxide gabbronorite	-	50	40	10	3.5	30	Brown amphibole, sulphide, apatite	Cpx symplectites; foliation on left side of section; same as other 5X4's; more fresh cpx; plag with irregular grain boundaries; bottom left corner becomes hornfelsic in texture

Table A.1: continued

Sample	Lat (N) (*WGS 84*)	Lon (W) (*WGS 84*)	Water depth (*mbsl*)	Lithology[a]		Modal phase abundances[b]					Alteration (~%)	Accesory minerals	Notes on thin section
				Handsample	Thin Section	Ol	Pl	Cpx	Opx	Ox			
JC21-78R-5X4E	2.3077	101.52283	3116	oxide gabbronorite	oxide gabbronorite	-	50	40	10	3	35	Brown amphibole, sulphide, apatite	Interstitial plag; Cpx symplectites; high-strain plag; foliation in large blocky plag; plag is very irregular and reacted in places
JC21-78R-5X5B	2.3077	101.52283	3116	gabbronorite	oxide gabbronorite	-	45	50	5	5	25	Brown amphibole, apatite, sulphide	Fresh Opx; abundant Cpx symplectites; oscilatory plag; patches of very fine granular plag and px
JC21-78R-6A	2.3088	101.52498	3165	disseminated oxide gabbronorite	disseminated oxide olivine-bearing gabbronorite	**5**	**40**	**28**	**27**	**1**	20	Zircon, sulphide	Zircons near large Ol grain; bottom right corner plag contains altered, rounded Ol and cpx; large Ol has plag alligning around it as if being deflected by Ol growth; most Ol is altered; oscilatory twinned plag (undulose); other areas with profuse Ol alteration products show same deflection of plag; foliation in large, tabular-elongate plag; Where Ol or Ol-alt products present, plag grain boundaries seriate and irregular; Some symplectite CPX, but less profuse
JC21-78R-6B	2.3088	101.52498	3165	disseminated oxide gabbronorite	oxide gabbronorite	3	40	35	20	2	20	Zircon, sulphide	Zircons present in matrix; Olivine grains are subhedral/euhedral. Moderate foliation present and defined by elongate, thin plagioclase.
JC21-78R-6C	2.3088	101.52498	3165	disseminated oxide gabbronorite	oxide gabbronorite	4	47	32	15	2	30	Zircon, sulphide	Plag foliation in large grains; plag is strained (oscil and undulose); same Ol situation as 6A; blebs of granular sub-hornfelsic material-- deflect plag foliation in larger grains; grade outward and intercalate into larger grains-- if symplectite is present, it is very hard to find
JC21-78R-7A	2.3085	101.5250	3143	disseminated oxide gabbronorite	oxide gabbronorite	-	40	50	8	2	30	Zircon, apatite, sulphide, brown amphibole; Quartz alteration	Undulose and osscilatory plag, irregular seriate edges tend to be larger and more equant or diffuse interstial; no obvious foliation; PXs have seriate, very chaotic grain boundaries not easily observed in PPL; small patches/blebs of hornfelsic px and plag; acting like grains: larger plag deflected around them; deformation more altered?; possibly zoned core to rim plag!; large blocky elongate plag with continuous extinction but cut by irregular PX
JC21-78R-7C	2.3085	101.5250	3143	disseminated oxide gabbronorite	oxide gabbronorite	-	46	32	20	2	35	Quartz, apatite, zircon, minor brown amphibole and sulphides	More profuse alteration of PX to AMPH; maybe zircon; similar plag characteristics; OPX less effect on plag fabric (twinning?); same occurrence and characteristic of hornfelsic patches
JC21-78R-8A	2.3081	101.5251	3117	disseminated oxide gabbronorite	oxide gabbronorite	-	45	45	7	3	35	Brown amphibole, quartz (alt), apatite and sulphides	Very similar to R7 but without hornfelsic blebs; fractures filled with fine, well rounded quartz and clinozoisite throughout sample (alteration vein); patches here and there of this stuff (not obvious in ppl)
JC21-78R-9	2.3081	101.5251	3117	disseminated oxide gabbronorite	disseminated oxide gabbronorite	-	**50**	**44**	**5**	**1**	60	Brown amphibole	Heavily altered with abundant clinozoisite. Bown amphibole is also altered. Difficult to discern anything else.
JC21-78R-14A	2.3054	101.53322	3105	aphyric dolerite	oxide microgabbro with pegmatite vein	-	**45**	**20**	-	**9**	25	Quartz 20%; brown amphibole 5%; apatite 1%; zircon	Quartz present; 2 domains-- in coarse domain, Qtz is heavily reactive with plag with very chaotic rounded to lobate grain bound when reacting with CPX, even smaller grains (very nasty)
JC21-78R-14E	2.3054	101.53322	3105	aphyric dolerite	oxide microgabbro	-	**46**	**42**	-	**4**	20	Brown amphibole 7%; apatite 1%; zircon; sulphide	Vague foliation in background of the sample.
JC21-78R-15A	2.3047	101.5344	3130	dolerite with gabbroic patch	oxide microgabbro	-	**43**	**20**	-	**15**	30	Quartz 2%; Brown amphibole 20%; apatite; zircon	No primary Amphibole; intergranular; Qtz; vague orient in places; some coarser patches
JC21-78R-16A	2.3035	101.5351	3073	aphyric dolerite	oxide microgabbro	-	45	39	-	8	20	8% brown amphbiole; Sulphide and apatite	Primary rxn AMPH; symplectite CPX; CPX is fresh!; subophitic; no obvious quartz

A2 Oman: Wadi Saq

Table A2 contains the locations, station numbers and field and thin section notes for each of the samples analysed for this study.

Table A.2: Sample locations and their respective field and thin section descriptions.

	UTM WGS 84[a]			Field Station			Description	
Sample	Easting	Northing	Depth[b] (m)	Station No.	Unit[c]	Reason	Field Notes	Thin Section Notes
OM14-ML8	667167	2529192	-62.8	EF7	XD	Dolerite	mafic enclave within mingling spotty gabbro and diorite	Clusters of larger plagioclase with interstitial amphibole surrounded by fine-grained matrix of granular plagioclase and amphibole, altered clinopyroxene.
OM14-ML9	667167	2529192	-62.8	EF7	XD	Dyke	youngest cross-cutting dyke	Fine-grained dyke the same as the matrix of ML8 with a single cluster of large plagioclase and altered clinopyroxene.
OM14-ML10	667167	2529192	-62.8	EF7	SG	Gabbro	spotty gabbro	Intergranular gabbro with heavily altered clinopyroxene and pegmatitic patches. Very pegmatite-like. Large blocky and interstitial oxide grains with minor amphibole.
OM14-ML11	667167	2529192	-62.8	EF7	SG	Gabbro	varitextured gabbro exhibiting spotty gabbro characteristics	Texture similar to a finer-grained version of ML21 and ML22 with abundant interstitial amphibole and oxide. Very heavily altered.
OM14-ML12	667167	2529192	-62.8	EF7	XD	Tonalite	cross-cutting tonalitic dyke	Medium-grained tonalite consisting of dominantly plagioclase with interstitial amphibole and quartz. No visible oxides.
OM14-ML13	667167	2529192	-62.8	EF7	DRT	Diorite	varitextured diorite mingling with spotty gabbro	Typical medium-grained diorite with very large, very long acicular amphiboles and large (up to 1.5 mm) oxides. Minor quartz present with occasional myrmekitic patches. Heavy alteration.
OM14-ML14	667167	2529192	-62.8	EF7	XD	Dyke	fine grained, sugary textured dyke rock cutting diorite and altered to epidote	Heavily altered (green anphibole and epidote) transitioning to a fine-grained felsic (most likely diorite) portion with granular plagioclase, amphibole, quartz and minor oxides.
OM14-ML15	667167	2529192	-62.8	EF7	XD	Dyke	dyke cross-cutting gabbro with a possible microgabbro core	Fine-grained, heavily altered (greenschist facies) dyke rock.
OM14-ML16	667171	2529183	-59.2	EF8	XD	Dyke	cross-cutting dyke chilled against varitextured spotty gabbro	Coarser-grained (relative to other dykes) plagioclase dominated dyke with a doleritic texture. Reasonably altered and consisting of subequal amounts of plagioclase and amphibole/clinopyroxene with minor oxide.
OM14-ML17	667171	2529183	-59.2	EF8	SG	Gabbro	spotty gabbro adjacent to the ML16 dyke	A lot of oxides with a dominantly subophitic matrix containing patches of more blocky plagioclase. Heavily altered.
OM14-ML18	667169	2529163	-51.2	EF9	XD	Dyke	dyke cutting VT gabbro	Fine-grained, reasonably altered micro-gabbroic texture consisting of subordinate amphibole/pyroxene to blocky plagioclase. Minor oxides and patches of very-fine-grained granular quartz. Large rounded patches within the section become finer-grained with more doleritic textures
OM14-ML19	667052	2529158	-49.2	EF13	XD	Dyke	dolerite dyke cutting diorite	Reasonably altered leucocratic dyke, resembling the coarser portions of ML18, with abundant brown amphibole and oxides.

[a] Coordinates are provided in UTM WGS 84 and correspond to the field maps provided in the text

[b] Depth is calculated as the distance between the sample location and the contact between the sheeted dykes and diorite, corrected to true thickness

[c] Unit abbreviations are as follows: XD = cross-cutting dykes, SD = sheeted dykes, SG = spotty gabbro, PG = patchy gabbros, FG = foliated gabbros, and DRT = diorite

Table A.2: continued

Sample	UTM WGS 84[a] Easting	Northing	Depth[b] (m)	Field Station Station No.	Unit[c]	Reason	Description Field Notes	Thin Section Notes
OM14-ML20	666705	2529745	-284	EF14	FG	Gabbro	equigranular gabbro with a fabric (foliated); S1 DD 284:54; Oriented Surface- 118:64NE	Relatively weathered olivine-gabbro. Large granular clinopyroxene and smaller olivines that are pretty altered. Large interstitial oxides and amphibole present. Foliation defined by plagioclase.
OM14-ML21	666662	2529760	-290	EF16	FG	Gabbro	equigranular 50:50 foliated gabbro; S1 DD 278:58; Oriented Surface- 136:vertical	Similar in texture to ML20, but more medium-grained with less oxide and amphibole. Pretty altered. Minor olivine which is pretty altered.
OM14-ML22	666647	2529781	-298.4	EF17	FG	Gabbro	foliated very fresh gabbro; S1 DD 273:51; Oriented Surface- 004:61W	Same as ML22 with less plagioclase.
OM14-ML23	666587	2529796	-304.4	EF19	FG-P	Gabbro	gradational pegmatite lens within foliated gabbro	Very coarse pegmatite with small, lobate oxides and altered amphibole and clinopyroxene. Growing within the textures seen in ML21 and ML22 but separated from the main foliated gabbros by a solid wall of plagioclase.
OM14-ML24	666587	2529796	-304.4	EF19	FG	Gabbro	host foliated gabbro to ML23 and ML25	Finer-grained version of ML21 and ML22 with a less developed foliation and more abundant interstitial amphibole and oxide. Occasional patches of slightly coarser-grained material.
OM14-ML25	666570	2529803	-307.2	EF20	FG-P	Gabbro	pegmatite with gradational contact with host foliated gabbro	Like ML23 but with smaller grains.
OM14-ML26	666552	2529831	-318.4	EF21	FG	Gabbro	granular px-clots in a plag matrix within the foliated gabbro	Heavily altered clots of former clinopyroxene amongst a transition between a coarser and finer-grained texture as seen in ML21 and ML22. Some of the larger patches within the medium-grained material contain subophitic patches.
OM14-ML27	666549	2529838	-321.2	EF22	FG	Gabbro	more melacratic foliated gabbro facies; medium to coarse grain size; plagioclase may be interstitial in some portions	Heavily altered subophitic to pegmatitic (half-way to a pegmatite) sample with no visible oxides and large brown amphiboles.
OM14-ML28	666515	2529869	-333.6	EF24	FG	Gabbro	foliation defined by clots of Px in a plag matrix; S1 DD 135:90; Oriented face- 117:29NE	More oxidised than weathered sample consisting of a matrix of smaller plagioclase with large clinopyroxene oikocrysts and patches of interstitial amphibole and oxide.
OM14-ML29	666505	2529884	-339.6	EF25	FG	Gabbro	oriented spotty, granular pyroxene defining a weak foliation within the gabbro; S1 DD 341:71; oriented face- 084:70SE	Large altered olivines with oxidised oxides. Granular clinopyroxene in a plagioclase dominated sample with minor interstitial amphibole. Similar to ML21 and ML22.
OM14-ML30	666489	2529890	-342	EF26	FG	Gabbro	leucocratic facies running parallel to foliation within foliated gabbro; S1 DD 292:93; oriented face- 093:52NNW	Transition from a more plagioclase dominated texture like ML21 and ML22 into a texture dominted by more granular clinopyroxene with heavily altered oliving and interstitial ocide and amphibole.
OM14-ML31	666480	2529887	-340.8	EF26	FG-P	Gabbro	coarser pegmatite lens gradational to foliated gabbro	Textures transitional between that of ML26 and ML22 with minor interstitial oxide and amphibole. The pegmatitic material resembles the other foliated gabbro-pegmatites.

Table A.2: continued

Sample	UTM WGS 84[a] Easting	Northing	Depth[b] (m)	Field Station Station No.	Unit[c]	Reason	Description Field Notes	Thin Section Notes
OM14-ML32	666480	2529887	-340.8	EF26	FG	Gabbro	finer foliated gabbro associated with pegmatite	Half-way between a pegmatite and the texture of ML26 with abundant brown-anphibole, minor oxides and minor altered olivine.
OM14-ML33	666938	2529108	-29.2	EF29	XD	Dyke	dolerite dyke cutting coarse-grained diorite and anastamosing around fine-grained diorite (ML34)	Reasonably altered, doleritic dyke with abundant oxides, minor brown amphibole and clusters of blocky plagioclase and quartz.
OM14-ML34	666938	2529108	-29.2	EF29	DRT	Diorite	fine-grained diorite lens between anastamosing dyke (ML33)	Very fine-grained, heavily altered diorite with tiny, granular, interstitial quartz and abundant acicular amphibole with minor oxides. Oxidation weathering is present.
OM14-ML35	666947	2529072	-14.8	EF30	DRT	Diorite	blocky, coarse-grained diorite with oriented face roughly parallel to a joint- 000:80E	Fine to medium-grained granular quartz and plagioclase with both granular to interstitial amphibole and oxide. Occasional large acicular brown amphibole. Large, abundant patches of myrmekite.
OM14-ML36	666939	2529030	2	EF32	SD	Dyke	thicker felsic dyke oriented surface- 241:61E	Microgabbroic texture with abundant oxide and intergranular amphibole. Abundant quartz and patches of coarser plagioclase and quartz.
OM14-ML37	667134	2528847	75.2	EF38	SD	Dyke	margin of xenocryst-rich felsic dyke; xenocrysts resemble medium-grained diorite that dominates the diorite unit	Finer-grained, microgabbroic dyke resembling a finer-grained version of the typical diorite. Heavily altered with abundant quartz, oxide and amphibole.
OM14-ML38	667134	2528847	75.2	EF38	SD	Dyke	core of xenocryst-rich felsic dyke; xenocrysts derived from xenolith of medium-grained diorite	Heavily altered, dioritic xenolith with a mixture of medium-grained diorite dominated by interstitial and acicular amphibole and portions of finer-grained typical diorite. Oxide is abundant along with potential sulphides. Beautiful mixture of textures.
OM14-ML39	667127	2528791	97.6	EF39	SD	Dyke	felsic dyke with small, acicular amphiboles	Heavily altered, fine-grained with abundant oxides and amphibole. Phenocrysts of quartz and altered clinopyroxene and plagioclase.
OM14-ML40	666695	2529753	-287.2	EF15	FG	Gabbro	block of granular gabbro, weak foliation, with a strip of anorthosite, oriented surface- 078:74S; weak S1 DD 312:70 and S2? DD 276:59	Heavily foliated gabbro exactly like ML20. Minor large oxides.
OM14-ML41	666699	2529818	-313.2	EF43	FG	Gabbro	more mafic portion of foliated gabbro; S1 DD 240:69; L1 273:58; Oriented face- 147:90E	Like the clinopyroxene dominated portion of ML30 with abundant interstitial oxide and amphibole. Relatively altered.
OM14-ML42	666685	2529826	-316.4	EF44	FG	Gabbro	well foliated granular 50:50 gabbro; S1 DD 258:63; L1 303:54; oriented face- 097:70 SSE	Finer-grained texture akin to ML21 and ML22 with strips containing abundant interstitial oxide and amphibole.
OM14-ML43	666663	2529831	-318.4	EF45	FG-P	Gabbro	subophitic' coarse-grained gabbro, ~patchy gabbro, with very weak foliation	Halfway between ML21/ML22 and ML31 and heavily altered with oxidised, small oxides.

Table A.2: continued

Sample	UTM WGS 84[a] Easting	Northing	Depth[b] (m)	Field Station Station No.	Unit[c]	Reason	Description Field Notes	Thin Section Notes
OM14-ML44	666656	2529844	-323.6	EF46	FG	Gabbro	foliated olivine-gabbro; S1 DD 285:71; oriented face-080:34	Fine to medium-grained granular plagioclase and clinopyroxene with elongate clusters of fresh, granular olivine. Minor interstitial oxides and amphibole.
OM14-ML45	666615	2529857	-328.8	EF47	FG-A	Gabbro	anorthosite transitional to foliated gabbro; oriented face-285:81NNE; S1 DD 285:90	Textures transitional between ML44 and ML22, but finer-grained and dominated by plagioclase.
OM14-ML46	666615	2529857	-328.8	EF47	FG-P	Gabbro	bag of pegmatite from lens within foliated gabbro	No Thin Section
OM14-ML47	666615	2529857	-328.8	EF47	FG	Gabbro	very fresh leucogabbro with moderate foliation	Altered olivine-gabbro with intergranular texture. Large, intergranular clinopyroxene and very little interstitial oxide and amphibole.
OM14-ML48	666615	2529857	-328.8	EF47	FG	Gabbro	very mafic, px-rich gabbro; oriented face- 347:22ENE; S1 DD 285:90	Ophitic to pegmatitic gabbro with completely altered patches of olivine and abundant interstitial oxide and amphibole.
OM14-ML49	666615	2529857	-328.8	EF47	FG-A	Gabbro	anorthositic gabbro, very leuco-rich and fairly uniform; oriented face- 134:78NE	Dominated by plagioclase with clots of oikocrystic clinopyroxene as in ML26. Strips of interstitial oxide are present.
OM14-ML50	666619	2529474	-175.6	EF48	PG	Gabbro	isotropic gabbro, relatively fresh, little to no foliation	Typical of other patchy gabbros
OM14-ML51	666619	2529474	-175.6	EF48	PG	Gabbro	2 pieces of isotropic gabbro with pegmatite patches	Altered, subophitic gabbro with abundant large, interstitial to lobate oxides. Both large blocky plag and small, elongate grains. Both clinopyroxene (former) and amphibole present. Vaguely pegmatitic texture and assemblage.
OM14-ML52	666619	2529474	-175.6	EF48	XD	Dyke	dolerite dyke rock cross-cutting patchy gabbro	Very-fine-grained, heavily altered dyke consisting of granular former plagioclase and pyroxene (minor amphibole) with large (up to 1 mm) altered phenocrysts of former clinopyroxene.
OM14-ML53	666619	2529474	-175.6	EF48	SG	Gabbro	spotty gabbro from transition area with patchy gabbro	Mixture of pegmatitic gabbro with large clinopyroxene oikocrysts and patches of subophitic gabbrow ith large blocky oxides.
OM14-ML54	666601	2529506	-188.4	EF49	PG	Gabbro	isotropic gabbro with patches	Finer-grained subophitic isotropic gabbro with large patches of mistly plagioclase and interstitial altered clinopyroxene. Extremely abundant oxide and some amphibole. Heavily altered.
OM14-ML55	666640	2529539	-201.6	EF51	XD	Gabbro	cross-cutting granoblastic, sugary (altered) dyke and host patchy gabbro	Both the host gabbro and the dyke are heavily altered. The dyke is dominantly granular and can be observed mingling and reacting with the host gabbro. The host gabbro is subophitic, heavily altered and contains varitextured pegmatitic patches with large, altered clinopyroxenes.
OM14-ML56	666523	2529577	-216.8	EF51	SG	Dyke	3 pieces of dyke margin from ML55	Very fine, light coloured dyke. Heavily altered with small oxidised oxide phenocrysts

Table A.2: continued

Sample	UTM WGS 84[a] Easting	Northing	Depth[b] (m)	Field Station Station No.	Unit[c]	Reason	Description Field Notes	Thin Section Notes
OM14-ML57	666637	2529551	-206.4	EF53	XD	Gabbro	Johan sampled a cross-cutting dyke within the patchy gabbro	Very heavily altered, fine-grained granular assemblage with large pegmatitic patches like ML56
OM14-ML58	666637	2529551	-206.4	EF54	PG	Gabbro	spotty gabbro from transition area with patchy gabbro	A varitextured sample with subophitic, and granular patches. Portions with very large, oikocrystic clinopyroxenes and abundant oxides with only few small amphiboles.
OM14-ML59	666649	2529575	-216	EF55	SG	Dyke	cross-cutting dyke with minimal spotty gabbro xenoliths	Greenschist facies altered microgabbroic/doleritic dyke rock. Dominantly subophitic texture with minor patches of more granular textures.
OM14-ML60a	666678	2529565	-212	EF56	PG	Dyke	cross-cutting dyke with abundant gabbroic xenolith	Finer-grained subophitic gabbro with larger interstitial and lobate oxide grains. Most plagiolcase has lobate boundaries. Heavily altered.
OM14-ML60b	666829	2529558	-209.2	EF58	XD	dyke	cross-cutting dyke in patchy gabbro	Doleritic to fine-grained granular dyke similar to ML59 but finer-grained, containing minor oxidised oxide and amphibole phenocrysts.
OM14-ML61	666678	2529565	-212	EF58	PG	Gabbro	cross-cutting dyke patchy gabbro, mostly fine-grained variety	Varitextured subophitic gabbro with large pegmatitic patches containing very large oxides and amphibole.
OM14-ML62	666811	2529573	-215.2	EF59	PG	Gabbro	small, finer-grained patchy gabbro	Transitional between foliated gabbros with ML21/ML22 textures and patchy gabbros. Abundant interstitial oxide and amphibole and heavily altered olivine.
OM14-ML63	666811	2529573	-215.2	EF59	PG	Gabbro	slightly fresher patchy gabbro with smaller more diffuse patches	Finer-grained subophitic patchy gabbro, varitextured with abundant interstitial oxide and amphibole. Patches of more granular material. Similar to ML60
OM14-ML64	666811	2529573	-215.2	EF59	PG	Gabbro	more medium-grained patchy gabbro	Similar to ML63 but more uniform with abundant granular to interstitial oxide and amphibole.
OM14-ML65	666721	2529624	-235.6	EF61	PG	Gabbro	weakly foliated patchy gabbro; S1 DD 263:71; oriented face-101:45N	Like ML48 with no olivine and more abundant large amphibole and oxide.
OM14-ML66	666721	2529624	-235.6	EF61	FG	Gabbro	coarser patchy gabbro with oriented face- 246:40NW	Weakly foliated transitional between foliated and patchy gabbro with abundant interstitial amphibole and oxide. Occasional small, heavily altered olivine.
OM14-ML67	666697	2529639	-241.6	EF62	PG	Gabbro	transitional foliated-patchy gabbro with possible slight foliation; oriented face- 285:42; granular to subophitic	Another transitional foliated/patchy gabbro with abundant acicular to elongate/blocky plagioclase with a weak foliation and minor amounts of interstitial amphibole and oxide.
OM14-ML68	666671	2529642	-242.8	EF64	PG	Gabbro	2 pegmatite veins in patchy gabbro	Large, typical pegmatite patch within a foliated, finer-grained pegmatitic gabbro with oxie and amphibole.

Table A.2: continued

Sample	UTM WGS 84[a] Easting	Northing	Depth[b] (m)	Field Station No.	Unit[c]	Reason	Description Field Notes	Thin Section Notes
OM14-ML69	666671	2529642	-242.8	EF64	PG	Gabbro	large pegmatite lens in patchy gabbro	Olivine-bearing (abundant) patchy gabbro texturally similar to ML60, 63, and 64 with abundant interstitial oxide and amphibole.
OM14-ML70	666654	2529629	-237.6	EF65	FG	Gabbro	foliated gabbro; S1 DD 272:74; oriented face- 110:53	Heavily altered, abundant interstitial oxide and amphibole with a texture akin to ML21/ML22 transitioning to a more plagioclase-dominated texture.
OM14-ML71	666654	2529629	-237.6	EF65	PG	Gabbro	transitional foliated-patchy gabbro; patches of foliated gabbros	Olivine-bearing (abundant) patchy gabbro texturally similar to ML60, 63, and 64 with abundant interstitial oxide and amphibole. Patches of foliated gabbro (olivine-bearing) surrounded by pegmatitic to subophitic matrix of patchy gabbro.
OM14-ML72	666654	2529629	-237.6	EF65	XD	Dyke	cross-cutting dyke within patchy-foliated gabbro transition	Heavily oxidised fine-grained rock dominated by blocky, subhedral plagioclase with altered interstitial amphibole/pyroxene. Occasional plagioclase phenocrysts (up to 1mm) and possible minor oxide.
OM14-ML73	666636	2529641	-242.4	EF67	FG-P	Gabbro	coarse pegmatite in contact with foliated gabbros	Like the other foliated gabbro-pegmatites.
OM14-ML74	666620	2529622	-234.8	EF69	PG	Gabbro	classic patchy gabbro, sorta fresh, medium grained, granular AND subophitic bits	Coarser-grained blocky plagioclase with interstitial clinopyroxene (altered) and abundant oxide with minor interstitial amphibole.
OM14-ML75	666664	2529564	-211.6	EF70	XD	Gabbro	cross-cutting dyke rocks intruded by pegmatite veins	Dyke is heavily altered and very little remains of the original rock. Pegmatite vein consists of dominantly plagioclase and altered clinopyroxene with oxide and minor brown amphibole. The pegmatite vein fines over a short distance into a microgabbroic intergranular texture with subophitic patches. Brown amphibole is more abundant within the finer-grained portions of the sample.
OM14-ML76	666942	2529034	0.4	EF32	SD	Dyke	felsic dyke	Fine-grained to microgabbroic dyke. Dominantly microgranular plagioclase, clinopyroxene, and amphibole with minor quartz. Small patches of slightly coarser plagioclase and quartz.
OM14-ML77	666942	2529034	0.4	EF32	SD	Dyke	dolerite dyke	Very-fine-grained dyke. Heavily altered. Minor oxide and a few larger altered plagioclase phenocrysts.
OM14-ML78	666999	2529012	9.2	EF71	SD	Dyke	mafic dyke	Heavily altered doleritic texture with abundant oxide and some larger glomerocrysts of plagioclase.
OM14-ML79	666999	2529012	9.2	EF71	SD	Dyke	felsic/mafic dyke	Finer-grained version of ML78 with slightly larger phenocrysts and a few xenoliths containing plagioclase, quartz, and amphibole. Pretty altered.
OM14-ML80	666999	2529012	9.2	EF71	SD	Dyke	dyke x-cut by ML79	Very fine-grained, large oxidised oxide and altered plagioclase phenocrysts.

Table A.2: continued

Sample	UTM WGS 84[a] Easting	Northing	Depth[b] (m)	Field Station Station No.	Unit[c]	Reason	Description Field Notes	Thin Section Notes
OM14-ML81	666999	2529012	9.2	EF71	SD	Dyke	felsic endmember	A fine-grained dioritic dyke with acicular amphiboles and abundant, small oxides
OM14-ML82	666999	2529012	9.2	EF71	SD	Dyke	mafic x-cutting ML81	Heavily altered, fine-grained mafic dyke with abundant altered pyroxene and plagioclase phenocrysts.
OM14-ML83	666999	2529012	9.2	EF71	SD	Dyke	mafic x-cutting felsic	Very fine-grained and altered dyke with a few small plagioclase and oxide phenocrysts
OM14-ML84	666999	2529012	9.2	EF71	SD	Dyke	felsic dyke x-cut by ML83	Typical fine-grained version of a slightly varitextured diorite. Oxide rich with patches of slightly coarser-grained plagioclase and quartz.
OM14-ML85	666920	2529248	-85.2	EF73	DRT	Tonalite	quartz-rich (tonalitic) cross-cutting diorite-- these were later found to be pegmatitic sweats in the melt lens	Very oxide and quartz-rich granular plagioclase and quartz with intergranular brown amphibole (also acicular) and abundant oxides.
OM14-ML86	666920	2529248	-85.2	EF73	DRT	Diorite	reasonably altered diorite	Relatively altered, medium-grained typical diorite with abundant quartz (both granular and myrmekitic) and large (up to 1.5 mm) oxides and acicular amphiboles.
OM14-ML87	666920	2529248	-85.2	EF73	XD	Dyke	cross-cutting dyke within diorite	A less varitextured version of ML84 with abundant amphibole and oxide. Dominated by a plagioclase with subordinate quartz matrix.
OM14-ML88	666892	2529309	-109.6	EF74	DRT	Diorite	diorite cut by package of dolerite dykes	Altered diorite alternating between plagioclase-quartz patches with abundant myrmekite textures and portions with interstitial to granular amphibole (some are large and acicular) and medium-sized oxides (0.5 mm).
OM14-ML89	666900	2529372	-134.8	EF75	SG	Gabbro	spotty gabbro, relatively fresh, possible grains of amphibole	Heavily altered, coarse-grained gabbro with very large clinopyroxene clots containing small, interstitial amphibole and oxide. Pegmatitic patches. Possible few small grains of mostly altered olivine.
OM14-ML90	666924	2529378	-137.2	EF76	XD	Dyke	dyke cross-cutting spotty gabbro	Microgabbroic dyke containing a mixture of blocky to tabular plagioclase and both granular and interstitial former clinopyroxenes with minor, tiny oxides and amphibole. The sample is varitextured with a mixture of granular subophitic patches.
OM14-ML91	666940	2529397	-144.8	EF77	SG	Gabbro	spotty gabbro	Bog standard intergranular gabbro alternating between more melacratic and leucocratic portions. Abundant interstitial oxides and small amounts of amphibole.
OM14-ML92	666846	2529484	-179.6	EF80	SG	Gabbro	reasonably fresh spotty gabbro	Altered, boderline pegmatitic to subophitic gabbro with large oxides and occasional amphibole.

Table A.2: continued

Sample	UTM WGS 84[a] Easting	Northing	Depth[b] (m)	Field Station Station No.	Unit[c]	Reason	Description Field Notes	Thin Section Notes
OM14-ML93	666846	2529484	-179.6	EF80	PG	Gabbro	new facies in patchy gabbro: thicker layer-like patches of material very much like the pegmatite patches in terms of mineralogy, but with a slightly different texture	Plagioclase (medium-grained and blocky) supported by interstitial clinopyroxene (altered) with patches of interstitial oxide and amphibole. Reasonably altered.
OM14-ML94	666801	2529448	-165.2	EF83	SG	Gabbro	zebra (elongate) spots in spotty gabbro	Similar to ML93, but more plagioclase dominated. Very large, elongate clinopyroxene oikocrysts with abundant interstitial and granular oxides and minor amphibole.
OM14-ML95	666651	2529524	-195.6	EF110	PG	Gabbro	dyke cutting pegmatite veins in patchy gabbro	Patchy gabbro with interstitial matrix of more granular, finer-grained material. Abundant oxides and minor amphibole.
OM14-ML96	666563	2529541	-202.4	EF115	SG	Gabbro	relatively fresh spotty gabbro	Akin to ML11 but dominated by more, blockier plagioclase. Large oikocrysts of oxide and possibly amphibole. Large clinopyroxene oikocrysts. Pretty altered.
OM14-ML97	666566	2529594	-223.6	EF118	XD	Dyke	cross-cutting dyke with phenocrysts and a cross-cutting pegmatite vein	Heavily altered, fine-grained dyke containing granular quartz and abundant, large (up to 1.5 mm), altered phenocrysts. Some phenocrysts contain heavily oxidised oxides and brown amphibole.
OM14-ML98	666397	2529686	-260.4	EF133	FG-A	Anorthosite	Anorthosite in foliated gabbro; S1 DD 283:71; oriented face-044:55SE; may be quartz alteration vein	Fine to medium-grained blocky plagioclase with very minor interstitial patches of amphibole.
OM14-ML99	666473	2529340	-122	EF147	XD	Dyke	cross-cutting dyke in spotty gabbro with sharp, chiled margins	Heavily altered, finer-grained spotty gabbro with a subophitic texture and evidence for former amphibole. General lack of oxides noted
OM14-ML100	666605	2529277	-96.8	EF152	DRT	Diorite	diorite with rather large amphibole	Varitextured diorite containing gamut of textures and phases observed within the diorite unit. Abundant amphibole (both acicular and granular to interstitial), oxide, and quartz (even large myrmekitic patches) are present thoughout the rock.
OM14-ML101	666808	2529157	-48.8	EF156	DRT	Diorite	finer grained and coarser grained 'spotty' diorite	Heavily altered patches of very-fine-grained diorite with anastamosing veins of coarser, varitextured amphibole, quartz, and oxide with occasional, large, altered plagioclase. Myrmekite is present within the anastamosing portions.
OM14-ML102	666783	2529097	-24.8	EF157	SD	Dyke	felsic dyke	A less varitextured version of ML84 with abundant amphibole and oxide. Dominated by a plagioclase with subordinate quartz matrix.
OM14-ML103	666685	2529254	-87.6	EF162	DRT	Diorite	medium grained, more typical diorite	Typical medium-grained diorite with both interstitial and acicular amphibole and oxide. Both large granular quartz grains and patches of myrmekite are abundant.

Table A.2: continued

Sample	UTM WGS 84[a] Easting	Northing	Depth[b] (m)	Field Station Station No.	Unit[c]	Reason	Description Field Notes	Thin Section Notes
OM14-ML104	666702	2529297	-104.8	EF166	DRT	Diorite	diorite with xenoliths	Fine to medium-grained varitextured diorite with abundant acicular amphiboles and oxides and xenoliths of medium to coarse-grained diorite with interstitial amphibole and granular quartz.
OM14-ML105	666702	2529297	-104.8	EF166	DRT	Diorite	diorite with xenoliths	Medium-grained plagioclase, quartz, and granular to interstitial amphibole and quartz with patches of finer-grained, acicular amphibole-rich matieral. Portions of the contact between the two dominant domains contain very-fine-grained patches at their contacts with even more amphibole.
OM14-ML106	666922	2529246	-84.4	EF212	DRT	Diorite	fine-grained pegmatitic sweat veins in diorite	Heavily altered, varitextured diorite with subequal, granular to blocky plagioclase and quartz which occasionally form myrmekitic patches. The coarser portions of the rock contain large, interstitial to granular brown amphibole and minor oxide. Large patches of finer-grained material contain abundant, small, acicular amphibole and oxides.
OM14-ML107	667070	2529197	-64.8	EF229	DRT	Diorite	relatively fresh varitextured diorite	Reasonably fresh, medium-grained diorite with blocky plagioclase, both interstitial and large, acicular amphibole and oxides with minor patches of quartz which occasionally form myrmekitic textures.
OM14-ML108	667114	2529065	-12	EF258	DRT	Diorite	varitextured diorite	Same as ML108
OM14-ML109	667097	2529073	-15.2	EF259	DRT	Diorite	spotty, varitextured diorite	The heavily altered section is dominated by a granular plagiolcase, quartz, amphibole assemblage with minor oxide that contains patches of finer-grained material with higher concentrations of smaller, acicular brown amphiboles and oxides. These amphibole-rich patches are what give the rock a spotty appearance.
OM14-ML110	667054	2529051	-6.4	EF263	DRT	Diorite	finer grained diorite with pieces of contact with cross-cutting coarse diorite	The contact with the coarse diorite is very sharp. The coarse diorite is heavily altered with quartz, plagioclase, oxide, and brown amphibole. The other diorite coarsens to a typical medium-grained diorite away from the contact with abundant myrmekitic textures and large oxides and granular to interstitial amphibole.

APPENDIX B
Whole rock method

B1 Preparation of rock samples into powder

Rock samples were prepared into powder using the rock preparation facilities at Cardiff University. Weathered surfaces, veins and alteration patches were removed from the rock samples using a diamond-bladed rock saw. Samples were then crushed to a coarse grit by a steel jaw crusher. Approximately 80 ml of each sample was reduced to a fine powder in an agate ball mill. Afterwards, approximately 2 g of each powdered sample was ignited for two hours in a furnace at 900°C to drive off volatile substances and determine loss on ignition (LOI) values. The LOI of a sample was calculated using the following equation:

$$LOI\ (wt.\%) = \frac{Mass\ of\ wet\ powder - Mass\ of\ ignited\ powder}{Mass\ of\ wet\ powder} \times 100$$

Equation B1

B2 Preparation of solutions for ICP-OES and ICP-MS

Samples in this study were prepared for ICP analysis using the lithium metaborate fusion method. To prepare the samples, 0.1 ± 0.001 g of each ignited sample was mixed with 0.6 ± 0.004 g of lithium metaborate flux in a platinum crucible. A few drops of lithium iodide wetting agent were added to each mixture which was then fused using the Claisse Fluxy automated fusion system. After the mixture was then dissolved in a 50 ml solution of 20 ml of 10% HNO_3 and 30 ml of 18.2 Ω deionised water obtained using a Milli-Q purification system. After the mixture had fully dissolved, 1 ml of 100 ppm Rh spike was added to the solution which was then made up to 100 ml with 18.2 Ω deionised water. Approximately 20 ml of each solution was run on ICP-OES to obtain major element and some trace element abundances. An aliquot of 1 ml of each solution was added to 1 ml of In and Tl and 8 ml of 2% HNO_3 and run on the ICP-MS to obtain trace element abundances. The instruments at Cardiff University used to analyse elemental abundances are a Jobin Yvon Horiba Ultima 2 ICP-OES and a Thermo Elemental X7 series ICP-MS. The samples were run on the mass spectrometers by Dr. Iain McDonald.

B3 Evaluation of the accuracy and precision of the geochemical data

B3.1 Standards

In order to assess the accuracy and precision of the whole rock elemental data obtained by ICP-OES and ICP-MS, external and internal standards were analysed. The external standards used were JB-1, GP13 and MRG1. JB1-A is a basalt issued by the Geological Survey of Japan with certified element values published in Imai et al. (1995). GP13 is a peridotite with values reported by Ottley et al. (2003). MRG1 is a gabbro standard issued by the Canadian Certified Reference Materials Project of CANMET's Mining and Mineral Sciences Laboratories with values reported in Abbey (1981). These three standards were run in every batch of samples analysed mainly to assess the accuracy of the results but also to help determine the precision of the results. Three internal standards were also run in every sample batch. These three samples were… and were used to assess the precision of the elemental data.

B3.2 Accuracy

All of the results from the different runs of standards are given in tables B1 & 2 along with percentage errors of the measured values compared to certified values. The percentage error for each element was calculated using the following equation:

$$\%\ error = \frac{Difference\ between\ measured\ and\ certified\ concentration}{Certified\ concentration\ of\ the\ element} \times 100$$

Equation B2

B3.3 Precision

The precision of the elemental data can be determined by examining the multiple analyses of the external and internal standards. The precision of a standard sample with respect to each element is represented by the relative standard deviation (RSD). The RSD is a percentage value and is calculated for each element using equations B3 through B5 below. The standard values and their corresponding RSDs are reported in tables B3 & 4.

$$x_\alpha = \frac{\sum x}{n}$$

Equation B3

Where x_α is the average element concentration, x is the element concentration and n is the number of measurements.

$$s = \frac{\sqrt{\sum(x - x_\alpha)^2}}{n - 1}$$

Equation B4

Where s is the standard deviation.

$$RSD(\%) = \frac{100s}{x_\alpha}$$

Equation B5

Table B.1: ICP-OES element concentrations for the external standards used in the two batches of Wadi Saq samples analysed and their percentage differences from accepted values.

	Certified/Preferred values			*Analytical Run 1*						*Analytical Run 2*					
	JB1a	**MRG1**	**GP13**	**JB1a**	**% error**	**MRG1**	**% error**	**GP13**	**% error**	**JB1a**	**% error**	**MRG1**	**% error**	**GP13**	**% error**
Major elements (wt. %)															
SiO_2	52.16	39.12	-	52.04	0.22	38.97	0.37	40.26	-	51.97	0.36	39.65	1.36	47.15	-
TiO_2	1.30	3.74	0.12	1.31	0.98	3.71	0.86	0.13	6.65	1.29	0.56	3.83	2.51	0.14	17.15
Al_2O_3	14.51	8.47	-	14.33	1.26	8.43	0.51	3.34	-	14.42	0.61	8.38	1.11	3.79	-
Fe_2O_3	9.10	17.94	-	9.37	2.92	17.82	0.67	8.26	-	9.07	0.34	18.04	0.56	9.47	-
MnO	0.15	0.17	0.122	0.15	0.18	0.18	3.05	0.13	6.88	0.14	4.02	0.16	7.36	0.13	7.97
MgO	7.75	13.55	-	8.35	7.69	13.67	0.92	34.05	-	8.12	4.82	13.49	0.44	34.80	-
CaO	9.23	14.70	-	9.89	7.17	15.03	2.22	3.02	-	9.39	1.76	14.76	0.43	2.77	-
Na_2O	2.74	0.74	-	2.76	0.78	0.70	5.58	0.24	-	2.79	1.88	0.75	1.71	0.31	-
K_2O	1.42	0.18	-	1.40	1.18	0.15	18.97	0.01	-	1.47	3.41	0.19	6.67	0.01	-
P_2O_5	0.25	0.08	-	0.26	4.71	0.06	30.96	0.00	-	0.25	1.57	0.07	13.06	0.01	-
Trace elements (ppm)															
Sc	27.9	55	15	28.25	1.24	54.48	0.95	14.62	2.56	28.78	3.16	56.20	2.18	16.55	10.33
V	206	526	66.3	215.46	4.59	535.45	1.80	70.39	6.16	209.70	1.79	527.49	0.28	62.14	6.27
Cr	415.0	430	2420	418.98	0.96	415.69	3.33	2459.87	1.65	422.52	1.81	419.59	2.42	2747.75	13.54
Co	39.5	87	97.9	40.42	2.32	87.78	0.89	99.08	1.21	39.51	0.03	91.19	4.82	49.10	49.85
Ni	134.0	193	2030	141.26	5.42	199.25	3.24	1935.39	4.66	139.16	3.85	203.09	5.23	1990.07	1.97
Cu	55.0	134	23.4	58.46	6.29	133.32	0.51	21.11	9.78	53.90	1.99	134.13	0.10	25.56	9.22
Zn	82	191	-	158.61	93.43	201.22	5.35	34.26	-	82.36	0.44	200.32	4.88	38.88	-
Sr	443	266	11.2	451.69	1.96	269.27	1.23	10.73	4.16	438.80	0.95	268.92	1.10	11.04	1.41
Y	24.0	14	3.31	24.49	2.03	13.22	5.54	3.34	0.79	22.42	6.60	13.06	6.74	3.61	8.93
Zr	146.0	108	5.35	145.58	0.28	104.07	3.64	4.74	11.48	143.96	1.40	100.72	6.74	2.35	56.15
Ba	497.0	61	-	506.16	1.84	55.50	9.02	0.08	-	503.14	1.24	56.78	6.91	2.95	-

Table B.2: ICP-MS element concentrations for the external standards used in the two batches of Wadi Saq samples analysed and their percentage differences from accepted values.

	Certified/Preferred values			*Analytical Run 1*						*Analytical Run 2*					
	JB1a	**MRG1**	**GP13**	**JB1a**	**% error**	**MRG1**	**% error**	**GP13**	**% error**	**JB1a**	**% error**	**MRG1**	**% error**	**GP13**	**% error**
Major elements (wt. %)															
TiO_2	1.30	3.74	0.12	1.27	2.30	3.69	1.36	0.11	4.28	1.34	2.89	3.84	2.74	0.13	6.52
MnO	0.15	0.17	0.122	0.15	0.34	0.19	9.61	0.12	1.58	0.15	2.76	0.17	1.89	0.13	8.34
Fe_2O_3	9.10	17.94	-	9.04	0.63	17.52	2.35	7.62	-	8.80	3.33	18.14	1.09	8.48	-
Trace elements (ppm)															
V	206.00	526.00	66.30	211.41	2.62	524.39	0.31	67.47	1.77	213.33	3.56	529.54	0.67	70.20	5.88
Cr	415.00	430.00	2420.00	420.02	1.21	428.74	0.29	2500.12	3.31	438.17	5.58	400.79	6.79	3693.72	52.63
Co	39.50	87.00	97.90	39.08	1.07	85.94	1.22	95.35	2.60	35.36	10.48	90.04	3.49	97.92	0.02
Ni	134.00	193.00	2030.00	149.50	11.57	203.08	5.22	1975.55	2.68	129.34	3.48	206.09	6.78	1999.53	1.50
Cu	55.00	134.00	23.40	52.79	4.03	136.33	1.74	24.05	2.79	59.84	8.79	142.36	6.24	29.91	27.82
Zn	82.00	191.00	-	84.51	3.06	193.33	1.22	29.89	-	79.08	3.56	191.41	0.22	40.83	-
Ga	18.00	17.00	2.51	17.52	2.67	16.64	2.09	2.85	13.55	17.63	2.06	18.07	6.28	3.20	27.46
Rb	42.00	8.50	0.32	40.29	4.08	6.01	29.34	0.26	17.19	36.44	13.24	7.97	6.19	0.33	3.81
Sr	443.00	266.00	11.20	447.64	1.05	260.36	2.12	10.73	4.16	445.79	0.63	274.33	3.13	9.72	13.19
Y	24.00	14.00	3.31	23.73	1.12	13.90	0.72	3.29	0.56	23.01	4.13	14.31	2.22	3.07	7.24
Zr	146.00	108.00	5.35	146.58	0.40	102.41	5.17	6.10	14.05	138.50	5.14	110.64	2.44	5.69	6.38
Nb	27.00	20.00	0.14	27.66	2.43	18.77	6.17	0.17	24.53	27.92	3.40	20.21	1.03	0.20	39.98
Cs	1.20	0.57	0.06	1.21	0.77	0.45	21.19	0.10	69.82	1.20	0.28	0.62	9.06	0.06	4.22
Ba	497.00	61.00	-	490.98	1.21	60.21	1.30	0.52	-	496.04	0.19	60.00	1.64	1.25	-
La	38.10	9.80	0.19	37.70	1.06	8.61	12.19	0.23	20.93	37.48	1.63	9.53	2.77	0.20	5.91
Ce	66.10	26.00	0.59	65.42	1.03	23.80	8.48	0.65	10.62	64.84	1.90	26.03	0.11	0.59	0.22
Pr	7.30	3.40	0.11	7.21	1.21	3.39	0.41	0.10	9.60	6.82	6.57	3.78	11.06	0.10	4.77
Nd	25.50	19.20	0.65	24.96	2.13	16.28	15.23	0.68	4.89	26.13	2.46	19.04	0.85	0.66	1.03
Sm	5.02	4.50	0.24	4.99	0.60	4.22	6.16	0.23	6.20	4.85	3.40	4.42	1.80	0.23	6.06
Eu	1.47	1.39	0.11	1.46	0.39	1.29	7.01	0.10	6.55	1.45	1.43	1.41	1.57	0.11	3.06
Gd	4.54	4.00	0.40	4.97	9.52	3.87	3.25	0.40	0.14	4.70	3.49	4.12	2.97	0.38	4.25
Tb	0.69	0.51	0.08	0.70	1.44	0.50	2.64	0.07	2.89	0.68	1.67	0.55	8.27	0.07	6.41
Dy	4.19	2.90	0.51	4.04	3.55	2.76	4.93	0.49	3.91	3.98	5.07	2.97	2.29	0.49	3.35
Ho	0.72	0.49	0.11	0.75	3.87	0.46	5.48	0.11	6.04	0.74	3.13	0.48	1.06	0.11	2.05
Er	2.18	1.12	0.33	2.06	5.38	1.08	3.85	0.31	6.12	2.05	6.14	1.14	1.92	0.33	0.62
Tm	0.31	0.11	0.05	0.33	7.23	0.13	16.92	0.05	2.88	0.30	2.33	0.14	24.32	0.05	0.70
Yb	2.10	0.60	0.36	2.04	2.71	0.71	18.17	0.35	0.43	1.91	8.87	0.82	36.06	0.34	4.40
Lu	0.32	0.12	0.06	0.32	0.16	0.11	4.21	0.05	5.99	0.30	7.38	0.12	0.43	0.06	1.49
Hf	3.48	3.76	0.17	3.45	0.94	3.65	3.03	0.15	6.11	3.47	0.27	3.64	3.12	0.15	8.12
Ta	1.60	0.80	0.02	1.67	4.24	0.72	9.89	0.02	13.21	1.66	3.63	0.86	7.03	0.02	10.54
Pb	7.40	10.00	0.29	6.45	12.87	8.17	18.33	0.31	7.63	7.50	1.36	9.35	6.46	0.48	66.96
Th	8.80	0.93	0.01	8.82	0.28	0.90	3.47	0.02	34.98	8.89	1.05	0.93	0.44	0.02	36.55
U	1.60	0.24	0.01	1.52	4.93	0.22	9.17	0.01	80.45	1.53	4.33	0.23	2.35	0.01	14.00

Table B.3: Comparison between the accepted and averaged measured element concentrations by ICP-OES and the standard deviation and relative standard deviation (RSD) of the external standards.

	Certified/Preferred values			Average			Standard deviation			RSD (%)		
	JB1a	**GP13**	**MRG1**	**JB1a**	**GP13**	**MRG1**	**JB1a**	**GP13**	**MRG1**	**JB1a**	**GP13**	**MRG1**
Major elements (wt. %)												
SiO_2	52.16	-	39.12	52.01	43.71	39.31	0.05	4.87	0.48	0.10	11.15	1.22
TiO_2	1.30	0.12	3.74	1.30	0.13	3.77	0.01	0.01	0.09	1.09	6.64	2.37
Al_2O_3	14.51	-	8.47	14.37	3.56	8.40	0.07	0.32	0.04	0.47	9.10	0.43
Fe_2O_3	9.10	-	17.94	9.22	8.86	17.93	0.21	0.86	0.16	2.27	9.66	0.87
MnO	0.15	0.122	0.17	0.15	0.13	0.17	0.00	0.00	0.01	3.03	0.71	7.52
MgO	7.75	-	13.55	8.23	34.42	13.58	0.16	0.53	0.13	1.91	1.53	0.95
CaO	9.23	-	14.70	9.64	2.89	14.89	0.35	0.18	0.19	3.66	6.06	1.25
Na_2O	2.74	-	0.74	2.78	0.28	0.73	0.02	0.05	0.04	0.77	17.06	5.26
K_2O	1.42	-	0.18	1.44	0.01	0.17	0.05	0.00	0.03	3.21	20.99	19.32
P_2O_5	0.25	-	0.08	0.26	0.01	0.06	0.01	0.00	0.01	2.15	67.07	16.24
Trace elements (ppm)												
Sc	27.9	15	55	28.51	15.58	55.34	0.38	1.37	1.22	1.33	8.78	2.20
V	206	66.3	526	212.58	66.26	531.47	4.08	5.83	5.63	1.92	8.80	1.06
Cr	415.0	2420	430	420.75	2603.81	417.64	2.50	203.56	2.75	0.59	7.82	0.66
Co	39.5	97.9	87	39.96	74.09	89.48	0.64	35.34	2.41	1.60	47.71	2.70
Ni	134.0	2030	193	140.21	1962.73	201.17	1.48	38.66	2.72	1.06	1.97	1.35
Cu	55.0	23.4	134	56.18	23.34	133.73	3.22	3.14	0.58	5.73	13.47	0.43
Zn	82	-	191	120.49	36.57	200.77	53.92	3.27	0.64	44.75	8.93	0.32
Sr	443	11.2	266	445.25	10.89	269.10	9.11	0.22	0.25	2.05	2.00	0.09
Y	24.0	3.31	14	23.45	3.47	13.14	1.46	0.19	0.12	6.24	5.49	0.90
Zr	146.0	5.35	108	144.77	3.54	102.39	1.15	1.69	2.37	0.79	47.72	2.31
Ba	497.0	-	61	504.65	1.52	56.14	2.13	2.02	0.91	0.42	133.61	1.62

Table B.4: Comparison between the accepted and averaged measured element concentrations by ICP-MS and the standard deviation and relative standard deviation (RSD) of the external standards.

	Certified/Preferred values			Average			Standard deviation			RSD (%)		
	JB1a	**GP13**	**MRG1**	**JB1a**	**GP13**	**MRG1**	**JB1a**	**GP13**	**MRG1**	**JB1a**	**GP13**	**MRG1**
Major elements (wt. %)												
TiO_2	1.30	0.12	3.74	1.30	0.12	3.77	0.05	0.01	0.11	3.66	7.55	2.88
MnO	0.15	0.122	0.17	0.15	0.13	0.18	0.00	0.01	0.01	1.74	4.55	5.16
Fe_2O_3	9.10	-	17.94	8.92	8.05	17.83	0.17	0.61	0.44	1.94	7.63	2.45
Trace elements (ppm)												
V	206.00	66.30	526.00	212.37	68.84	526.96	1.36	1.93	3.64	0.64	2.80	0.69
Cr	415.00	2420.00	430.00	429.09	3096.92	414.77	12.83	844.00	19.76	2.99	27.25	4.77
Co	39.50	97.90	87.00	37.22	96.63	87.99	2.63	1.81	2.90	7.07	1.88	3.29
Ni	134.00	2030.00	193.00	139.42	1987.54	204.59	14.26	16.96	2.12	10.23	0.85	1.04
Cu	55.00	23.40	134.00	56.31	26.98	139.34	4.99	4.14	4.26	8.85	15.35	3.06
Zn	82.00	-	191.00	81.79	35.36	192.37	3.84	7.74	1.35	4.69	21.89	0.70
Ga	18.00	2.51	17.00	17.57	3.02	17.36	0.08	0.25	1.01	0.44	8.16	5.80
Rb	42.00	0.32	8.50	38.36	0.30	6.99	2.72	0.05	1.39	7.09	15.91	19.90
Sr	443.00	11.20	266.00	446.72	10.23	267.35	1.31	0.71	9.88	0.29	6.99	3.70
Y	24.00	3.31	14.00	23.37	3.18	14.10	0.51	0.16	0.29	2.19	4.92	2.06
Zr	146.00	5.35	108.00	142.54	5.90	106.53	5.71	0.29	5.82	4.01	4.92	5.46
Nb	27.00	0.14	20.00	27.79	0.19	19.49	0.19	0.02	1.02	0.67	8.26	5.23
Cs	1.20	0.06	0.57	1.20	0.08	0.54	0.01	0.03	0.12	0.75	39.42	22.77
Ba	497.00	-	61.00	493.51	0.88	60.11	3.57	0.51	0.15	0.72	58.06	0.24
La	38.10	0.19	9.80	37.59	0.22	9.07	0.15	0.02	0.65	0.41	9.37	7.19
Ce	66.10	0.59	26.00	65.13	0.62	24.91	0.40	0.05	1.58	0.62	7.29	6.34
Pr	7.30	0.11	3.40	7.02	0.10	3.58	0.28	0.00	0.28	3.94	3.68	7.69
Nd	25.50	0.65	19.20	25.54	0.67	17.66	0.83	0.02	1.95	3.24	2.65	11.06
Sm	5.02	0.24	4.50	4.92	0.23	4.32	0.10	0.00	0.14	2.02	0.10	3.21
Eu	1.47	0.11	1.39	1.46	0.10	1.35	0.01	0.01	0.08	0.75	6.91	6.24
Gd	4.54	0.40	4.00	4.84	0.39	3.99	0.19	0.01	0.18	4.00	3.17	4.40
Tb	0.69	0.08	0.51	0.69	0.07	0.52	0.02	0.00	0.04	2.20	2.62	7.50
Dy	4.19	0.51	2.90	4.01	0.49	2.86	0.04	0.00	0.15	1.12	0.41	5.17
Ho	0.72	0.11	0.49	0.75	0.11	0.47	0.00	0.00	0.02	0.51	2.94	3.23
Er	2.18	0.33	1.12	2.05	0.32	1.11	0.01	0.01	0.05	0.57	4.02	4.12
Tm	0.31	0.05	0.11	0.32	0.05	0.13	0.02	0.00	0.01	6.60	2.50	4.34
Yb	2.10	0.36	0.60	1.98	0.35	0.76	0.09	0.01	0.08	4.62	2.88	9.95
Lu	0.32	0.06	0.12	0.31	0.06	0.12	0.02	0.00	0.00	5.53	3.31	2.73
Hf	3.48	0.17	3.76	3.46	0.15	3.64	0.02	0.00	0.00	0.47	1.53	0.07
Ta	1.60	0.02	0.80	1.66	0.02	0.79	0.01	0.00	0.10	0.42	16.58	12.14
Pb	7.40	0.29	10.00	6.97	0.40	8.76	0.74	0.12	0.84	10.67	30.56	9.58
Th	8.80	0.01	0.93	8.86	0.02	0.91	0.05	0.00	0.02	0.54	0.82	2.18
U	1.60	0.01	0.24	1.53	0.01	0.23	0.01	0.00	0.01	0.44	31.91	5.12

APPENDIX C
Whole rock results

Tables C1 through C6 report whole rock ICP-OES analyses of major and some trace elements for the Wadi Saq samples. Tables C7 through C12 report whole rock ICP-MS analyses of trace elements for the Wadi Saq samples. Samples are grouped according to their igneous unit as mapped in the field area (i.e., diorites = C1, C7; foliated gabbros = C2, C8; patchy gabbros =C3, C9; spotty gabbros = C4, C10; sheeted dykes = C5, C11; cross-cutting dykes = C6, C12). The foliated gabbros have been grouped within their respective tables by dominant sub-lithology (i.e., foliated gabbro, foliated gabbro-anorthosite, foliated gabbro-pegmatite). In each table, all iron is calculated as total Fe^{3+} (i.e., Fe_2O_3(T)).

Table C.1: ICP-OES results for samples of the diorite unit.

Sample	ML13	ML34	ML35	ML85	ML86	ML88	ML100	ML101a	ML101b	ML103	ML104	ML105	ML106	ML107	ML108	ML109	ML110
Major elements (wt. %)																	
SiO_2	62.37	64.37	67.74	72.72	58.33	62.62	64.73	77.62	72.95	68.48	60.25	62.44	69.08	62.26	71.62	65.34	72.99
TiO_2	1.05	0.85	0.49	0.33	1.37	1.14	1.32	0.22	0.46	0.41	1.14	0.94	0.63	1.21	0.40	0.70	0.28
Al_2O_3	13.78	13.62	13.89	13.53	14.13	13.96	14.61	10.91	11.77	13.23	15.30	15.09	12.99	14.51	12.00	14.69	13.54
Fe_2O_3(T)	9.02	7.04	6.19	4.07	12.09	8.51	6.62	2.63	4.70	6.46	8.15	7.50	4.96	8.49	5.34	7.24	3.12
MnO	0.09	0.06	0.06	0.02	0.17	0.10	0.07	0.02	0.03	0.02	0.09	0.10	0.05	0.12	0.05	0.09	0.02
MgO	1.61	1.83	0.75	0.58	1.64	1.39	0.98	0.07	0.41	0.43	2.08	1.70	0.62	1.82	0.47	1.15	0.64
CaO	4.06	3.26	2.07	1.81	4.22	3.86	3.25	3.10	5.60	1.95	4.16	3.79	2.57	4.22	2.65	2.37	1.01
Na_2O	4.56	5.23	6.46	6.96	5.78	5.72	6.40	4.73	3.44	6.56	5.59	5.92	6.06	4.84	5.79	6.60	7.06
K_2O	0.32	0.07	0.27	0.16	0.09	0.20	0.16	0.02	0.05	0.08	0.35	0.46	0.17	0.21	0.02	0.20	0.11
P_2O_5	0.39	0.31	0.12	0.05	0.40	0.37	0.32	0.02	0.10	0.08	0.25	0.23	0.13	0.32	0.06	0.21	0.08
LOI	2.00	2.35	1.16	0.91	1.28	1.23	1.33	0.88	1.25	1.20	2.34	1.69	0.92	1.94	1.40	1.64	1.01
Total	99.25	99.00	99.20	101.14	99.50	99.10	99.79	100.20	100.74	98.91	99.71	99.87	98.18	99.94	99.80	100.22	99.84
Trace elements (ppm)																	
Sc	12.8	13.4	6.7	8.4	14.1	11.8	7.7	4.8	11.2	10.0	14.7	14.7	7.6	12.4	8.9	10.6	5.6
V	19.7	24.1	9.4	9.3	26.1	15.3	13.1	4.8	2.6	5.7	38.8	25.3	9.0	44.4	5.1	7.4	6.5
Cr	4.2	10.7	5.7	7.4	7.9	6.4	130.3	1.2	6.8	14.7	4.4	38.7	9.4	3.2	10.8	4.7	11.0
Co	8.2	7.2	7.5	2.0	10.0	10.6	10.5	2.6	5.7	6.7	11.5	9.1	5.8	11.8	3.3	5.1	4.4
Ni	36.1	31.5	25.3	64.0	27.5	21.2	149.2	21.8	23.6	13.5	26.8	143.6	16.4	8.3	16.6	28.1	40.4
Cu	29.3	23.8	12.1	10.7	18.9	16.8	15.3	4.9	4.2	13.7	5.0	33.1	23.7	19.2	20.4	51.9	11.7
Zn	81.2	59.3	39.2	19.2	44.4	22.7	15.4	13.3	16.1	4.1	32.5	24.4	22.1	28.5	12.0	22.7	8.6
Sr	176.4	120.9	119.0	119.9	137.6	150.6	168.2	117.5	197.6	122.8	216.2	181.6	126.3	187.6	106.0	147.8	57.6
Y	76.5	75.1	93.4	132.0	76.3	70.3	71.8	132.4	93.1	111.1	94.7	78.9	75.4	67.1	91.6	91.2	79.6
Zr	313.9	278.8	493.9	459.1	206.6	302.0	279.2	542.4	370.1	428.8	238.7	341.9	415.9	259.5	348.5	1002.7	666.1
Ba	20.6	9.3	71.6	54.5	56.7	67.5	59.6	17.5	11.7	44.8	28.1	68.8	76.8	31.7	13.8	48.8	22.1

Table C.2: ICP-OES data for samples of the foliated gabbro unit. Anorthosite and pegmatite samples are grouped separately.

	Foliated Gabbro														
Sample	ML20	ML21	ML22	ML24	ML26	ML27	ML28	ML29	ML30	ML32	ML40	ML41	ML42	ML44	ML47
Major elements (wt. %)															
SiO_2	46.99	46.35	46.68	49.61	46.65	46.08	47.52	47.93	47.53	46.74	48.56	48.28	46.97	44.79	44.96
TiO_2	0.79	0.51	0.45	0.46	0.28	0.33	0.26	0.34	0.63	0.36	0.65	0.64	0.77	0.34	0.20
Al_2O_3	20.41	20.23	16.57	17.09	19.01	16.02	20.58	21.86	15.44	16.78	19.67	17.64	19.80	13.13	19.84
Fe_2O_3(T)	6.96	5.03	5.55	6.77	4.97	6.38	5.46	4.75	7.93	6.61	6.02	8.43	6.46	8.99	6.02
MnO	0.10	0.08	0.09	0.14	0.08	0.11	0.08	0.07	0.13	0.12	0.09	0.12	0.11	0.15	0.10
MgO	6.40	7.30	11.21	7.46	8.19	10.79	8.30	7.03	10.06	9.98	7.09	8.49	8.01	15.19	10.86
CaO	12.60	15.22	14.67	13.65	15.69	15.43	14.96	15.55	14.33	15.00	13.34	13.52	13.41	13.78	15.09
Na_2O	3.42	2.78	1.85	2.64	1.84	1.55	1.81	1.89	1.48	1.62	2.90	2.62	2.65	1.10	1.24
K_2O	0.08	0.07	0.26	0.10	0.08	0.07	0.08	0.08	0.04	0.09	0.08	0.12	0.07	0.03	0.05
P_2O_5	0.04	0.07	0.03	0.02	0.02	0.01	0.01	0.03	0.02	0.02	0.06	0.04	0.03	0.03	0.00
LOI	2.25	3.34	2.89	1.27	2.29	2.66	1.76	1.66	1.28	1.85	2.09	1.17	2.79	1.50	2.47
Total	100.05	100.98	100.25	99.20	99.08	99.41	100.83	101.19	98.88	99.16	100.56	101.08	101.06	99.01	100.83
Trace elements (ppm)															
Sc	38.1	35.8	47.6	38.9	33.6	40.1	35.7	36.7	49.1	37.3	33.5	46.4	41.7	51.6	20.1
V	219.0	140.0	162.7	158.3	125.1	148.6	115.8	121.3	238.7	144.7	167.9	237.2	196.3	154.0	82.5
Cr	44.9	120.0	336.4	49.0	295.6	528.0	259.4	234.7	238.0	335.5	174.6	74.0	135.3	356.6	372.7
Co	27.6	27.8	31.9	35.5	27.1	34.2	29.4	26.7	40.2	35.1	30.0	33.9	24.2	49.3	42.7
Ni	48.0	234.9	250.4	65.9	114.1	150.7	114.1	78.0	248.2	159.0	73.6	69.4	97.7	191.1	238.6
Cu	33.1	15.6	12.6	24.2	19.2	28.3	18.7	84.0	64.0	67.9	33.0	16.6	21.7	57.9	20.7
Zn	33.5	28.5	35.6	57.9	39.5	36.1	16.5	19.5	39.9	44.6	13.7	21.1	30.8	53.8	26.5
Sr	235.7	269.4	207.1	178.6	203.5	167.1	169.5	183.3	132.7	162.1	212.4	164.5	209.0	116.4	177.9
Y	13.0	9.5	10.1	14.3	6.5	7.5	7.4	7.4	10.4	8.3	12.0	13.1	10.3	8.4	3.8
Zr	26.6	27.6	10.5	24.3	5.6	3.7	11.6	10.0	14.7	25.6	28.0	32.2	37.3	3.7	4.1
Ba	20.2	33.8	16.4	13.2	31.3	8.1	11.1	12.2	14.7	22.4	18.3	18.2	16.4	12.5	7.7

Table C.2 *continued...*

	Foliated Gabbro			Foliated Gabbro-Anorthosite			Foliated Gabbro-Pegmatite					
Sample	ML48	ML65	ML70	ML45	ML49	ML98	ML23	ML25	ML31	ML43	ML46	ML73
Major elements (wt. %)												
SiO_2	49.02	49.33	47.42	44.18	46.84	48.02	48.81	48.17	48.09	46.84	45.43	51.61
TiO_2	0.26	0.57	0.55	0.36	0.14	0.12	0.52	0.64	0.38	0.37	0.25	0.91
Al_2O_3	20.48	17.45	23.14	16.45	26.82	30.75	21.30	16.75	16.76	17.54	19.37	17.63
Fe_2O_3(T)	3.01	7.68	5.27	7.40	1.77	1.26	6.08	7.86	5.72	5.72	5.46	7.80
MnO	0.06	0.13	0.09	0.12	0.03	0.01	0.09	0.13	0.10	0.08	0.11	0.14
MgO	6.55	7.51	4.42	12.07	2.15	0.35	4.46	7.75	9.15	9.79	7.79	5.78
CaO	17.48	11.97	14.32	14.89	16.76	15.01	11.60	13.03	15.26	14.16	16.32	10.72
Na_2O	1.96	2.73	2.87	1.36	2.45	2.66	3.94	2.97	2.08	2.17	1.50	4.43
K_2O	0.03	0.29	0.15	0.07	0.04	0.03	0.14	0.12	0.09	0.06	0.17	0.19
P_2O_5	0.01	0.05	0.06	0.01	0.01	0.01	0.05	0.02	0.02	0.03	0.04	0.02
LOI	2.43	1.69	1.20	2.52	2.18	1.68	3.01	2.08	2.46	3.07	2.77	0.70
Total	101.29	99.40	99.49	99.43	99.19	99.92	100.00	99.50	100.11	99.83	99.21	99.93
Trace elements (ppm)												
Sc	46.5	37.3	28.3	45.1	8.5	1.1	24.5	41.9	39.6	43.5	19.3	38.3
V	138.4	201.5	145.3	156.4	48.4	22.3	175.7	217.2	154.8	142.0	95.7	201.6
Cr	667.2	97.2	79.5	763.0	131.9	27.0	10.3	46.7	355.3	305.8	155.0	17.5
Co	17.4	34.1	20.1	41.0	9.3	6.8	23.2	41.9	33.6	30.8	32.9	30.2
Ni	74.5	81.0	42.9	222.5	321.1	39.8	58.5	103.6	131.9	185.9	151.3	61.8
Cu	3.7	88.6	64.1	85.8	26.4	100.2	89.3	91.5	24.9	19.9	30.1	23.3
Zn	7.3	43.1	47.8	31.1	15.4	14.4	33.8	46.7	29.6	22.6	50.0	91.2
Sr	208.0	209.8	218.5	144.0	224.8	284.4	238.3	184.7	181.8	222.0	198.0	223.3
Y	6.2	12.9	10.3	8.1	2.8	1.3	12.1	11.4	10.8	8.2	7.0	17.9
Zr	7.4	47.1	35.7	9.3	8.4	4.9	21.1	19.5	17.1	17.3	7.4	21.5
Ba	6.5	28.6	21.9	9.7	8.9	8.6	18.7	8.7	11.2	12.8	23.4	18.3

Table C.3: ICP-OES results for samples from the patchy gabbro unit.

Sample	ML50	ML51	ML54	ML57	ML61	ML62	ML63	ML64	ML66	ML67	ML68	ML71	ML74	ML93	ML95
Major elements (wt. %)															
SiO_2	46.76	48.16	44.95	48.96	47.91	47.80	48.34	47.96	48.24	48.25	49.05	48.70	50.49	46.23	51.20
TiO_2	1.81	1.35	2.78	1.49	1.10	1.56	1.61	1.44	0.52	0.68	0.80	0.64	1.96	1.65	1.34
Al_2O_3	13.61	14.31	12.61	14.80	15.03	13.87	14.24	13.91	18.45	20.16	16.78	15.37	16.66	13.47	15.55
Fe_2O_3(T)	12.85	11.03	17.44	11.25	11.21	13.36	13.33	13.47	7.88	6.48	8.61	9.06	11.60	14.34	10.26
MnO	0.18	0.16	0.23	0.16	0.20	0.22	0.23	0.23	0.14	0.12	0.14	0.15	0.19	0.20	0.13
MgO	7.61	7.57	6.69	5.44	7.87	6.66	6.88	7.90	7.57	5.79	7.36	9.42	4.63	9.25	5.49
CaO	10.44	10.47	9.83	8.48	12.51	11.01	11.02	12.20	12.74	12.81	11.79	13.39	8.31	10.92	9.45
Na_2O	2.97	3.08	3.15	4.24	2.80	3.07	3.05	2.65	2.77	2.90	3.13	2.16	4.56	2.14	4.48
K_2O	0.25	0.29	0.22	0.21	0.25	0.14	0.13	0.05	0.13	0.16	0.23	0.05	0.30	0.14	0.06
P_2O_5	0.06	0.08	0.08	0.09	0.06	0.04	0.08	0.04	0.04	0.02	0.06	0.06	0.19	0.03	0.12
LOI	3.05	2.75	1.43	3.80	1.91	1.70	2.22	1.35	2.01	2.14	1.41	1.27	1.02	1.95	2.22
Total	99.58	99.26	99.41	98.92	100.84	99.44	101.13	101.21	100.49	99.51	99.36	100.27	99.91	100.33	100.31
Trace elements (ppm)															
Sc	44.4	37.8	43.7	34.8	42.6	45.0	43.1	46.7	34.6	36.7	42.4	41.3	30.8	48.5	32.8
V	492.0	291.0	831.0	342.3	351.7	410.6	355.3	348.2	172.7	187.9	223.0	188.6	372.6	554.9	280.5
Cr	64.0	70.2	190.3	17.9	138.9	46.2	120.1	179.7	116.9	88.7	89.7	402.9	8.4	88.0	29.2
Co	48.1	39.8	59.8	49.0	38.9	41.0	40.9	46.8	30.1	28.1	38.9	46.4	39.0	50.9	31.8
Ni	83.9	76.2	390.5	216.5	253.0	54.9	210.3	85.0	229.9	90.1	352.0	109.3	35.7	91.3	91.6
Cu	24.6	28.1	83.5	129.2	31.7	52.0	37.7	36.4	33.2	86.1	49.0	63.0	32.9	50.5	66.5
Zn	146.0	76.2	61.4	46.7	130.4	108.5	131.2	110.8	45.1	47.3	67.8	72.2	58.2	59.6	49.2
Sr	168.8	192.0	156.7	185.7	159.1	155.3	168.2	178.2	197.4	202.7	162.7	138.6	203.1	141.6	202.5
Y	25.1	25.9	31.1	37.6	25.4	28.5	29.2	22.5	11.2	10.1	16.1	17.4	34.9	16.8	30.5
Zr	49.4	62.6	71.5	106.4	66.3	59.3	43.2	41.0	23.2	28.1	78.0	25.3	49.3	29.5	85.2
Ba	20.1	84.9	24.2	18.3	43.9	28.8	116.4	19.3	15.0	15.4	50.4	13.4	33.7	14.6	22.6

Table C.4: ICP-OES results for samples from the spotty gabbro unit.

Sample	ML10	ML11	ML17	ML53	ML55b	ML58	ML89	ML91	ML92	ML94	ML96
Major elements (wt. %)											
SiO_2	47.90	47.66	50.40	48.80	48.42	48.38	47.46	48.54	49.86	50.50	52.60
TiO_2	1.25	0.59	1.41	1.01	1.11	2.20	0.70	0.53	0.96	1.26	0.80
Al_2O_3	13.62	15.37	14.48	14.30	15.24	15.74	18.67	15.41	16.07	14.92	20.26
Fe_2O_3(T)	12.91	8.23	10.90	10.68	10.37	13.94	6.46	5.22	9.54	11.18	6.86
MnO	0.20	0.15	0.15	0.15	0.16	0.20	0.07	0.06	0.16	0.15	0.10
MgO	7.96	10.78	6.96	8.07	7.45	4.87	8.15	10.09	7.24	6.59	4.21
CaO	10.44	13.38	9.18	11.99	12.22	8.93	13.28	16.12	11.72	8.74	12.19
Na_2O	2.98	1.93	3.75	2.70	2.82	4.26	2.62	1.72	2.95	3.79	3.87
K_2O	0.15	0.18	0.26	0.32	0.17	0.15	0.25	0.13	0.24	0.12	0.06
P_2O_5	0.11	0.04	0.12	0.05	0.05	0.09	0.06	0.05	0.05	0.11	0.06
LOI	2.26	1.89	2.85	2.26	1.29	1.77	2.84	1.69	2.17	1.85	1.71
Total	99.78	100.21	100.45	100.36	99.29	100.52	100.55	99.56	100.95	99.21	102.72
Trace elements (ppm)											
Sc	35.0	38.3	35.9	44.7	39.8	31.6	33.8	50.6	37.9	26.9	28.2
V	312.9	205.2	315.8	349.5	323.8	605.0	175.7	199.1	250.1	252.0	188.7
Cr	45.4	449.9	66.6	50.8	94.8	85.6	328.0	277.0	74.7	36.4	27.4
Co	56.0	42.6	37.1	45.6	44.0	46.0	26.6	29.0	39.6	37.2	25.6
Ni	87.8	157.5	75.5	69.4	78.1	225.7	139.9	149.1	80.0	61.8	50.1
Cu	29.7	35.7	31.9	22.0	70.7	71.0	35.4	14.2	64.7	8.0	32.7
Zn	64.3	73.5	52.6	46.3	56.8	49.8	29.9	32.4	39.7	87.7	90.5
Sr	182.3	117.2	247.0	198.3	176.8	167.4	248.5	157.8	195.5	201.1	220.3
Y	29.5	14.5	33.5	19.0	15.8	30.5	14.6	11.5	18.5	29.1	18.8
Zr	80.8	24.3	107.8	47.6	34.1	97.9	34.0	37.8	39.6	94.0	48.0
Ba	27.6	22.6	16.7	16.1	22.2	25.1	11.4	12.2	17.6	27.1	27.4

Table C.5: ICP-OES results for samples from the sheeted dykes.

Sample	ML102	ML36	ML37	ML38	ML39	ML76	ML77	ML78	ML79	ML80	ML81	ML82	ML83	ML84
Major elements (wt. %)														
SiO_2	58.17	55.81	58.63	62.62	54.57	55.72	50.97	49.83	51.94	50.15	52.32	50.48	51.66	54.61
TiO_2	1.63	1.97	1.11	0.97	1.47	1.64	1.51	1.36	2.15	1.69	1.94	1.22	1.91	1.65
Al_2O_3	14.02	15.04	14.75	14.66	14.23	14.36	15.42	15.21	13.71	14.79	14.70	14.93	14.29	15.63
Fe_2O_3(T)	9.60	9.37	10.45	8.91	10.95	10.25	12.02	11.57	13.70	12.13	11.98	10.64	12.92	10.79
MnO	0.05	0.06	0.14	0.10	0.14	0.09	0.16	0.17	0.12	0.12	0.08	0.10	0.11	0.09
MgO	2.58	2.91	1.89	1.28	3.20	3.00	6.76	6.97	5.09	6.19	4.10	7.92	4.75	3.09
CaO	5.03	5.54	6.04	3.79	5.85	6.50	9.44	7.77	7.73	8.36	5.70	6.90	6.34	6.26
Na_2O	6.59	6.23	5.17	6.31	5.49	5.22	3.44	4.05	4.85	4.44	6.04	4.09	5.42	5.62
K_2O	0.14	0.36	0.06	0.05	0.10	0.13	0.11	0.46	0.21	0.28	0.31	0.45	0.24	0.21
P_2O_5	0.36	0.31	0.39	0.31	0.30	0.26	0.14	0.12	0.24	0.17	0.27	0.12	0.23	0.26
LOI	1.97	1.49	1.88	1.43	2.86	2.33	1.28	2.11	1.00	2.91	1.97	3.96	1.70	1.28
Total	100.13	99.11	100.50	100.42	99.15	99.50	101.24	99.62	100.73	101.26	99.42	100.79	99.58	99.50
Trace elements (ppm)														
Sc	19.8	21.6	14.6	12.8	22.5	22.7	35.5	33.3	33.8	34.2	25.3	36.1	28.5	22.6
V	131.0	158.1	76.8	10.7	143.2	205.0	310.5	310.2	312.1	284.7	221.6	258.3	310.7	202.9
Cr	2.9	5.5	10.4	5.4	20.3	345.4	42.8	33.1	28.6	47.5	14.0	101.2	19.1	6.9
Co	19.0	15.0	13.8	11.0	25.0	22.1	39.7	37.6	35.1	32.0	19.2	30.3	25.1	17.0
Ni	25.6	29.8	18.6	361.8	35.8	1043.8	61.0	53.7	27.7	57.1	46.3	381.1	36.0	16.5
Cu	10.8	11.9	48.2	9.3	28.8	20.5	107.0	70.1	7.0	41.4	11.4	11.2	19.2	15.8
Zn	14.5	9.3	59.1	53.8	40.2	15.2	49.6	64.6	16.7	61.1	89.3	38.4	35.0	5.6
Sr	167.1	180.3	225.0	141.3	136.3	170.3	165.9	206.0	206.2	218.1	218.9	218.8	187.0	176.5
Y	67.2	54.5	73.3	83.1	61.0	59.5	35.5	30.3	51.9	38.4	56.6	30.3	47.5	54.9
Zr	180.5	344.2	234.6	307.5	206.1	214.8	110.7	79.1	182.1	118.7	172.9	73.7	156.8	242.7
Ba	15.2	30.3	6.2	4.2	22.4	30.1	20.2	51.1	37.8	40.7	30.8	52.0	37.7	35.6

Table C.6: ICP-OES results for samples from the cross-cutting dykes.

	ML12	ML14	ML15	ML16	ML18	ML19	ML33	ML52	ML55a	ML56	ML59	ML60	ML72	ML75	ML8	ML87	ML9	ML90	ML97	ML99
Major elements (wt. %)																				
SiO_2	66.36	47.99	48.39	50.99	48.66	50.34	50.65	49.76	50.71	48.95	49.07	49.97	49.41	50.29	59.64	47.53	49.61	49.40	49.32	51.74
TiO_2	0.77	1.43	1.40	1.42	1.40	1.57	1.74	1.40	1.25	1.27	1.52	1.15	1.32	1.86	1.38	1.25	1.46	1.47	1.36	1.76
Al_2O_3	14.95	14.42	14.64	15.00	15.11	14.58	14.46	14.74	14.97	15.63	14.81	15.18	15.67	16.29	14.35	15.03	14.64	15.05	14.95	14.15
Fe_2O_3(T)	4.00	18.58	19.57	11.62	10.87	12.28	12.20	11.71	10.84	11.19	12.15	11.00	11.69	10.99	8.75	11.18	10.88	6.09	11.73	4.66
MnO	0.05	0.10	0.11	0.15	0.11	0.16	0.19	0.12	0.15	0.17	0.19	0.17	0.19	0.15	0.13	0.15	0.11	0.10	0.15	0.05
MgO	1.62	4.97	6.55	6.55	7.21	5.84	5.77	6.45	6.38	6.06	6.41	6.60	6.61	4.64	2.48	7.32	6.95	7.57	5.77	6.29
CaO	5.74	7.30	2.48	7.43	8.63	8.08	8.03	8.55	9.99	9.42	10.64	9.06	11.65	10.15	4.97	11.99	10.25	14.35	9.23	15.09
Na_2O	4.93	0.06	1.87	4.32	3.90	2.92	2.87	3.87	4.02	3.81	3.47	4.07	3.11	4.42	5.31	1.56	3.38	3.22	3.86	3.85
K_2O	0.25	0.03	0.06	0.35	0.27	0.17	0.31	0.31	0.19	0.21	0.21	0.20	0.06	0.14	0.31	0.03	0.18	0.35	0.10	0.34
P_2O_5	0.20	0.15	0.15	0.13	0.16	0.15	0.18	0.12	0.10	0.11	0.12	0.09	0.09	0.12	0.19	0.10	0.13	0.13	0.16	0.15
LOI	1.57	4.10	4.93	2.47	3.24	3.68	3.78	2.60	1.68	2.95	2.31	2.60	0.98	0.84	1.64	3.23	3.25	3.27	3.04	2.72
Total	100.44	99.14	100.16	100.43	99.57	99.78	100.18	99.64	100.27	99.77	100.89	100.09	100.77	99.91	99.15	99.37	100.84	101.00	99.66	100.80
Trace elements (ppm)																				
Sc	12.7	28.7	30.8	35.0	35.0	32.2	31.2	33.3	36.6	33.9	37.7	34.0	39.3	33.4	18.0	36.4	38.2	34.9	31.4	29.5
V	33.3	271.5	287.6	328.7	316.6	352.4	333.8	320.1	338.4	318.5	359.2	308.4	313.5	385.7	149.9	311.0	326.7	306.4	287.2	327.4
Cr	8.4	22.2	22.7	48.0	34.0	16.4	33.7	47.4	35.7	48.0	59.5	68.3	23.1	32.0	12.8	30.3	61.4	50.6	59.1	7.8
Co	6.2	84.9	79.4	40.3	37.2	37.9	33.4	39.1	36.1	38.6	40.5	35.6	37.9	35.7	18.7	37.6	37.7	20.9	40.9	15.3
Ni	30.8	58.9	365.3	68.4	3608.0	49.8	37.5	44.0	64.7	136.2	71.6	210.5	144.2	35.2	40.6	58.3	201.3	64.0	86.9	34.3
Cu	13.3	20.7	23.5	49.7	246.2	16.9	102.9	20.2	13.5	90.1	50.0	17.8	63.8	22.2	26.6	13.4	13.4	23.0	150.9	4.4
Zn	35.3	315.0	63.8	99.8	58.9	55.2	77.7	32.3	56.7	51.6	69.6	100.9	104.4	79.2	50.3	27.1	40.4	21.3	65.3	37.3
Sr	209.0	201.1	62.2	210.1	190.1	197.6	184.3	200.1	199.8	202.0	168.6	201.8	168.3	219.8	138.6	227.0	243.8	272.7	184.9	301.4
Y	75.7	37.4	40.4	35.5	34.2	36.4	43.9	35.2	32.0	26.6	32.0	26.8	26.4	31.7	64.5	25.2	35.5	31.6	32.8	37.4
Zr	420.0	108.8	107.9	100.7	99.8	123.6	130.8	95.4	78.0	66.3	101.5	58.0	42.7	46.2	244.8	73.3	83.6	97.5	72.4	76.7
Ba	27.5	5.6	4.6	16.7	28.8	21.3	30.7	34.9	20.1	23.8	24.0	27.2	25.9	15.2	55.1	57.3	19.4	12.3	27.0	11.5

Table C.7: ICP-MS results for samples of the diorite unit

Sample	ML13	ML34	ML35	ML85	ML86	ML88	ML100	ML101a	ML101b	ML103	ML104	ML105	ML106	ML107	ML108	ML109	ML110
Major elements (wt. %)																	
TiO_2	1.07	0.85	0.50	0.31	1.42	1.18	1.30	0.21	0.45	0.40	1.16	0.94	0.62	1.20	0.42	0.70	0.28
MnO	0.09	0.23	0.26	0.02	0.17	0.10	0.07	0.02	0.03	0.02	0.09	0.10	0.05	0.12	0.05	0.09	0.01
Fe_2O_3(T)	8.39	31.42	28.45	4.00	11.85	8.65	6.60	2.34	4.73	6.42	7.93	6.95	4.74	8.35	6.00	6.98	1.89
Trace elements (ppm)																	
V	23.58	26.16	9.84	3.02	24.60	13.58	10.80	4.04	2.11	4.94	39.34	23.70	7.49	44.71	3.65	7.43	6.29
Cr	2.47	9.34	5.12	5.57	4.84	5.59	126.08	2.01	4.70	11.52	2.17	37.76	8.55	1.47	10.22	3.25	9.12
Co	8.87	9.38	6.27	3.32	9.94	8.12	8.80	1.48	4.83	6.19	10.23	8.50	4.36	11.04	2.85	5.82	3.82
Ni	33.01	29.84	22.52	54.54	15.18	16.86	137.87	16.91	15.90	14.18	17.90	140.29	10.88	11.28	14.30	19.38	31.09
Cu	35.07	23.90	9.90	7.50	13.10	12.92	12.02	5.20	3.84	11.78	6.88	32.80	13.37	13.09	16.77	50.28	14.46
Zn	85.80	55.34	43.30	17.21	48.69	23.69	13.33	12.98	19.73	3.70	26.55	27.30	19.71	32.28	19.06	19.46	5.52
Ga	19.45	14.73	22.96	19.93	21.42	21.04	20.44	17.21	20.03	20.23	20.25	21.59	20.49	20.67	21.91	21.94	17.23
Rb	1.23	0.16	1.20	0.47	0.34	1.06	1.23	0.19	0.46	0.39	1.84	1.68	0.75	1.16	0.08	0.90	0.60
Sr	174.39	111.78	114.97	106.14	136.99	147.32	161.95	117.20	199.70	119.25	216.33	183.13	126.30	178.06	110.00	143.44	58.98
Y	70.00	68.25	87.34	111.26	72.76	69.64	66.58	124.13	88.70	99.86	88.57	81.94	70.12	60.72	92.10	91.86	79.57
Zr	314.79	270.38	504.57	470.14	217.84	315.36	279.35	560.35	391.91	447.86	237.71	339.02	394.13	246.02	349.44	974.14	662.79
Nb	7.36	5.64	7.48	7.00	8.37	8.31	10.05	9.56	8.67	8.79	9.80	8.93	7.69	5.50	11.91	9.75	9.20
Cs	0.07	0.09	0.12	0.17	0.08	0.08	0.10	0.07	0.21	0.08	0.07	0.05	0.12	0.10	0.28	0.03	0.02
Ba	21.96	9.76	73.82	49.63	58.33	57.22	58.58	19.22	13.85	46.15	29.70	61.04	71.68	31.68	16.66	45.72	20.77
La	7.49	10.65	16.77	21.64	10.54	10.63	9.99	21.49	12.93	15.86	10.20	12.97	13.11	10.02	14.25	14.30	13.94
Ce	22.91	30.32	43.76	58.30	30.89	29.90	29.55	58.83	36.66	45.74	32.40	33.78	35.30	28.06	40.45	37.64	37.17
Pr	4.04	5.01	6.60	9.04	5.30	4.84	5.06	9.29	6.03	7.37	5.90	5.28	5.49	4.60	6.52	5.68	5.60
Nd	21.08	23.86	29.10	39.38	25.06	23.45	23.64	41.06	27.96	33.49	29.30	27.68	24.11	21.63	29.46	28.52	26.95
Sm	7.17	7.45	8.95	11.99	8.01	7.60	7.00	12.16	8.77	10.39	9.50	7.68	7.02	6.68	9.09	7.84	6.97
Eu	2.00	1.88	2.02	1.81	2.31	2.36	2.13	1.90	2.24	2.23	2.37	2.15	2.31	2.26	2.26	2.28	1.12
Gd	8.21	8.56	9.52	12.61	9.32	8.82	8.59	14.06	10.67	12.20	11.74	10.07	8.45	8.10	10.80	10.55	8.97
Tb	1.60	1.60	1.90	2.50	1.80	1.72	1.59	2.74	2.05	2.37	2.22	1.85	1.61	1.46	2.10	1.95	1.63
Dy	10.81	10.17	13.02	16.86	11.81	10.82	10.49	18.60	14.05	16.32	15.05	12.69	11.04	9.79	14.27	13.51	11.83
Ho	2.18	2.10	2.76	3.45	2.42	2.24	2.15	3.87	2.85	3.34	3.00	2.63	2.31	1.96	2.97	2.89	2.47
Er	6.63	6.44	8.59	10.69	7.15	6.78	6.49	12.38	8.85	10.58	9.09	8.07	7.35	6.12	9.56	9.29	8.16
Tm	1.10	1.08	1.42	1.79	1.19	1.17	1.01	2.02	1.44	1.75	1.42	1.25	1.22	0.95	1.51	1.48	1.31
Yb	7.14	7.12	9.25	11.92	7.44	7.51	6.71	13.77	9.64	12.00	9.52	8.38	8.61	6.30	10.35	10.42	9.42
Lu	1.10	1.09	1.44	1.79	1.16	1.16	1.05	2.13	1.51	1.89	1.48	1.31	1.41	1.03	1.66	1.71	1.49
Hf	6.72	6.09	10.95	11.27	5.37	6.79	7.19	13.54	9.95	11.40	5.86	8.37	10.27	6.04	8.58	20.19	14.73
Ta	0.46	0.41	0.58	0.70	0.56	0.51	0.69	0.87	0.62	0.70	0.59	0.57	0.97	0.38	0.83	0.55	0.57
Pb	1.35	0.92	1.12	1.28	1.21	1.38	1.01	1.05	1.08	1.15	1.33	1.05	1.44	1.16	2.12	1.34	0.18
Th	0.78	0.71	1.57	1.80	0.79	0.80	0.81	1.92	1.20	1.46	0.80	1.07	1.58	0.75	1.21	1.65	1.76
U	0.26	0.27	0.41	0.52	0.27	0.27	0.31	0.66	0.41	0.58	0.32	0.40	0.57	0.26	0.46	0.65	0.61

Table C.8: ICP-MS data for samples of the foliated gabbro unit. Anorthosite and pegmatite samples are grouped separately.

	Foliated Gabbro														
Sample	ML20	ML21	ML22	ML24	ML26	ML27	ML28	ML29	ML30	ML32	ML40	ML41	ML42	ML44	ML47
Major elements (wt. %)															
TiO_2	0.80	0.53	0.45	0.45	0.28	0.33	0.26	0.33	0.63	0.34	0.64	0.64	0.77	0.33	0.21
MnO	0.10	0.08	0.10	0.14	0.08	0.12	0.09	0.07	0.13	0.49	0.10	0.12	0.11	0.14	0.42
Fe_2O_3(T)	6.51	4.79	5.73	6.60	23.82	30.55	5.31	3.76	7.91	30.95	6.00	8.07	5.81	8.77	6.13
Trace elements (ppm)															
V	207.86	139.00	168.55	161.84	129.16	154.58	116.24	126.49	232.69	150.32	167.27	237.91	190.73	156.31	81.97
Cr	41.96	116.77	337.17	46.94	289.50	531.26	247.40	236.12	223.45	326.52	171.91	74.62	129.18	346.76	373.73
Co	26.14	22.16	32.60	33.37	28.35	35.60	26.36	25.15	39.10	37.98	29.64	34.14	26.64	53.08	43.26
Ni	42.90	225.99	264.51	67.38	120.83	159.88	106.53	80.78	248.20	161.11	69.34	66.61	91.14	200.85	242.51
Cu	29.62	16.53	14.54	22.88	18.96	34.08	17.60	86.97	66.86	61.76	29.73	18.06	21.97	61.67	19.71
Zn	30.78	30.35	30.64	57.21	30.49	38.82	15.70	21.89	37.59	48.10	12.00	24.72	29.84	53.62	32.57
Ga	14.97	12.23	11.57	13.48	11.99	10.15	13.13	13.95	11.58	11.33	14.81	13.94	13.51	9.88	11.74
Rb	0.41	0.43	0.84	0.12	0.11	0.22	0.31	0.33	0.46	0.31	0.57	0.72	0.68	0.23	0.02
Sr	233.57	262.13	196.84	175.94	199.13	167.17	164.57	175.15	126.88	162.06	207.19	159.73	204.20	108.93	178.86
Y	12.76	9.30	10.55	14.38	6.73	7.92	7.72	7.38	10.41	8.27	12.77	13.30	10.29	8.44	4.32
Zr	27.10	23.04	13.22	28.69	7.38	7.74	14.10	10.68	16.72	27.09	30.89	33.38	39.31	3.95	5.12
Nb	0.73	0.63	0.30	0.70	0.40	0.40	0.28	0.27	0.49	0.75	1.00	0.69	1.23	0.14	0.34
Cs	0.02	0.02	0.02	0.05	0.04	0.05	0.02	0.05	0.02	0.03	0.02	0.02	0.02	0.02	0.04
Ba	21.99	13.22	15.89	15.27	9.21	9.46	13.75	11.73	17.17	21.07	17.31	19.97	18.93	10.80	9.13
La	1.28	0.97	0.73	1.55	0.60	0.64	0.84	0.67	0.71	0.70	1.45	1.14	1.13	0.52	0.58
Ce	3.41	2.63	2.17	3.95	1.70	1.76	2.07	1.84	2.07	2.09	3.93	3.34	3.04	1.51	1.47
Pr	0.59	0.45	0.40	0.67	0.27	0.30	0.35	0.29	0.35	0.33	0.64	0.58	0.51	0.27	0.22
Nd	3.44	2.53	2.37	3.51	1.60	1.67	1.97	1.87	2.26	1.91	3.47	3.17	2.83	1.66	1.23
Sm	1.16	0.83	0.90	1.32	0.61	0.68	0.66	0.65	0.84	0.75	1.24	1.23	1.02	0.75	0.42
Eu	0.62	0.47	0.49	0.56	0.38	0.34	0.52	0.41	0.40	0.38	0.56	0.61	0.51	0.39	0.29
Gd	1.61	1.25	1.29	1.76	0.88	0.98	0.95	0.95	1.17	1.01	1.66	1.70	1.38	1.13	0.56
Tb	0.30	0.21	0.25	0.32	0.14	0.17	0.19	0.16	0.22	0.17	0.29	0.32	0.26	0.20	0.10
Dy	2.19	1.63	1.82	2.29	1.06	1.25	1.36	1.22	1.57	1.26	2.12	2.18	1.75	1.50	0.66
Ho	0.44	0.32	0.37	0.46	0.21	0.26	0.28	0.25	0.35	0.26	0.43	0.46	0.38	0.31	0.13
Er	1.22	0.88	0.99	1.34	0.62	0.73	0.73	0.68	0.97	0.77	1.18	1.28	0.98	0.83	0.36
Tm	0.19	0.12	0.14	0.22	0.10	0.12	0.11	0.11	0.15	0.12	0.18	0.19	0.15	0.12	0.06
Yb	1.29	0.92	0.96	1.40	0.61	0.75	0.76	0.70	0.99	0.76	1.20	1.39	1.00	0.87	0.39
Lu	0.19	0.13	0.14	0.20	0.09	0.11	0.11	0.10	0.15	0.11	0.18	0.19	0.15	0.12	0.05
Hf	0.74	0.63	0.39	0.77	0.23	0.28	0.38	0.31	0.46	0.56	0.78	0.90	0.92	0.16	0.15
Ta	0.04	0.04	0.02	0.04	0.02	0.02	0.02	0.02	0.03	0.03	0.06	0.04	0.06	0.01	0.02
Pb	1.59	3.25	0.77	0.93	1.35	0.97	1.15	1.48	0.29	1.37	1.26	1.53	0.67	0.76	1.27
Th	0.13	0.08	0.07	0.07	0.02	0.02	0.06	0.03	0.04	0.16	0.09	0.54	0.12	1.03	0.02
U	0.03	0.03	0.01	0.01	0.01	0.01	0.02	0.02	0.03	0.01	0.04	0.04	0.03	0.11	0.00

Table C.8 *continued…*

	Foliated Gabbro			Foliated Gabbro-Anorthosite			Foliated Gabbro-Pegmatite					
Sample	ML48	ML65	ML70	ML45	ML49	ML98	ML23	ML25	ML31	ML43	ML46	ML73
Major elements (wt. %)												
TiO_2	0.26	0.57	0.53	0.36	0.14	0.12	0.53	0.62	0.38	0.37	0.25	0.90
MnO	0.06	0.13	0.08	0.12	0.03	0.01	0.09	0.13	0.40	0.08	0.46	0.13
Fe_2O_3(T)	2.27	7.30	5.02	7.25	1.23	0.80	5.77	7.70	27.64	5.38	5.47	7.68
Trace elements (ppm)												
V	132.15	210.02	148.98	146.43	45.05	21.48	173.33	229.03	165.22	145.32	98.01	225.17
Cr	686.89	90.06	74.90	779.14	132.11	26.99	9.27	43.18	354.71	299.02	150.85	17.50
Co	15.61	33.70	20.01	41.58	7.74	4.31	24.37	38.27	34.71	30.09	33.28	32.84
Ni	81.82	73.08	37.98	230.56	322.04	36.65	52.75	107.76	133.70	179.85	153.09	61.92
Cu	5.38	83.06	67.27	85.05	30.27	95.69	80.95	99.05	23.61	21.82	23.17	20.92
Zn	8.11	43.18	47.56	30.84	18.77	14.42	29.30	48.92	33.13	23.31	44.83	89.37
Ga	11.44	14.77	15.64	10.57	14.53	18.84	15.62	13.06	11.97	11.89	12.93	15.01
Rb	0.18	1.29	0.82	0.42	0.22	0.13	0.43	0.33	0.45	0.39	0.47	1.11
Sr	199.47	209.65	213.51	138.37	219.43	279.67	229.56	181.91	185.54	212.27	198.76	223.86
Y	6.18	12.86	10.97	7.97	2.76	1.63	12.44	11.75	10.79	8.40	7.31	17.23
Zr	6.55	44.08	38.19	10.21	8.61	7.86	21.49	16.39	17.64	10.91	11.74	25.44
Nb	0.14	0.95	0.98	0.28	0.20	0.50	0.74	0.66	0.58	0.27	0.59	1.44
Cs	0.01	0.04	0.02	0.02	0.01	0.01	0.03	0.06	0.04	0.02	0.04	0.13
Ba	8.50	25.79	21.10	12.84	11.50	10.75	18.27	9.26	13.03	10.32	22.59	20.27
La	0.33	1.45	1.32	0.55	0.50	0.46	1.50	1.05	1.32	0.57	1.38	1.62
Ce	1.01	4.01	3.54	1.58	1.31	1.05	4.28	3.10	3.64	1.60	3.47	4.85
Pr	0.20	0.68	0.60	0.29	0.20	0.16	0.72	0.50	0.57	0.29	0.51	0.79
Nd	1.30	3.66	3.17	1.81	1.06	0.81	4.09	2.69	3.00	1.90	2.53	4.20
Sm	0.53	1.20	1.04	0.67	0.32	0.20	1.28	1.08	1.03	0.78	0.74	1.62
Eu	0.32	0.58	0.58	0.37	0.35	0.34	0.65	0.54	0.46	0.44	0.49	0.74
Gd	0.79	1.61	1.40	0.93	0.43	0.23	1.72	1.47	1.45	1.07	0.91	2.12
Tb	0.15	0.31	0.26	0.19	0.08	0.04	0.31	0.28	0.24	0.20	0.15	0.40
Dy	1.05	2.25	1.86	1.34	0.55	0.25	2.13	1.88	1.67	1.49	1.13	2.77
Ho	0.22	0.44	0.37	0.28	0.11	0.05	0.42	0.37	0.34	0.30	0.23	0.56
Er	0.60	1.32	1.07	0.76	0.29	0.12	1.18	1.10	0.98	0.79	0.73	1.69
Tm	0.09	0.19	0.16	0.11	0.05	0.02	0.18	0.18	0.16	0.12	0.12	0.27
Yb	0.60	1.24	1.04	0.75	0.30	0.10	1.18	1.14	1.00	0.79	0.74	1.63
Lu	0.08	0.20	0.16	0.12	0.04	0.02	0.17	0.18	0.15	0.12	0.13	0.25
Hf	0.20	1.15	1.00	0.30	0.21	0.13	0.58	0.53	0.53	0.34	0.30	0.76
Ta	0.01	0.07	0.05	0.02	0.02	0.02	0.04	0.04	0.03	0.02	0.04	0.09
Pb	0.07	0.73	1.08	0.60	0.98	0.58	1.54	1.02	1.09	0.81	3.22	1.44
Th	0.06	0.14	0.11	0.04	0.04	0.02	0.14	0.10	0.07	0.04	0.16	0.15
U	0.01	0.04	0.05	0.01	0.01	0.01	0.03	0.02	0.03	0.01	0.01	0.03

Table C.9: ICP-MS results for samples from the patchy gabbro unit.

Sample	ML50	ML51	ML54	ML57	ML61	ML62	ML63	ML64	ML66	ML67	ML68	ML71	ML74	ML93	ML95
Major elements (wt. %)															
TiO_2	1.78	1.35	2.78	1.46	1.12	1.54	1.56	1.45	0.51	0.68	0.79	0.62	1.96	1.70	1.36
MnO	0.16	0.15	0.21	0.15	0.20	0.21	0.21	0.23	0.13	0.12	0.14	0.16	0.19	0.21	0.13
Fe_2O_3(T)	12.51	10.93	17.67	10.85	11.51	13.17	12.58	13.32	7.22	6.63	8.30	9.57	11.32	14.55	10.42
Trace elements (ppm)															
V	489.6	300.4	819.1	336.9	357.6	420.3	358.3	357.1	175.2	181.3	225.9	205.3	384.4	560.2	287.8
Cr	60.0	71.1	181.0	16.8	137.4	43.7	108.9	167.7	114.0	88.6	86.8	395.6	6.4	90.0	25.6
Co	44.5	43.3	54.3	49.5	41.5	38.6	39.0	44.4	31.6	28.4	35.7	45.2	40.3	54.4	35.8
Ni	84.6	77.2	372.3	201.4	255.2	53.7	212.5	86.1	242.0	90.8	361.9	114.0	29.2	88.7	87.7
Cu	20.0	29.4	71.8	134.4	33.2	39.2	39.3	33.3	30.6	82.1	48.6	67.1	27.3	48.0	61.9
Zn	138.4	73.7	57.4	44.1	125.6	99.7	126.4	110.6	38.4	51.3	67.0	70.1	58.1	63.7	50.0
Ga	15.2	15.6	17.6	16.1	15.4	15.5	14.8	14.3	14.1	15.1	14.6	12.4	18.2	14.3	16.5
Rb	0.7	0.9	0.5	0.4	2.0	1.7	1.7	0.8	0.8	1.0	1.5	0.5	1.6	0.7	0.2
Sr	168.0	187.5	150.5	176.7	162.0	150.0	162.0	176.4	189.4	197.3	167.2	137.5	201.5	137.8	204.0
Y	23.6	24.4	26.5	33.5	24.4	26.6	27.5	21.3	12.7	10.6	16.0	16.6	33.2	16.5	29.4
Zr	55.7	64.7	74.3	107.4	67.9	73.0	45.3	43.5	26.3	25.3	74.6	27.6	47.7	28.0	83.7
Nb	1.79	1.87	2.57	2.50	1.32	1.37	1.62	1.06	0.72	0.91	1.30	0.78	3.69	0.87	2.29
Cs	0.03	0.08	0.11	0.05	0.08	0.03	0.07	0.08	0.03	0.02	0.03	0.05	0.06	0.03	0.06
Ba	20.2	20.3	21.2	18.3	43.7	30.6	114.7	20.7	17.6	18.7	48.4	14.0	33.4	15.7	23.7
La	2.40	2.91	2.87	3.27	2.56	2.41	2.69	1.86	1.35	1.09	1.95	1.79	3.44	1.43	3.62
Ce	6.68	8.14	8.56	9.14	7.56	7.15	8.05	5.61	3.66	3.09	5.11	5.44	10.04	4.29	11.10
Pr	1.23	1.33	1.44	1.57	1.29	1.27	1.38	0.92	0.60	0.51	0.80	0.91	1.72	0.70	1.90
Nd	6.05	6.85	7.39	8.48	6.60	6.59	7.36	5.19	3.42	3.00	4.46	4.83	9.22	4.03	9.15
Sm	2.28	2.52	2.57	3.24	2.43	2.47	2.72	1.93	1.15	0.99	1.43	1.76	3.50	1.54	2.98
Eu	0.91	0.98	1.13	0.99	1.01	1.09	1.10	0.96	0.58	0.55	0.69	0.65	1.13	0.65	1.12
Gd	2.95	3.09	3.42	4.18	3.17	3.27	3.42	2.66	1.59	1.25	1.93	2.22	4.22	2.04	3.88
Tb	0.57	0.58	0.63	0.81	0.58	0.63	0.66	0.54	0.30	0.26	0.36	0.41	0.81	0.39	0.69
Dy	3.89	3.99	4.46	5.53	4.14	4.23	4.44	3.48	2.06	1.76	2.51	2.68	5.19	2.67	4.76
Ho	0.81	0.80	0.93	1.17	0.83	0.92	0.95	0.71	0.42	0.35	0.52	0.55	1.08	0.54	0.96
Er	2.34	2.30	2.72	3.38	2.42	2.63	2.75	2.10	1.29	0.99	1.53	1.61	3.04	1.50	2.91
Tm	0.37	0.38	0.44	0.53	0.38	0.44	0.43	0.34	0.18	0.15	0.23	0.26	0.49	0.26	0.46
Yb	2.34	2.31	2.94	3.54	2.42	2.81	2.76	2.06	1.19	1.01	1.55	1.55	2.97	1.66	2.94
Lu	0.35	0.36	0.43	0.52	0.39	0.43	0.42	0.32	0.19	0.16	0.24	0.24	0.45	0.24	0.48
Hf	1.43	1.55	1.89	2.57	1.71	1.86	1.21	1.01	0.82	0.75	1.89	0.77	1.36	0.78	2.21
Ta	0.12	0.12	0.21	0.18	0.09	0.09	0.13	0.07	0.05	0.07	0.10	0.04	0.38	0.06	0.17
Pb	1.22	1.46	0.92	0.96	1.43	1.36	1.96	1.38	0.94	0.38	1.10	1.43	1.44	1.06	1.00
Th	0.21	0.17	0.18	0.22	0.21	0.18	0.19	0.10	0.12	0.05	0.10	0.08	0.24	0.09	0.22
U	0.06	0.05	0.05	0.08	0.07	0.09	0.04	0.04	0.04	0.04	0.04	0.01	0.07	0.03	0.08

Table C.10: ICP-MS results for samples from the spotty gabbro unit.

Sample	ML10	ML11	ML17	ML53	ML55b	ML58	ML89	ML91	ML92	ML94	ML96
Major elements (wt. %)											
TiO_2	1.28	0.60	1.41	1.01	1.10	2.19	0.74	0.56	1.00	1.29	0.78
MnO	0.19	0.14	0.14	0.15	0.14	0.18	0.06	0.06	0.16	0.15	0.10
Fe_2O_3(T)	13.06	8.11	11.19	10.39	9.97	13.53	6.46	5.11	9.68	10.80	7.06
Trace elements (ppm)											
V	325.8	215.1	333.2	357.3	321.0	590.6	182.9	204.1	257.4	262.8	182.7
Cr	45.9	456.3	63.7	51.0	89.8	81.0	315.3	274.4	71.2	32.1	24.1
Co	54.3	43.1	37.2	44.6	45.3	43.7	28.8	29.3	40.2	38.5	23.5
Ni	89.5	163.1	65.7	73.6	79.1	223.7	138.1	156.7	85.5	56.3	44.5
Cu	31.0	34.6	33.5	21.1	67.2	71.0	31.7	8.6	61.2	8.7	28.5
Zn	61.6	76.4	50.0	39.8	52.3	52.7	33.9	33.4	40.4	92.2	89.0
Ga	15.6	12.1	15.1	14.2	14.0	17.5	13.7	10.7	15.1	16.3	15.3
Rb	0.4	0.7	1.5	1.4	0.4	0.5	1.0	0.5	1.2	0.4	0.8
Sr	189.3	122.7	204.1	198.3	176.8	161.2	251.8	159.7	198.0	194.7	209.8
Y	27.9	14.6	32.4	18.2	15.0	27.8	15.5	12.2	18.4	27.4	16.5
Zr	90.0	30.9	99.5	48.1	27.5	96.9	36.3	38.4	41.8	90.6	48.2
Nb	2.15	0.69	2.48	1.04	0.86	3.09	1.19	0.90	1.14	2.18	0.79
Cs	0.04	0.06	0.06	0.08	0.04	0.07	0.06	0.02	0.05	0.05	0.08
Ba	28.9	24.0	16.2	15.8	14.9	25.2	13.0	11.4	19.6	25.8	23.7
La	3.68	1.55	4.43	2.23	1.29	2.71	1.67	1.62	1.86	4.56	1.65
Ce	10.39	4.36	12.72	6.42	3.75	8.37	5.19	4.69	5.48	12.69	4.96
Pr	1.72	0.69	2.10	1.09	0.64	1.48	0.88	0.73	0.93	2.09	0.86
Nd	8.35	3.69	10.59	5.91	3.55	7.79	4.75	3.78	4.98	9.88	4.41
Sm	2.95	1.36	3.38	2.06	1.41	2.68	1.67	1.22	1.84	3.05	1.50
Eu	1.00	0.55	1.16	0.74	0.72	1.01	0.63	0.51	0.76	1.14	0.76
Gd	3.61	1.81	3.95	2.52	1.97	3.49	2.00	1.63	2.34	3.72	2.10
Tb	0.68	0.34	0.75	0.46	0.34	0.66	0.36	0.29	0.44	0.67	0.39
Dy	4.59	2.28	5.27	3.03	2.57	4.59	2.42	2.06	2.87	4.56	2.66
Ho	0.93	0.49	1.04	0.61	0.52	0.94	0.49	0.40	0.59	0.92	0.53
Er	2.83	1.44	3.15	1.70	1.51	2.79	1.44	1.20	1.76	2.74	1.67
Tm	0.44	0.21	0.50	0.27	0.24	0.45	0.23	0.20	0.28	0.46	0.26
Yb	2.87	1.43	3.31	1.73	1.52	2.97	1.49	1.26	1.78	3.10	1.67
Lu	0.42	0.22	0.51	0.26	0.23	0.44	0.23	0.18	0.29	0.46	0.27
Hf	2.03	0.85	2.21	1.12	0.73	2.35	0.79	0.97	1.09	2.12	1.25
Ta	0.14	0.05	0.18	0.07	0.06	0.21	0.09	0.05	0.08	0.16	0.08
Pb	2.01	1.65	1.20	0.87	1.13	1.12	1.09	0.94	1.38	1.11	2.77
Th	0.24	0.10	0.28	0.13	0.06	0.23	0.13	0.20	0.11	0.26	0.12
U	0.11	0.02	0.10	0.03	0.02	0.08	0.02	0.02	0.02	0.08	0.04

Table C.11: ICP-MS results for samples from the sheeted dykes.

Sample	ML102	ML36	ML37	ML38	ML39	ML76	ML77	ML78	ML79	ML80	ML81	ML82	ML83	ML84
Major elements (wt. %)														
TiO_2	1.60	1.95	1.14	0.98	1.50	1.60	1.53	1.36	2.15	1.70	1.98	1.18	1.93	1.69
MnO	0.05	0.04	0.28	0.40	0.14	0.09	0.16	0.16	0.49	0.12	0.08	0.09	0.12	0.08
Fe_2O_3(T)	9.50	8.67	10.38	8.16	10.75	10.13	11.83	10.97	13.22	11.77	11.16	9.80	12.03	9.36
Trace elements (ppm)														
V	140.6	150.5	71.5	11.8	146.6	221.5	318.7	314.9	324.7	308.0	236.4	267.0	310.9	204.2
Cr	3.5	5.8	7.8	5.1	16.5	333.0	40.1	28.0	32.9	43.7	12.5	104.3	17.0	5.6
Co	16.5	14.8	15.0	9.3	24.0	21.1	39.6	38.0	33.1	34.6	21.5	27.0	27.8	18.4
Ni	24.2	20.3	16.6	351.7	30.1	1028.5	54.3	46.3	33.8	48.4	38.6	352.6	24.6	6.7
Cu	9.2	15.4	40.4	10.0	25.7	20.8	98.2	73.2	11.4	39.6	10.4	14.4	19.2	15.3
Zn	16.2	7.4	58.7	47.1	39.9	17.9	51.3	59.3	20.8	57.4	84.7	38.4	31.7	7.7
Ga	16.9	19.6	24.5	17.4	20.4	18.5	18.5	16.0	18.9	17.2	18.9	16.9	18.4	18.6
Rb	0.5	1.1	0.1	0.1	0.4	0.5	0.3	1.9	1.1	1.5	1.7	1.9	1.1	0.7
Sr	164.4	171.2	224.2	135.9	134.0	167.2	169.8	205.4	210.2	214.0	211.8	206.8	179.6	174.3
Y	61.3	54.5	70.5	75.5	58.8	56.3	35.1	29.0	49.8	37.3	52.8	27.9	44.2	55.7
Zr	186.6	327.4	260.6	325.1	228.1	224.0	113.1	83.3	181.4	129.6	179.0	79.8	158.4	241.9
Nb	5.32	9.29	7.43	8.06	5.79	5.65	2.80	2.03	5.14	3.69	4.64	1.93	4.70	6.35
Cs	0.12	0.03	0.11	0.05	0.12	0.04	0.05	0.14	0.10	0.07	0.06	0.09	0.13	0.02
Ba	16.3	28.8	6.9	6.1	21.0	32.1	21.1	48.3	40.7	40.5	31.9	51.3	37.0	33.3
La	7.95	10.65	11.52	12.11	8.79	8.59	4.69	3.63	7.72	5.65	8.15	3.38	6.70	8.04
Ce	21.97	25.05	31.42	33.37	24.66	24.38	13.31	10.26	21.17	15.33	22.49	9.77	18.73	21.95
Pr	3.83	3.73	5.21	5.54	4.03	3.90	2.22	1.75	3.50	2.56	3.62	1.74	3.18	3.56
Nd	18.99	19.72	25.18	26.27	19.78	18.91	10.97	8.71	16.89	12.16	17.02	8.56	14.91	18.87
Sm	6.57	5.50	8.25	8.65	6.51	6.06	3.65	3.07	5.47	4.02	5.55	2.90	4.84	5.40
Eu	1.79	1.86	2.95	2.55	2.03	1.67	1.36	1.06	1.63	1.25	1.82	1.04	1.46	1.63
Gd	7.81	6.77	9.08	9.37	7.63	6.94	4.45	3.67	6.42	4.72	6.46	3.49	5.45	6.95
Tb	1.50	1.17	1.67	1.79	1.42	1.35	0.83	0.67	1.19	0.88	1.26	0.69	1.05	1.24
Dy	10.17	8.07	10.90	11.71	9.45	8.73	5.67	4.69	7.96	5.94	8.34	4.47	7.12	8.73
Ho	1.98	1.72	2.25	2.42	1.90	1.81	1.14	0.96	1.60	1.23	1.73	0.90	1.46	1.81
Er	6.04	4.71	6.71	7.26	5.64	5.39	3.37	2.81	4.73	3.58	5.09	2.68	4.25	5.45
Tm	0.93	0.75	1.04	1.18	0.91	0.89	0.53	0.46	0.76	0.57	0.83	0.41	0.66	0.82
Yb	6.16	5.34	6.66	7.33	5.71	5.69	3.51	2.87	4.90	3.68	5.31	2.71	4.51	5.55
Lu	0.96	0.83	1.08	1.15	0.89	0.90	0.53	0.45	0.74	0.57	0.83	0.43	0.69	0.88
Hf	4.56	7.07	5.49	6.79	4.91	4.89	2.61	1.99	4.15	2.98	4.15	1.90	3.54	5.73
Ta	0.34	0.51	0.46	0.50	0.36	0.37	0.19	0.14	0.37	0.25	0.34	0.14	0.34	0.38
Pb	0.99	0.61	1.40	1.28	1.27	1.29	0.87	0.87	0.91	1.70	1.32	1.12	1.03	0.23
Th	0.62	0.79	0.72	0.87	0.61	0.56	0.28	0.23	0.49	0.38	0.59	0.24	0.48	0.69
U	0.23	0.25	0.27	0.30	0.22	0.19	0.09	0.06	0.19	0.12	0.13	0.07	0.17	0.23

Table C.12: ICP-MS results for samples from the cross-cutting dykes.

	ML12	ML14	ML15	ML16	ML18	ML19	ML33	ML52	ML55a	ML56	ML59	ML60	ML72	ML75	ML8	ML87	ML9	ML90	ML97	ML99
Major elements (wt. %)																				
TiO_2	0.78	1.43	1.41	1.36	1.38	1.58	1.70	1.37	1.25	1.26	1.50	1.11	1.28	1.85	1.38	1.25	1.50	1.50	1.34	1.76
MnO	0.05	0.10	0.11	0.13	0.12	0.15	0.17	0.12	0.14	0.15	0.19	0.17	0.18	0.15	0.12	0.15	0.12	0.10	0.15	0.05
Fe_2O_3(T)	3.85	18.57	19.67	10.37	10.36	12.30	11.75	11.25	10.72	10.47	11.73	10.27	11.09	10.96	8.20	10.84	10.78	6.48	11.19	4.38
Trace elements (ppm)																				
V	41.8	276.5	291.7	321.0	315.4	363.5	331.1	321.6	337.3	316.5	342.4	284.2	333.2	415.5	153.8	320.4	337.9	312.0	297.4	340.8
Cr	6.8	19.9	18.8	42.4	29.1	15.2	30.3	45.8	33.3	43.7	48.2	58.6	21.5	32.7	10.7	29.2	62.4	47.9	54.6	5.1
Co	7.3	89.1	79.5	40.3	39.5	36.9	33.8	42.3	41.1	41.0	38.0	35.5	41.8	36.1	17.3	37.8	39.7	22.6	41.0	18.1
Ni	25.9	55.8	356.6	68.9	3493.4	48.0	34.6	43.1	62.1	130.4	64.3	188.5	144.1	33.5	37.6	48.4	206.6	58.4	82.6	28.3
Cu	18.3	16.9	27.7	54.5	243.6	19.6	97.2	23.2	15.1	88.6	43.2	15.2	71.9	19.5	21.3	15.4	15.9	19.0	51.5	3.1
Zn	29.6	316.2	56.8	105.6	40.7	57.3	79.2	37.9	52.5	43.3	66.4	96.4	98.9	78.2	57.3	29.7	42.9	24.8	68.5	33.9
Ga	19.6	20.3	18.0	15.3	15.3	17.4	16.7	16.2	16.2	15.2	15.8	14.1	15.5	18.4	19.7	17.5	16.4	15.3	16.1	13.5
Rb	0.8	0.0	0.1	0.9	1.3	0.8	1.3	0.9	0.4	0.5	0.4	0.5	0.3	0.6	0.9	0.2	0.6	1.3	0.3	1.7
Sr	208.2	198.6	61.6	237.9	190.1	194.9	175.0	193.7	195.6	185.6	161.9	184.6	158.4	225.3	138.7	229.7	248.0	273.8	182.6	299.0
Y	70.0	34.2	38.0	30.1	31.9	36.2	39.8	31.3	29.6	23.2	27.9	23.2	23.9	30.8	56.7	25.8	32.4	31.7	30.9	35.6
Zr	402.7	113.2	106.8	105.5	97.6	123.4	129.3	98.1	81.5	75.9	104.0	57.5	46.1	49.7	249.0	71.8	97.3	100.8	76.8	79.3
Nb	7.61	2.90	2.99	2.55	2.76	3.17	3.36	2.21	1.95	1.97	2.35	1.61	1.53	2.23	4.70	1.76	2.06	2.63	1.80	2.31
Cs	0.03	0.10	0.09	0.09	0.09	0.07	0.07	0.06	0.09	0.04	0.06	0.11	0.07	0.07	0.09	0.09	0.07	0.05	0.05	0.04
Ba	24.4	6.1	5.2	16.8	19.2	14.4	30.7	34.9	19.4	26.2	23.6	23.6	25.8	17.3	54.1	13.2	21.0	13.2	23.7	12.0
La	9.41	5.25	5.56	3.87	4.74	4.81	5.25	4.06	2.85	2.95	3.76	2.56	2.20	3.50	9.55	3.00	4.33	4.23	4.41	6.93
Ce	26.42	14.43	14.78	11.20	13.02	13.78	15.22	11.13	8.77	8.20	10.69	7.99	6.72	10.24	27.81	8.51	12.29	11.97	11.81	16.91
Pr	4.42	2.31	2.35	1.85	2.12	2.28	2.54	1.85	1.55	1.35	1.75	1.35	1.20	1.68	4.52	1.41	1.99	1.97	1.86	2.59
Nd	21.32	11.29	11.36	9.33	10.34	11.12	12.41	9.29	8.21	6.84	8.64	6.90	6.28	8.55	20.38	7.25	9.82	9.71	9.31	11.86
Sm	6.82	3.53	3.68	3.16	3.49	3.78	4.13	3.20	2.99	2.42	2.90	2.40	2.39	3.04	6.38	2.53	3.33	3.39	2.99	3.74
Eu	1.71	1.12	1.42	1.07	1.13	1.30	1.36	1.14	0.99	0.79	1.07	0.82	0.95	1.29	1.40	0.98	1.15	1.10	1.14	1.37
Gd	7.62	4.24	4.47	3.62	4.06	4.73	4.99	3.96	3.70	3.08	3.58	3.06	2.97	3.92	6.99	3.15	4.10	4.01	3.87	4.62
Tb	1.51	0.82	0.85	0.69	0.74	0.85	0.92	0.77	0.71	0.54	0.66	0.57	0.59	0.76	1.34	0.62	0.74	0.75	0.73	0.83
Dy	10.40	5.60	5.86	4.79	4.91	5.76	6.18	4.98	4.85	3.75	4.60	3.93	3.85	4.86	8.99	3.99	5.10	4.88	4.97	5.63
Ho	2.12	1.11	1.17	0.95	0.98	1.15	1.25	1.05	0.99	0.78	0.94	0.79	0.77	0.98	1.82	0.83	1.02	1.00	1.04	1.12
Er	6.62	3.33	3.52	2.81	2.98	3.50	3.68	3.03	2.92	2.26	2.77	2.34	2.37	2.97	5.50	2.48	3.17	2.99	3.00	3.51
Tm	1.11	0.54	0.56	0.45	0.49	0.58	0.61	0.48	0.48	0.36	0.43	0.37	0.38	0.49	0.88	0.42	0.48	0.51	0.46	0.55
Yb	7.34	3.55	3.57	3.01	3.16	3.77	3.84	3.02	3.20	2.45	2.83	2.48	2.35	3.00	5.86	2.62	3.25	3.20	3.08	3.80
Lu	1.22	0.57	0.55	0.46	0.47	0.58	0.59	0.48	0.46	0.36	0.42	0.37	0.36	0.46	0.85	0.37	0.48	0.48	0.49	0.57
Hf	8.26	2.49	2.35	2.32	2.18	2.88	2.85	2.35	2.10	1.81	2.52	1.46	1.06	1.29	6.01	1.65	2.16	2.20	2.10	2.09
Ta	0.48	0.21	0.20	0.16	0.19	0.22	0.24	0.15	0.14	0.16	0.16	0.12	0.10	0.14	0.30	0.12	0.16	0.18	0.16	0.19
Pb	1.64	1.63	0.86	1.02	0.97	1.09	0.83	0.82	1.00	1.02	1.48	1.41	1.19	1.31	1.69	1.18	1.60	0.90	0.94	0.87
Th	0.69	0.40	0.41	0.27	0.33	0.32	0.34	0.22	0.17	0.25	0.39	0.20	0.15	0.25	0.87	0.22	0.29	0.22	0.23	0.27
U	0.24	0.14	0.13	0.08	0.12	0.11	0.11	0.08	0.04	0.07	0.08	0.03	0.02	0.06	0.29	0.05	0.07	0.06	0.09	0.07

REFERENCES

Abbey, S., 1981. The search for ‘best values’- A study of three Candian rocks, *Geostandards Newsletter*, 5: 13-26.

Abily, B., Ceuleneer, G., Launeau, P., 2011. Synmagmatic normal faulting in the lower oceanic crust: Evidence from the Oman ophiolite, *Geology*, 39: 391–394.

Aharonov, E., Whitehead, J.A., Kelemen, P.B., Spiegelman, M., 1995. Channeling instability of upwelling melt in the mantle, *Journal of Geophysical Research*, 100(B10): 20433-20450.

Alabaster, T., Pearce, J.A., Malpas, J., 1982. The volcanic stratigraphy and petrogenesis of the Oman ophiolite complex, *Contributions to Mineralogy and Petrology*, 81(3): 168–183.

Aldiss, D.T.,1981. Oceanic plagiogranites from the ocean crust and ophiolites, *Nature*, 289: 577–578.

Amri, I., Benoit, M., Ceuleneer, G., 1996. Tectonic setting for the genesis of oceanic plagiogranites: Evidence from a paleo-spreading structure in the Oman ophiolite, *Earth and Planetary Science Letters*, 139(1–2): 177–194.

Anonymous, 1972. Penrose field conference on ophiolites. *Geotimes*, 17, 24–25.

Baines, A.G., Cheadle, M.J., Dick, H.J., Scheirer, A.H., John, B.E., Kusznir, N.J., Matsumoto, T., 2007. Evolution of the Southwest Indian Ridge from 55 45′ E to 62 E: Changes in plate-boundary geometry since 26 Ma, *Geochemistry Geophysics Geosystems*, 8(6).

Barkan, S., Saveliv, V., Iwanczyk, J., Feng, L., Tull, C., Patt, B., Newbury, D., Small, J. & Zaluzec, N., 2004. A new improved silicon multi-cathode detector (SMCD) for microanalysis and X-ray mapping applications, *Microscopy Today,* 12:36–37.

Barth, G.A., Kleinrock, M.C., Helz, R.T., 1994. The magma body at Kilauea Iki lava lake: Potential insights into mid-ocean ridge magma chambers, *Journal of Geophysical Research: Solid Earth*, 99(B4): 7199-7217.

Beccaluva, L., Ohnenstetter, D., Ohnenstetter, M., Venturelli, G., 1977. The trace element geochemistry of Corsican ophiolites, *Contributions to Mineralogy and Petrology*, 64: 11–31.

Beccaluva, L., Chinchilla-Chaves, A.L., Coltorti, M., Giunta, G., Siena, F., Vaccaro, C., 1999. Petrological and structural significance of the Santa Elena-Nicoya ophiolitic complex in Costa Rica and geodynamic implications, *European Journal of Mineralogy*, 11: 1091–1107.

Bedard, J.H., 1993. Oceanic crust as a reactive filter: Synkinematic intrusion, hybridization, and assimilation in an ophiolitic magma chamber, western Newfoundland, *Geology*, 21(1): 77-80.

Bence, A.E., Albee, A.L., 1968. Empirical correction factors for the electron microanalysis of silicates and oxides, *The Journal of Geology*, 76(4): 382-403.

Benoit, M., Polvé, M., Ceuleneer, G., 1996. Trace element and isotopic characterization of mafic cumulates in a fossil mantle diapir (Oman ophiolite), *Chemical Geology*, 134(1–3): 199–214.

Benoit, M., Ceuleneer, G., Polvé, M., 1999. The remelting of hydrothermally altered peridotite at mid-ocean ridges by intruding mantle diapirs, *Nature*, 402: 514–518.

Berndt, J., Koepke, J., Holtz, F., 2005. An experimental investigation of the influence of water and oxygen fugacity on differentiation of MORB at 200 MPa, *Journal of Petrology*, 46:135–167.

Bibby, L.E., MacLeod, C.J., Lissenberg, C.J., 2011. OmanDB: The role of water in axial lavas and dykes from the Oman ophiolite and geochemical segmentation of the palaeo-spreading ridge, Abstract OS11B-1485 presented at 2011 Fall Meeting, AGU, San Francisco, CA, 5–9 Dec.

Bonev, N., Stampfli, G.,2009. Gabbro, plagiogranite and associated dykes in the supra-subduction zone Evros Ophiolites, NE Greece, *Geological Magazine*, 146(1):72–91.

Bosch, D., Jamais, M., Boudier, F., Nicolas, A., Dautria, J.M., Agrinier, P., 2004. Deep and high-temperature hydrothermal circulation in the Oman ophiolite—Petrological and isotopic evidence, *Journal of Petrology*, 45(6): 1181–1208.

Boudier, F., Coleman, R.G., 1981. Cross section through the peridotite in the Samail ophiolite, southeastern Oman Mountains, *Journal of Geophysical Research*, 86(B4): 2573–2592.

Boudier, F., Nicolas, A., 2007. Comment on “dating the geologic history of Oman’s Semail ophiolite: Insights from U–Pb geochronology” by C. J. Warren, R. R. Parrish, D. J. Waters and M. P. Searle, *Contributions to Mineralogy and Petrology*, 154(1): 111–113.

Boudier, F., Nicolas, A., 2011. Axial melt lenses at oceanic ridges—A case study in the Oman ophiolite, *Earth and Planetary Science Letters*, 304(3–4): 313–325.

Boudier, F., Ceuleneer, G., Nicolas, A., 1988. Shear zones, thrusts and related magmatism in the Oman ophiolite: Initiation of thrusting on an oceanic ridge, *Tectonophysics*, 151(1–4): 275–296.

Boudier, F., Nicolas, A., Ildefonse, B., 1996. Magma chambers in the Oman ophiolite: fed from the top and the bottom, *Earth and Planetary Science Letters*, 144: 239–250.

Boudier, F., Nicolas, A., Ildefonse, B., Jousselin, D., 1997. EPR microplates, a model for the Oman ophiolite, *Terra Nova*, 9(2): 79-82.

Boudier, F., Godard, M., Armbruster, C., 2000. Significance of gabbronorite occurrences in the crustal section of the Semail ophiolite, *Marine Geophysical Researches*, 21: 289–305.

Braun, M.G., 2004. Petrologic and microstructural constraints on focused melt transport in dunites and the rheology of the shallow mantle, PhD thesis, 212 pp., MIT-WHOI Joint Program, Cambridge, Mass.

Bright, D.S., 1987. A LISP-based image analysis system with applications to microscopy, *Journal of microscopy*, 148(1): 51-87.

Brophy, J.G., 2008. A study of rare earth element (REE)-SiO2 variations in felsic liquids generated by basalt fractionation and amphibole melting: a potential test for discriminating between the two different processes, *Contributions to Mineralogy and Petrology*, 156: 337-357.

Brophy, J.G., 2009. La-SiO2 and Yb-SiO2 systematics in mid-ocean ridge magmas: implications for the origin of oceanic plagiogranites, *Contributions to Mineralogy and Petrology*, 158: 99-111.

Brophy, J.G., Pu, X., 2012. Rare earth element (REE)-SiO2 systematics of mid-ocean ridge plagiogranites and host gabbros from the Fournier oceanic fragment, New Brunswick, Canada: a field evaluation of some model predictions, *Contributions to Mineralogy and Petrology*, 164: 191-204.

Browning, P., Smewing, J.D., 1981. Processes in magma chambers beneath spreading axes: Evidence from magmatic associations in the Oman Ophiolite, *Journal of the Geological Society*, 138(3): 279–280.

Canales, J.P., Singh, S.C., Detrick, R.S., Carbotte, S.M., Harding, A., Kent, G.M., Diebold, J.B., Babcock, J., Nedimović, M.R., 2006. Seismic evidence for variations in axial magma chamber properties along the southern Juan de Fuca Ridge, *Earth and planetary Science Letters*, 246: 353–366.

Canales, J.P., Nedimovic, M.R., Kent, G.M., Carbotte, S.M., Detrick, R.S., 2009. Seismic reflection images of a near-axis melt sill within the lower crust at the Juan de Fuca ridge, *Nature,* 460: 89-94.

Canales, J.P., Carton, H., Carbotte, S.M., Mutter, J.C., Nedimovic, M.R., Xu, M., Aghaei, O., Marjanovic, M., Newman, K., 2012. Network of off-axis melt bodies at the East Pacific Rise, *Nature Geoscience*, 5: 279-283.

Carbotte, S., Mutter, C., Mutter, J., Ponce-Correa, G., 1998. Influence of magma supply and spreading rate on crustal magma bodies and emplacement of the extrusive layer: Insights from the East Pacific Rise at lat 16 N, *Geology*, 26(5): 455-458.

Carbotte, S.M., Solomon, A., Ponce-Correa, G., 2000. Evaluation of morphological indicators of magma supply and segmentation from a seismic reflection study of the East Pacific Rise 15300–17N, *Journal of Geophysical Research*, 105: 2737–2759.

Carbotte, S.M., Marjanovic, M., Carton, H., Mutter, J.C., Canales, J.P., Nedimovic, M.R., … Perfit, M.R., 2013. Fine-scale segmentation of the crustal magma reservoir beneath the East Pacific Rise, *Nature Geoscience*, 6(10): 866–870.

Carbotte, S.M., Smith, D.K., Cannat, M., Klein, E.M., 2015. Tectonic and magmatic segmentation of the Global Ocean Ridge System: a synthesis of observations, *Geological Society of London Special Publications*, 10: 1144/SP420.5.

Caress, D.W., Burnett, M.S., Orcutt, J.A., 1992. Tomographic image of the axial-low velocity zone at 12◦50’N on the East Pacific Rise, *Journal of Geophysical Research*, 97: 9243–9264.

Cashman, K., Blundy, J., 2013. Petrological cannibalism: the chemical and textural consequences of incremental magma body growth. *Contributions to Mineralogy and Petrology*, 166:703-729.

Castaing, R., 1951. Application of electron beams to a method of local chemical and crystallographic analysis. Paris: University of Paris.

Ceuleneer, G., Nicolas, A., Boudier, F., 1988. Mantle flow patterns at an oceanic spreading centre: The Oman peridotites record, *Tectonophysics*, 151(1–4): 1-26.

Clarke, G.L., Daczko, N.R., Nockolds, C., 2001. A method for applying matrix corrections to X-ray intensity maps using the Bence–Albee algorithm and Matlab, *Journal of metamorphic Geology*, 19(6): 635-644.

Coleman, R.G., 1977. Ophiolites. Springer-Verlag, New York, 229 p.

Coleman, R.G., Donato, M.M., 1979. Oceanic plagiogranite revisited. In: Barker F (ed) Trondhjemites, dacites, and related rocks. Elsevier, Amsterdam, pp 149–167

Coleman, R.G., Hopson, C.A., 1981. Introduction to the Oman Ophiotite special issue. *Journal of Geophysical Research*, 86: 2495-2496.

Collier, J.S., Singh, S.C., 1997. Detailed structure of the top of the melt body beneath the East Pacific Rise at 9◦40'N from waveform inversion of seismic reflection data, *Journal of Geophysical Research*, 102(B9):20287–20304.

Collier, J.S., Singh, S.C., 1998. A seismic inversion study of the axial magma chamber reflector beneath the East Pacific Rise near 10◦N, in *Modern Ocean Floor Processes and the Geological Record*, pp. 17–28, eds Mills, R.A. & Harrison, K., Geological Society.

Coogan, L.A., Thompson, G., MacLeod, C.J., 2002a. A textural and geochemical investigation of high level gabbros from the Oman ophiolite: Implications for the role of the axial magma chamber at fast spreading ridges, *Lithos*, 63: 67-82.

Coogan, L.A., Jenkin, G.R.T., Wilson, R.N., 2002b. Constraining the cooling rate of the lower oceanic crust: A new approach applied to the Oman ophiolite, *Earth and Planetary Science Letters*, 199: 127-146.

Coogan, L.A., Mitchell, N.C., O'Hara, M.J., 2003. Roof assimilation at fast spreading ridges: An investigation combining geophysical, geochemical, and field evidence, *Journal of Geophysical Research*, 108(B1): 2002.

Coogan, L.A., Thompson, G.M., MacLeod, C.J., Dick, H.J.B., Edwards, S.J., Scheirer, A.H., Barry, T.L., 2004, A combined basalt and peridotite perspective on 14 million years of melt generation at Atlantis Bank segment of the Southwest Indian Ridge: Evidence for temporal changes in mantle dynamics? *Chemical Geology*, 207: 13–30.

Cossio, R., Borghi, A., Ruffini, R., 2002. Quantitative modal determination of geological samples based on X-ray multielemental map acquisition, *Microscopy and Microanalysis*, 8(02): 139-149.

Cosslett, V.E., Duncumb, P., 1956. Micro-analysis by a flying spot X-ray method, *Nature*, 177: 1172–1174.

Crawford, W.C., Webb, S.C., 2002. Variations in the distribution of magma in the lower crust and at the Moho beneath the East Pacific Rise at 9◦ –10◦ N, *Earth and Planetary Science Letters*, 203: 117-130.

Crawford, W.C., Webb, S.C., Hildebrand, J.A., 1999. Constraints on melt in the lower crust and Moho at the East Pacific Rise, 9°480N, using sea- floor compliance measurements, *Journal of Geophysical Research*, 104: 2933-2939.

Cunningham, C.G., Arribas Jr, A., Rytuba, J.J., Arribas, A., 1990. Mineralized and unmineralized calderas in Spain; Part I, evolution of the Los Frailes Caldera, *Mineralium Deposita*, 25(1): S21-S28.

de Andrade, V., Vidal, O., Lewin, E., O'Brien, P., Agard, P., 2006. Quantification of electron microprobe compositional maps of rock thin sections: an optimized method and examples, *Journal of Metamorphic Geology*, 24(7): 655-668.

de Gramont, X., Le Métour, J., Villey, M., 1986. Samad geologic map, sheet NF40-7C, *Ministry of Commerce. and Industry*, Direct. Gen. of Miner., Muscat.

Detrick, R.S., Buhl, P., Vera, E., Mutter, J., Orcutt, J., Madsen, J., Brocher, T., 1987. Multi-channel seismic imaging of a crustal magma chamber along the East Pacific Rise, *Nature,* 326: 35-41.

Detrick, R.S., Harding, A.J., Kent, G.M., Orcutt, J.A., Mutter, J.C., Buhl, P., 1993. Seismic structure of the Southern East Pacific Rise, *Science*, 259: 499–503.

Dewey, J.F., Casey, J.F., 2011. The origin of obducted large-slab ophiolite complexes, in Arc-Continent Collision, edited by D. Brown and P. Ryan, pp. 431–444, Springer, Berlin.

Dick, H.J., Natland, J.H., Alt, J.C., Bach, W., Bideau, D., Gee, J.S., Haggas, S., Hertogen, J.G., Hirth, G., Holm, P.M., Ildefonse, B., 2000. A long in situ section of the lower ocean crust: results of ODP Leg 176 drilling at the Southwest Indian Ridge, *Earth and planetary science letters*, 179(1): 31-51.

Dick, H.J.B., Natland, J.H., Ildefonse, B., 2006. Past and future impact of deep drilling in the oceanic crust and mantle, *Oceanography* 19, 72-80.

Dixon-Spulber, S., Rutherford, M.J., 1983. The origin of rhyolite and plagiogranite in oceanic crust: an experimental study, *Journal of Petrology*, 24:1–25.

Dubois, M., 1983. Plagiogranite and hydrothermalism: an approach from Cyprus and Oman ophiolitic complexes. Ph.D. dissertation, University of Nancy 1, France

Duncumb, P., Cosslett, V.E., 1957. A scanning microscope for X-ray emission pictures. *X-ray Microscopy and Microradiography*, pp.374-380.

Dunn, R.A., Toomey, D.R., Solomon, S.C., 2000. Three-dimensional seismic structure and physical properties of the crust and shallow mantle beneath the East Pacific Rise at 9◦ 30′ N, *Journal of Geophysical Research*, 105: 23537-23555.

Ebel, D.S., Crapster-Pregont, E.J., Friedrich, J.M., 2014. Image Analysis of 2D X-ray Intensity Maps: Element Abundances, Mineralogy, and Modal Analysis of Meteorites, *Microscopy and Microanalysis*, 20(S3): 752-753.

El Amin, O., Peters, T., Blechschmidt, I., Al-Battashi, M., Al-Khumasani, N., Al-Towaya, A., 2005. Ibra geologic map, sheet NF40-8A, *Ministry of Commerce. and Industry*, Direct. Gen. of Miner., Muscat.

Ernewein, M., Pflumio, C., Whitechurch, H., 1988. The death of an accretion zone as evidenced by the magmatic history of the Sumail ophiolite (Oman), *Tectonophysics*, 151: 247–274.

Feig, S., Koepke, J., Snow, J., 2006. Effect of water on tholeiitic basalt phase equilibria—an experimental study under oxidizing conditions, *Contributions to Mineralogy and Petrology*, 152:611–638.

Fitzgerald, R., Keil, K., Heinrich, K.,1968. Solid-state energy dispersion spectrometer for electron-microprobe X-ray analysis, *Science*, 159: 528–530.

Flagler, P.A., Spray, J.G., 1991. Generation of plagiogranite by amphibolite anatexis in oceanic shear zones, *Geology*, 19:70–73

Floyd, P.A., Yaliniz, M.K., Goncuoglu, M.C., 1998. Geochemistry and petrogenesis of intrusive and extrusive ophiolitic plagiogranites, central Anatolian Crystalline Complex, Turkey, *Lithos*, 42: 225–241

Fornari, D.J., Haymon, R.M., Perfit, M.R., Gregg, T.K.P., Edwards, M.H., 1998. Axial summit trough of the east pacific rise 9°-10°N: Geological characteristics and evolution of the axial zone on fast spreading mid-ocean ridges, *Journal of Geophysical Researches: Solid Earth*, 103: 9827-9855.

Forsyth, D.W., Scheirer, D.S., Webb, S.C., Dorman, L.M., Orcutt, J.A., Harding, A.J., Blackman, D.K., Morgan, J.P., Detrick, R.S., Shen, Y., Wolfe, C.J., Canales, J.P., Tommey, D.R., Sheehan, A.F., Solomon, S.C., Wilcock, W.S.D., Team, M.S., 1998. Imaging the deep seismic structure beneath a mid-ocean ridge: The MELT experiment, *Science*, 280: 1215-1218.

France, L., Ildefonse, B., Koepke, J., 2009a. Interactions between magma and hydrothermal system in Oman ophiolite and in IODP Hole 1256D: Fossilization of a dynamic melt lens at fast spreading ridges, *Geochemistry Geophysics Geosystems*, 10: Q10O19.

France, L., Ildefonse, B., Koepke, J., 2009b. The sheeted dike/Gabbro transition in the Oman ophiolite and in the IODP Hole 1256D: fossilisation of a dynamic melt lens at fast spreading ridges, *Geochemistry Geophysics Geosystems*, 10: Q10O19.

France, L., Koepke, J., Ildefonse, B., Cichy, S.B., Deschamps, F., 2010. Hydrous partial melting in the sheeted dike complex at fast spreading ridges: experimental and natural observations, *Contributions to Mineralogy and Petrology*, 160: 683-704.

France, L., Koepke, J., MacLeod, C.J., Ildefonse, B., Godard, M., Deloule, E., 2014. Contamination of MORB by anatexis of magma chamber roof rocks: constraints from a geochemical study of experimental melts and associated residues, *Lithos*, 202-203: 120-137.

Francheteau, J., Armijo, R., Cheminee, J.L., Hekinian, R., Lonsdale, P., Blum, N., 1990. 1 Ma East Pacific Rise oceanic crust and uppermost mantle exposed

by rifting in Hess Deep (equatorial Pacific Ocean), *Earth and Planetary Science Letters*, 101: 281–295.

Friel, J.J., Lyman, C.E., 2006. Tutorial review: X-ray mapping in electron-beam instruments, *Microscopy and Microanalysis*, 12(01): 2-25.

Garmany, J., 1989. Accumulations of melt at the base of young oceanic crust, *Nature*, 340: 628–632.

Garrido, C.J., Kelemen, P.B., Hirth, G., 2001. Variation of cooling rate with depth in lower crust formed at an oceanic spreading ridge plagioclase crystal size distributions in gabbros from the Oman ophiolite, *Geochemistry Geophysics Geosystems*, 2: 2000GC000136.

Gass, I.G., 1980. Open University Oman ophiolite project, maps 1 and 2, *Open University*, Milton Keynes.

Geotimes, 1972. Penrose conference report, ophiolites. 17: 24-25.

Gerlach D.C., Leeman, W.P., Ave´ Lallemant, H.G., 1981. Petrology and geochemistry of plagiogranite in the Canyon Mountain ophiolite, Oregon, *Contributions to Mineralogy and Petrology*, 72: 82–92

Ghiorso, M.S., Sack, R.O., 1995. Chemical mass transfer in magmatic processes IV. A revised and internally consistent thermodynamic model for the interpolation and extrapolation of liquid-solid equilibria in magmatic systems at elevated temperatures and pressures, *Contributions to Mineralogy and Petrology*, 119(2-3): 197–212.

Gillis, K.M., *et al.*, 1993. *Proceedings of Ocean Drilling Program, Initial Reports*, vol. 147, 366 pp., Ocean Drilling Program, College Station, Texas.

Gillis, K.M., Roberts, M.D., 1999. Cracking at the magma-hydrothermal transition: Evidence from the Troodos ophiolite, Cyprus, *Earth and Planetary Science Letters*, 169: 227–244.

Gillis, K.M., 2008. The roof of an axial magma chamber: A hornfelsic heat exchanger, *Geology*, 36(4): 299-302.

Gillis, K M., Snow, J.E., Klaus, A., Abe, N., Adrião, A.B., Akizawa, N., … Wintsch, R.P., 2014. Primitive layered gabbros from fast-spreading lower oceanic crust, *Nature*, 505(7482): 204–207.

Ginibre, C., Wörner, G., Kronz, A., 2007. Crystal zoning as an archive for magma evolution, *Elements*, 3(4): 261-266.

Glennie, K.W., Boeuf, M.G.A., Hughes Clark, M.W., Moody-Stuart, M., Pilaar, W.F.H. & Reinhardt, B.M. 1974. The geology of the Oman mountains. *Verhandelingen Van het Koninklijk Nederlands Geologisch-Mijnbouwkundig Genootschap*, 31.

Godard, M., Dautria, J.M., Perrin, M., 2003. Geochemical variability of the Oman ophiolite lavas: Relationship with spatial distribution and paleomagnetic directions, *Geochemistry Geophysics Geosystems*, 4(6): 8609.

Godard, M., Bosch, D., Einaudi, F., 2006. A MORB source for low-Ti magmatism in the Semail ophiolite, *Chemical Geology*, 234(1–2): 58–78.

Goldstein, J., Newbury, D., Joy, D., Lyman, C., Echlin, P., Lifshin, E., Sawyer, L., Michael, J., 2003. Scanning Electron Microscopy and X-ray Microanalysis, 3rd ed. New York: Kluwer Academic/Plenum Press.

Gorlen, K., Barden, L., Del Priore, J., Fiori, C., Gibson, C., Leapman, R., 1984. A computerized analytical electron microscope for elemental imaging, *Review of Scientific Instruments*, 55: 912.

Goss, A.R., Perfit, M.R., Ridley, W.I., Rubin, K.H., Kamenov, G.D., Soule, S.A., … Fornari, D.J., 2010. Geochemistry of lavas from the 2005-2006 eruption at the East Pacific Rise, 9°46'N-9°56N: Implications for ridge crest plumbing and decadal changes in magma chamber compositions, *Geochemistry Geophysics Geosystems*, 11(5): 2009GC002977.

Gray, D. R., Gregory, R.T., 2000. Implications of the structure of the Wadi Tayin metamorphic sole, the Ibra-Dasir block of the Samail ophiolite, and the Saih Hatat window for late stage extensional ophiolite emplacement, Oman, *Marine Geophysical Researches*, 21(3–4): 211–227.

Gregory, R.T., Taylor Jr., H.P., 1981. An oxygen isotope profile in a section of Cretaceous oceanic crust, Samail ophiolite, Oman: Evidence for d18O buffering of the oceans by deep (>5 km) seawater-hydrothermal circulation at mid-ocean ridges, *Journal of Geophysical Research*, 86(B4): 2737–2755.

Grimes, C., Ushikubo, T., Kozdon, R., Valley, J.W., 2013, Perspectives on the origin of plagiogranite in ophiolites from oxygen isotopes in zircon, *Lithos*, 179: 48-66.

Haase, K.M., Freund, S., Beier, C., Koepke, J., Erdmann, M., Hauff, F., 2016. Constraints on the magmatic evolution of the oceanic crust from plagiogranite intrusions in the Oman ophiolite, *Contributions to Mineralogy and Petrology*, 171(5): 1-16.

Hacker, B.R., Mosenfelder, J.L., Gnos, E., 1996. Rapid emplacement of the Oman ophiolite: Thermal and geochronologic constraints, *Tectonics*, 15(6): 1230–1247.

Han, S., Carbotte, S.M., Carton, H., Mutter, J.C., Aghaei, O., Nedimovic, M.R., Canales, J.P., 2014. Architecture of on- and off-axis magma bodies at EPR 9°37-40'N and implications for oceanic crustal accretion, *Earth and Planetary Science Letters*, 390: 31-44.

Hanghøj, K., Kelemen, P.B., Hassler, D., Godard, M., 2010. Composition and genesis of depleted mantle peridotites from the Wadi Tayin massif, Oman ophiolite; Major and trace element geochemistry, and Os isotope and PGE systematics, *Journal of Petrology*, 51(1–2): 201–227.

Harding, A.J., Orcutt, J.A., Kappus, M.E., Vera, E.E., Mutter, J.C., Buhl, P., Detrick, R.S., Brocher, T.M., 1989. Structure of young oceanic crust at 13°N on the East Pacific Rise from expanding spread profiles, *Journal of Geophysical Research*, 94: 12163–12196.

Haymon, R.M., McDonald, K.C., Benjamin, S.B., Ehrhardt, C.J., 2005. Manifestations of hydrothermal discharge from young abyssal hills on the fast-spreading East Pacific Rise flank, *Geology*, 33: 153-156.

Hekinian, R., Bideau, D., Francheteau, J., Cheminee, J.L., Armijo, R., Lonsdale, P., Blum, N., 1993. Petrology of the East Pacific Rise crust and upper mantle exposed in Hess Deep (East Equatorial Pacific), *Journal of Geophysical Research*, 98: 8069-8094.

Henstock, T.J., Woods, A.W., White, R.S., 1993. The accretion of oceanic crust by episodic sill intrusion, *Journal of Geophysical Research*, 98(B3): 4143-4161.

Higgins, M.D., 2006. *Quantitative textural measurements in igneous and metamorphic petrology*. Cambridge University Press.

Hooft, E.E., Detrick, R.S., Kent, G.M., 1997. Seismic structure and indicators of magma budget along the southern East Pacific Rise, *Journal of Geophysical Research*, 102: 27319–27340.

Hopson, C.A., Coleman, R.G., Gregory, R.T., Pallister, J.S., Bailey, E.H., 1981. Geological Section through the Samail opholite and associated rocks along a Muscat-Ibra Transect, S.E. Oman Mountains, *Journal of Geophysical Research*, 86: 2527–2544.

Hussenoeder, S.A., Collin, J.A., Kent, G.M., Detrick, R.S., the TERA Group, 1996. Seismic analysis of the axial magma chamber reflector along the southern East Pacific Rise from conventional reflection profiling, *Journal of Geophysical Research*, 101(B10): 22087–22105.

Imai, N., Terashima, H., Itoh, S., Ando, A., 1995. 1994 compilation values for GSJ reference samples, igneous rock series, *Geostandards Newsletter*, 19: 135-213.

Ishikawa, T., Nagaishi, K., Umino, S., 2002. Boninitic volcanism in the Oman ophiolite; implications for thermal condition during transition from spreading ridge to arc, *Geology*, 30: 899–902,

Katz, R.F., Spiegelman, M., Carbotte, S.M., 2004. Ridge migration, asthenospheric flow and the origin of magmatic segmentation in the global mid-ocean ridge system, *Geophysical Research Letters*, 31(15): L15605.

Katz, R.F., Spiegelman, M., Holtzman, B., 2006. The dynamics of melt and shear localization in partially molten aggregates, *Nature*, 442: 676-679.

Kelemen, P.B., Aharanov, E., 1998. Periodic formation of magma fractures and generation of layered gabbros in the lower crust beneath oceanic spreading ridges. In: Buck, W.R., Delaney, P.T., Karson, J.A., Lagrabrielle, Y. (Eds.), *Faulting and Magmatism at Mid-Ocean Ridges*, vol. 106. American Geophysical Union, Washington, pp. 267–289.

Kelemen, P.B., Koga, K., Shimizu, N., 1997. Geochemistry of gab- bro sills in the crust-mantle transition zone of the Oman ophiolite: implications for the origin of the oceanic lower crust, *Earth and Planetary Science Letters*, 146: 475–488.

Kent, G.M., Harding, A.J., Orcutt, J.A., 1990. Evidence for a smaller magma chamber beneath the East Pacific Rise at 9°300N, *Nature*, 344: 650.

Kent, G.M., Harding, A.J., Orcutt, J.A., 1993a. Distribution of magma beneath the East Pacific Rise between the Clipperton Transform and the 9°17'N deval

from forward modeling of common depth point data, *Journal of Geophysical Research,* 98: 13945-13969.

Kent, G.M., Harding, A.J., Orcutt, J.A., 1993b. Distribution of magma beneath the East Pacific Rise near the 9◦03'N overlapping spreading center from forward modeling of common depth point data, *Journal of Geophysical Research*, 98: 13971–13995.

Kent, G.M., Harding, A.J., Orcutt, J.A., Detrick, R.S., Mutter, J.C., Buhl, P., 1994. Uniform accretion of oceanic crust south of the Garrett Transform at 14 degrees 150S on the East Pacific Rise, *Journal of Geophysical Research*, 99: 9097–9116.

Key, K., Constable, S., Liu, L.J., Pommier, A., 2013. Electrical image of passive mantle upwelling beneath the Northern East Pacific Rise, *Nature*, 495: 500.

Kinzler, R.J., Grove, T.L., 1993. Corrections and further discussion of the primary magmas of mid-ocean ridge basalts, 1 and 2, *Journal of Geophysical Research: Solid Earth*, 98(B12): 22339-22347.

Klein, E.M., Langmuir, C.H., 1987. Global correlation of ocean ridge basalt chemistry with axial depth and crustal thickness. *Journal of Geophysical Research,* 92: 8089–8115.

Koepke, J., Feig, S.T., Snow, J., Freise, M.,2004. Petrogenesis of oceanic plagiogranites by partial melting of gabbros: an experimental study, *Contributions to Mineralogy and Petrology,* 146:414–432.

Koepke J., Berndt J., Feig S.T., Holtz F., 2007. The formation of SiO2- rich melts within the deep oceanic crust by hydrous partial melting of gabbros, *Contributions to Mineralogy and Petrology*, 153: 67–84.

Koepke, J., Christie, D.M., Dziony, W., Holtz, F., Lattard, D., Maclennan, J., Park, S., Scheibner, B., Yamasaki, T., Yamazaki, S., 2008. Petrography of the Dike/Gabbro Tran- sition at IODP Site 1256 (Equatorial Pacific): The evolution of the Granoblastic Dikes*, Geochemistry Geophysics Geosystems*, 9: Q07O09.

Koepke, J., Schoenborn, S., Oelze, M., Wittmann, H., Feig, S.T., Hellebrand, E., Boudier, F., Schoenberg, R., 2009. Petrogenesis of crustal wehrlites in the Oman ophiolite: Experiments and natural rocks, *Geochemistry Geophysics Geosystems*, 10: Q10002.

Koepke, J., France, L., Müller, T., Faure, F., Goetze, N., Dziony, W., Ildefonse, B., 2011. Gabbros from IODP Site 1256, equatorial Pacific: Insight into axial magma chamber processes at fast spreading ocean ridges, *Geochemistry Geophysics Geosystems*, 12(9): 2011GC003655.

Korenaga, J., Kelemen, P.B., 1997. Origin of gabbro sills in the Moho transition zone of the Oman ophiolite: Implications for magma transport in the oceanic crust, *Journal of Geophysical Research*, 102: 27729-27749.

Korenaga, J., Kelemen, P.B., 1998. Melt migration through the oceanic lower crust: a constraint from melt percolation modeling with finite solid diffusion, *Earth and Planetary Science Letters*, 156(1): 1-11.

Lanari, P., Vidal, O., De Andrade, V., Dubacq, B., Lewin, E., Grosch, E.G., Schwartz, S., 2014. XMapTools: A MATLAB©-based program for electron microprobe X-ray image processing and geothermobarometry, *Computers & Geosciences*, 62: 227-240.

Langmuir, C.H., Klein, E.M., Plank, T., 1992. In: Phipps Morgan, J., Blackman, D.K., Sinton, J.M. (Eds.), Mantle flow and melt generation at mid-ocean ridges, *AGU Geophysical Monograph series*., 71: 183–280.

Liebske, C., 2015. iSpectra: An Open Source Toolbox For The Analysis of Spectral Images Recorded on Scanning Electron Microscopes, *Microscopy and Microanalysis*, 21(04): 1006-1016.

Lippard, S.J., Shelton, A.W., Gass, I.G., 1986. The ophiolite of Northern Oman. In: *Geological Society Memoir*, 11. Blackwell, Oxford, pp 178.

Lissenberg, C.J., Bédard, J.H., & van Staal, C.R., 2004. The structure and geochemistry of the gabbro zone of the Annieopsquotch ophiolite, Newfoundland: implications for lower crustal accretion at spreading ridges, *Earth and Planetary Science Letters*, 229(1-2): 105–123.

Lissenberg, C.J., MacLeod, C.J., Howard, K.A., Godard, M., 2013. Pervasive reactive melt migration through fast-spreading lower oceanic crust (Hess Deep, equatorial Pacific Ocean), *Earth and Planetary Science Letters*, 361: 436-447.

Liu, L., Lowell, R.P., 2009. Models of hydrothermal heat output from a convecting, crystallizing, replenished magma chamber beneath an oceanic spreading center. *Journal of Geophysical Research,* 114.

Lloyd, S.P., 1982. Least square quantization in PCM. *IEEE Transactions on Information Theory*, 28(2):129-137.

Lonsdale, P., 1988. Structural Pattern of the Galapagos Microplate and Evolution of the Galapagos Triple Junctions, *Journal of Geophysical Research*, 93(B11): 13551–13574.

Love, G., Scott, V.D., 1978. Evaluation of a new correction procedure for quantitative electron probe microanalysis, *Journal of Physics D: Applied Physics*, 11(10): 1369.

Macdonald, K.C., 1998. Linkages between faulting, volcanism, hydrothermal activity and segmentation on fast spreading centers. pp. 27–58 in Faulting and Magmatism at Mid-Ocean Ridges. R. Buck, T. Delaney, A. Karson, and Y. Lagabrielle, eds, Geophysical Monograph Series, vol. 106, American Geophysical Union, Washington, DC.

Macdonald, K.C., Fox, P.J., Miller, S., Carbotte, S., Edwards, M.H., Eisen, M., Fornari, D.J., Perram, L., Pockalny, R., Scheirer, D., Tighe, S., 1992. The East Pacific Rise and its flanks 8–18 N: History of segmentation, propagation and spreading direction based on SeaMARC II and Sea Beam studies, *Marine Geophysical Researches*, 14(4): 299-344.

MacLeod, C.J., Rothery, D.A., 1992. Ridge axial segmentation in the Oman ophiolite: Evidence from along-strike variations in the sheeted dyke complex, *Geological Society of London Special Publication*, 60(1): 39–63.

MacLeod, C.J., Yaouancq, G., 2000. A fossil melt lens in the Oman ophiolite: implications for magma chamber processes at fast spreading ridges, *Earth and Planetary Science Letters*, 176: 357–373.

MacLeod, C.J., Lissenberg, C.J., Bibby, L., Pearce, J.A., Goodenough, K.M., Styles, M.T., Condon, D.J., 2012. Geodynamic setting and origin of the Oman/UAE ophiolite, paper presented at *International Conference on the Geology of the Arabian Plate and the Oman Mountains*, Sultan Qaboos Univ., Muscat, Sultanate of Oman, 7–9 Jan.

MacLeod, C.J., Lissenberg, C.J., Bibby, L., 2013. “Moist MORB” axial magmatism in the Oman ophiolite: the evidence against a mid-ocean ridge origin, *Geology*, 41: 459–462.

Malpas, J., 1979. Two contrasting trondhjemite associations from transported ophiolites in Western Newfoundland: initial report. In: Barker F (ed) Trondhjemites, dacites, and related rocks. Elsevier, Amsterdam, pp 465–487.

Marjanović, M., Carton, H., Carbotte, S.M., Nedimović, M.R., Mutter, J.C., & Canales, J.P., 2015. Distribution of melt along the East Pacific Rise from 9°30’ to 10°N from an amplitude variation with angle of incidence (AVA) technique, *Geophysical Journal International*, 203(1): 1–21.

Marsh, B.D., 1989. Magma chambers, *Annual Review of Earth and Planetary Sciences*, 17: 439-474.

McCulloch, M.T., Gregory, R.T., Wasserburg, G.J., Taylor, H.P., 1981. Sm-Nd, Rb-Sr, and 18O/16O isotopic systematics in an oceanic crustal section: Evidence from the Samail Ophiolite, *Journal of Geophysical Research*, 86(B4): 2721–2735.

Michael, P.J., Langmuir, C.H., Dick, H.J.B., Snow, J.E., Goldstein, S.L., Graham, D.W., Lehnert, K., Kurras, G., Jokat, W., Mühe, R., Edmonds, N.H., 2003. Magmatic and amagmatic seafloor generation at the ultraslow-spreading Gakkel ridge, Arctic Ocean, *Nature*, 423: 956-961.

Montigny, R., Le Mer, O., Thuizat, R., Whitechurch, H., 1988. K-Ar and Ar study of metamorphic rocks associated with the Oman ophiolite: Tectonic implications, *Tectonophysics*, 151(1–4): 345–362.

Moore, A., Coogan, L.A., Costa, F., Perfit, M.R., 2014. Primitive melt replenishment and crystal-mush disaggregation in the weeks preceding the 2005–2006 eruption, EPR, *Earth and Planetary Science Letters*, 403(0): 15–26.

Morgan, J.P., Chen, Y.J., 1993. The genesis of oceanic crust: Magma injection, hydrothermal circulation, and crustal flow, *Journal of Geophysical Research*, 98(B4): 6283–6297.

Morton, J.L., Sleep, N.H., 1985. Seismic reflections from a Lau basin magma chamber, in Geology and Offshore Resources of Pacific Island Arcs-Tonga Region, edited by D.W. Scholl and T.L. Vallier, pp. 441-453, Circum-Pacific Council for Energy and Mineral Resources, Houston, Texas.

Muir, D.D., Blundy, J.D., Rust, A.C., 2012. Multiphase petrography of volcanic rocks using element maps: a method applied to Mount St. Helens, 1980–2005, *Bulletin of volcanology*, 74(5): 1101-1120.

Mutter, J.C., Carbotte, S.M., Su, W., Xu, L., 1995. Seismic images of active magma systems beneath the East Pacific Rise between 17°05' and 17°35'S, *Science*, 268(5209): 391.

Mutter, J.C., Carbotte, S., Nedimović, M.R., Canales, J.P., Carton, H., 2009. Seismic imaging in three dimensions on the East Pacific Rise, *Eos Transactions AGU*, 90: 374–375.

Natland, J.H., Dick, H.J.B., 1996. Melt migration through high-level gabbroic cumulates of the East Pacific Rise at Hess Deep: the origin of magma lenses and the deep crustal structure of fast spreading ridges. In: Mevel, C., Gillis, K.M., Allan, J.F., Meyer, P.S. (Eds.), *Proceedings of the ODP Scientific Results*, vol. 147. Ocean Drilling Program, College Station TX, pp. 21–58.

Natland, J.H., Dick, H.J.B., 2009. Paired melt lenses at the East Pacific Rise and the pattern of melt flow through the gabbroic layer at a fast-spreading ridge. *Lithos*, 112(1-2): 73–86.

Nedimović, M.R., Carbotte, S.M., Harding, A.J., Detrick, R.S., Canales, J.P., Diebold, J.B., Kent, G.M., Tischer, M., Babcock, J.M., 2005. Frozen magma lenses below the oceanic crust. Nature 436: 1149–1152.

Newbury, D., 2005. X-ray spectrometry and spectrum image mapping at output count rates above 100 kHz with a silicon drift detector on a scanning electron microscope, *Scanning*, 27: 227–239.

Newbury, D., 2006. The new X-ray mapping: X-ray spectrum imaging above 100 kHz output count rate with the silicon drift detector, *Microscopy Microanalysis*,12: 26-35.

Newbury, D., Bright, D., 2005. “Derived Spectra”: Software tools for detecting spatial and spectral features in spectrum images. Scanning 27, 15–22. Small, J. (1976). An elemental and morphological characterization of emissions from the Dickerson and Chalk Point coal fired power plants. Ph.D. thesis, Department of Environmental Chemistry, University of Maryland.

Newbury, D.E, Ritchie, N.W., 2016. Measurement of Trace Constituents by Electron-Excited X-Ray Microanalysis with Energy-Dispersive Spectrometry, *Microscopy and Microanalysis*, 22(03): 520-535.

Nicolas, A., 1989. Structures of ophiolites and dynamics of oceanic lithosphere: Dordrecht, Netherlands, Kluwer Academic Publishers, 367 p.

Nicolas, A., Boudier, F., 1991. Rooting of the sheeted dike complex in the Oman ophiolite, *in* Ophiolite Genesis and Evolution of the Oceanic Lithosphere, edited by T. Peters, A. Nicolas, and R. G. Coleman, pp. 39–54, Kluwer Acad., Dordrecht, Netherlands.

Nicolas, A., Boudier, F., 2007. Comment on “dating the geologic history of Oman's Semail ophiolite: insights from U–Pb geochronology” by C.J. Warren, R.R. Parrish, D.J. Waters and M.P. Searle. *Contributions to Mineralogy and Petrology*, 154: 111–113.

Nicolas, A., Boudier, F., 2011. Structure and dynamics of ridge axial melt lenses in the Oman ophiolite, *Journal of Geophysical Research*, 116: B03103.

Nicolas, A., Boudier, F., France, L., 2009. Subsidence in magma chamber and the development of magmatic foliation in Oman ophiolite gabbros, *Earth and Planetary Science Letters*, 284(1–2): 76–87.

Nicolas, A., Boudier, F., Ildefonse, B., 1996. Variable crustal thickness in the Oman ophiolite: implication for oceanic crust, *Journal of Geophysical Research: Solid Earth*, 101(B8): 17941-17950.

Nicolas, A., Boudier, F., Ildefonse, B., Ball, E., 2000. Accretion of Oman and United Arab Emirates ophiolite—Discussion of a new structural map, *Marine Geophysical Researches*, 21(3–4): 147–180.

Nicolas, A., Boudier, F., Koepke, J., France, L., Ildefonse, B., Mevel, C., 2008. Root zone of the sheeted dike complex in the Oman ophiolite, *Geochemistry Geophysics Geosystems*, 9: Q05001.

Nicolas, A., Reuber, I., Benn, K., 1988. A new magma chamber model based on structural studies in the Oman ophiolite. *Tectonophysics*, 151: 87–105.

Niu, Y., Batiza, R., 1991. An empirical method for calculating melt compositions produced beneath mid-ocean ridges: application for axis and off-axis (seamounts) melting. *Journal of Geophysical Research*, 96: 21753–21777.

Niu, Y., Hekinian, R., 1997. Spreading-rate dependence of the extent of mantle melting beneath ocean, *Nature*, 385: 326–329.

Niu, Y., Gilmore, T., Mackie, S., Greig, A., Bach, W., 2002. Mineral chemistry, whole-rock compositions, and petrogenesis of Leg 176 gabbros: data and discussion. In: Natland JH, Dick HJB, Miller DJ, Von Herzen RP (*eds*) *Proceedings of ODP, Scientific Results* 176. Ocean Drilling Program, College Station, TX, pp 1–60.

O'Neill, H.S.C., Jenner, F.E., 2012. The global pattern of trace-element distributions in ocean floor basalts, *Nature*, 491(7426): 698–704.

Ottley, C.J., Pearson, D.G., Irvine, G.J., 2003. A routine method for the dissolution of geological samples for the analysis of REE and trace elements via ICP-MS. In: Holland, J.G., Taner, S.D. (*eds*.), Plasma Source Mass Spectrometry. Applications and Emerging Technologies, The Royal Society of Chemistry, pp. 221–230.

Pallister, J.S., 1981. Structure of the sheeted dike complex of the Samail ophiolite near Ibra, Oman, *Journal of Geophysical Research*, 86(B4): 2661–2672.

Pallister, J.S., Hopson, C.A., 1981. Samail ophiolite Plutonic suite—Field relations, phase variation, cryptic variation and layering, and a model of a spreading ridge magma chamber, *Journal of Geophysical Research*, 86: 2593-2644.

Pallister, J.S., Knight, R.J., 1981. Rare-earth element geochemistry of the Samail ophiolite near Ibra, Oman, *Journal of Geophysical Research*, 86(B4): 2673–2697.

Pan, Y., Batiza, R., 2002. Mid-ocean ridge magma chamber processes: Constraints from olivine zonation in lavas from the East Pacific Rise at 9°30' N and 10°30' N, *Journal of Geophysical Research: Solid Earth*, 107(B1): 2001JB000435.

Pan, Y., Batiza, R., 2003. Magmatic processes under mid-ocean ridges: A detailed mineralogic study of lavas from East Pacific Rise 9°30′N, 10°30′N, and 11°20′N, *Geochemistry Geophysics Geosystems*, 4(11): 2002GC000309.

Pearce, J.A., Alabaster, T., Shelton, A.W., Searle, M.P., 1981. The Oman ophiolite as a Cretaceous arc-basin complex: Evidence and implications, *Philosophical Transactions of the Royal Society of London*, Ser. A, 300(1454): 299–317.

Pearce, J.A., Lippard, S.J., Roberts, S., 1984. Characteristics and tectonic significance of supra-subduction zone ophiolites, in Kokelaar, B.P., and Howells, M.F., eds., Marginal basin geology: *Geological Society of London Special Publication* 16: 77–94.

Pearce, J.A., Parkinson, I.J., 1993. Trace element models for mantle melting: application to volcanic arc petrogenesis, *Geological Society, London, Special Publications*, 76(1): 373-403.

Pearce, T.H.,1994. Recent work on oscillatory zoning in plagioclase. In Feldspars and their reactions (pp. 313-349). Springer Netherlands.

Pedersen, R.B., Malpas, J., 1984. The origin of oceanic plagiogranites from the Karmoy ophiolite, Western Norway. *Contributions to Mineralogy and Petrology,* 88:36–52.

Pedersen, R. B., Malpas, J., Falloon, T., 1996. Petrology and geochemistry of gabbroic and related rocks from Site 894, Hess Deep, *Proceedings of ODP, Scientific Results*, 147, 3–19, 1996.

Perfit, M.R., Chadwick Jr., W.W., 1998. Magmatism at mid-ocean ridges: Constraints from volcanological and geochemical investigations. Pp. 59–116 in *Faulting and Magmatism at Mid-Ocean Ridges*. R. Buck, T. Delaney, A. Karson, and Y. Lagabrielle, eds, Geophysical Monograph Series, vol. 106, American Geophysical Union, Washington, DC.

Philibert, J., 1963. A method for calculating the absorption correction in electron probe microanalysis. *X-ray Optics and X-ray Microanalysis*, pp.379-392.

Philpotts, A. R., Carroll, M.,1996. Physical properties of partly melted tholeiitic basalt, *Geology*, 24: 1029–1032.

Pirrie, D., Butcher, A.R., Power, M.R., Gottlieb, P., Miller, G.L., 2004. Rapid quantitative mineral and phase analysis using automated scanning electron microscopy (QemSCAN); potential applications in forensic geoscience. Pp. 123-136 in *Forensic Geoscience: Principles, Techniques and Applications*. Pye, K. and Croft, D.J., eds, Geological Society of London, Special Publications, vol. 232, Geological Society of London, London.

Prêt, D., Sammartino, S., Beaufort, D., Meunier, A., Fialin, M., Michot, L.J., 2010a. A new method for quantitative petrography based on image processing of chemical element maps: Part I. Mineral mapping applied to compacted bentonites, *American Mineralogist*, 95(10): 1379-1388.

Prêt, D., Sammartino, S., Beaufort, D., Fialin, M., Sardini, P., Cosenza, P., Meunier, A., 2010b. A new method for quantitative petrography based on image processing of chemical element maps: Part II. Semi-quantitative porosity

maps superimposed on mineral maps, *American Mineralogist*, 95(10): 1389-1398.

Python, M., Ceuleneer, G., 2003. Nature and distribution of dykes and related melt migration structures in the mantle section of the Oman ophiolite, *Geochemistry Geophysics Geosystems*, 4(7): 8612.

Quick, J.E., Denlinger, R.P., 1993. Ductile deformation and the origin of layered gabbro in ophiolites, *Journal of Geophysical Research,* 98: 14015 – 14027.

Rao, D.R., Rai, H., Kumar, J.S., 2004. Origin of oceanic plagiogranite in the Nidar ophiolitic sequence of eastern Ladakh, India. Curr Sci, 87(7):999–1005.

Reagan, M.K., Ishizuka, O., Stern, R.J., Kelley, K.A., Ohara, Y., Blichert-Toft, J., Bloomer, S.H., Cash, J., Fryer, P., Hanan, B.B., Hickey-Vargas, R., Ishii, T., Kimura, J., Peate, D.W., Rowe, M.C., Woods, M., 2010. Fore-arc basalts and subduction initiation in the Izu-Bonin Mariana system. *Geochemistry Geophysics Geosystems*, 11(3):Q03X12.

Rioux, M., Lissenberg, C.J., McLean, N.M., Bowring, S.A., MacLeod, C.J., Hellebrand, E., Shimizu, N., 2012a. Protracted timescales of lower crustal growth at the fast-spreading East Pacific Rise. *Nature Geoscience*, 5(4): 275–278.

Rioux, M., Bowring, S., Kelemen, P., Gordon, S., Dudás, F., Miller, R., 2012b. Rapid crustal accretion and magma assimilation in the Oman-U.A.E. ophiolite: High precision U-Pb zircon geochronology of the gabbroic crust, *Journal of Geophysical Research*,117.

Ritchie, N.W.M., Davis, J., Newbury, D.E., 2008. DTSA-II: A New Tool for Simulating and Quantifying EDS Spectra - Application to Difficult Overlaps, *Microscopy and Microanalysis*, 14, Suppl. 2: 1176-1177.

Ritchie, N.W.M., 2009. Spectrum Simulation in DTSA-II, *Microscopy and Microanalysis,* 15: 454-468.

Rollinson, H., 2009. New models for the genesis of plagiogranites in the Oman Ophiolite, *Lithos*, 112: 603–614.

Rothery, D.A.,1983. The base of a sheeted dyke complex, Oman ophiolite: Implications for magma chambers at oceanic spreading axes, *Journal of the Geological Society*, 140: 287–296.

Rubin, K.H., Sinton, J.M., 2007. Inferences on mid-ocean ridge thermal and magmatic structure from MORB compositions, *Earth and Planetary Science Letters,* 260:257–276.

Rubin, K.H., Soule, S.A., Chadwick, W.W., Fornari, D.J., Clague, D.A., Embley, R.W., Baker, E.T., Perfit, M.R., Caress, D.W., Dziak, R.P., 2012. Volcanic eruptions in the deep sea, *Oceanography*, 25(1): 142-157.

Rytuba, J.J., Arribas Jr, A., Cunningham, C.G., McKee, E.H., Podwysocki, M.H., Smith, J.G., ... Arribas, A., 1990. Mineralized and unmineralized calderas in Spain; Part II, evolution of the Rodalquilar caldera complex and associated gold-alunite deposits, *Mineralium Deposita*, 25(1): S29-S35.

Saunders, K., Buse, B., Kilburn, M.R., Kearns, S., Blundy, J., 2014. Nanoscale characterisation of crystal zoning, *Chemical Geology*, 364: 20-32.

Schouten, H., Klitgord, K.D., Whitehead, J.A., 1985. Segmentation of mid-ocean ridges, *Nature*, 317(6034): 225–229.

Searle, M.P., Cox, J., 1999. Tectonic setting, origin, and obduction of the Oman ophiolite, *Geological Society of America Bulletin*, 111(1): 104–122.

Searle, M.P., Malpas, J., 1980. The structure and metamorphism of rocks beneath the Semail Ophiolite of Oman and their significance in ophiolite obduction, *Transactions of the Royal Society of Edinburgh: Earth Sciences*, 71: 247–262.

Searle, R.C., Murton, B.J., Achenbach, K., LeBas, T., Tivey, M., Yeo, I., Cormier, M.H., Carlut, J., Ferreira, P., Mallows, C., *et al*., 2010. Structure and development of an axial volcanic ridge: Mid-Atlantic Ridge, 45°N, *Earth and Planetary Science Letters*, 299: 228–241.

Selbekk, R.S., Furnes, H., Pedersen, R.B., Skjerlie, K.P., 1998. Contrasting tonalite genesis in the Lyngen magmatic complex, north Norwegian Caledonides, *Lithos*, 42: 243–268.

Singh, S.C., Kent, G.M., Collier, J.S., Harding, A.J., Orcutt, J.A., 1998. Melt to mush variations in crustal magma chamber properties along the ridge crest at the southern East Pacific Rise, *Nature*, 394: 874–878.

Singh, S.C., Collier, J.S., Harding, A.J., Kent, G.M., Orcutt, J.A., 1999. Seismic evidence for a hydrothermal layer above the solid roof of the axial magma chamber at the southern East Pacific Rise, *Geology*, 27(3): 219–222.

Singh, S.C., Harding, A.J., Kent, G.M., Sinha, M.C., Combier, V., Bazin, S., Tong, C.H., Pye, J.W., Barton, P.J., Hobbs, R.W. and White, R.S., 2006. Seismic reflection images of the Moho underlying melt sills at the East Pacific Rise, *Nature*, 442(7100): 287-290.

Sinton, J.M., Detrick, R.S., 1992. Mid-ocean ridge magma chambers, *Journal of Geophysical Research*, 97: 197-216.

Sleep, N.H., 1975. Formation of oceanic crust: some thermal constraints, *Journal of Geophysical Research,* 80: 4037–4042.

Small, C. 1998. Global systematics of mid-ocean ridge morphology, pp. 59–115 in Faulting and Magmatism at Mid-Ocean Ridges. R. Buck, T. Delaney, A. Karson, and Y. Lagabrielle, eds, Geophysical Monograph Series, vol. 106, American Geophysical Union, Washington, DC.

Smewing, J. D., 1981. Mixing characteristics and compositional differences in mantle-derived melts beneath spreading axes: Evidence from cyclically layered rocks in the ophiolite of North Oman, *Journal of Geophysical Research*, 86(B4): 2645–2659.

Spray, J.G., Dunning, G.R., 1991. A U/Pb age for the Shetland Islands oceanic fragment, Scottish Caledonides: evidence from anatectic plagiogranites in ‘layer 3’ shear zones, *Geological Magazine*, 128:667–671.

Stakes, D.S., Taylor, H.P., 1992. The northern Samail ophiolite: an oxygen isotope, microprobe, and field study, *Journal of Geophysical Research: Solid Earth*, 97(B5): 7043-7080.

Stakes, D.S., Taylor, H.P., 2003. Oxygen isotope and chemical studies on the origin of large plagiogranite bodies in northern Oman, and their relationship to the

overlying massive sulphide deposits, *Geological Society of London Special Publication*, 218(1): 315–351.

Stewart, M.A., Karson, J.A., Klein, E.M., 2005. Four-dimensional upper crustal construction at fast-spreading mid-ocean ridges: A perspective from an upper crustal cross-section at the Hess Deep Rift, *Journal of Volcanology and Geothermal Research*, 144(1–4): 287–309.

Stern, R.J., Bloomer, S.H., 1992, Subdution zone infancy: Examples from the Eocene Izu-Bonin-Mariana and Jurassic California arcs. Geological Society of America Bulletin, 104:1621-1636.

Struder, L., Fiorini, C., Gatti, E., Hartmann, R., Holl, P., Krause, N., Lechner, P., Longoni, A., Lutz, G., Kemmer, J., Meidinger, N., Popp, M., Soltau, H., van Zanthier, C., 1998. High resolution nondispersive X-ray spectroscopy with state of the art silicon detectors, *Mikrochimika Acta* 15 (Suppl.): 11–19.

Sun, S.S., McDonough, W.S., 1989. Chemical and isotopic systematics of oceanic basalts: implications for mantle composition and processes, *Geological Society, London, Special Publications*, 42(1): 313-345.

Tamura, A., Arai, S., 2006. Harzburgite-dunite-orthopyroxenite suite as a record of supra-subduction zone setting for the Oman ophiolite mantle, *Lithos*, 90(1–2): 43–56.

Tilton, G.R., Hopson, C.A., Wright, J.E., 1981. Uranium-lead isotopic ages of the Samail ophiolite, Oman, with applications to Tethyan ocean ridge tectonics, *Journal of Geophysical Research*, 86(B4): 2763–2775.

Tinkham, D.K., Ghent, E.D., 2005. XRMapAnal: A program for analysis of quantitative X-ray maps, *American Mineralogist*, 90(4): 737-744.

Tippit, P.R., Pessagno, E.A., Smewing, J.D., 1981. The biostratigraphy of sediments in the volcanic unit of the Samail ophiolite, *Journal of Geophysical Research: Solid Earth*, 86(B4): 2756-2762.

Toomey, D.R., Jousselin, D., Dunn, R.A., Wilcock, W.S.D., Detrick, R.S., 2007. Skew of mantle upwelling beneath the East Pacific Rise governs segmentation, *Nature*, 446: 409-414.

Tsuchiya, N., Shibata, T., Yoshikawa, M., Adachi, Y., Miyashita, S., Adachi, T., Nakano, N., Osanai, Y., 2013. Petrology of Lasail plutonic complex, northern Oman ophiolite, Oman: an example of arc-like magmatism associated with ophiolite detachment, *Lithos*,156: 120–138.

Umino, S., Miyashita, S., Hotta, F., Adachi, Y., 2003. Along-strike variation of the sheeted dike complex in the Oman Ophiolite: Insights into subaxial ridge segment structures and the magma plumbing system, *Geochemistry Geophysics Geosystems*, 4.

VanTongeren, J.A., Kelemen, P.B., Hanghøj, K., 2008. Cooling rates in the lower crust of the Oman ophiolite: Ca in olivine, revisited, *Earth and Planetary Science Letters*, 267(1–2): 69–82.

Vera, E.E., Mutter, J.C., Buhl, P., Orcutt, J.A., Harding, A.J., Kappus, M.E., Detrick, R.S. & Brocher, T.M., 1990. The structure of 0- to 0.2-m.y.- old oceanic crust

at 9◦N on the East Pacific Rise from expanded spread profiles, *Journal of Geophysical Research*, 95(B10): 15 529–15 556.

Walker, D., Shibata, T., DeLong, S.E., 1979. Abyssal tholeiites from the Oceanographer Fracture Zone, *Contributions to Mineralogy and Petrology*, 70(2): 111–125.

Wanless, V.D., Perfit, M.R., Ridley, W.I., Klein, E., 2010. Dacite petrogenesis on mid-ocean ridges: evidence for oceanic crustal melting and assimilation, *Journal of Petrology*, 51: 2377–2410.

Warren, C.J., Miller, J.M., 2007. Structural and stratigraphic controls on the origin and tectonic history of a subducted continental margin, Oman, *Journal of structural geology*, 29(3): 541-558.

Warren, C., Parrish, R., Waters, D., Searle, M., 2005. Dating the geologic history of Oman's Semail ophiolite: Insights from U-Pb geochronology, *Contributions to Mineralogy and Petrology*, 150(4): 403–422.

Wilcock, W.S.D., Solomon, S.C., Purdy, G.M., Toomey, D.R., 1992. The seismic attenuation structure of a fast-spreading mid-ocean ridge, *Science*, 258: 1470-1474.

Xu, M., Canales, J.P., Carbotte, S.M., Carton, H., Nedimović, M.R., Mutter, J.C., 2014. Variations in axial magma lens properties along the East Pacific Rise (9°30′N–10°00′N) from swath 3-D seismic imaging and 1-D waveform inversion, *Journal of Geophysical Research*, 119(4): 2013JB010730.

Summary of electronic appendices

APPENDIX A-C excel workbooks:
Contains excel workbooks containing the tables for each of the print appendices. The files are: APPENDIX A- Sample list and descriptions, APPENDIX B- Analytical tables for Whole Rock precision, and APPENDIX C- Whole Rock Tables.

APPENDIX E1- Wadi Saq Whole Rock Data:
This is an excel workbook which contains the entirety of the Wadi Saq whole rock data split between two worksheets for ICP-MS and ICP-OES data. Each of these worksheets are grouped according to mapped unit. A third worksheet is provided which contains Tables 6.1 and 6.2 of the text (unit averages by ICP-MS and ICP-OES).

APPENDIX E2- QACD Software:
The entirety of the python scripts and files needed for the QACD software. See the user manual for instructions. At this moment the software requires an installation of Python to work. The 'Main.py' file is the script that is used to execute the software.

APPENDIX E3- QACD User Manual:
A pdf of the most up-to-date version of the QACD User Manual. This guide is for familiarising the user with the QACD process and provides information regarding what modules need to be installed in the python libraries for operation. For future reference, the most up-to-date version of the QACD software and the user manual can be found on the GitHub repository (www.github.com/mloocke/QACD-quack).

APPENDIX E4- Hess Deep Element Maps and Histograms:
A copy of the supplementary files for the Hess Deep AML investigation as they were submitted to *Nature Geoscience*.

APPENDIX E5- Wadi Saq Thin Section Scans:
Scans of the Wadi Saq thin sections organised by lithology.

APPENDIX E6- High resolution thesis figures:
High-resolution copies of the figures used in the printed thesis, organised by chapter.